Optical near-fields & nearfield optics

Edited by Alfred J. Meixner and Paul Leiderer

Imprint

Optical near-fields & nearfield optics

Alfred J. Meixner[*1] and Paul Leiderer[*2]

Editorial

Address:
[1]Institute of Physical and Theoretical Chemistry, University of Tübingen, Auf der Morgenstelle 18, 72076 Tübingen, Germany and
[2]Physics Department, University of Konstanz, Universitätsstraße 10, 78464 Konstanz, Germany

Email:
Alfred J. Meixner[*] - alfred.meixner@uni-tuebingen.de; Paul Leiderer[*] - paul.leiderer@uni-konstanz.de

* Corresponding author

Optical methods provide exceedingly powerful tools in science and technology for measuring, analyzing and manipulating, from optical microscopy and spectroscopy to the characterization of ultrafast processes by femtosecond pulses and the modification of materials by intense laser radiation. However, when it comes to applications in the nanometer-regime, the conventional optical techniques suffer from the resolution limit – formulated by Ernst Abbe one and a half centuries ago – that light cannot be focused to a diameter much less than half its wavelength. This seems like a serious drawback for the use of optics in nanoscience and nanotechnology, since many of the nanostructures of interest are distinctly smaller than this limit of a few hundred nanometers. Fortunately, this restriction can be overcome, if one does not rely on focusing with lenses and mirrors in the optical far-field, but rather exploits the optical near-field in the vicinity of nanostructures. In this Thematic Series, various examples for the use of optical near-fields and near-field optics are presented.

Metallic nanostructures, especially noble metals such as gold and silver, are efficient for nano-focusing and controlling light on the nanoscale, because they support surface plasmons, i.e., collective excitations of the electron gas, which couple strongly to light. As a result, the optical near-field around such plasmonic structures can be enhanced by orders of magnitude compared to the incident light intensity, and can be localized in "hot spots" with a length of a few nanometers. This effect of strong near-field enhancement around sharp structures of noble metals has been known from Surface Enhanced Raman Scattering (SERS) for a long time [1]. Yet, the well-controlled tailoring of nanostructures necessary to quantitatively control the optical near-field has only emerged a few years ago. In this issue, Katrin and Harald Kneipp [2] address in their contribution the possibility to probe the plasmonic near-fields by one- and two-photon excited surface enhanced Raman scattering at the level of single molecules. In addition to SERS, there are numerous other applications of near-field enhancement, e.g., in biosensors, solar cells and semiconductor quantum dots to name but a few.

A challenging question, investigated in this series by Esmann et al. [3], is how light can be most efficiently coupled into sub-wavelength dimensions by means of an "optical antenna". Since the fabrication of suitable structures with electron beam or

focused ion beam lithography is a tedious and time-consuming task, the experiments are more and more supported by modeling with numerical methods such as Finite Difference Time Domain (FDTD) and Discrete Dipole Approximation (DDA). For the modeling to be reliable, it is essential to quantitatively compare the results of simulations with experimental data. To this end, various schemes have been developed, like Scanning Near-field Optical Microscopy (SNOM) and Photoelectron Electron Microscopy (PEEM), in order to image optical near-fields of nanostructures. Since the field enhancement can be quite large, light-induced local changes of the material can also be utilized to map the spatial distribution of the near-fields as demonstrated by Dickreuter et al. [4]. For this purpose, light-induced local changes of the material of both the nanostructure itself by local melting and the substrate by ablation at the positions of the hot spots may be used.

The interaction of plasmonic structures with their surroundings can be employed to tune their optical properties, e.g., by using a dielectric phase change material like GeSbTe as a substrate, whose refractive index can be externally adjusted in various ways. As shown by Hong et al. [5], this is a promising new approach for nano-circuitry, bio-assay addressing and imaging applications. A particularly intriguing effect, investigated by Arnold et al. [6], is the interaction of plasmonic structures with dielectric material that is doped with fluorescent molecules: when the emission line of the dye and the absorption resonance of the nanostructures coincide, the damping of the plasmons can be compensated by the gain in the dielectric material, so that laser-like radiation could emerge from such structures (so-called spasers).

The mechanical effects of the optical near-fields can be substantial. Examples are specially shaped nano-holes, studied by Rosa et al. [7], which can be much more efficiently used as plasmonic optical tweezers for nano-objects than the usual far-field tweezers.

In spite of the high efficiency of plasmonic metal nanostructures, the near-field enhancement of dielectric structures is preferable for some applications. Walhorn et al. [8] have developed a method for the simultaneous recording of topography and fluorescence that allows for the localization of distinct building blocks of supramolecular structures below the usual optical resolution. This is facilitated by using the optical near-field around a sharp dielectric AFM tip to excite the fluorescent molecules – a metallic tip would quench the fluorescence. The optical near-fields of dielectric objects can also be used to study the interaction of intense laser radiation with surfaces on ultra-short time scales, which avoids complications like self-focusing that arise otherwise, as shown by Kühler et al. [9].

The examples given above illustrate the broad spectrum of applications of optical near-fields and near-field optics. The goal of this Thematic Series is not to provide a comprehensive review of all the aspects of this theme, but rather to highlight several facets in a rapidly developing research field. We sincerely thank all colleagues who contributed to this Thematic Series with their interesting and exciting results.

Alfred J. Meixner and Paul Leiderer

Tübingen, Konstanz, January 2014

References

1. Moskovits, M. *Rev. Mod. Phys.* **1985,** *57,* 783–826. doi:10.1103/RevModPhys.57.783
2. Kneipp, K.; Kneipp, H. *Beilstein J. Nanotechnol.* **2013,** *4,* 834–842. doi:10.3762/bjnano.4.94
3. Esmann, M.; Becker, S. F.; da Cunha, B. B.; Brauer, J. H.; Vogelgesang, R.; Groß, P.; Lienau, C. *Beilstein J. Nanotechnol.* **2013,** *4,* 603–610. doi:10.3762/bjnano.4.67
4. Dickreuter, S.; Gleixner, J.; Kolloch, A.; Boneberg, J.; Scheer, E.; Leiderer, P. *Beilstein J. Nanotechnol.* **2013,** *4,* 588–602. doi:10.3762/bjnano.4.66
5. Kao, T. S.; Chen, Y. G.; Hong, M. H. *Beilstein J. Nanotechnol.* **2013,** *4,* 632–637. doi:10.3762/bjnano.4.70
6. Arnold, N.; Ding, B.; Hrelescu, C.; Klar, T. A. *Beilstein J. Nanotechnol.* **2013,** *4,* 974–987. doi:10.3762/bjnano.4.110
7. Seniutinas, G.; Rosa, L.; Gervinskas, G.; Brasselet, E.; Juodkazis, S. *Beilstein J. Nanotechnol.* **2013,** *4,* 534–541. doi:10.3762/bjnano.4.62
8. Harder, A.; Dieding, M.; Walhorn, V.; Degenhard, S.; Brodehl, A.; Wege, C.; Mitting, H.; Anselmetti, D. *Beilstein J. Nanotechnol.* **2013,** *4,* 510–516. doi:10.3762/bjnano.4.60
9. Kühler, P.; Puerto, D.; Mosbacher, M.; Leiderer, P.; Garcia de Abajo, F. J.; Siegel, J.; Solis, J. *Beilstein J. Nanotechnol.* **2013,** *4,* 501–509. doi:10.3762/bjnano.4.59

Femtosecond-resolved ablation dynamics of Si in the near field of a small dielectric particle

Paul Kühler[1,2], Daniel Puerto[1,3], Mario Mosbacher[4], Paul Leiderer[4], Francisco Javier Garcia de Abajo[5], Jan Siegel[*1] and Javier Solis[*1]

Full Research Paper

Address:
[1]Laser Processing Group (LPG), Instituto de Optica, CSIC, Serrano 121, 28006 Madrid, Spain, [2]Current affiliation: Faculty of Physics, Ludwig-Maximilians-Universität München, Amalienstraße 54, 80799 München, Germany, [3]Current affiliation: Centro de Tecnología Nanofotónica, Universidad Politécnica de Valencia, Edificio 8B, Camino de Vera s/n., 46022 Valencia, Spain, [4]Faculty of Physics, Universität Konstanz, Universitätsstraße 10, 78457 Konstanz, Germany and [5]Instituto de Química Física "Rocasolano", CSIC, Serrano 119, 28006 Madrid, Spain

Email:
Jan Siegel[*] - j.siegel@io.cfmac.csic.es;
Javier Solis[*] - j.solis@io.cfmac.csic.es

* Corresponding author

Keywords:
crystalline Si; fs-resolved microscopy; laser ablation; near-field enhancement; ultrafast dynamics

Abstract

In this work we analyze the ablation dynamics of crystalline Si in the intense near field generated by a small dielectric particle located at the material surface when being irradiated with an infrared femtosecond laser pulse (800 nm, 120 fs). The presence of the particle (7.9 μm diameter) leads to a strong local enhancement (ca. 40 times) of the incoming intensity of the pulse. The transient optical response of the material has been analyzed by means of fs-resolved optical microscopy in reflection configuration over a time span from 0.1 ps to about 1 ns. Characteristic phenomena like electron plasma formation, ultrafast melting and ablation, along with their characteristic time scales are observed in the region surrounding the particle. The use of a time resolved imaging technique allows us recording simultaneously the material response at *ordinary* and *large* peak power densities enabling a direct comparison between both scenarios. The time resolved images of near field exposed regions are consistent with a remarkable temporal shift of the ablation onset which occurs in the sub-picosend regime, from about 500 to 800 fs after excitation.

Introduction

The term "near field optics" is used to describe the phenomena associated to non-propagating and highly localized electromagnetic fields and their interaction with matter. Optical near fields (ONF's) can be generated in the vicinity of metal or dielectric nanoparticles, leading to physical properties that are drastically different from their free-propagating counterparts [1]. Evanes-

cent waves, for instance, are not purely transverse and ONF's have the ability to localize electromagnetic energy to length scales well below the diffraction limit [2]. Moreover, the localization of electromagnetic energy in the vicinity of a small metallic or dielectric scattering particle leads to a local increase of the intensity of an incoming electric field. As a consequence, the electric field can be enhanced by several orders of magnitude which is particularly useful for exciting optical non-linearities (Kerr, Raman, … [3,4]) in the vicinity of metal particles.

For dielectric particles, Mie scattering can similarly lead to strong field enhancement effects [5,6] which have found increasing applications in nano-structuring [7,8] and materials nano-fabrication [9,10]. As an example, Figure 1 shows a schematic 3D representation of the calculated intensity distribution at the surface of a crystalline Si wafer in the vicinity of a 7.9 μm-diameter SiO_2 spherical particle, illuminated at oblique incidence by a laser with a wavelength of 800 nm. The intensity distribution shows a bright spot corresponding to an enhancement factor of the order of 40, evidencing that in a first approach the particle (with a Mie parameter $ka \approx 40$, where a is the particle radius and k the wave vector of the scattered light) behaves like a spherical lens. A closer look at the spatial distribution of intensities reveals a fine structure with characteristic maxima and minima that cannot be predicted by a simple geometrical model and that depends on the complex interference of the incoming laser beam, the light reflected at the substrate surface, and the light scattered by the particle [11]. If we consider an excitation pulse of 100 femtoseconds (fs) duration reaching the surface with a homogenous fluence of 1 J/cm^2, the local fluence at the maximum of the near field distribution would reach 40 J/cm^2 or 400 TW/cm^2. To reach such a peak power density using a short focal length lens would be difficult, among other reasons, due to the fact that we would exceed by large the critical power for self-focusing and induce dielectric breakdown of air, leading to pulse distortion. ONF's enable thus to investigate laser–matter interaction processes at large power densities, difficult to achieve using conventional means.

In this work we have analyzed the ablation dynamics of crystalline silicon (c-Si) under the intense near field caused by a small dielectric sphere located at the material surface when being irradiated with a 120 fs long 800 nm wavelength laser pulse. In the study, we have reached locally enhanced fluences up to 35 J/cm^2 ($\approx$300 TW/cm^2) (for comparison the fluence threshold for surface ablation is $\approx$0.5 J/cm^2 [12]) and used fs-resolved microscopy in order to access time scales associated to characteristic events, like plasma formation, ultrafast melting or material ablation. The material behavior in the near field region is consistent with a pronounced temporal shift of the characteristic interaction events with respect to that
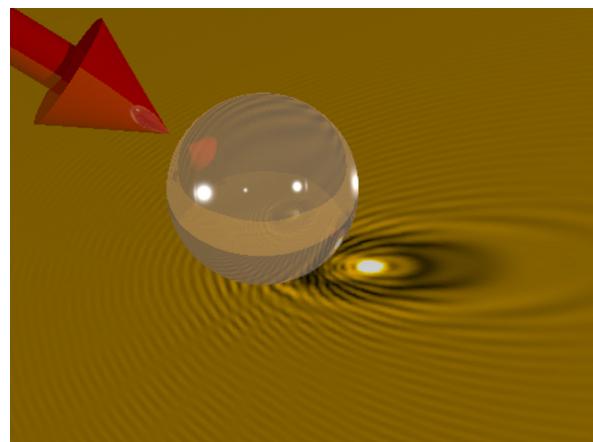

Figure 1: Schematic view of the spatial intensity distribution at the surface of a crystalline Si substrate in the vicinity of a 7.9 μm-diameter SiO_2 spherical particle illuminated at oblique incidence by a laser with 800 nm wavelength. The bright spot corresponds to the enhancement of the incoming field. The fine fringe structure is caused by interference of the incoming laser beam, light reflected at the substrate, and light scattered by the particle.

observed at the much lower fluences present outside the ONF region (up to 0.91 J/cm^2). Interestingly, the lift-up time of the particle upon ablation of the near field exposed region is beyond 20 ns, which is the maximum temporal window accessible with our setup.

Experimental
Sample preparation
Spherical SiO_2 particles with 7.9 μm in diameter (Bangs Laboratories, Inc., nominal polydispersity 2%) stored in isopropanol, were deposited on a Si(001)-wafer by means of spin coating. Using this technique it is feasible to control the particle density as well as it features prevalent particle isolation in the resulting distribution, with a particle separation much larger than the size of the irradiation beam.

In order to image the expected near field structure upon surface illumination a sample consisting of 40-nm-thick, face-centered-cubic (fcc) polycrystalline $Ge_2Sb_2Te_5$ (GST) on a Si(001) substrate covered by a 10-nm-thick amorphous SiO_2 film was used. Further details regarding the preparation procedure and optical properties of the different substrates and particles used, as well as near field imaging using GST films can be found elsewhere [11].

Femtosecond laser irradiation and time-resolved microscopy
Figure 2 shows a scheme of the set-up used for irradiating the samples and acquiring the fs-resolved surface reflectivity images. The pump-probe microscope uses a single 120 fs pump
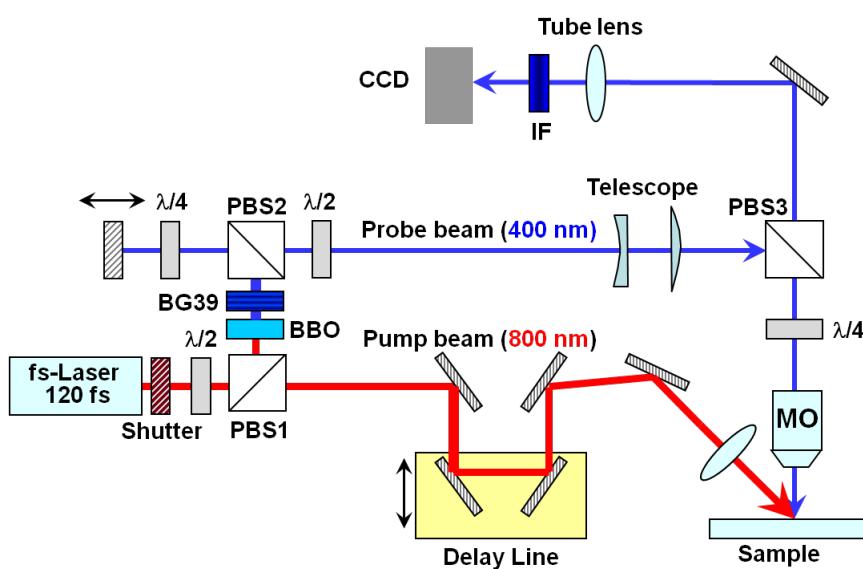
Figure 2: Scheme of the experimental set-up used for sample irradiation and fs-resolved microscopy. (IF) interferential band-pass filter centered at 400 nm, PBS (polarizing beam-splitter cubes), (BBO) beta barium borate frequency doubling crystal, (MO) microscope objective, (λ/2, λ/4) wave-plates, (BG39) high frequency band-pass filter.

pulse at 800 nm, which was selected by using an electro-mechanical shutter. The pump beam (s-polarized) is focused at an angle of incidence of 54° onto the sample surface to a (elliptical) size of 106.6 μm × 62.2 μm ($1/e^2$ intensity diameter). An optical delay line allows controlling the relative times of arrival to the surface of the pump and probe pulse. The combination of a λ/2-wave-plate at 800 nm and a polarizing beam splitter (PBS1) enables extracting a small fraction of the pump beam which is used for generating the frequency-doubled probe beam by means of a β-BaB_2O_4 (BBO) crystal and a BG39 optical short pass filter. A coarse delay line for the probe pulses is then configured by means of another polarizing beam splitter PBS2 and a λ/4-wave-plate at 400 nm. The region irradiated by the pump pulse is imaged (for a given delay) by using the 400 nm probe pulse as illumination source, combined with a telescope, a long working distance microscope objective (MO, 20×, NA = 0.42), and a tube lens. A polarizing cube beam splitter (PBS3) is used to steer the probe beam in order to illuminate the surface at normal incidence while a λ/4-wave-plate at 400 nm ensures that the light reflected from the sample passes back through PBS3 towards the imaging system. A narrow band-pass filter centered at 400 nm blocks the pump pulse scatter and plasma emission while the probe light reaches the (12-bit) CCD, which records the images. The temporal resolution of the system (mostly limited by group velocity dispersion of the 400 nm probe beam in the PBS3 and the MO) is about 300 fs. Further details about the irradiation and imaging setup can be found elsewhere [13,14]. It is worth noting, though, that the spatial Gaussian intensity profile of the irradiation beam results in a position-

dependent fluence distribution. As a consequence, a reflectivity image for a given delay contains not only spatial information but also information about the fluence dependence of the process.

The sample is mounted on a computer controlled micrometer-adjustable three-axis translation stage. Since irradiation leads, in most cases, to permanent structural modifications of the surface, each region containing a particle is irradiated only once for a given delay between the pump and probe pulses. Irradiations under the same conditions are similarly acquired in particle-free regions for comparison purposes.

Image processing
During the image acquisition process, three different images are acquired for a given delay. A first image, blocking the pump beam, is used for normalization purposes. This enables normalizing the transient reflectivity changes recorded in the second image, acquired for a given delay with the pump beam unblocked. A third image of the already irradiated surface is acquired and normalized as indicated in order to observe the state of the surface after irradiation. This image is acquired typically a few seconds after irradiating the surface. When a particle is present in the irradiated regions surface this normalization procedure also helps in reducing the strong scattering caused by the particle. As a consequence, in the time-resolved images, the particle is barely visible, although small beam pointing fluctuations can render an image normalization process not completely effective.

Near field distribution simulations

The spatial intensity distribution produced by the particle at the substrate plane upon illumination has been calculated by a rigorous solution of Maxwell's equations for a sphere sitting on a planar substrate, using the method fully elaborated in [11], based on the methods described in [15].

Results and Discussion
Structural transformation dynamics of the particle-free Si surface

In order to compare the temporal evolution of the material in a particle's near field to that of a particle-free surface we have performed a dedicated experiment on bare Si. Figure 3 shows several images of the evolution of the reflectivity of a particle-free, c-Si surface upon exposure to a 120 fs laser pulse with a peak fluence of 0.91 J/cm^2. With a reflectivity of 0.52 of the surface at 54° for s-polarized light, this corresponds to an absorbed fluence of 0.44 J/cm^2. Since the melting and ablation dynamics of c-Si upon fs-laser excitation has already been analyzed in detail [16,17] we will briefly describe only the main features of the process. To facilitate the description we have included in Figure 4 the evolution of the surface reflectivity measured at the center of the irradiated region, i.e., at the position of maximum fluence.

The image at 200 fs delay shows the formation of a bright region in the laser irradiated zone due to the formation of a dense free-electron plasma. The decrease of the plasma reflectivity along the horizontal axis from the left to the right is the consequence of the irradiation angle which makes the pulse to reach the surface with an increasing delay. The difference in the "landing time" of the irradiation pulse over the $1/e^2$ diameter of
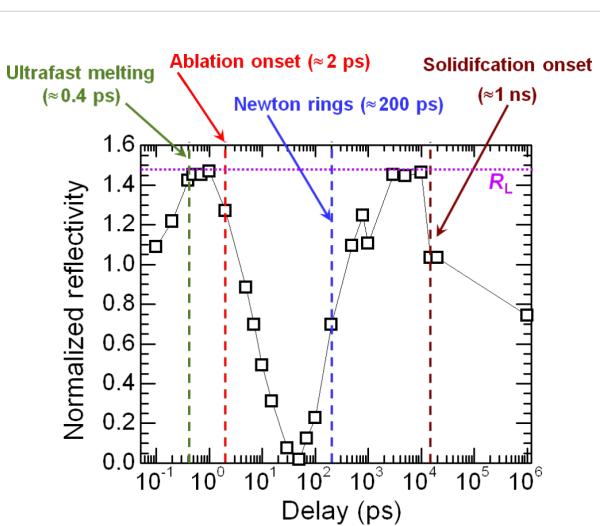
Figure 4: Normalized reflectivity as a function of delay measured for a particle-free, c-Si surface, at the center of the irradiated region for a peak fluence of 0.91 J/cm^2. The point at 10^6 ps corresponds to an actual delay of several seconds (denoted as ∞ in Figure 3). The onset of the most characteristic events is indicated by arrows. R$_L$ indicates the relative reflectivity at 400 nm (1.48) of an optically thick molten liquid layer. The line is a guide to the eye.

the beam is about 200 fs. At longer delays, the reflectivity of the irradiated region increases and reaches a saturation value very close to the reflectivity expected for molten Si at approximately 400 fs (see Figure 4). It is worth noting that this saturation value is "fluence independent", i.e., it is the same over the whole bright region showing a sharp threshold. This points to the fact that the material has undergone the so called *ultrafast* or *non-thermal* melting process, a structural transition due to the instability of the crystal lattice in the presence of a dense
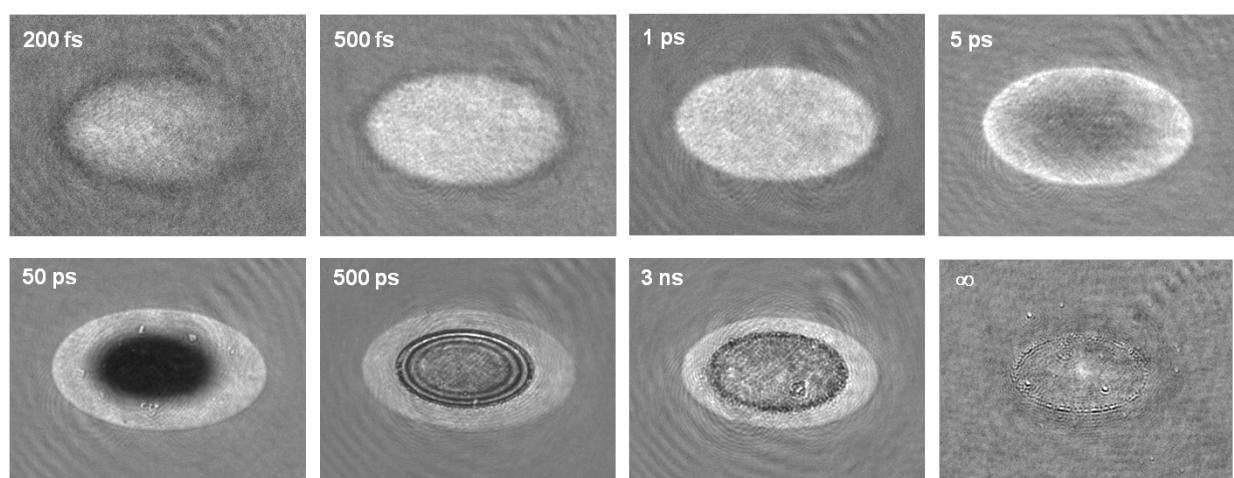
Figure 3: Surface reflectivity images of a particle-free c-Si surface exposed to a 120 fs laser pulse for different time delays between the excitation and illumination pulses. The peak fluence is 0.91 J/cm^2. The frame size is 93 × 69 µm^2. The brightness and contrast of each image have been adjusted to improve the visibility of the main features.

electron–hole plasma ($\approx 10^{22}$ cm^{-3}, 10% of the whole valence population) [18]. Approximately 1 ps after excitation, the highly excited material relaxes to *thermal* liquid-Si.

The reflectivity at the center of the irradiated zone starts to decrease afterwards (see in Figure 3 the image at 5 ps delay) showing a characteristic dark zone which will be observable for delays up to 100 ps. This reflectivity decrease is indicative of the ablation of the surface. The emission of ions and neutral species in the ablating region leads to a strong absorption of the illumination probe beam. The ablation onset occurs at about 2 ps, although strong ablation effects (a reflectivity decrease below half of the maximum) are observed later, at about 10 ps (see Figure 4). The dark zone is surrounded by a brighter ring corresponding to liquid Si. The reflectivity in the center reaches its minimum in 50 ps and starts to recover showing a characteristic ring structure (Newton rings) over a time window of 200–1000 ps (see in Figure 3 the image at 500 ps delay). The observation of Newton rings is due the formation of a transparent but dense ablating layer with a sharp interface [18]. The rings disappear after a few nanoseconds, as can be seen in the image for a 3 ns delay in Figure 3. At this delay it can also be noticed that the extension of the molten region surrounding the ablated crater is shrinking as a consequence of solidification. After ca. 20 ns no further structural changes are observed at the surface, which features an ablated crater (see in Figure 3 the image at ∞, corresponding to a few seconds delay). The thresholds for thermal melting and ablation deduced from the images are 0.26 J/cm^2 and 0.54 J/cm^2, respectively (corresponding to absorbed fluences of about 0.13 J/cm^2 and about 0.26 J/cm^2).

Structural transformation dynamics at the near field excited Si surface

In order to gain a better insight of the expected features when irradiating a particle placed on the Si surface, we have calculated the expected near field intensity distribution as shown in Figure 5a. Nearby the dielectric particle a very small spot where the incoming intensity is enhanced by a factor of about 40 can be observed. A closer look at the image indicates the presence of a fine structure showing characteristic interference maxima and minima. In order to better appreciate these details, in Figure 5b, the same intensity distribution has been plotted with a saturated intensity scale (displaying only up to 1.6) and inverting colors for clarity (the region of maximum enhancement now looks black). A complex intensity distribution is seen around the particle, where the observed ring period is larger in the beam propagation direction (forward) than in the backscattered one. Regions with local intensity values above and below that of the incoming illumination beam can be distinguished. The period of the observed intensity distribution along the surface projection of the beam propagation axis far from the particle corresponds to $\lambda_{inc}/(1 \pm \sin\theta)$ (i.e., ≈ 0.4 and ≈ 4.0 µm, respectively, for the backward and forward directions, where θ is the angle of incidence) as expected for the interference of a spherical wave with a scattering source [11]. For comparison, in Figure 5c we have included an optical micrograph (in reflection) obtained upon illumination of a GST film with a 120 fs laser pulse with a peak fluence of 12.3 mJ/cm^2, at the same angle of incidence. As shown in [11], GST (see above) has been successfully used to image and quantitatively analyze the spatial near field intensity distribution generated by a particle on a surface by imprinting a corresponding pattern through local amorphization.

We can see that the intensity modulation associated to the near field is replicated by a periodic variation of the reflectivity of the illuminated material, which is formed by alternating amorphous and crystalline regions depending on whether the local fluence is above or below the melting threshold of polycrystalline GST. We have checked that the calculated spatial distribution of the near field is essentially the same for both Si and GST substrates.

Figure 5: (a) Calculated near field distribution at the surface of a Si substrate for a SiO$_2$ dielectric particle of 7.9 µm diameter homogenously illuminated at a wavelength of 800 nm and at an angle of 54°. The position of the particle is shown as a semitransparent circle. The spatial intensity distribution has been normalized to the incoming beam intensity (I_0). (b) Same as (a) but re-scaling the color scale to a maximum enhancement factor (I/I_0) of 1.6. As a consequence the intensity distribution at the region of the maximum intensity of (a) is saturated (black color). (c) Optical reflectivity micrograph of the surface of a GST film on c-Si after exposure to a 12.3 mJ/cm^3 peak fluence pulse at the same angle of incidence.

The comparison between the imprinted and calculated near field distribution shows an excellent agreement which allows us to conclude that our calculation of the maximum field enhancement expected ($\approx$40) on the Si substrate for the particle size and irradiation geometry considered is quite accurate. When a pulsed laser of moderate fluence illuminates the surface, the local fluence close to the particle can thus reach easily a value above the ablation threshold of the surface. This leads to the removal of the particle, which is ejected from the surface due to the pressure generated by the expanding plasma, as shown in several "dry" laser cleaning experiments with short laser pulses [5].

Figure 6 shows the reflectivity evolution at the particle location for illumination with a peak fluence of 0.11 J/cm^2, which is below the melting threshold of the surface (0.26 J/cm^2) but above the threshold for particle removal (0.09 J/cm^2). Images corresponding to the surface before and after the arrival of the illumination pulse to the surface are included for reference. The image "before" shows the particle as a round scattering, dark contrasted circle. In order to reduce scattering artifacts in the time-resolved images they have been normalized (except in the one obtained "after", with a delay of several seconds, as above indicated) by dividing them by an image obtained blocking the pump laser. As a consequence, the position of the particle can be appreciated as a set of concentric rings with a smooth grey contrast.

In the following we will compare the behavior observed in the images of Figure 6 to the behavior of the particle-free surface in Figure 3. In this latter case the surface experiences a peak fluence of 0.91 J/cm^2 while the region of maximum field enhancement for the particle corresponds to ca. 4 J/cm^2. For the comparison of both sets of images we have to consider that the spatial resolution of the imaging system is limited ($\approx$1 µm). As a consequence, any spatial feature, even with a strong reflectivity contrast, will appear blurred and feature a reduced contrast if its size is below the resolution limit. As a consequence, it is not possible to provide a plot with the quantitative temporal evolution of the reflectivity similar to that shown in Figure 6.

As we can see in Figure 6, already for a delay of 200 fs we can observe the formation of a bright spot located adjacent to the particle position (coinciding with the bright region in Figure 5a where maximum field enhancement is induced) which evidences the formation of a dense electron plasma. The next image, at 300 fs, shows that both the intensity and size of the bright region at the edge of the particle are reduced. For further delays (0.5–2 ps), the images show a very similar appearance, with a small ellipse (see the insets with a 2× zoom of the relevant region) with a bright perimeter that scatters the probe beam light. We know from the behavior of the particle-free surface that the ablation onset occurs (for much lower local fluences) for delays as short as 2 ps (see Figure 4). The similarity of the images in the delay interval from 500 fs up to 2 ps thus strongly suggest that the formation of the ellipse with bright borders (lower reflectivity at the center) might be indicative of the onset of ablation at large local fluences (4 J/cm^2) already after less than 1 ps (500–800 fs, considering the time resolution of the experimental setup). When considering this temporal delay, (500–800 fs) it must be emphasized that the ablation process (thermal) requires the transfer of energy from excited carriers to the lattice via e-ph scattering. The ablation onset cannot there-
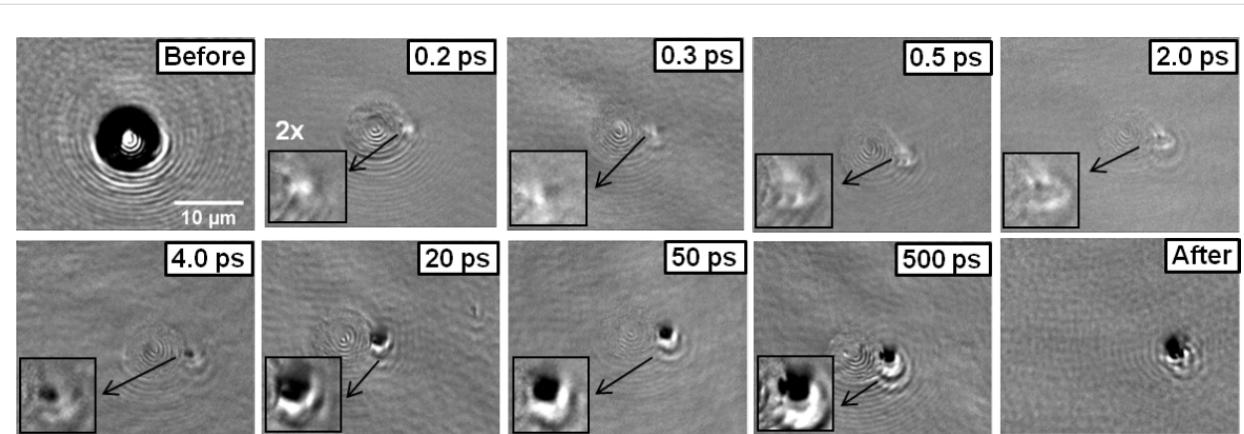
Figure 6: Surface reflectivity images at the particle location for different time delays, upon exposure to a 120 fs-laser pulse with a peak fluence of 0.11 J/cm^2 reaching the surface at 54°. With the exception of the images corresponding to the surface before and after the arrival of the laser pulse, the images have been normalized to an image obtained blocking the pump pulse in order to minimize the scattering effects caused by the 7.9 µm-diameter particle. The delay is indicated in each image. A zoom (2×) has been applied to the relevant part of the image and pasted as an inset to facilitate the description in the text.

fore be temporally shifted to times shorter than the characteristic e-phonon scattering time.

Different carrier density dependent relaxation mechanisms have been proposed to explain extremely large collision frequencies ($>2 \times 10^{15}$ s^{-1}) in c-Si for carrier densities above 10^{22} cm^{-3} (see [16] and references quoted therein). For what concerns the e-phonon scattering time, a carrier relaxation lifetime of only 240 fs, involving ultrafast lattice heating, has recently been reported for Si using two-photon photoemission spectroscopy [19]. Even assuming the fact that ablation is in itself a thermal process and considered as slow [20], the temporal border between electronic excitation alone and lattice heating is somewhat diffuse. The fact that thermal melting is already observed at a 2 ps delay at lower peak fluences in the particle-free surface points to a shorter (<1 ps) ablation onset for the much larger fluence in the near field exposed region. Indeed, at a 4 ps delay, the formerly bright region (at 200 fs) turns dark, indicating that strong ablation is already taking place. A comparison of the images at 5 ps and 50 ps delays for the particle-free surface (Figure 3) and the image for 4 ps in Figure 6 clearly shows that the onset of strong ablation has clearly shifted to shorter times in the near field region. These observations are consistent with an ablation onset occurring 500–800 fs after excitation in the near field region, as indicated in the previous paragraph. This delay, of the order of twice the e-ph scattering time, is close to the temporal limit for which ablation can be first observed after excitation.

Interestingly, unlike the case of the particle-free surface, in the time lapse from 4 ps to 20 ps the size of the ablating region expands (see 2× zoom region for both delays in Figure 6). This is indicative of collateral effects of the ablating region, initially confined to a very small region, unlike in Figure 3. The maximum contrast of the ablating dark region is reached within about 50 ps. Still, in the 50–500 ps interval, the lateral dimensions of the black spot and its contrast remain essentially unchanged. It is therefore not possible to assess when the ablation process terminates, as the observed contrast in both images may be caused by plasma absorption or by the formation of a hole of several tens of nm depth, as seen in the image labeled "After" in Figure 6. We can conclude though, from images for a delay of 20 ns (not shown) where the particle is still observed that the particle lift-up is largely delayed. A crude estimation of the maximum velocity of the particle can be obtained by assuming the particle travels a distance of the order of the Rayleigth range of the imaging lens used, ≈1 μm at 400 nm (equivalent to half of its depth of focus, DOF) in time lapse of the order of more than 20 nanoseconds. This leads to a maximum value below 50 m/s, or an acceleration below roughly 10^9 m/s^2 (10^8 g$_0$), equivalent to a force of ≈0.5 × 10^{-3} N. Obviously the relative slowness of particle lift up process is related to the large mass of the particle when compared to that of light ablation products (neutrals, ions, …).

In order to analyze the material response at even higher local fluences and confirm the apparent temporal shift of the ablation process above discussed, experiments with a peak fluence of 0.87 J/cm^2 (corresponding to a field-enhanced fluence 34.8 J/cm^2) were also performed. Figure 7 includes two relevant images corresponding to delays of 2 and 20 ps. In this case, the images have not been normalized to minimize the noise scattering effect associated to the particle which appears as a black sphere at the center. The peak fluence used is above the ablation threshold and comparable to the one corresponding to the images in Figure 3 (0.91 J/cm^2). We can see how a molten silicon layer is present at the surface (see above description of Figure 3) for a delay of 2 ps. A close-up look to the region
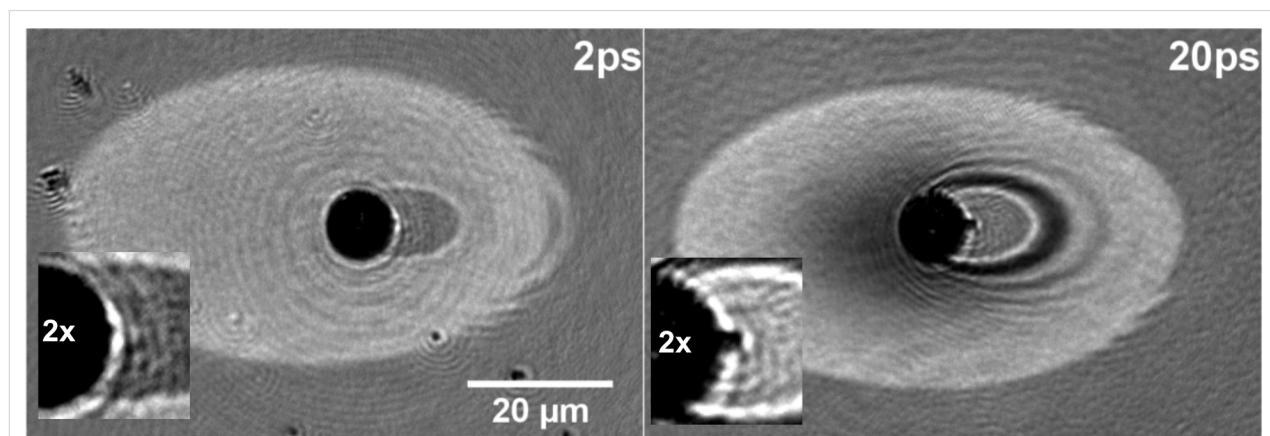

Figure 7: Surface reflectivity images at the particle location for two different delays (indicated), upon exposure to a 120 fs-laser pulse with a peak fluence of 0.87 J/cm^2 reaching the surface at 54°. A zoom (2×) has been applied to the relevant part of the image and pasted as an inset to facilitate the description in the text.

nearby the particle (see the 2× zoomed inset) shows though a tiny black dot adjacent to the position of the sphere which evidences that for this delay the focus region is already undergoing strong ablation. This observation is consistent with the above discussed temporal shift of the ablation process into the sub-picosecond range. The effect of the field enhancement can actually also be seen at the right edge of the molten region where part of the fine structure of the near field and far field scatter distribution is visible in form of a structured distribution of molten material. Indeed, the light scattered by the particle in the forward direction induces melting outside the region where the pump beam is concentrated.

The region where maximum field enhancement is achieved is more evident in the image for 20 ps, as the dimensions of the strongly ablating spot are now larger (see also the 2× zoomed inset). The "tiny black dot" observed in the 2 ps image is now a nearly elliptically shaped region undergoing, as expected, strong ablation. The effect of the near field, apart from the region of maximum field enhancement, is also visible as a characteristic ring pattern. It shows bright regions where destructive interference has inhibited the onset of ablation and dark regions where constructive interference drives the material into the strong ablation regime. This is evident when comparing the overall appearance of the image to that shown in Figure 5b. It is interesting to notice that there are no completely "shaded" regions and material melting occurs also within the shadow region of the sphere. This is an effect of the near field and fully consistent with the calculated intensity distribution shown in Figure 5b.

Conclusion

In this work we have analyzed the ablation dynamics of crystalline Si in the near field region of a dielectric particle upon illumination with a 120 fs laser pulses at 800 nm. For this purpose we have used fs-resolved microscopy to compare the behavior of regions excited inside and outside the near field region generated by a 7.9 μm-diameter SiO_2-sphere for different time delays where characteristic interaction events (plasma formation, ultrafast and thermal melting and ablation) can be observed. The recorded time resolved images are consistent with a temporal shift of both the ablation onset and the strong ablation regime to shorter delays. For the ablation onset, enhanced local intensities of the order of 4 J/cm^2 lead to an ablation onset in the sub-picosecond range (500–800 fs) while for local intensities of the order of 35 J/cm^2 strong ablation can be observed for delays as short as 2 ps. These time scales are likely in the limit of observable ablation (thermal) processes as the delays for which ablation is first observable reach values close to the e-phonon scattering time in crystalline Si [19]. Images of the surface obtained for long delays indicate that in spite of the large local fluences achieved, particle lift up, caused by the ablation of the underneath material is a relatively slow process. The time required for the particle to traverse a distance of the order of the Rayleigh range of the imaging optics used is beyond 20 ns which indicates that maximum particle accelerations achievable are of the order, or below, 10^9 m/s^2 (at least for particles with a Mie parameter well above one).

The results achieved also show that near field effects can be used to analyze ultrafast laser-matter interaction phenomena at large fluences avoiding, in a relatively simple manner, undesirable side effects of large peak power interactions, like self-focusing and dielectric breakdown in air. Time-resolved microscopy provides then extremely valuable information of the interaction dynamics.

References

1. Novotny, L. The History of Near-field Optics. In *Progress in Optics;* Wolf, E., Ed.; Elsevier: Amsterdam, 2007; Vol. 50, Chapter 5, pp 137–184.
2. Ohtsu, M. *Optical Near Fields: Introduction to Classical and Quantum Theories of Electromagnetic Phenomena at the Nanoscale;* Springer: Germany, 2009.
3. Flytzanis, C.; Hache, F.; Klein, M. C.; Ricard, D.; Roussignol, P. Nonlinear optics in composite materials. In *Progress in Optics;* Wolf, E., Ed.; Elsevier: Amsterdam, 1991; Vol. 29, Chapter 5, pp 321–411.
4. Sha, M. Y.; Xu, H.; Penn, S. G.; Cromer, R. *Nanomedicine* **2007,** *2,* 725–734. doi:10.2217/17435889.2.5.725
5. Mosbacher, M.; Münzer, H.-J.; Zimmermann, J.; Solis, J.; Boneberg, J.; Leiderer, P. *Appl. Phys. A* **2001,** *72,* 41–44. doi:10.1007/s003390000715
6. Kühler, P.; García de Abajo, F. J.; Solis, J.; Mosbacher, M.; Leiderer, P.; Afonso, C. N.; Siegel, J. *Small* **2009,** *5,* 1825–1829. doi:10.1002/smll.200900393
7. McLeod, E.; Arnold, C. B. *Nat. Nanotechnol.* **2008,** *3,* 413–417. doi:10.1038/nnano.2008.150
8. Brodoceanu, D.; Landström, L.; Bäuerle, D. *Appl. Phys. A* **2007,** *86,* 313–314. doi:10.1007/s00339-006-3781-z
9. Wang, Z. B.; Hong, M. H.; Luk'yanchuk, B. S.; Huang, S. M.; Wang, Q. F.; Shi, L. P.; Chong, T. C. *Appl. Phys. A* **2004,** *79,* 1603–1606. doi:10.1007/s00339-004-2860-2
10. Pereira, A.; Grojo, D.; Chaker, M.; Delaporte, P.; Guay, D.; Sentis, M. *Small* **2008,** *4,* 572–576. doi:10.1002/smll.200700256
11. Kühler, P.; García de Abajo, F. J.; Leiprecht, P.; Kolloch, A.; Solis, J.; Leiderer, P.; Siegel, J. *Opt. Express* **2012,** *20,* 22063–22078. doi:10.1364/OE.20.022063

12. Bonse, J.; Brzezinka, K.-W.; Meixner, A. J. *Appl. Surf. Sci.* **2004,** *221,* 215–230. doi:10.1016/S0169-4332(03)00881-X
13. Bonse, J.; Bachelier, G.; Siegel, J.; Solis, J. *Phys. Rev. B* **2006,** *74,* 134106. doi:10.1103/PhysRevB.74.134106
14. Puerto, D.; Gawelda, W.; Siegel, J.; Bonse, J.; Bachelier, G.; Solis, J. *Appl. Phys. A* **2008,** *92,* 803–808. doi:10.1007/s00339-008-4586-z
15. García de Abajo, F. J.; Gómez-Santos, G.; Blanco, L. A.; Borisov, A. G.; Shabanov, S. V. *Phys. Rev. Lett.* **2005,** *95,* 067403. doi:10.1103/PhysRevLett.95.067403
16. Sokolowski-Tinten, K.; Bialkowski, J.; von der Linde, D. *Phys. Rev. B* **1995,** *51,* 14186–14198. doi:10.1103/PhysRevB.51.14186
17. Sokolowski-Tinten, K.; Bialkowski, J.; Cavalieri, A.; von der Linde, D.; Oparin, A.; Meyer-ter-Vehn, J.; Anisimov, S. I. *Phys. Rev. Lett.* **1998,** *81,* 224–227. doi:10.1103/PhysRevLett.81.224
18. Sokolowski-Tinten, K.; Bialkowski, J.; Boing, M.; Cavalleri, A.; von der Linde, D. *Phys. Rev. B* **1998,** *58,* R11805–R11808. doi:10.1103/PhysRevB.58.R11805
19. Ichibayashi, T.; Tanimura, K. *Phys. Rev. Lett.* **2009,** *102,* 087403. doi:10.1103/PhysRevLett.102.087403
20. Rethfeld, B.; Sokolowski-Tinten, K.; von der Linde, D.; Anisimov, S. I. *Appl. Phys. A* **2004,** *79,* 767–769. doi:10.1007/s00339-004-2805-9

Apertureless scanning near-field optical microscopy of sparsely labeled tobacco mosaic viruses and the intermediate filament desmin

Alexander Harder[1], Mareike Dieding[1], Volker Walhorn[*1], Sven Degenhard[2], Andreas Brodehl[3,4], Christina Wege[2], Hendrik Milting[3] and Dario Anselmetti[1]

Full Research Paper

`Open Access`

Address:
[1]Experimental Biophysics and Applied Nanoscience, Faculty of Physics and Bielefeld Institute for Biophysics and Nanoscience (BINAS), Bielefeld University, Universitätsstrasse 25, D-33615 Bielefeld, Germany, [2]Department of Molecular Biology and Plant Virology, Institute of Biology, University of Stuttgart, Pfaffenwaldring 57, D-70569 Stuttgart, Germany, [3]Erich and Hanna Klessmann Institute for Cardiovascular Research & Development (EHKI), Heart and Diabetes Center NRW, Ruhr University Bochum, Georgstraße 11, D-32545 Bad Oeynhausen, Germany and [4]Libin Cardiovascular Institute of Alberta, Department of Cardiac Sciences, University of Calgary, 3280 Hospital Drive NW, T2N4Z6, AB, Canada

Email:
Volker Walhorn[*] - volker.walhorn@physik.uni-bielefeld.de

* Corresponding author

Abstract

Both fluorescence imaging and atomic force microscopy (AFM) are highly versatile and extensively used in applications ranging from nanotechnology to life sciences. In fluorescence microscopy luminescent dyes serve as position markers. Moreover, they can be used as active reporters of their local vicinity. The dipolar coupling of the tip with the incident light and the fluorophore give rise to a local field and fluorescence enhancement. AFM topographic imaging allows for resolutions down to the atomic scale. It can be operated in vacuum, under ambient conditions and in liquids. This makes it ideal for the investigation of a wide range of different samples. Furthermore an illuminated AFM cantilever tip apex exposes strongly confined non-propagating electromagnetic fields that can serve as a coupling agent for single dye molecules. Thus, combining both techniques by means of apertureless scanning near-field optical microscopy (aSNOM) enables concurrent high resolution topography and fluorescence imaging. Commonly, among the various (apertureless) SNOM approaches metallic or metallized probes are used. Here, we report on our custom-built aSNOM setup, which uses commercially available monolithic silicon AFM cantilevers. The field enhancement confined to the tip apex facilitates an optical resolution down to 20 nm. Furthermore, the use of standard mass-produced AFM cantilevers spares

elaborate probe production or modification processes. We investigated tobacco mosaic viruses and the intermediate filament protein desmin. Both are mixed complexes of building blocks, which are fluorescently labeled to a low degree. The simultaneous recording of topography and fluorescence data allows for the exact localization of distinct building blocks within the superordinate structures.

Introduction

Scanning near-field optical microscopy (SNOM) provides sub-wavelength optical resolution [1]. The sample is excited by the strongly confined near-field at the tip apex, which is induced by the dipolar coupling between the incident light and the probe. Moreover, coupling between the fluorophore dipole and the tip can lead to both, fluorescence enhancement and quenching. In summary, all these effects highly depend on several experimental parameters such as the distance between tip and fluorophore, the probe geometry and material and the polarization of the incident light. Furthermore, the distance-control feedback loop of the probe can be used to gain topographical information as it is done in atomic force microscopy (AFM). Thus, SNOM generally allows the acquisition of both optical and topographical information. Various conceptual approaches have been reported: In fiber SNOM the sample is illuminated through the aperture of a metal coated optical fiber tip [2]. Due to the blunt tip this method shows low topographic resolution. Besides, the optical resolution can be increased by the diminution of the tip aperture, which chokes the optical throughput. Therefore, apertureless SNOM probes appear favorable [3-7]. Commonly, metallic and metallized probes expose a strong field enhancement and dipolar coupling between fluorophore and tip, which result in a remarkable increase of the observable fluorescence emission. However, the interaction between dye and tip apex can be manifold and depend crucially on the experimental setup and the sample. As a result the fluorescence emission rate can be both significantly enhanced or reduced at distances up to some 10 nm [6,8-11], and single-molecule images can show complex fluorescence patterns [3,12,13]. Silicon probes expose only a moderate field enhancement and the dipolar coupling between probe and dye is less pronounced [4]. Even though, silicon tips can quench the fluorescence emission at close proximity [14]. Moreover, the elaborate probe design of custom-made tips demand complex fabrication processes and substantial experience [3,7,12,13,15-17]. Here, we report on an aSNOM approach using commercially available monolithic silicon AFM cantilevers. These expose a sharp tip apex for high topographic resolution and strong field confinement. Additionally, the field enhancement is sufficient for an adequate signal to noise ratio (SNR). Besides, fluorescence and topography data are inherently aligned allowing easy superposition and localization of single fluorescence peaks within topographic features. Many biological systems from single molecules to cells and viruses are mixed complexes that

are composed of specific building blocks. Their structure and function directly depend on the exact composition of all constituents. By using two exemplary systems we demonstrate that aSNOM enables the precise localization of single fluorescently labeled components within these structures.

The desmin intermediate filament protein assembles to extensive fibrous networks, which are an integral part of the cytoskeleton of heart muscle cells. Several mutations of the desmin gene are associated with severe muscle diseases like arrhythmogenic right ventricular cardiomyopathy (ARVC) [18-22]. ARVC leads to cardiac arrhythmia and a degeneration of the heart muscle predominantly of the right ventricle. It has been found recently that the desmin filament assembly can be heavily affected by mutations (Figure 1) [23]. Nevertheless, the molecular patho-mechanism leading to a degeneration of the heart muscle is still unknown. Of note, desmin mutations follow a dominant inheritance, which means that only one of the two alleles carries the mutation. Consequently, both mutant and wild-type desmin forms are present in the same cell. Moreover, it has been shown recently by means of dual color photo activation localization microscopy (PALM) that both protein species coexist within the same filaments [23]. However, the distribution of both protein types in the early stage of the desmin filament formation, i.e., oligomers and unit length filaments (ULF), respectively, is still not known and might give insight in the patho-mechanism.

The tobacco mosaic virus (TMV) is a tubular shaped plant virus with a length of 300 nm and a diameter of 18 nm. It is composed of 2130 identical capsid protein subunits helically arranged on a single RNA strand thereby enclosing an inner longitudinal channel [25]. Apart from plant research, TMV is also important for nanotechnology applications of virus-derived biotemplates [26-29]. The self-assembly of the capsid components and the homogeneous nucleoprotein tube diameter make TMV an attractive scaffold for nanotechnological applications such as the formation of TMV-based semiconductive ZnO composites in field effect transistors [30]. Modifications of the viral shell proteins allow the introduction of target-oriented chemical functionalities on the nanotube surface [31]. By means of fluorescent labeling these modifications can now easily be localized by the use of aSNOM.

Figure 1: AFM topography scans of desmin filaments under ambient conditions. a) Filaments assembled from wild-type proteins are several micrometers long and expose a vague right handed twist. b) Filaments assembled from mutated desmin protein (deletion mutation p.E114del, for details see [22]) are significantly shorter and show a completely different surface morphology. c) Assembly model of type II intermediate filaments [24]. Desmin monomers associate to parallel coiled coil dimers. Dimers form antiparallel tetramers which assemble to unit length filaments (ULF). Filaments elongate by longitudinal assembly of ULF.

Results and Discussion

We used a home-built aSNOM setup that consists of an AFM head mounted on a discretely designed inverted optical microscope (Figure 2a). To center the cantilever tip in the confocal detection volume the AFM is positioned on a separate 2D linear stage. The sample holder is attached on a 3D piezo stage (P-733.3, Physik Instrumente, Karlsruhe, Germany) for lateral sample scanning and vertical fine alignment. The AFM head holds a separate piezo actuator (PSt 150/2x3/5, Piezomechanik, München, Germany) for vibrational excitation of the AFM cantilever and surface distance control. The system is controlled by a commercially available scanning probe microscopy control system (Nanonis OC4, Specs, Zürich, Switzerland). The sample is evanescently illuminated by a laser diode (RLT6830MG, λ = 685 nm, 30mW, Roithner Lasertechnik, Vienna, Austria) through a high numerical aperture (NA) microscope objective (CFI Apochromat 100× TIRF, NA = 1.49, Nikon, Tokyo,

Japan). The laser diode is linearly polarized and directed to the sample such that the polarization is parallel to the plane of incidence (p-polarization). Thus, the component of the wave vector perpendicular to the sample surface is enhanced. For detection of the fluorescence emission we used a confocal scheme with a gated avalanche photodiode (APD) (SPCMAQR-13, Perkin Elmer, Waltham, MA, USA). Notable, the sample illumination and fluorescence detection is synchronized with the cantilever oscillation in such a way that we gain two fluorescence images corresponding to both reversal points of the cantilever oscillation (Figure 2b). The gating window corresponds to a phase width of 20–40°.

Modified TMV with sparsely distributed fluorescent dyes, which label selectively addressable groups, were immobilized as described and investigated. A single aSNOM scan yields three different data sets: AFM topography, far-field (Figure 3a)

Figure 2: a) Scheme of the experimental setup. b) The sample illumination and fluorescence readout is correlated with the cantilever position. The far-field readout is triggered at the upper reversal point of the cantilever whereas the near-field data is recorded at the lower reversal point.
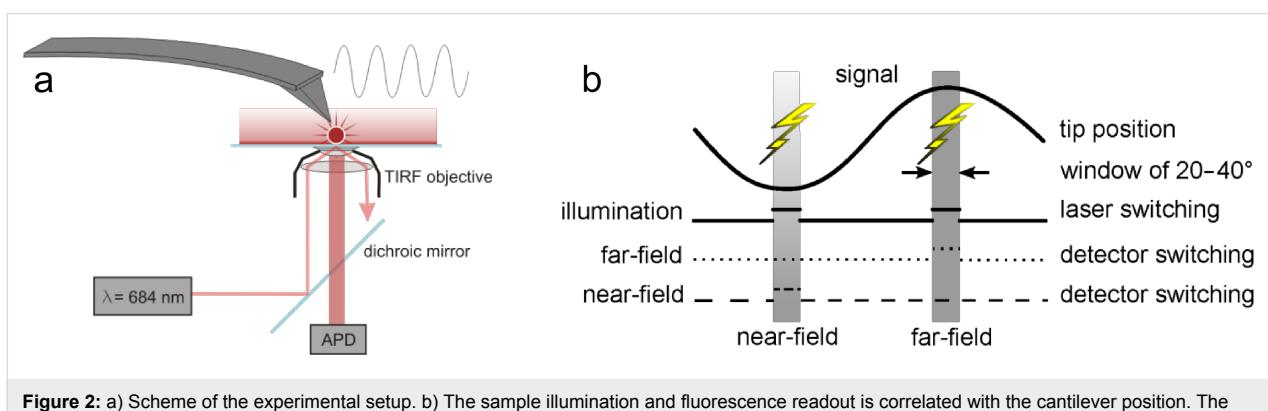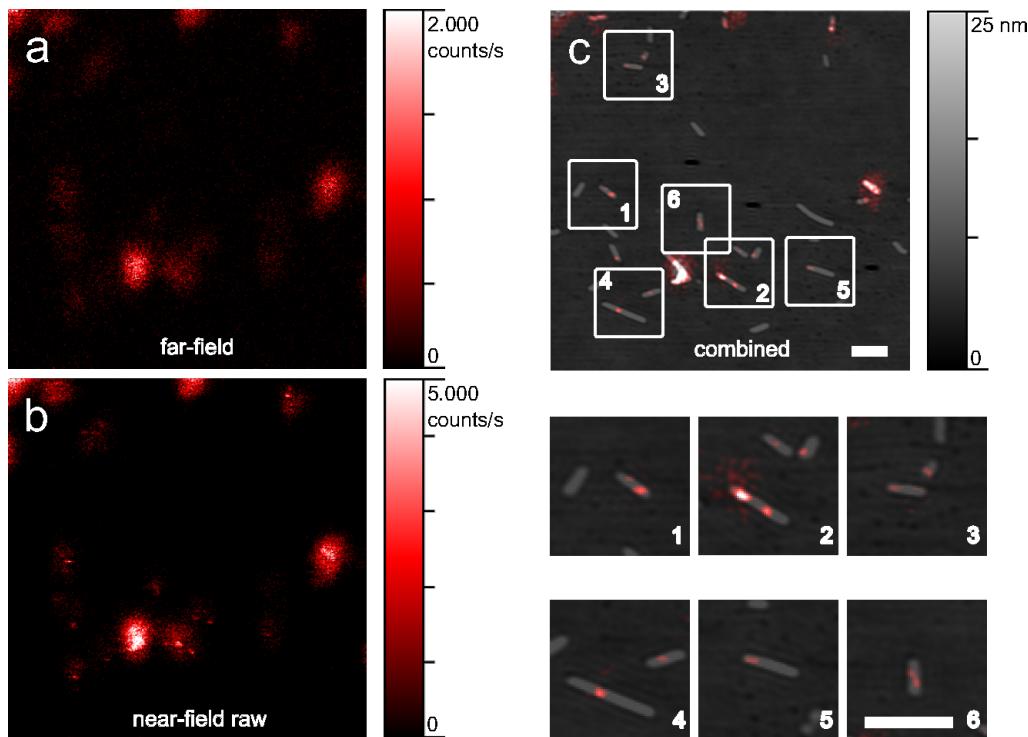
Figure 3: aSNOM dataset of TMV (a–c, 5×5 μm^2). a) Blurry far-field fluorescence acquired at the upper reversal point of the oscillating cantilever. b) The raw near-field fluorescence was recorded at the lower reversal point of the cantilever. The near-field contribution is located at the center of the dim stray fluorescence. c) The plain near-field fluorescence data is superimposed on the AFM topography. The marked areas are magnified for better visibility. All scale bars indicate 500 nm.

and (raw) near-field fluorescence (Figure 3b) data. The unprocessed near-field fluorescence image still contains a significant far-field background. When a single dye molecule is moved through the focal detection volume which has a characteristic radius of approx. 300 nm, the fluorescence emission is only enhanced at dye–tip distances lower than approx. 10 nm. Consequently, the raw near-field data exposes stray far-field fluorescence. During post-processing the far-field image is subtracted from the near-field image. The result is subsequently low-pass filtered as described. Even though silicon probes can also quench the fluorescence emission at close proximity, we did not detect the same. This is most probably due to the fact that the detector count rate is integrated over a comparably broad phase window of 20–40°. Topography and processed near-field fluorescence can then be superimposed without further lateral adjustment (Figure 3c). The combined data allow to easily determine the degree of modification and the loci of anchor groups equipped with dye molecules.

Similar to the TMV capsid, desmin is a construct of (quasi-) identical building blocks, which assemble to a complex higher-level structure. We prepared sparsely labeled wild type desmin and immobilized the filaments as described. The topography

data shows fibrous structures as it is known from unlabeled desmin filaments. The labeling procedure was derived from a protocol for the homologue intermediate filament vimentin [32]. Even though fluorescence labeling can disturb the directed association of proteins due to steric hindrance, the filament assembly was apparently not inhibited. The merged dataset exposes filaments with sharp and clearly detectable sparsely distributed fluorophores. Even in the case of fluorescence signals, which were detected adjacently, we observed distances in the range of 50–70 nm, which coincide very well with the length of ULF (about 60 nm, Figure 4) [33]. Consequently, the labeled monomers are most likely located in vicinal ULF. The optical resolution was estimated by means of approximating a Gaussian distribution to the fluorescence peaks. We found single fluorophores with a full width at half maximum (FWHM) down to 17 nm. The average FWHM was 25 nm (Figure 5). Moreover, the optical SNR was better than 10 for all analyzed dyes, which corresponds nicely to recently published results [5]. It is noteworthy that the resolution for individual fluorophores can differ significantly (Figures 3, 4 and 5) from the average. This is most probably due to the comparably high corrugation and complexity of TMV and desmin, which can limit the accessibility of individual dyes. The topographic resolution was
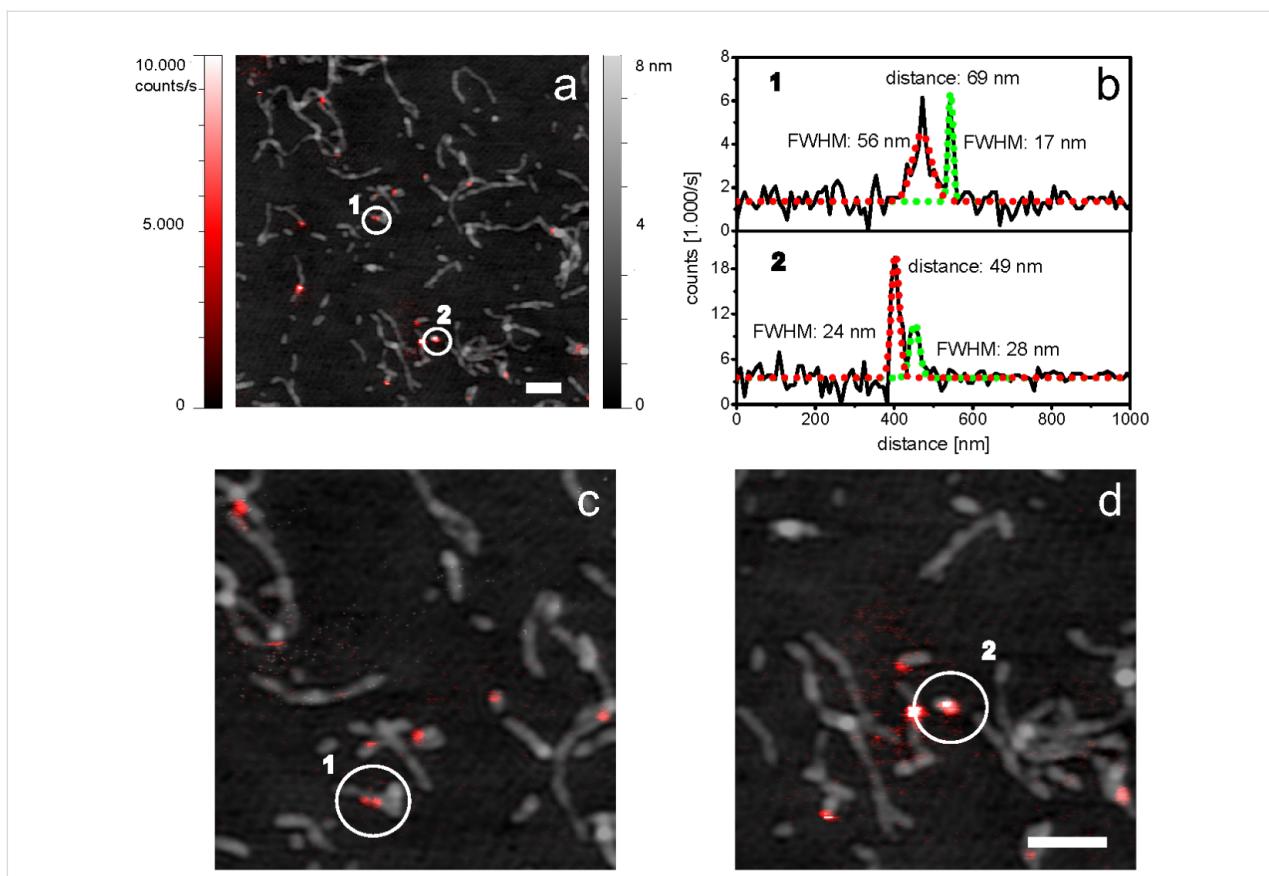
Figure 4: aSnom data of fluorescently labeled desmin filaments. a) Combined fluorescence and topography dataset of wild type desmin. b) Fluorescence intensity cross sections of two adjacent fluorophores are extracted to estimate the optical resolution. The peaks are approximated by a Gaussian distribution to determine the FWHM. c,d) The marked areas are magnified for better visibility. All scale bars indicate 500 nm.
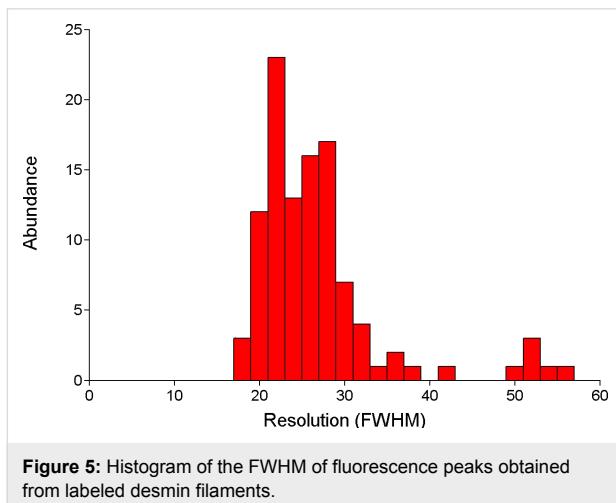
Figure 5: Histogram of the FWHM of fluorescence peaks obtained from labeled desmin filaments.

found to be lower compared to conventional AFM, since the morphology of the filaments could not be resolved. Moreover, the filaments appeared slightly broader (data not shown). This still seems to be a conceptual issue of combined optical and scanning probe microscopy: The sample has to be accessible from top and bottom. Furthermore, high numerical aperture objectives constrict to the use of thin glass cover slips with a thickness of 150–170 μm as sample substrates. Consequently, the setup, as well as the substrates, is more susceptible to vibrational noise. Nevertheless, aSNOM has shown to be an ideal tool for the localization of single building blocks within superordinate structures.

Conclusion

We demonstrated that aSNOM is an appropriate tool to simultaneously image topography and fluorescence of complex higher level structures down to the single-molecule level. The achieved resolution allows the allocation of single molecular building blocks within these constructs. In the case of the intermediate filament desmin this enables a detailed analysis of the filament assembly mechanism to explore the molecular patho-mechanism. Furthermore, the use of unmodified, commercially available standard AFM cantilevers is timesaving and cost-effective compared to other elaborate near-field probes. Since the tip apex serves as probe for topography and fluorescence the datasets are intrinsically aligned. Consequently, image

processing is very easy and the data can be superimposed without further adjustment. Both, the AFM and the fluorescence part of the setup are highly versatile: For example the extension to dual color fluorescence is possible without major modifications. Generally, the setup also allows imaging in liquid media, which makes it predestined for biological samples. Furthermore, the intermittent fluorophore excitation reduces photo-bleaching and thus extends imaging time.

Experimental
Image processing
The unprocessed near-field image contains a significant amount of parasitic far-field fluorescence. By subtracting the background far-field fluorescence signal from the near-field fluorescence signal and applying an additionally line-by-line low-pass filter to the subtraction in order to reduce artificial noise, we generated a corrected near-field image with considerably reduced far-field artifacts. Of note, the low-pass filter primarily smoothes individual "noisy pixels" and hardly alters the shape or the width of the fluorescence peaks. The resulting high resolution fluorescence data are then superimposed on the topography. All image processing is done with the SPIP image processing software (Image Metrology A/S, Hørsholm, Denmark). All SNOM experiments were done with monolithic silicon cantilevers (ATEC-NC, Nanosensors, Neuchatel, Switzerland). The tetrahedral tip protruding from the end of the lever ensures visibility of the tip apex and consequently facilitates the alignment relative to the illumination laser. As fluorescent dye we used maleimide-modified Atto740 (Atto-Tec, Siegen, Germany) which has a remarkable photo-stability and a preferably low quantum yield of 10%. Low quantum efficiencies are beneficial as dipole–dipole coupling effects between the cantilever tip and dye increase the radiative decay rate and thus enhance the quantum yield [34].

Sample preparation
The desmin protein was expressed in *E.coli*, isolated and purified as reported recently [20]. Desmin monomers expose a single cysteine, which is an ideal anchor for dye attachment. The labeling procedure is derived from the protocol which has recently been published for the homologue IF vimentin [32]. Briefly: desmin is dialyzed for one hour at room temperature against labeling buffer (5 M urea, 5 mM Tris-HCl , pH 7.0–7.5). Atto740 is solubilized in water-free DMSO to 5 mg/mL and added in a 10:1 molar excess. After 30 minutes the unbound dye is blocked by the addition of cysteamine (1 M in H_2O to a concentration of 100 mM and incubation for 1 hour at room temperature). The labeled desmin is separated from free dye molecules by dialysis (against 8 M urea, 5 mM Tris-HCl, 1 mM DTT pH 8.4) and stored at −8 °C. The degree of labeling (DOL) is determined by absorption spectra to DOL = 2.2. Labeled and

unlabeled desmin are mixed in a 1:10 molar ratio and stepwise dialysed against 5 mM Tris-HCl, 1 mM DTT at pH 8.4. Assembly is initialized by addition of an equal volume of assembly buffer (200 mM NaCl, 45 mM Tris-HCl, pH 7) to a desmin solution with a concentration of 0.55g/L and incubated for one hour at 37 °C.

TMV particles are isolated from systemically infected *Nicotiana tabacum* 'Samsun' nn plants according to Gooding and Hebert [35]. A TMV mutant, which presents a single thiol-group on every capsid protein subunit of the virus surface (TMV$_{Cys}$, 2130 coupling sites per viral nanotube), is used [31]. The labeling procedure is performed with a substoichiometric molar ratio of 0.02:1 of Atto740 maleimide (Sigma-Aldrich, München, Germany) to viral capsid protein, in sodium potassium phosphate (SPP) buffer (10 mM SPP buffer, pH 7.2), with a virus concentration of 1 µg/µL in a total volume of 100 µL. The reaction mixture is incubated for 9 h at 30 °C in the dark, gently shaken at 300 rpm (Thermomixer Compact, Eppendorf, Hamburg, Germany). An amount of 300 µL SPP buffer is added and the unbound dye is removed by ultracentrifugation for 2 h at 15 °C and 120,000*g* (Sorvall Ultra Pro 80, Thermo Fisher Scientific Inc., Waltham, USA). The pellet containing the modified virions is resuspended in 100 µL SPP buffer and the degree of labeling is determined by absorption spectra (NanoDrop ND-1000, PEQLAB, Erlangen, Germany) to DOL = 1.8%.

Fluorophore-exposing desmin filaments (130 ng/µL) and TMV$_{Cys}$ (1 ng/µL) are immobilized onto etched and cleaned glass slides (Menzel Gläser, Germany) as follows: The slides are sonicated for 20 min in acetone p. a. (Sigma, Germany) and thoroughly rinsed with ethanol p. a. (Sigma, Germany) and Milli-Q water (18.2 MΩ·cm; Millipore, Germany). The cleaned glass slides are additionally etched with 65% nitric acid p. a. (Roth, Germany) for 2 min to activate the glass surface. Subsequently the glass slides are washed with Milli-Q water and dried in a gentle nitrogen stream. Desmin and TMV, respectively, are pipetted on the slides to incubate for several seconds. Unbound desmin or TMV are rinsed from the slides with Milli-Q water. Finally the samples are dried in a nitrogen stream.

References
1. Novotny, L. In *Progress in Optics;* Wolf, E., Ed.; Elsevier, 2007; Vol. 50, pp 137–184.
2. Pohl, D. W.; Denk, W.; Lanz, M. *Appl. Phys. Lett.* **1984,** *44,* 651. doi:10.1063/1.94865
3. Frey, H. G.; Bolwien, C.; Brandenburg, A.; Ros, R.; Anselmetti, D. *Nanotechnology* **2006,** *17,* 3105–3110. doi:10.1088/0957-4484/17/13/004
4. Frey, H. G.; Paskarbeit, J.; Anselmetti, D. *Appl. Phys. Lett.* **2009,** *94,* 241116. doi:10.1063/1.3155190

5. Ma, Z.; Gerton, J. M.; Wade, L. A.; Quake, S. R. *Phys. Rev. Lett.* **2006,** *97,* 260801. doi:10.1103/PhysRevLett.97.260801

6. Yoskovitz, E.; Hadar, I.; Sitt, A.; Lieberman, I.; Banin, U. *J. Phys. Chem. C* **2011,** *115,* 15834–15844. doi:10.1021/jp2035604

7. Höppener, C.; Beams, R.; Novotny, L. *Nano Lett.* **2009,** *9,* 903–908. doi:10.1021/nl803903f

8. Anger, P.; Bharadwaj, P.; Novotny, L. *Phys. Rev. Lett.* **2006,** *96,* 113002. doi:10.1103/PhysRevLett.96.113002

9. Zhang, D.; Heinemeyer, U.; Stanciu, C.; Sackrow, M.; Braun, K.; Hennemann, L. E.; Wang, X.; Scholz, R.; Schreiber, F.; Meixner, A. J. *Phys. Rev. Lett.* **2010,** *104,* 056601. doi:10.1103/PhysRevLett.104.056601

10. Walhorn, V.; Paskarbeit, J.; Frey, H. G.; Harder, A.; Anselmetti, D. *Beilstein J. Nanotechnol.* **2011,** *2,* 645–652. doi:10.3762/bjnano.2.68

11. Eckel, R.; Walhorn, V.; Pelargus, C.; Martini, J.; Enderlein, J.; Nann, T.; Anselmetti, D.; Ros, R. *Small* **2007,** *3,* 44–49. doi:10.1002/smll.200600130

12. Gersen, H.; García-Parajó, M. F.; Novotny, L.; Veerman, J. A.; Kuipers, L.; van Hulst, N. F. *Phys. Rev. Lett.* **2000,** *85,* 5312–5315. doi:10.1103/PhysRevLett.85.5312

13. Frey, H. G.; Witt, S.; Felderer, K.; Guckenberger, R. *Phys. Rev. Lett.* **2004,** *93,* 200801. doi:10.1103/PhysRevLett.93.200801

14. Schulz, O.; Zhao, Z.; Ward, A.; Koenig, M.; Koberling, F.; Liu, Y.; Enderlein, J.; Yan, H.; Ros, R. *Opt. Nanosc.* **2013,** *2,* 1. doi:10.1186/2192-2853-2-1

15. Muranishi, M.; Sato, K.; Hosaka, S.; Kikukawa, A.; Shintani, T.; Ito, K. *Jpn. J. Appl. Phys., Part 2* **1997,** *36,* L942–L944. doi:10.1143/JJAP.36.L942

16. Farahani, J. N.; Eisler, H.-J.; Pohl, D. W.; Pavius, M.; Flückiger, P.; Gasser, P.; Hecht, B. *Nanotechnology* **2007,** *18,* 125506. doi:10.1088/0957-4484/18/12/125506

17. Göttlich, H.; Heckl, W. M. *Ultramicroscopy* **1995,** *61,* 145–153. doi:10.1016/0304-3991(95)00124-7

18. van Tintelen, J. P.; van Gelder, I. C.; Asimaki, A.; Suurmeijer, A. J. H.; Wiesfeld, A. C. P.; Jongbloed, J. D. H.; van den Wijngaard, A.; Kuks, J. B. M.; van Spaendonck-Zwarts, K. Y.; Notermans, N.; Boven, L.; van den Heuvel, F.; Veenstra-Knol, H. E.; Saffitz, J. E.; Hofstra, R. M. W.; van den Berg, M. P. *Heart Rhythm* **2009,** *6,* 1574–1583. doi:10.1016/j.hrthm.2009.07.041

19. Vernengo, L.; Chourbagi, O.; Panuncio, A.; Lilienbaum, A.; Batonnet-Pichon, S.; Bruston, F.; Rodrigues-Lima, F.; Mesa, R.; Pizzarossa, C.; Demay, L.; Richard, P.; Vicart, P.; Rodriguez, M.-M. *Neuromuscular Disord.* **2010,** *20,* 178–187. doi:10.1016/j.nmd.2010.01.001

20. Klauke, B.; Kossmann, S.; Gärtner, A.; Brand, K.; Stork, I.; Brodehl, A.; Dieding, M.; Walhorn, V.; Anselmetti, D.; Gerdes, D.; Bohms, B.; Schulz, U.; zu Knyphausen, E.; Vorgerd, M.; Gummert, J.; Milting, H. *Hum. Mol. Genet.* **2010,** *19,* 4595–4607. doi:10.1093/hmg/ddq387

21. Otten, E.; Asimaki, A.; Maass, A.; van Langen, I. M.; van der Wal, A.; de Jonge, N.; van den Berg, M. P.; Saffitz, J. E.; Wilde, A. A. M.; Jongbloed, J. D. H.; van Tintelen, J. P. *Heart Rhythm* **2010,** *7,* 1058–1064. doi:10.1016/j.hrthm.2010.04.023

22. Brodehl, A.; Dieding, M.; Cakar, H.; Klauke, B.; Walhorn, V.; Gummert, J.; Anselmetti, D.; Milting, H. *Eur. J. Hum. Genet.* **2013,** *21,* 589–590. doi:10.1038/ejhg.2012.212

23. Brodehl, A.; Hedde, P. N.; Dieding, M.; Fatima, A.; Walhorn, V.; Gayda, S.; Šarić, T.; Klauke, B.; Gummert, J.; Anselmetti, D.; Heilemann, M.; Nienhaus, G. U.; Milting, H. *J. Biol. Chem.* **2012,** *287,* 16047–16057. doi:10.1074/jbc.M111.313841

24. Kirmse, R.; Portet, S.; Mücke, N.; Aebi, U.; Herrmann, H.; Langowski, J. *J. Biol. Chem.* **2007,** *282,* 18563–18572. doi:10.1074/jbc.M701063200

25. Lewandowski, D. In *Virus Taxomony;* Fauquet, C. M., Ed.; Elsevier Academic Press, 2005.

26. Gerasopoulos, K.; McCarthy, M.; Royston, E.; Culver, J. N.; Ghodssi, R. *J. Micromech. Microeng.* **2008,** *18,* 104003. doi:10.1088/0960-1317/18/10/104003

27. Demir, M.; Stowell, M. H. B. *Nanotechnology* **2002,** *13,* 541. doi:10.1088/0957-4484/13/4/318

28. Yi, H.; Nisar, S.; Lee, S.-Y.; Powers, M. A.; Bentley, W. E.; Payne, G. F.; Ghodssi, R.; Rubloff, G. W.; Harris, M. T.; Culver, J. N. *Nano Lett.* **2005,** *5,* 1931–1936. doi:10.1021/nl051254r

29. Atanasova, P.; Rothenstein, D.; Schneider, J. J.; Hoffmann, R. C.; Dilfer, S.; Eiben, S.; Wege, C.; Jeske, H.; Bill, J. *Adv. Mater.* **2011,** *23,* 4918–4922. doi:10.1002/adma.201102900

30. Eber, F. J.; Eiben, S.; Jeske, H.; Wege, C. *Angew. Chem., Int. Ed.* **2013,** *52,* 7203–7207. doi:10.1002/anie.201300834

31. Geiger, F. C.; Eber, F. J.; Eiben, S.; Mueller, A.; Jeske, H.; Spatz, J. P.; Wege, C. *Nanoscale* **2013,** *5,* 3808–3816. doi:10.1039/c3nr33724c

32. Winheim, S.; Hieb, A. R.; Silbermann, M.; Surmann, E.-M.; Wedig, T.; Herrmann, H.; Langowski, J.; Mücke, N. *PLoS One* **2011,** *6,* e19202. doi:10.1371/journal.pone.0019202

33. Herrmann, H.; Aebi, U. *Annu. Rev. Biochem.* **2004,** *73,* 749–789. doi:10.1146/annurev.biochem.73.011303.073823

34. Lakowicz, J. R. *Anal. Biochem.* **2001,** *298,* 1–24. doi:10.1006/abio.2001.5377

35. Gooding, G.; Herbert, T. *Phytopathology* **1967,** *57,* 1285.

3D nano-structures for laser nano-manipulation

Gediminas Seniutinas[1,2], Lorenzo Rosa[*,1,2], Gediminas Gervinskas[1,2],
Etienne Brasselet[3] and Saulius Juodkazis[1,2]

Full Research Paper

Address:
[1]Centre for Micro-Photonics, Faculty of Engineering and Industrial
Sciences, Swinburne University of Technology, Hawthorn, VIC 3122,
Australia, [2]The Australian National Fabrication Facility – ANFF,
Victoria node, Faculty of Engineering and Industrial Sciences,
Swinburne University of Technology, Hawthorn, VIC 3122, Australia
and [3]Laboratoire Ondes et Matière d'Aquitaine (UMR5798) Université
Bordeaux 1, 351 Cours de la Libération, 33405 Talence, France

Email:
Gediminas Seniutinas - gdseniutinas@gmail.com; Lorenzo Rosa[*] -
lrosa@ieee.org; Saulius Juodkazis - sjuodkazis@swin.edu.au

* Corresponding author

Abstract

The resputtering of gold films from nano-holes defined in a sacrificial PMMA mask, which was made by electron beam lithography, was carried out with a dry plasma etching tool in order to form well-like structures with a high aspect ratio (height/width $\approx$ 3–4) at the rims of the nano-holes. The extraordinary transmission through the patterns of such nano-wells was investigated experimentally and numerically. By doing numerical simulations of 50-nm and 100-nm diameter polystyrene beads in water and air, we show the potential of such patterns for self-induced back-action (SIBA) trapping. The best trapping conditions were found to be a trapping force of 2 pN/W/μm^2 (numerical result) exerted on a 50-nm diameter bead in water. The simulations were based on the analytical Lorentz force model.

Introduction

Optical trapping is a fundamental experimental technique for physics and biology, which allows to precisely control and position micrometer-sized objects such as dielectric parts for nano-assembly, and biomaterials such as cells and bacteria, through the use of gradient forces, which originate from the interaction with a focused laser beam [1].

Nano-focusing and light control, which are possible with metallic plasmonic structures, are very attractive to engineer optical traps, in order to accurately position and manipulate objects down to the nanometer-scale [2]. Plasmonic nano-antennas have been designed for the trapping of dielectric and metallic particles in the size range of 10 nm [3-5], while fishnet

metamaterials have been shown to optically pull 100-nm dielectric beads in simulations [6]. Double nano-hole structures have been built to trap yet smaller 12-nm objects [7], and later even objects of single-protein size [8]. When nanometer-sized objects are handled by this technique, the trapping force weakens and the trap loses stability due to Brownian motion. This forces the laser intensity to be increased up to the point where damage occurs to the delicate biomaterials.

Self-induced back-action (SIBA) [9] has recently emerged as a promising technique to address this shortcoming. The main feature of SIBA trapping is the contribution of the object in defining the optical field distribution in the trap as well as the trapping conditions through focusing/diffraction and the interaction with the localized field on the substrate surface. This opens new degrees of freedom to the device, which can be exploited to reduce the optical intensity required for trapping, and thus to prevent damage to the biological material. The trapping position can also be moved farther away from the device, which provides access to the object from all directions. This technique has been employed with photonic crystals to trap spheres in nano-cavities [10] and to control the translation and the rotation of nano-rods by using resonators etched in waveguides [11].

SIBA trapping and slot-guiding of nano-particles using plasmonic devices [12,13] can be realized by using patterns of hole arrays and grooves. The extraordinary transmission in plasmonics can be exploited in metal hole arrays (MHA) at visible and IR spectral wavelengths as a promising method to introduce narrow-band wavelength-selective filtering [14]. A combination of extraordinary transmission and trapping is a promising direction for handling, moving, and sorting nano-materials. By the creation of patterns, which make plasmonic nano-particles chiral, one can envisage the creation of a controlled delivery of force and torque, hence, nano-hands. Recently, it was demonstrated that even optical pulling can be exerted using plasmonic nano-structures [15].

The fabrication of large areas filled with three-dimensional (3D) nano-structures with SIBA functionality requires a multi-step processing and is slow in throughput. Here, we show a parallel processing route for the fabrication of 3D nano-well structures over large areas of cross-sections in the sub-mm range. We explore experimentally and numerically whether extraordinary transmission [16] can be controlled in terms of intensity and spectral width using such 3D nano-well patterns, and we show the suitability of the fabricated structures for SIBA trapping.

Experimental

Gold re-sputtering was carried out for 3.5 min in Ar plasma (Samco RIE-101iPH) at a bias power of 200 W and at a process pressure of 2 Pa. The inductively coupled plasma (ICP) etching mode was turned off. Patterns on a sacrificial 300-nm thick PMMA mask were defined by electron beam lithography (EBL; Raith 150$^{\text{TWO}}$). The mask was spin coated on a cover glass which was magnetron sputter-coated (AXXIS, JKLesker) with a 100 nm thick gold film. Figure 1a and Figure 1b show a sketch of the sample structure before and after the re-sputtering step, with conical well structures formed at the rim of holes in the Au film. The plasma etching rate of PMMA was approximately 2.0–2.5 times higher than that of Au. The opening of the holes in the Au-film and the structural quality of samples were characterized by scanning electron microscopy (SEM).

Numerical simulations

The structure was modeled as a glass substrate on which a gold layer of 100 nm thickness was patterned with a lattice of water-filled ($n = 1.33$) holes of 200 nm diameter. The nano-wells were placed on top of the holes as 100 nm high cylindrical gold rings

Figure 1: Illustration of the nano-well fabrication by (a) dry plasma etching of Au-film and PMMA mask, which results in Au re-sputtering and (b) formation of a nano-well around the rim of the hole. The experimental outcome is shown as (c) SEM image of the 3D Au nano-wells array; in (d) the magnified slanted view shows details of the nano-well edges. The inset in panel (c) shows the cross-section of a nano-well after deposition of a protective Pt layer.

filled with water. Two cases were considered: one with cylindrical rings of 30 nm wall thickness, and one with conical rings, in which the wall thickness tapers from 30 nm at the bottom to zero at the top, leaving the conical shape on the inside (Figure 1b). The refractive index spectra of the materials were fitted from the experimental values obtained in literature, by means of a built-in polynomial model.

The finite-difference time-domain (FDTD) included a section of the substrate, enclosed in all directions by perfectly matched layers (PML) to avoid spurious reflections. The central area of 5×5 periods was illuminated by a total-field/scattered-field (TFSF) source, in order to measure separately the total field in the central area, and the field scattered outside and to calculate the cross-sections. For the calculation of transmitted and reflected power by the substrate, the domain was changed to a plane-wave illumination from the bottom, also modifying the lateral domain boundaries to periodic boundary conditions (PBC) to avoid diffraction of the plane wave from the borders. In this case, the reflected and transmitted power were measured by two power monitors, placed at either end of the domain, to gather evidence of extraordinary transmission. For the force calculation, the trapped object (a polystyrene bead) was introduced in the total-field region, and surrounded by a 3D monitor recording the vectorial E- and H-fields, discriminating the object volume by the refractive index change, and applying the Lorentz force formulation explained in the following section. The source was linearly *x*-polarized with a bandwidth range from 400 to 1400 nm.

The simulations were performed on the swinSTAR supercomputer at Swinburne University with 16-core nodes of 64 GB memory each. Each simulation took about 1 hour on a 16-node cluster with 256 total cores.

Background: Lorentz force

The Lorentz force calculation is presented below for the "bound" and "free" charges and currents as $\rho_{b,f}$ and $\mathbf{j}_{b,f}$, respectively. Let us consider a monochromatic field and consider nonmagnetic media only. Using the complex representation for the light field, the real Lorentz force density [N·m^{-3}] is:

$$\mathbf{f} = \frac{1}{2}\mathrm{Re}(\rho\mathbf{E}^*) + \frac{1}{2}\mathrm{Re}(\mathbf{j}\times\mathbf{B}^*) = \mathbf{f}_e + \mathbf{f}_h \, , \qquad (1)$$

where $\rho = \rho_b + \rho_f$ and $\mathbf{j} = \mathbf{j}_b + \mathbf{j}_f$ are the total charge densities.

First, let us consider the case of pure dielectrics without a free charge or a free current density. On the one hand, we have $\rho_b = -\nabla \cdot \mathbf{P}$ and $\rho_f = 0$, hence $\nabla \cdot \mathbf{D} = 0$ with $\mathbf{D} = \varepsilon_0\varepsilon_r\mathbf{E} = \varepsilon_0\mathbf{E} + \mathbf{P}$ where $\mathbf{P}$ is the material polarization due to the bound charges

and ε_r is complex if the medium is not transparent. On the other hand, we have $\mathbf{j}_f = 0$, $\mathbf{j}_b = \partial_t\mathbf{P}$, which leads to:

$$\rho = \varepsilon_0\nabla\cdot\mathbf{E}; \qquad \mathbf{j} = \varepsilon_0\left(\varepsilon_r - 1\right)\partial_t\mathbf{E}. \qquad (2)$$

For materials whose dielectric permittivity accounts for conduction electrons, i.e., metals, one would have $\rho_b = -\nabla \cdot \mathbf{P}$ and $\nabla \cdot \mathbf{D} = \rho_f$. On the other hand, $\nabla \times \mathbf{H} = \mathbf{j}_f + \varepsilon_0\varepsilon_r\partial_t\mathbf{E}$ and $\mathbf{j}_b = \partial_t\mathbf{P} = \varepsilon_0(\varepsilon_r - 1)\partial_t\mathbf{E}$. Therefore, we obtain:

$$\rho = \varepsilon_0\nabla\cdot\mathbf{E}; \qquad \mathbf{j} = \nabla\times\mathbf{H} - \varepsilon_0\partial_t\mathbf{E}. \qquad (3)$$

The 3D monitor in the FDTD returns the **E** and **H** fields and we calculate $\mathbf{B} = \mu_0\mathbf{H}$, and, supposing linear media, $\mathbf{D} = \varepsilon_0\varepsilon_r\mathbf{E}$. At the interface between metal and dielectric, the component of **E** parallel to the interface is continuous. The component of **D** perpendicular to the interface must also be continuous, which means the perpendicular component of **E** must be discontinuous and generate a charge density $\rho = \rho_b + \rho_f$.

When calculating the charge density, ρ, through the divergence of the electric field, one must take into account an unavoidable feature of the FDTD method in that each field component (E_x, E_y, E_z, H_x, H_y, H_z) is calculated for a different point of the Yee cell. As it was recently shown [17], an interpolation scheme can be used to estimate the field at the boundary. Similarly, for the magnetic force, the cross product calculation requires to interpolate the **B** vector components in the positions where the components of **j** are defined. In this case, both B_x and B_y are discontinuous at the interface. However, with the employed scheme [17] the interpolation error only affects the magnetic *z*-component of the Lorentz force $\left\langle f_z \right\rangle = 1/2\,\mathrm{Re}\left(j_x B_y^* - j_y B_x^*\right)$.

The total force per unit volume $\left\langle\mathbf{f}\right\rangle = \left\langle\mathbf{f}_e\right\rangle + \left\langle\mathbf{f}_h\right\rangle$ is then integrated on the trapped object volume $\mathcal{V}$ obtaining

$$\mathbf{F} = \iiint\limits_{\mathcal{V}} \left\langle\mathbf{f}\right\rangle \mathrm{d}v \, . \qquad (4)$$

The Maxwell stress tensor (MST) approach can also be used for force calculation, however, there is an ambiguity in the placement of the monitors across the interfaces [17]. In case of the method outlined here, the 3D field monitors, which capture the complex values of the fields provide direct means to remove the ambiguity and calculate the Lorentz force. The analytical formulas presented here were implemented in the simulations.

Results and Discussion

Optical transmission

Figure 1c and Figure 1d show SEM images of the fabricated structures. Following the usual PMMA resist development procedure after dry etching, the formation of uniform well-like structures was observed at the rim of the etched holes. The structures were approximately 100 nm in height and about 20–30 nm in width at the base. Their formation can be understood as a re-deposition of the sputtered gold film. During sputtering some gold is deposited on the inner walls of the openings in the sacrificial PMMA layer. This results in a free-standing pattern with enough structural strength to withstand the wet-bath development. A lengthy one-hour treatment at 70 °C in an ultrasonic bath would be necessary to remove these nano-well structures. The wells are made of Au as confirmed by using energy dispersive X-ray spectroscopy using tilted slices, as shown in the inset of Figure 1c.

Figure 2a compares transmission and reflectivity spectra of the hole array structure with cylindrical and conical nano-well patterns. The major spectral features are similar, and by tuning the geometrical parameters of the pattern it is possible to maximize the transmission of specific wavelengths. Manifestation of extraordinary transmission can be seen at the major transmission peak around 830 nm. The classical Bethe transmission ratio through a hole of radius $D/2$ in an opaque screen would follow a $T \propto [(D/2)/\lambda]^4$ scaling; for $D = 200$ nm and $\lambda = 800$ nm it would be $T \approx 0.02$ %. By adding the nano-well structure, the spectral properties are not affected strongly and the transmission is reduced. The extinction cross-sections $\sigma_{ext} = \sigma_{abs} + \sigma_{scat}$ defined by the sum of absorption and scattering are shown in Figure 2b. The wavelengths of 760 and 808 nm are chosen for analysis of the light intensity distribution and force mapping (discussed below) because there is no strong pushing (scattering force), which exists at the extraordinary transmis-

Figure 2: (a) Transmission *T* and reflectivity *R* coefficients for different geometries of the hole/well-array structures (see Figure 1 for geometry: hole diameter *D* = 200 nm, well height *h* = 100 nm, width of the well structure at the base *w* = 30 nm, and thickness of Au film 100 nm). Calculated for immersion in water with refractive index n_w = 1.33. (b) Extinction cross-sections normalized to the geometrical cross section (dashed line). (c) and (d) are the same as (a) and (b), but for air.

sion maxima. Also, these are the wavelengths for the planned future laser trapping experiments.

The transmission of the nano-well arrays was experimentally characterized for hole diameters of 70, 90, and 120 nm, as shown in Figure 3. The extinction, *Ext*, was calculated as *Ext* = ln(T_{ref}/T_{sample}), where T_{ref} is the transmissivity of a 100-nm Au layer. When the diameter is increased, the extinction peak is red-shifted and becomes negative, which corresponds to extraordinary transmission through the array, which in case of the 120-nm array extends over a wide band between 500 and 730 nm. The spectral tunability of the extinction in the plasmonic band around 600 nm is clearly discernable, and makes it possible to tune the peak up to the laser wavelength to optimize the trapping effect.

The light intensity distributions in the top-illuminated substrates reveals the configuration of the trapping field: while the field enhancement is not very strong (less than 10) in water, as shown in Figure 4a and Figure 4b, we see the formation of large spots hovering above the nano-well apertures: These spots vary little with the wavelength and are useful for trapping dielectric objects. In air the enhancement is much weaker, as shown in Figure 4c, and at the longer wavelength in Figure 4d there occurs the formation of hot-spots at the upper and lower corner of the nano-wells.

Next, we employed the full-3D vectorial model to numerically determine the optical trapping force $\mathbf{F}(\mathbf{r},\omega) = 1/2\left[\alpha'(\omega) + i\alpha''(\omega)\right]\nabla\mathbf{E}(\mathbf{r},\omega)^2$ experienced by the bead, which is usually approximated in theory as an optical dipole oscillator, in the vicinity of a nano-well, where ($\alpha' + i\alpha''$) is the polariz-

ability at the angular frequency ω (linked to the permittivities through the Clausius–Mossotti equation [18]), **r** is the position vector, and $\nabla\mathbf{E}^2$ is the E-field intensity gradient [19]. For stable trapping, the force given by the light intensity gradient (proportional to α′) must exceed the force resulting from the momentum transfer by the photons, which are back-scattered by the particle (proportional to α″), and generate a potential minimum low enough to curb the combined effect of gravity, buoyancy, and the Brownian motion of the particle [20]. The polarizability of the nano-materials determines the sign of the force: metallic-like particles are repelled from high intensity regions, while dielectric nano-particles will be attracted.

Force mapping

The force mapping was calculated by using the Lorentz force formalism (from section "Background: Lorentz force") on a polystyrene-bead probe (*n* = 1.504) of diameter *d* with the 3D-FDTD method. In order to build the map, the bead is moved in 10-nm steps along the *xz*-plane at different heights in the proximity of the top of the well. At each position the simulation is repeated and the 3D Lorentz force is calculated. Due to the density of polystyrene being approximately equal to that of water, buoyancy and gravity almost compensate each other, leaving a residual force about three orders of magnitude lower than the Lorentz force under normal illumination conditions. Figure 5 and Figure 6 show the force field map at the rim of the nano-well.

The best trapping conditions were found for the conical nano-wells at 760 nm wavelength. The trapping locations depicted by arrow plots in Figure 5 for a bead with *d* = 50 nm and Figure 6 for a bead with *d* = 100 nm, show very different equilibria
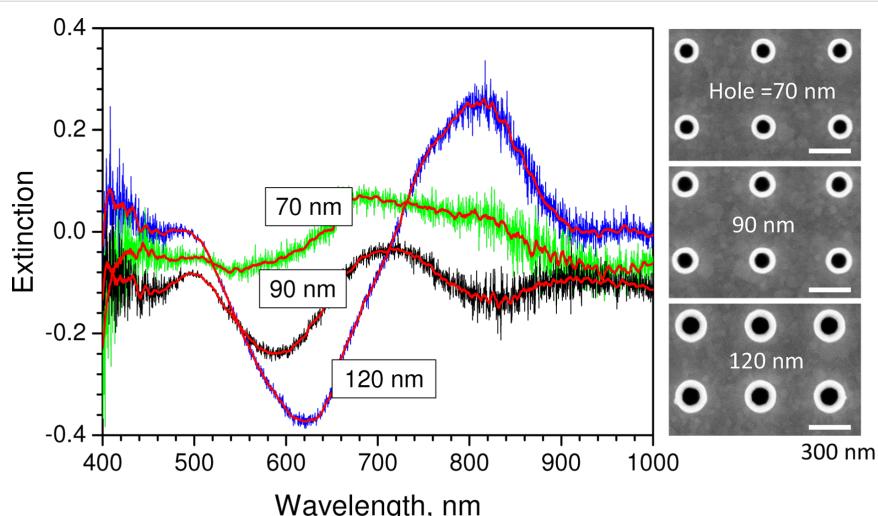
Figure 3: Experimentally measured extinction of the nano-well substrate for hole diameters of 70, 90, and 120 nm. The value is normalized to a continuous 100-nm Au layer, thus the negative regions offer proof of extraordinary transmission [16] through the array.
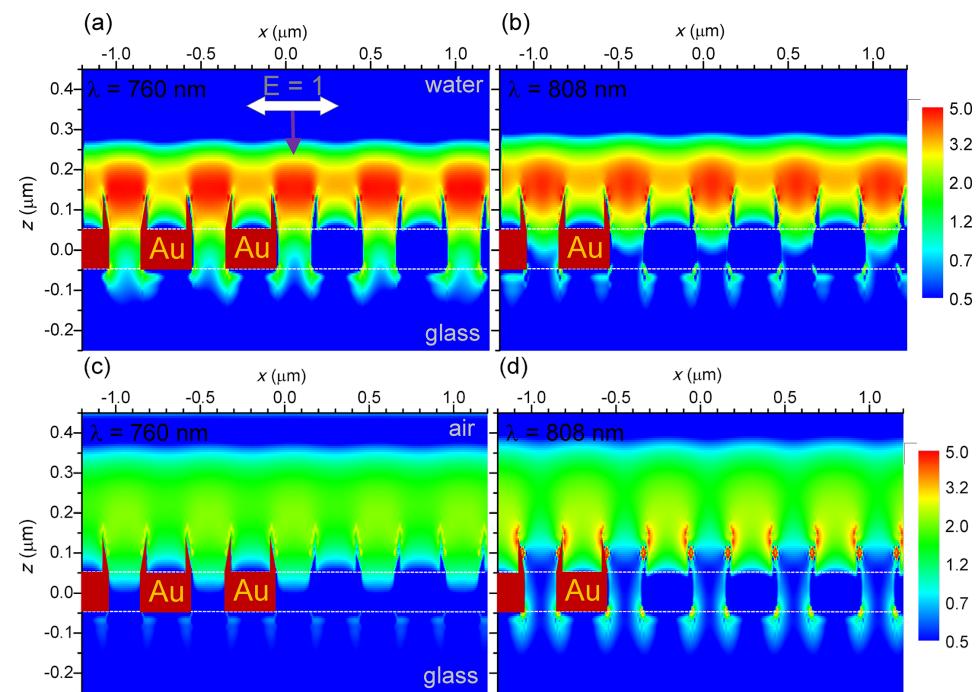
Figure 4: Light intensity distribution in the *xz*-plane simulated by 3D-FDTD at the two laser wavelengths (a,c) 760 nm and (b,d) 808 nm, in (a,b) water and (c,d) air. Incident light intensity $|\mathbf{E}_0|^2 = 1$; propagation in negative *z*-direction.
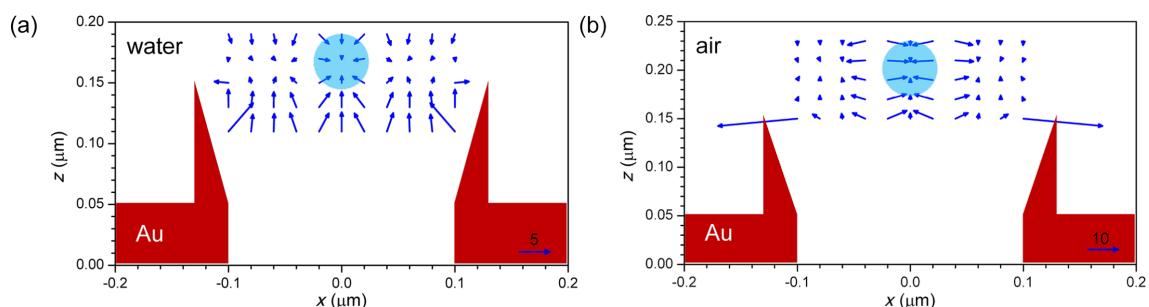
Figure 5: Arrow plot of the trapping force for plane-wave illumination in medium-to-substrate direction (as in Figure 4) at 760 nm wavelength for a 50-nm diameter polystyrene bead in (a) water and (b) air. The conical Au-well profile is schematically shown by the triangular shapes and the circle indicates the position of the bead in the central trap. The scale arrows at the lower right indicate forces of 5 and 10 pN/W/μm^2.
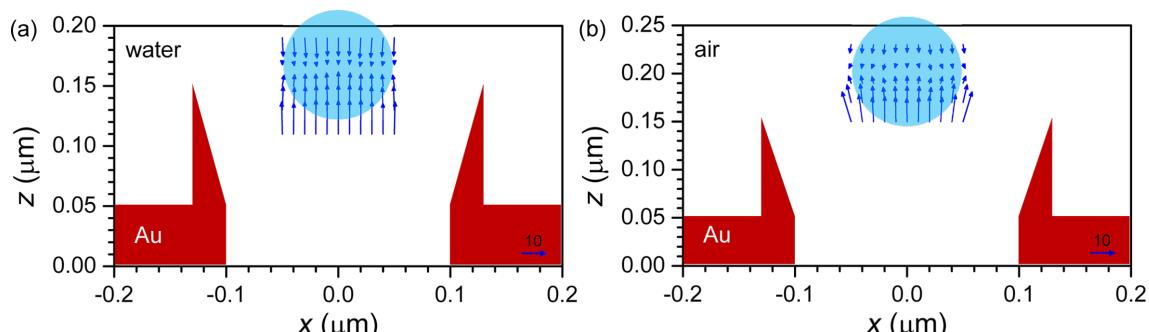
Figure 6: Arrow plot of the trapping force as in Figure 5 at 760 nm wavelength for a 100-nm diameter bead in (a) water and (b) air. The scale arrows at the lower right indicate a force of 10 pN/W/μm^2.

between the transverse force f_x and the longitudinal force f_z. In all cases, there is a central trapping spot at $(0,z_0)$, while the 50-nm bead also shows lateral ones (making a ring at about 50 nm distance from the center) with weaker transverse confinement and a tendency to easily escape the nano-well. This provides a strategy for moving the particles from one well to the neighboring ones by 'storing' them in the ring. The trapping height z_0 of about 165 nm in water and about 200 nm in air, measured from the center of the metal layer, is relatively independent of the particle size. However, due to the particle altering the field distribution, the force balance is strongly affected.

The most balanced trapping is achieved in water for the 50-nm particle in Figure 5a, with a maximum force of 2 pN/W/μm^2 in all directions in the particle vicinity. In air (Figure 5b) the longitudinal confinement is similar, but the lateral confinement is much stronger at 5 pN/W/μm^2, which makes it more difficult to shift the particle between neighboring wells. In the transverse direction, the smaller particle shows the escape distance from the central trap to be around half of the diameter, with the maximum force occurring at the maximum field gradient, which is consistent with the behavior of a single-beam optical tweezer [21]. One would then expect this distance to be independent of the diameter, as the particle size is much smaller than the

wavelength. However for the 100-nm particle in Figure 6 we have a very strong longitudinal force f_z of more than 20 pN/W/μm^2, but a very weak lateral confinement as the dielectric particle is attracted by the hot-spots along the nano-well walls. Because of this, the particle will tend to move randomly across the well, eventually escaping it in the case of air, while for water-trapping the lower position permits confinement by the walls, as long as the mechanical strength of the metal cone is enough to resist the impact of the particle. The increase in z-force with the diameter is also consistent with single-beam tweezers, where the maximal force scales with the bead volume for particles, which are small with respect to the wavelength [20].

This is confirmed by examining the force components in the trap to calculate the stiffness around the trapping spot [22] as shown in Figure 7. Considering an incident intensity of 1 W/μm^2, for the longitudinal z-direction we see that for the 50-nm bead in Figure 7a, the trap has a stiffness of about 0.06 pN/nm in water and 0.04 pN/nm in air. In the transverse x-direction in Figure 7b, the stiffness is about 0.05 pN/nm in water and 0.25 pN/nm in air for the central spot. Because the diameter is small with respect to the wavelength, the stiffness is expected to increase with the diameter, as the amount of material intercepted by the field is larger, which increases the trap-
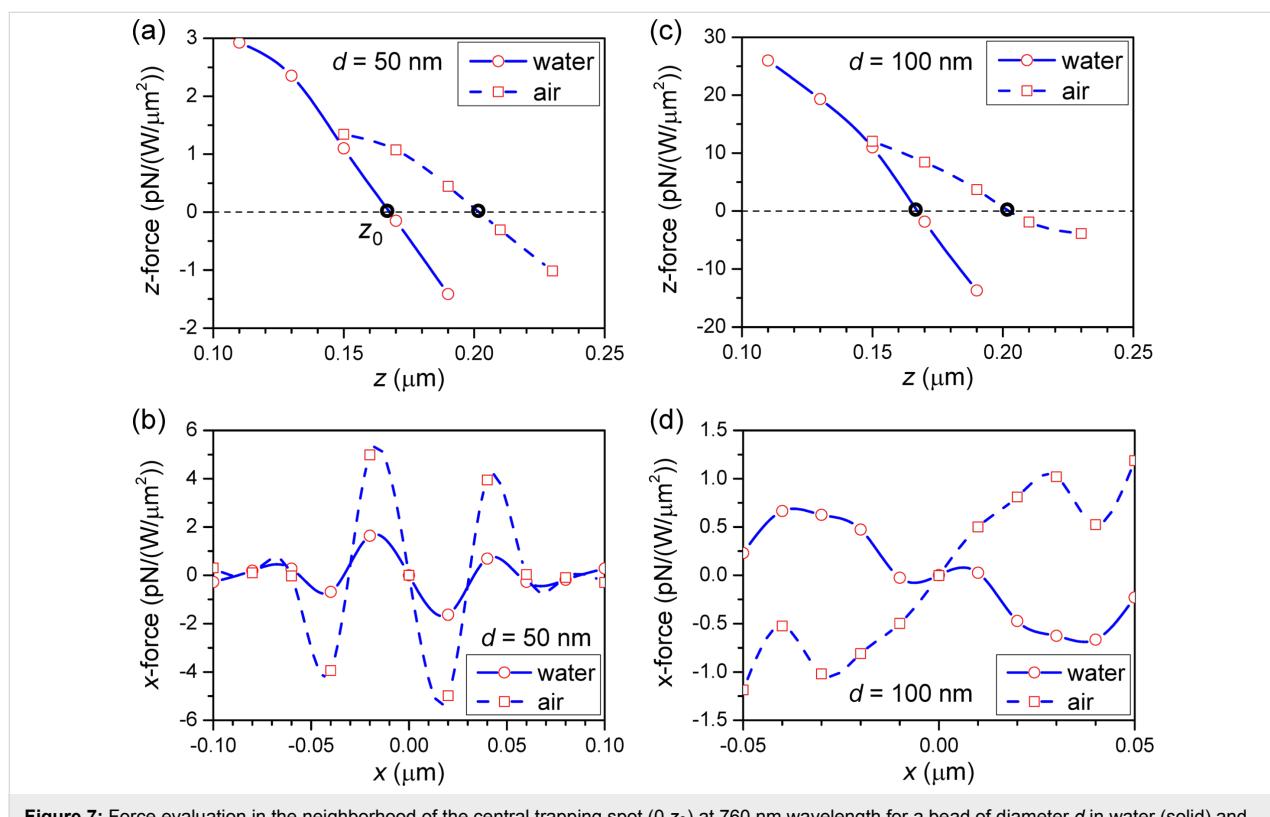

Figure 7: Force evaluation in the neighborhood of the central trapping spot $(0,z_0)$ at 760 nm wavelength for a bead of diameter d in water (solid) and air (dashed): (a,c) $f_z(z)$ at $x = 0$ and (b,d) $f_x(x)$ at $z = z_0$. The calculated values are indicated by the red markers, the blue lines are guides to the eye.

ping power [21]. However, due to the close SIBA interaction and redistribution of field, the *z*-direction stiffness increases by about one order of magnitude for the 100-nm bead in Figure 7c, while the transverse confinement is very different in Figure 7d at about 0.01 pN/nm in water. In air we notice that the particle is actually pushed away from the center and tends to escape the well, except for a weak confinement ring at a distance of 40 nm from the center.

Because the trapping position is relatively far away from strong field gradients, the escape force in the nano-wells is about one hundredth, and the stiffness is about one tenth, in comparison to the original SIBA trapping-substrate [9]. Yet, they are still significantly stronger than the maximum force given by Brownian motion. However, there is a significant benefit in that the nano-wells trap the particle at a much more exposed position, which makes the particle accessible from all sides to inspection and imaging. In addition the distance from the substrate makes it easier to probe the particle without interfering with the trap.

Conclusions

We demonstrate a simple plasma etching procedure which produces conical nano-well structures. The potential use in laser-trapping through the SIBA mechanism is numerically corroborated and analytical formulas are presented. The complex extinction spectra of the structures show that wavelength tunable lasers would be the best candidates to explore the peculiarities of nano-tweezing. We can foresee an enhancement of nano-material delivery into regions of high light intensity via Marangoni flow induced by localized heating and convection [23].

Acknowledgements

References

1. Ashkin, A.; Dziedzic, J. M.; Bjorkholm, J. E.; Chu, S. *Opt. Lett.* **1986,** *11,* 288–290. doi:10.1364/OL.11.000288
2. Juan, M. L.; Righini, M.; Quidant, R. *Nat. Photonics* **2011,** *5,* 349–356. doi:10.1038/nphoton.2011.56
3. Zhang, W.; Huang, L.; Santschi, C.; Martin, O. J. F. *Nano Lett.* **2010,** *10,* 1006–1011. doi:10.1021/nl904168f
4. Kohoutek, J.; Dey, D.; Bonakdar, A.; Gelfand, R.; Sklar, A.; Memis, O. G.; Mohseni, H. *Nano Lett.* **2011,** *11,* 3378–3382. doi:10.1021/nl201780y
5. Kang, J.-H.; Kim, K.; Ee, H.-S.; Lee, Y.-H.; Yoon, T.-Y.; Seo, M.-K.; Park, H.-G. *Nat. Commun.* **2011,** *2,* No. 582. doi:10.1038/ncomms1592
6. Cao, T.; Zhang, L.; Cryan, M. J. *Photonics J., IEEE* **2012,** *4,* 1861–1869. doi:10.1109/JPHOT.2012.2218589
7. Pang, Y.; Gordon, R. *Nano Lett.* **2011,** *11,* 3763–3767. doi:10.1021/nl201807z
8. Pang, Y.; Gordon, R. *Nano Lett.* **2012,** *12,* 402–406. doi:10.1021/nl203719v
9. Juan, M. L.; Gordon, R.; Pang, Y.; Eftekhari, F.; Quidant, R. *Nat. Phys.* **2009,** *5,* 915–919. doi:10.1038/nphys1422
10. Descharmes, N.; Dharanipathy, U. P.; Diao, Z.; Tonin, M.; Houdré, R. *Phys. Rev. Lett.* **2013,** *110,* 123601. doi:10.1103/PhysRevLett.110.123601
11. Kang, P.; Serey, X.; Chen, Y.-F.; Erickson, D. *Nano Lett.* **2012,** *12,* 6400–6407. doi:10.1021/nl303747n
12. Yang, A. H. J.; Moore, S. D.; Schmidt, B. S.; Klug, M.; Lipson, M.; Erickson, D. *Nat. Phys.* **2009,** *457,* 71–75. doi:10.1038/nature07593
13. Chen, C.; Juan, M. L.; Li, Y.; Maes, G.; Borghs, G.; Van Dorpe, P.; Quidant, R. *Nano Lett.* **2012,** *12,* 125–132. doi:10.1021/nl2031458
14. Nishijima, Y.; Nigorinuma, H.; Rosa, L.; Juodkazis, S. *Opt. Mater. Express* **2012,** *2,* 1367–1377. doi:10.1364/OME.2.001367
15. Dogariu, A.; Sukhov, S.; Sáenz, J. *Nat. Photonics* **2013,** *7,* 24–27. doi:10.1038/nphoton.2012.315
16. Ebbesen, T. W.; Lezec, H. J.; Ghaemi, H. F.; Thio, T.; Wolff, P. A. *Nature* **1998,** *391,* 667–669. doi:10.1038/35570
17. Gervinskas, G.; Rosa, L.; Brasselet, E.; Juodkazis, S. *Proc. SPIE* **2013,** *8613,* 861304. doi:10.1117/12.2002281
18. Jackson, J. D. *Classical Electrodynamics,* 3rd ed.; John Wiley & Sons: New York, NY, 1998.
19. Ramanandan, G.; Dharmadhikari, A. K.; Dharmadhikari, J. A.; Ramachandran, H.; Mathur, D. *Opt. Express* **2009,** *17,* 9614–9619. doi:10.1364/OE.17.009614
20. Agayan, R. R.; Gittes, F.; Kopelman, R.; Schmidt, C. F. *Appl. Opt.* **2002,** *41,* 2318–2327. doi:10.1364/AO.41.002318
21. Ashkin, A. *Biophys. J.* **1992,** *61,* 569–582. doi:10.1016/S0006-3495(92)81860-X
22. Simmons, R. M.; Finer, J. T.; Chu, S.; Spudich, J. A. *Biophys. J.* **1996,** *70,* 1813–1822. doi:10.1016/S0006-3495(96)79746-1
23. Louchev, O. A.; Juodkazis, S.; Murazawa, N.; Wada, S.; Misawa, H. *Opt. Express* **2008,** *16,* 5673–5680. doi:10.1364/OE.16.005673

Mapping of plasmonic resonances in nanotriangles

Simon Dickreuter, Julia Gleixner, Andreas Kolloch, Johannes Boneberg,
Elke Scheer and Paul Leiderer[*]

Abstract

Plasmonic resonances in metallic nano-triangles have been investigated by irradiating these structures with short laser pulses and imaging the resulting ablation and melting patterns. The triangular gold structures were prepared on Si substrates and had a thickness of 40 nm and a side length of ca. 500 nm. Irradiation was carried out with single femtosecond and picosecond laser pulses at a wavelength of 800 nm, which excited higher order plasmon modes in these triangles. The ablation distribution as well as the local melting of small parts of the nanostructures reflect the regions of large near-field enhancement. The observed patterns are reproduced in great detail by FDTD simulations with a 3-dimensional model, provided that the calculations are not based on idealized, but on realistic structures. In this realistic model, details like the exact shape of the triangle edges and the dielectric environment of the structures are taken into account. The experimental numbers found for the field enhancement are typically somewhat smaller than the calculated ones. The results demonstrate the caveats for FDTD simulations and the potential and the limitations of "near field photography" by local ablation and melting for the mapping of complex plasmon fields and their applications.

Introduction

Considering classical optics, light cannot be focused to a scale much smaller than half its wavelength. This phenomenon, commonly known as "diffraction limit", represents a major obstacle in modern nanotechnology, as it prevents the use of well-established optical methods in the preparation of struc-tures on the lower nanometer scale or the integration of optical parts into nanodevices. The diffraction limit can be overcome, however, by making use of the optical near fields of nano-structures, in particular metallic nanoparticles, which display pronounced plasmon resonances. These highly localized near

fields of plasmonic particles have been demonstrated to be a very efficient tool for nanomachining [1], optical pumping of nanoscale objects such as quantum dots [2], surface enhanced Raman scattering [3,4] and extreme light confinement for nonlinear effects [5-7].

While the basic principles of computing plasmonic resonances are well understood (i.e., by using Maxwell's equations on small objects), it has proven to be difficult to predict the field distribution for a given nanoscopic object. Two main factors are complicating this task: Firstly, solving Maxwell's equations for a system more complex than a simple geometric object requires a certain amount of simplification or a careful numerical treatment. Commonly used numerical simulation methods are, for example, discrete dipole approximation (DDA) or finite-difference in the time-domain (FDTD). Secondly, the outcome of these simulations has to be compared to a measurement of the field distribution. Since the field enhancement can be highly confined, direct probing of the field distribution is rather challenging. Experimental approaches to visualize the near field include techniques like scanning nearfield optical microscopy (SNOM), in which a fine tip consisting of a thin optical fiber coated with metal is scanned across the sample. This probe can either be used to illuminate a small volume of the sample or to collect light from the near field of a sample, which is illuminated conventionally [8-10]. A related approach is to use a very fine metal or dielectrical tip as a scatterer in the vicinity of the optical near field of the sample [11-13]. Another method for mapping near fields is photoemission electron microscopy (PEEM), in which photoelectrons emitted from the plasmonic structure out of regions of high field enhancement are imaged in an electron microscope [14,15].

Roughly a decade ago, several techniques with ex-situ analysis have been developed, which can be considered as types of "near-field photography". In these approaches, the near field is depicted in a matrix on which the scattering particle is placed or which encloses the particle itself [16-23]. These techniques share the common advantage that the resolution is believed to be limited mainly by the read-out process. As it is done after irradiation, highly advanced standard high-resolution microscopy methods can be used. Direct nanoscale ablation is a relatively straight-forward near-field photography technique that was demonstrated to depict the near field of nanostructures in great detail [21].

In this work, we describe our results for two techniques, which we have used to quantify optical near fields of plasmonic nanotriangles: on the one hand near-field photography by direct ablation of the substrate (silicon), on the other hand a new method, which utilizes the local melting of the gold nano-

structures at sites of high field enhancement. These two techniques are variations of the same methods: The substrates carrying the nanostructures are irradiated with pulsed laser light. The ablation experiments are realized by using irradiation with femtosecond laser pulses, i.e., pulses shorter than the internal heat diffusion times. When using pico- and nanosecond pulses instead, the heat diffusion results in controlled melting of the nanostructures. The findings will be compared to the results of FDTD simulations, and also the limitations of the two techniques will be discussed. Finally we discuss the field-enhancing effects of the nano-triangles by comparison to equivalent experiments carried out on bare substrates. (We note that the enhancement factors discussed here do not refer to the electric field E, but to the field intensity, i.e., E^2.) Triangles were chosen here instead of spheres or rods studied in other recent investigations [1,24-26], because they have sharp tips where the localization of the field enhancement can be particularly pronounced. The size of these triangles was relatively large, so that not a simple dipole mode, but higher order modes were excited by the incident light, demonstrating the potential of these methods for imaging also complex field distributions in fine detail.

Experimental
Optical set-up

In our femtosecond experiments we used laser irradiation provided by a multi-pass Ti:sapphire amplifier system with a maximum pulse energy of up to 8 mJ, a nominal pulse length of 150 fs, and a center wavelength of 800 nm. For picosecond experiments, the laser beam was coupled out of the amplifier before passing the compressor stage. In this case the pulse length of the laser was measured to be 300 ps (full width at half maximum, FWHM).

In our measurements, the spatial beam profile of the laser is of vital importance: To gain insight into more than the distribution of the near-field enhancement of a nanoscale object, the absolute enhancement factor has to be measured. In near-field photography, this is commonly done by comparing the threshold of the imaging mechanism (e.g., ablation threshold) without near-field enhancement to one with a scattering nanostructure present during illumination (nanoscale ablation threshold). This route requires the precise knowledge of the fluence distribution of the illuminating laser spot. When a well-defined function describing the energy distribution of the laser spot is known, the determination of the local fluence is reduced to a measurement of the distance from the beam center in combination with a measurement of the total energy of the illuminating laser pulse. For a Gaussian intensity distribution on the sample surface, a simple method to measure the important parameters (the FWHM and the peak intensity I_0) of the distrib-

ution has been suggested by J. M. Liu. [27]. Using this method, a substrate with a threshold behavior is illuminated with laser pulses of different total power. The threshold as well as the width of the Gaussian intensity distribution can be directly deduced from the power dependence of the spot size obtained on substrates with an ablation threshold fluence. With a TEM00 mode as the illuminating laser mode and a large lens, the assumption of a Gaussian intensity distribution is justified. In the case of the set-up used in this work, however, the intensity distribution of the laser amplifier system was rather inhomogeneous. Therefore, in order to produce a well-defined intensity distribution on the sample surface, a circular 2 mm aperture was positioned in a region of the beam with nearly constant intensity. Afterwards, the selected beam was focused onto the sample surface (Figure 1).
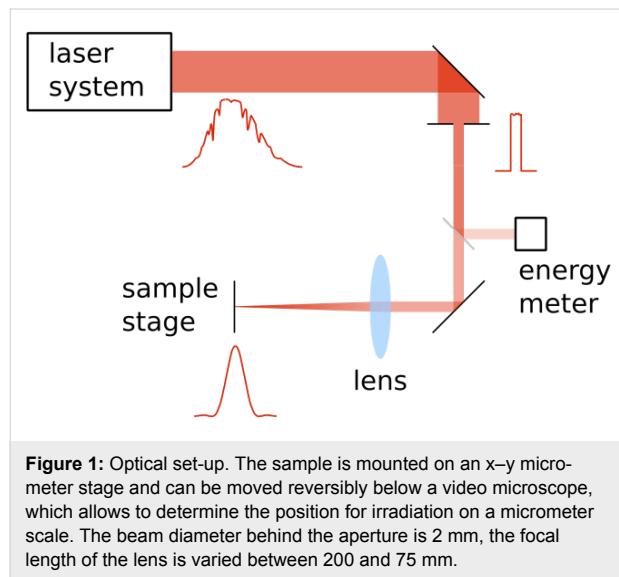
This situation is described by Fraunhofer diffraction and leads to an Airy-like intensity distribution in the focal plane of the lens [28]:

$$I = I(0)\left[\frac{2J_1\left(k\,a\,r/f\right)}{k\,a\,r/f}\right]^2 \qquad (1)$$

with

$$I(0) = \frac{P_0 A}{\lambda^2 f^2} \qquad (2)$$

(J_1: first order Bessel function of the first kind; $k = \pi/\lambda$: wave vector of the incident irradiation; λ: wavelength of the incident irradiation; a: radius of the illuminated aperture; r: distance from the intensity maximum on the sample surface; f: focal length of the lens; P_0: total irradiation power; $A = \pi r^2$: area of aperture).

Figure 2a shows a cross section of such an Airy pattern, obtained with a simple CCD camera. For a more exact determination of the profile we have used films of crystalline $Ge_2Sb_2Te_5$ (GST) as detector material, which has already proven its versatility as a medium for quantitative imaging of fluence distributions earlier [16]. These films were irradiated by pulses with various total energies. Both femtosecond and picosecond pulses induce a phase transition in GST, changing the film from a highly reflecting crystalline into an optically absorbing amorphous state, when the local fluence exceeds a certain threshold fluence $I_{th,GST}$. As illustrated in Figure 2b, this leads to a circular amorphous region, whose radius depends on

Figure 1: Optical set-up. The sample is mounted on an x–y micrometer stage and can be moved reversibly below a video microscope, which allows to determine the position for irradiation on a micrometer scale. The beam diameter behind the aperture is 2 mm, the focal length of the lens is varied between 200 and 75 mm.

Figure 2: (a) Laser profile at the sample position taken with a CCD camera. Next to the central maximum the first Airy ring is clearly visible. (b) Optical microscope image of a $Ge_2Sb_2Te_5$ (GST) film, which was irradiated by a single laser pulse (15.5 µJ). In the central region the GST is completely ablated. The dark ring around this region shows were the local fluence was high enough to induce a phase change from the reflecting, crystalline to the amorphous, absorbing state of the GST.

the total energy of the respective pulse. The relation between the threshold fluence and the radius r_i for a certain total energy P_i is given by

$$I_{\text{th,GST}} = \frac{P_i A}{\lambda^2 f^2} \left[\frac{2J_1\left(k\,a\,r/f\right)}{k\,a\,r_i/f} \right]^2 \qquad (3)$$

The radii r_i obtained for the various pulses are determined by an optical microscope. From a fit of these data to Equation 3 the detailed fluence profile can be derived. (Such a fit is shown in Figure S1 in Supporting Information File 1.)

Sample preparation

For the preparation of the plasmonic structures two kinds of nanostructuring methods have been applied, namely colloid lithography and electron beam lithography. The material used was exclusively gold. Figure 3a and Figure 3b present an example for the first and Figure 3c and Figure 3d for the second technique, respectively. In colloid lithography, self-assembled monolayers of meso- or nanoscopic spherical particles are produced by self-organization and subsequently used as an evaporation mask, as described for the first time by Fischer and Zingsheim [29] and Deckman [30]. Since then, the technique has been improved by many groups to yield large arrays of different nanostructures in merely one step [31-36]. The main advantage of colloid lithography is that, while it is relatively easy to implement, periodic arrays of uniform nanostructures can be distributed over large areas (up to a few cm^2). Further-more, the triangular structures prepared with this method can have tip radii as small as 5 nm, a size which is difficult to achieve by conventional lithography. On the other hand, in contrast to e-beam lithography samples, the edges of colloid-lithography structures have somewhat inclined walls, and they are surrounded by an ensemble of small solid droplets, both as a result of the evaporation process. These features are clearly visible in Figure 4 as well as in Figure 3b. While the inclined
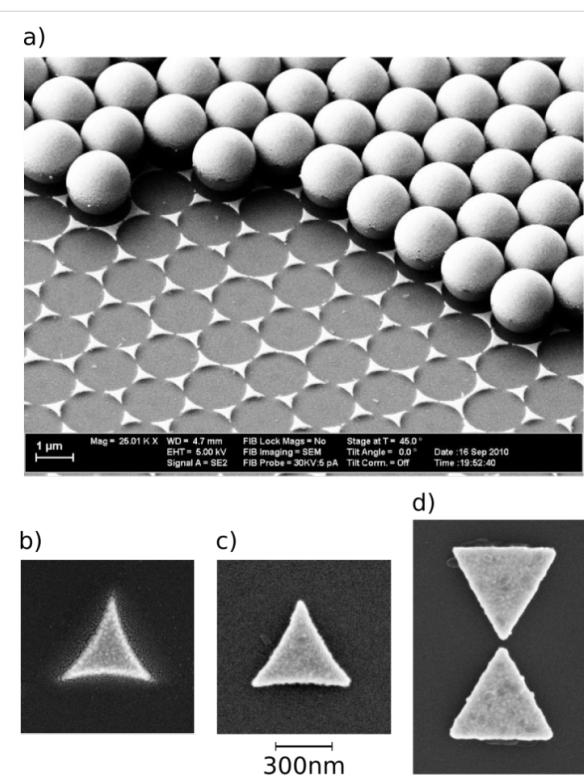
Figure 3: Scanning electron micrographs of different types of triangles used in the course of this work. The triangles in (a) and (b) were prepared by colloid lithography, the triangles in (c) and (d) were prepared by e-beam lithography. In (a) only part of the nanosphere evaporation mask has been removed to illustrate the pattern formation.

walls may have some influence on the details of the optical near fields, the droplets are negligible in this respect, and they can serve as useful marks for the original position of the triangles when the triangles themselves have been removed by the laser pulse (see, e.g., Figure 5, which will be discussed in detail below). The electron-beam lithography samples were prepared on a silicon (Si) wafer with a native silicon oxide (SiO$_2$) layer with a thickness of 2.4 nm (measured by ellipsometry), for the wafers used for colloid lithography the oxide was 1.5 nm thick.
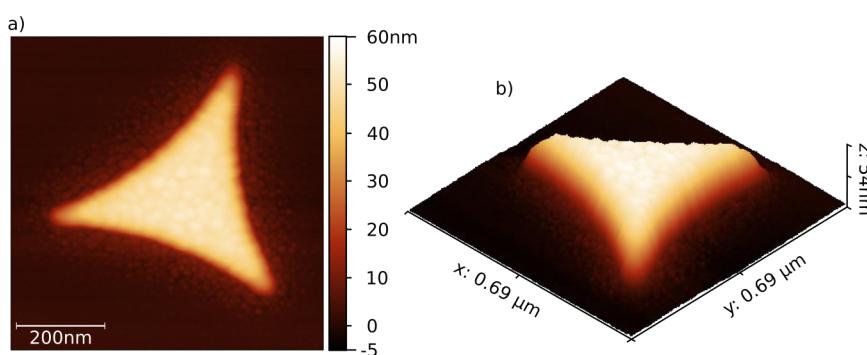
Figure 4: AFM image of a colloid lithography triangle. (a) Top view; (b) 3D image.

Figure 5: Upper left: Fluence distribution along the laser spot radius as described in the Experimental section. Lower left: SEM picture of one quadrant of an ablation pattern of gold triangles irradiated with a 150 fs laser pulse. The triangles were produced by colloid lithography using spheres with a diameter of 1.55 µm and had a side length of about 530 nm. Right: Detailed blow-ups of triangles and the Si surface in different states of modification. The radial position of each blow-up is marked in the fluence distribution. It has to be noted that the triangles exhibit two different modes, depending on the polarization of the exciting light. Thus two different ablation patterns can be observed. In this figure patterns for a polarization parallel to the edge of the triangle are shown. A comparison of the two different modes can be found in Figure 12.

Scanning electron microscopy (SEM) and atomic force microscopy (AFM) were used for measuring the dimensions of the plasmonic structures as well as the resulting modifications of these structures and the substrate.

Simulations

We used the program package "FDTD Solutions" by Lumerical Inc. to simulate the spatial distribution of the electric field of a triangle and the energy dissipated during its illumination. To get realistic results, an AFM image of a gold triangle like the one in Figure 4 was used as a basis for generating the geometry of the simulation. This method allows for taking into account the details of the shape of a triangle (the curvature of the corners, the profile of the edges and the surface roughness), which have significant influence on the coupling between the triangle and the incident light wave.

The substrate of the triangle used for the calculations was chosen to consist of a 1.5 nm thick SiO_2 layer on top of bulk Si. In Figure 6, the results of such a simulation are shown. Figure 6a depicts the field intensity around the triangle. The absolute values denote the intensity enhancement compared to the incident intensity (averaged over the whole height of the triangle (40 nm)). In Figure 6b the energy, which is dissipated inside the triangle, is shown. For this graph the results of two simulations were combined: The values gathered from a simulation describing a single triangle on a silicon surface were divided by the values of a simulation with the same parameters, describing a continuous gold film. This results in a factor, which depicts the local enhancement of the dissipated energy, as it is caused by the triangle. As before, the values were averaged over the triangle height. Figure 6c displays the electrical field vectors at 10 nm height inside the triangle.
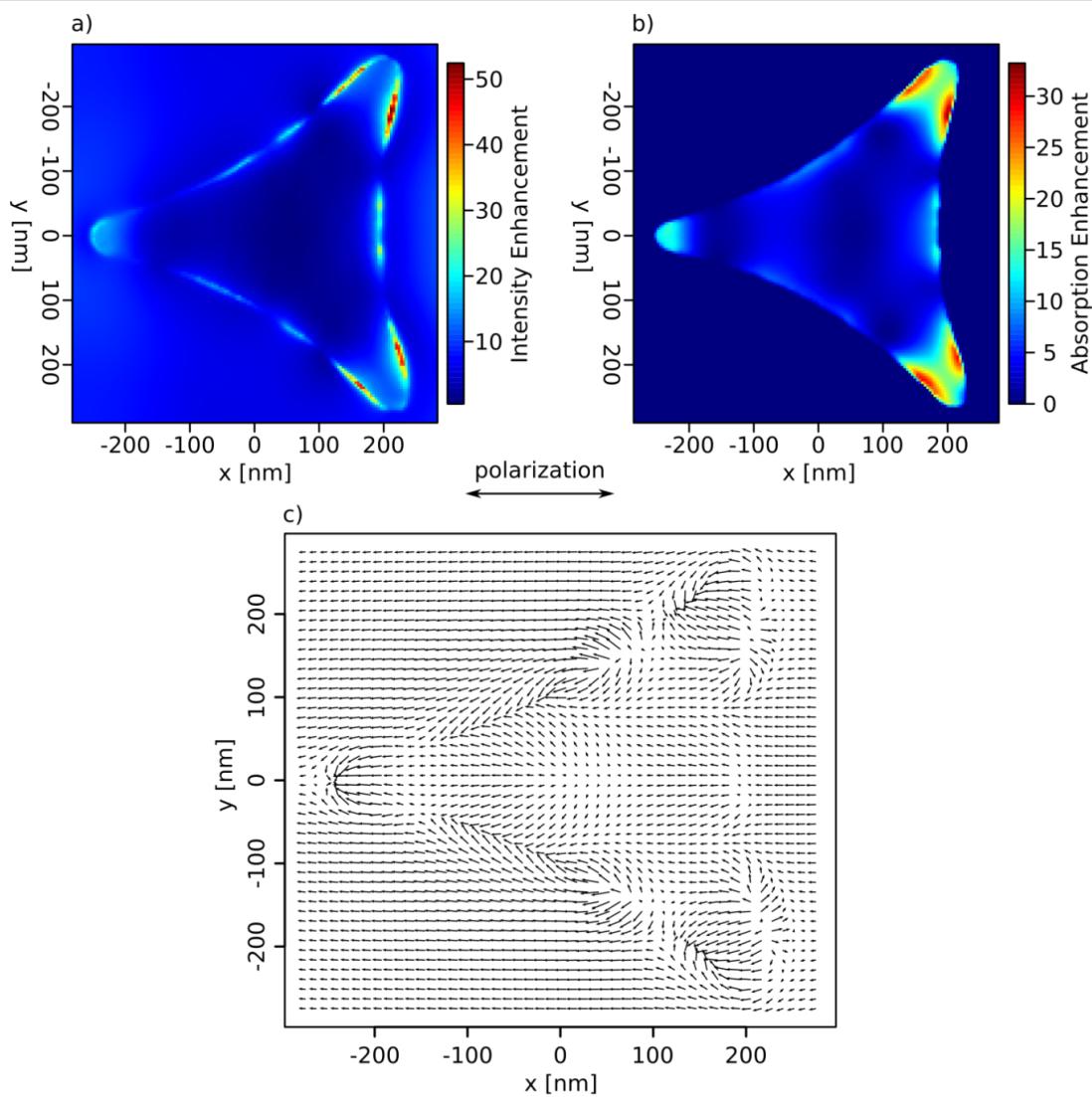
Figure 6: (a) Calculated field intensity enhancement, (b) dissipation, and (c) field distribution for a nanotriangle like in Figure 4. (The model structure on which the simulation was based is depicted in Figure S2 in Supporting Information File 1). The polarization of the incident laser radiation was here horizontal. The simulation volume was 1 × 1 × 1.2 μm³ with "perfectly matched layer" boundary conditions. The meshing was set to automatic mode far from the triangle and a manually refined mesh with a cell size of 1.3 × 1.3 × 0.5 nm³ was added around the particle.

Results and Discussion
Femtosecond laser ablation
General features

We first give an overview over the general features of femtosecond plasmonic ablation. Figure 5 shows an SEM micrograph of a typical femtosecond ablation site on a sample, which consists of gold nano-triangles prepared by colloid lithography. The plasmonic structures were irradiated with a single femtosecond laser pulse with a total energy of 30 μJ. The irradiation intensity increases towards the center of the irradiated spot, and, since the spot profile is known, the local fluence can be determined by measuring the distance from the ablation center. The details shown to the right of the overview visualize the different stages of the removal/ablation process as a function of the local

fluence. The *calculated* near-field distribution for similar triangles has been shown in Figure 6a. Looking at the SEM micrographs, several thresholds can be distinguished for single pulse femtosecond irradiation. Starting at low intensities, first a modification of the triangles is observed at those tips, where the field enhancement is largest. For somewhat higher intensities, the triangles are removed from the surface. In some cases, the complete triangle is tilted from its original position (see frame (2) of Figure 5) or found somewhere else on the sample surface. Note that, in contrast to picosecond (see below) or nanosecond [37] irradiation, the modification of the triangles is only slight for fluences below the removal threshold or even for redeposited triangles. Triangles in more advanced states of melting could not be found for femtosecond ablation.

For the particles presented in Figure 5, the removal threshold is followed by a region where no modification of the underlying surface is discernible by SEM or AFM measurements. Above a certain *incident* local fluence $I(x)$, however, which we denote as $I_{th,abl}^*$, an ablation of the substrate's surface is visible. (The asterisk indicates that $I_{th,abl}^*$ is smaller than the ablation threshold of the bare substrate, $I_{th,abl}$, due to the local field enhancement factor FE: $I_{th,abl}^* \cdot \text{FE} = I_{th,abl}$). The fluence associated with this ablation threshold of the plasmonic structures is strongly dependent on the particle size and shape and can be higher, the same or even lower than the removal threshold. Above the ablation threshold $I_{th,abl}^*$, the surface modification takes the form of material removal as well as droplets of apparently molten and resolidified material [38]. For even higher intensities, the ablated region increases, with the size of the accompanying droplets increasing accordingly. Eventually, the substrate is modified everywhere also between the positions of the plasmonic structures. We will focus here on the intensity range around the ablation threshold $I_{th,abl}^*$. The higher intensities are beyond the scope of this article and will be considered elsewhere.

Determination of the ablation threshold

A first estimate for the ablation threshold $I_{th,abl}^*$ in the near field of the plasmonic triangles can already be obtained from Figure 5, where the frames for 135 and 215 mJ/cm² are below and above the threshold, respectively. In order to determine the value of $I_{th,abl}^*$ more accurately, we have taken AFM scans, such as the one shown in Figure 7a, which allow one to measure the depth of the ablation holes. An example for the profile of an ablation crater at an incident (local) fluence of 220 mJ/cm² is given in Figure 7b. The depth of such holes has been measured

for various positions across the irradiated spot, i.e., as a function of the incident fluence $I(x)$. The result is plotted in Figure 8. Assuming, for simplicity, a linear relationship between depth and $(I(x) - I_{th,abl}^*)$ in the intensity regime close to threshold, we obtain a threshold value for $I_{th,abl}^*$ of 160 mJ/cm².
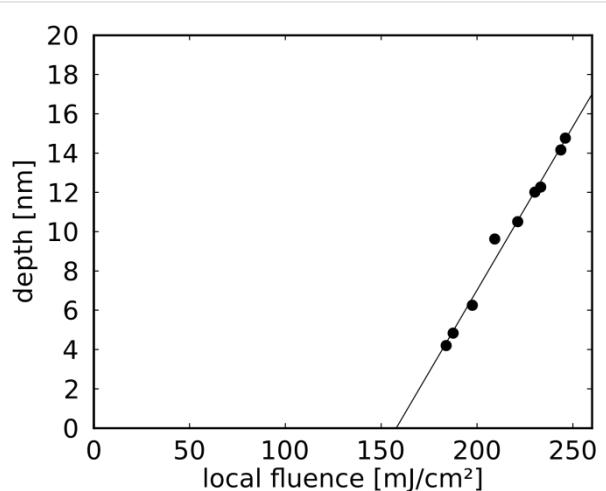
Figure 8: Hole depth (as determined from profiles such as in Figure 7b, measured with respect to the height of the flat surface) as a function of the incident local fluence.

This value can be compared to the ablation threshold of bare Si, $I_{th,abl}$, which according to the literature is close to 400 mJ/cm² for single laser pulses at similar wave length and pulse duration [24-26]. From the ratio of the two thresholds one arrives at an intensity enhancement of 2.5 at the two triangle tips which cause the ablation holes in Figure 7. This result has to be
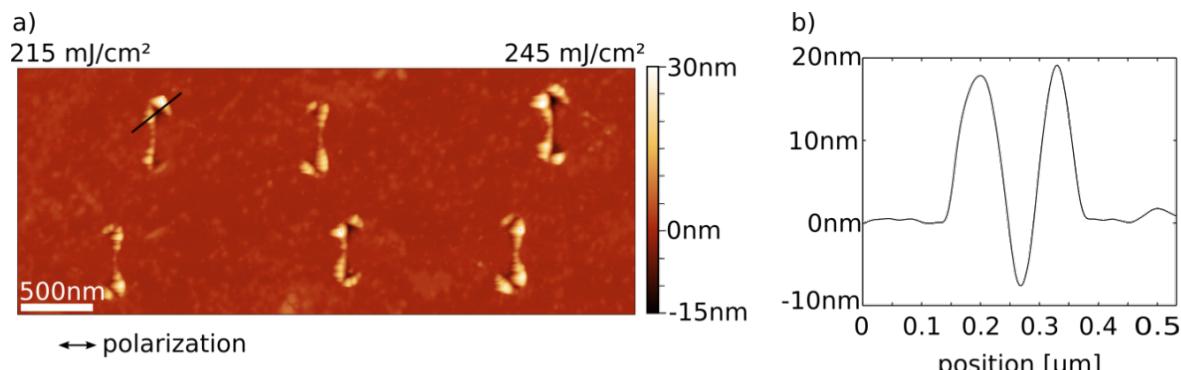
Figure 7: (a) AFM image of a Si surface with ablation holes, generated by irradiation of colloid lithography triangles with a single femtosecond laser pulse. (b) height profile of one of the holes taken along the black line in (a). The arrow indicates the polarization of the laser light. The incident intensity increases to the right from 215 to 245 mJ/cm². Gold droplets resulting from sample preparation and ablation have been removed with aqua regia. Here, the volume of the material deposited in the rim appears to be distinctly larger than the volume of the crater hole. This is due to a change in composition (the rim consists mostly of silicon oxide), and partly also due to the fact that the AFM tip is not sharp enough to trace out all details of the crater profile.

considered with care, however, because the threshold value for the ablation of bare Si appears to vary between different experiments and also depends on assumptions about the beam profile [25]. We have therefore determined the ablation threshold for bulk Si with the same set-up and under the same conditions as for the plasmonic structures described above.

Figure 9 shows an AFM image and the height profile of the ablation hole for a peak fluence of 3.2 J/cm^2. Carrying out this experiment for different total energies of the incident laser pulse provides the depth of the holes as a function of the fluence, as depicted in Figure 10. The extrapolation yields a threshold value of 1800 mJ/cm^2, nearly a factor of five higher than the literature value mentioned above. The absolute values of the hole depths are in close agreement with results of Nedyalkov et al. for fluences above 2 J/cm^2 [1]. The apparent difference in the threshold values can be ascribed to two regimes with different ablation mechanisms: whereas at low fluences non-thermal ablation dominates, the regime above about 2 J/cm^2 is governed by thermal effects, including explosive boiling, which give rise to distinctly higher ablation rates [39]. Since the craters generated by ablation in the near field of the nano-triangles resemble the craters on bulk Si generated by far-field illumination in the high-intensity regime, we compare the extrapolated values from the linear fits in Figures 8 and 10, namely 160 and 1800 mJ/cm^2 for near-field and far-field illuminations, respectively. Under this assumption the resulting intensity enhancement factor is about 10, a factor of two to five below the results of the simulations in Figure 6a and Figure 12 (shown below).

Shape dependence

To demonstrate the dependence of both field distribution and field enhancement on the details of the shape of a nanostructure,
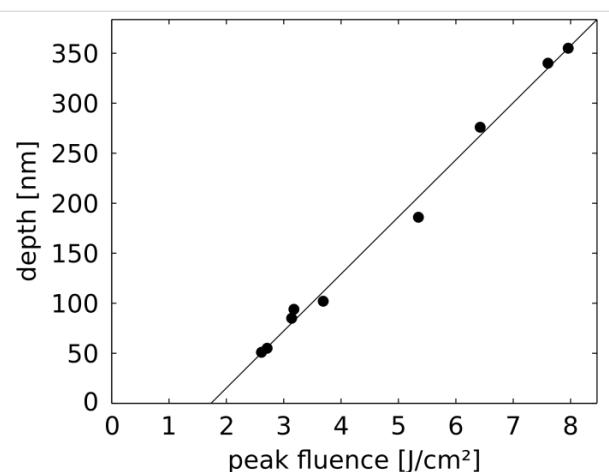
Figure 10: Depth of holes in Si, generated by far-field ablation, as a function of the peak fluence.

two similar types of gold nano-triangles with differently shaped edges have been used: For one type the edges were slightly curved inwards to mimic the shape of triangles prepared by nanosphere lithography, while for the second type the edges were straight, like the triangles simulated in early DDA calculations [21]. The structures in this case were prepared by e-beam lithography. Note that, even though the shape of the triangles prepared by colloid lithography and the structures with concave edges presented here seem similar when looked at from above, the triangles prepared by e-beam lithography have much steeper ridges due to the different preparation mechanism.

Figure 11 shows SEM micrographs of the triangles and their corresponding ablation patterns for two different orientations with respect to the polarization of the incident laser pulse, and for the two differently shaped edges. Comparing the ablation patterns for both structures and orientations, the ablation distrib-
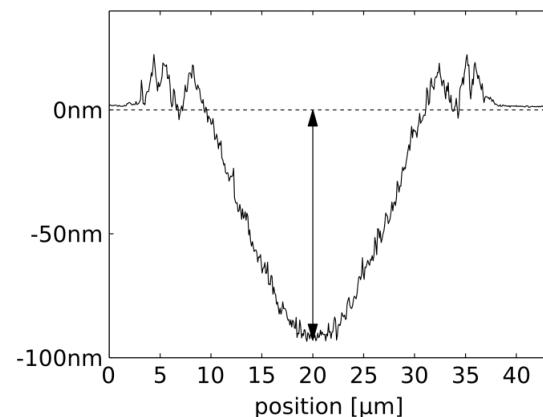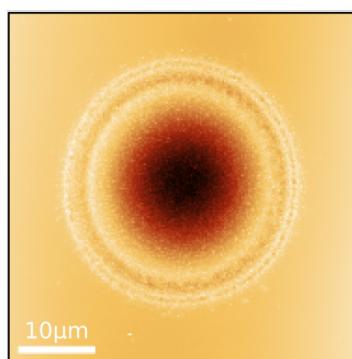
Figure 9: AFM image and height profile of an ablation hole generated by far-field ablation of bare Si (same wafer as in Figure 7). Note that the beam profile in this case is again described by an Airy distribution, comparable with the irradiation of the nanostructures.
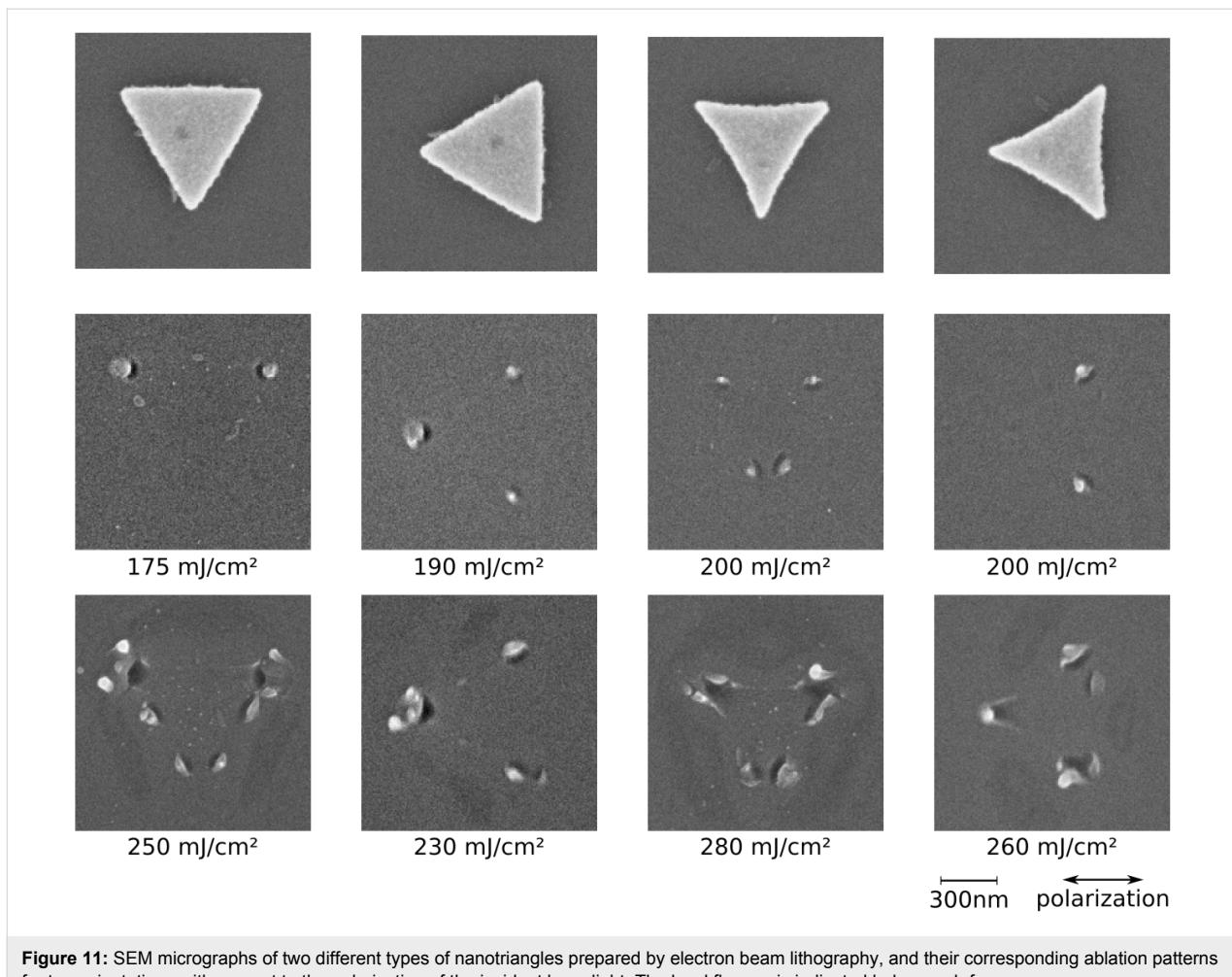
Figure 11: SEM micrographs of two different types of nanotriangles prepared by electron beam lithography, and their corresponding ablation patterns for two orientations with respect to the polarization of the incident laser light. The local fluence is indicated below each frame.

utions are evidently different. Even though the structures are of comparable size and their basic geometry is the same, the exact shape of the edges of the triangles has a major effect on the ablation distribution. The triangles with the concave edges, which resemble the colloid lithography triangles, exhibit an ablation pattern similar to the pattern of those (Figures 5 and 7), as expected. The straight-edged triangles, on the other hand, show an ablation pattern much closer to a simpler (dipolar-like) expectation: Slightly above the ablation threshold, ablation can only be found below the tips of the triangles which are oriented in the direction of the polarization. Only for higher local fluences, a more complex ablation distribution is revealed. The threshold values for plasmon-induced ablation $I^*_{\text{th,abl}}$ of these triangles were a factor of two lower than for the concave triangles.

FDTD simulations for both types of triangles can be found in Figure 12. Note that, in contrast to the simulation in Figure 6, the simulation in Figure 12 is based on a more idealized geometric structure with steeper ridges. This is justified, as

the ridges of the structures are less rounded down due to the preparation process. Again, the distribution of the local field enhancement matches the distribution of the ablation pattern quite well. Comparing the calculated patterns with the ablation patterns in Figure 11, one can see that the regions with highest calculated intensities already show ablation for local fluences slightly above the ablation threshold (Figure 11, second row). Ablation in the regions with lower calculated intensity becomes visible as the local fluence increases (Figure 11, third row). The comparison also shows that the calculated enhancement factors for the straight-edged triangles are roughly a factor of two higher than for the concave triangles, which goes in line with the ratio of the corresponding ablation thresholds mentioned above. The absolute enhancement values determined from experiment, however, are again distinctly lower than the FDTD results.

Minimum structure size
As mentioned in the introduction, plasmon-mediated ablation is an interesting method for optical patterning of surfaces far
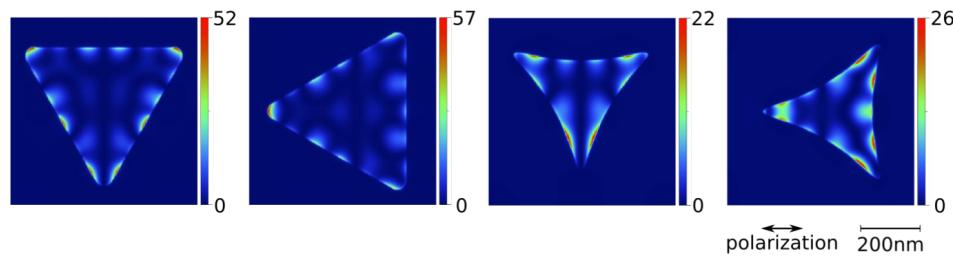
**Figure 12:** FDTD calculations for the structures presented in Figure 11. The field intensity enhancement was extracted in a plane between the SiO_2 layer (thickness: 2.4 nm) and the Si substrate below the triangle. The simulation volume was $3 \times 3 \times 6$ µm^3 with "perfectly matched layer" boundary conditions. The meshing was set to automatic mode far from the triangle, and a manually refined mesh with a cell size of $2 \times 2 \times 0.5$ nm^3 was added around the particle.

below the diffraction limit as well as for imaging optical near fields. The ablation hole shown as an example in the profile of Figure 7b has a depth of 7 nm and a width of 40 nm. The smallest holes we obtained in Si substrates so far, observed for plasmonic triangles of 70 nm side length, were 5–10 nm wide [40]. One might ask whether this is a fundamental limit, or whether by ablation of Si one could image even smaller details of the optical near-field distribution.

In order to address this problem we have investigated so-called bow-tie antennas, consisting of two triangles as shown in Figure 3d. Figure 13a shows the region between such a bow-tie antenna with a gap distance of 30 nm, after it has been irradiated with a local fluence of 90 mJ/cm^2. Figure 13b represents the calculated near-field intensity distribution of this configuration. The color scale for the distribution has been adjusted to visualize the intensity distribution between the triangles. One can see in Figure 13a that distinct nano-ablation between the two triangle tips has taken place (arrow in Figure 13a), potentially even with fine structure. The resolution of the SEM image

however does not allow one to unambiguously determine the shape of the ablation hole. Note that in this case the incident fluence was even below the triangle removal threshold. In the same region of Figure 13b the calculated enhancement factor is on the order of one, thus it is quite unlikely that the enhanced local fluence would reach the fluence $I_{th,abl}$ needed to ablate the underlying Si substrate, which is one order of magnitude higher.

This observation suggests that some broadening mechanism is effective, which disperses the energy deposited by the plasmonic near fields. Such a mechanism could not only explain the ablation in between the triangles in Figure 13a, but might also be one of the reasons for the significantly lower enhancement factors found in all our ablation experiments when compared to the intensity enhancement calculated by FDTD. When dissipated over a wider region, the overall effect of the near-field enhancement is diminished by a factor given by the ratio of the volume with an intense near field and the dissipation volume. A possible mechanism for the broadening has been outlined by Kolloch [40] based on the fast diffusion of the charge carriers in the light-induced electron–hole plasma in the silicon. A broadening of the ablated hole structure compared to the calculated intensity distribution has also been observed recently by Robitaille et al. [26] for Au *nanorods* on Si when irradiated with femtosecond pulses, and the quantitative agreement with a carrier-diffusion-based model is reported.

Picosecond laser melting

In contrast to the femtosecond irradiation studies presented above, thermal diffusion is the dominating factor when ablation is done with laser pulses with a duration in the higher picosecond and nanosecond regime [41]. For near-field ablation this leads to a significant decrease in imaging resolution and renders this timescale useless for nanoscale material processing of the substrate. The resulting modifications of the plasmonic structure itself, however, are interesting both from a technical as well as a fundamental point of view. For fundamental considerations, the dominance of thermal diffusion leads to a simplification in
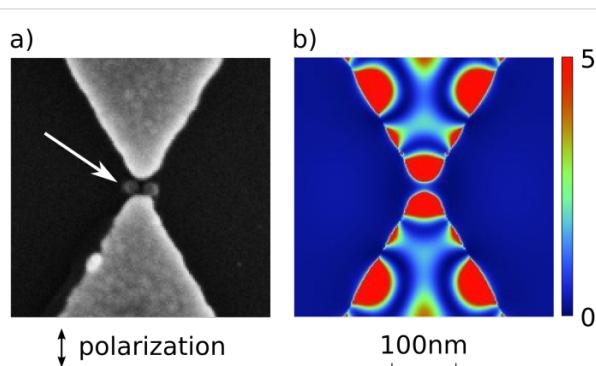
Figure 13: (a) SEM micrograph and (b) calculated field distribution for the center region of a bow-tie antenna with a distance of 30 nm. The structure has been irradiated with a 150 fs laser pulse (wavelength: 800 nm) with a local fluence of 90 mJ/cm^2. The arrow points towards the region in the feed gap where ablation of the Si has taken place. The color scale in (b) has been chosen such to show the field distribution in the region between the triangles.

the distribution of the energy provided by the incoming laser pulse. As the only discernible process of material modification is melting, the near-field distribution can simply be considered acting as a heat source. This reduces the complexity of the calculation and the simulation of the thermal and mechanical processes after irradiation considerably. From a technical point of view, the system provides a spatially confined heat source, which is only limited by the thermal diffusion length given by the pulse duration of the illuminating laser.

General features

Figure 14 gives an overview of the different stages of the picosecond melting/ablation for gold triangles with a side length of 530 nm. The plasmonic structures used for the melting experiments were again produced by colloid lithography.

For triangles just above the modification threshold (Figure 14, frame 1), the tip with the highest local plasmon intensity has

been deformed into a spherical droplet, while the tips with low near-field enhancement have not been altered. Additionally, the surface texture of the triangles in the modified region has changed. While the unmodified regions have a roughness comparable to the deposited gold film, the surface structure in the regions, which show a change due to the laser radiation, is much smoother. This phenomenon, which is ascribed to melting, can also be used for the determination of the melting threshold of a homogeneous film (see below). With increasing local fluence, larger parts of the triangles are deformed, until finally a spherical smooth particle has developed at the position of the original triangle.

Above a local fluence threshold of 180 mJ/cm^2, no gold particles comparable to the size of the original triangles can be found anywhere on the substrate. For even larger intensities, however, a formation of droplets in the former triangle positions and in between these positions is observed. The droplets
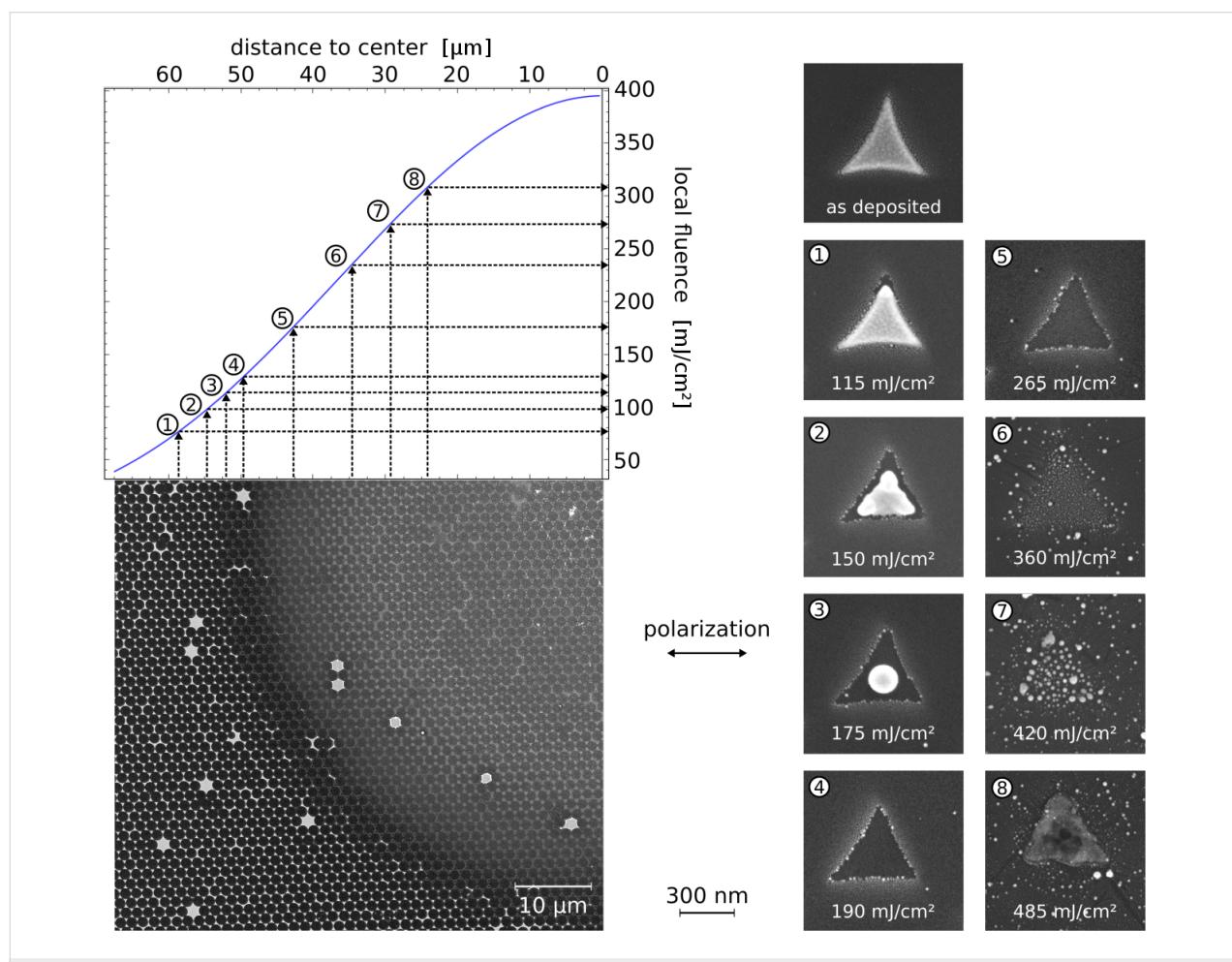
Figure 14: Evolution of laser-molten gold triangles (thickness: 40 nm, side length: 530 nm, prepared by colloid lithography with 1.55 μm diameter spheres) for increasing laser fluence in equivalent presentation as Figure 5: Upper left: Fluence distribution along the spot radius. Lower left: SEM micrograph of one quadrant of an ablation spot irradiated with a ps laser pulse (wavelength: 800 nm, FWHM: 300 ps). Right: Details at different levels of incident laser fluence. The local fluence is indicated in each frame.

consist of gold, since they can be removed by aqua regia. As in the previous chapter, the laser-induced modifications seen at high intensities well above the melting threshold will be discussed elsewhere.

Melting threshold

As shown in Figure 15, apparently also the local melting allows one to image the regions of high near-field enhancement. Due to thermal diffusion the spatial resolution reached here is lower than for local ablation, but the overall patterns of the intensity distribution turn out to be quite similar. In spite of the obvious broadening taking place during local melting, also in this case an estimate for the plasmonic field enhancement can be obtained. We have used the same strategy as in the previous chapter: When the volume of the affected zone is determined as a function of the local intensity, a threshold value for the onset of melting can be derived. This threshold for the plasmon-induced melting is then compared with the threshold for the melting of the homogeneous system, i.e., an unstructured Au film, under far-field illumination.

plasmon-enhanced threshold value $I_{\mathrm{th,melt}}^*$ of 60 mJ/cm^2 for the melting of the tips can be derived.
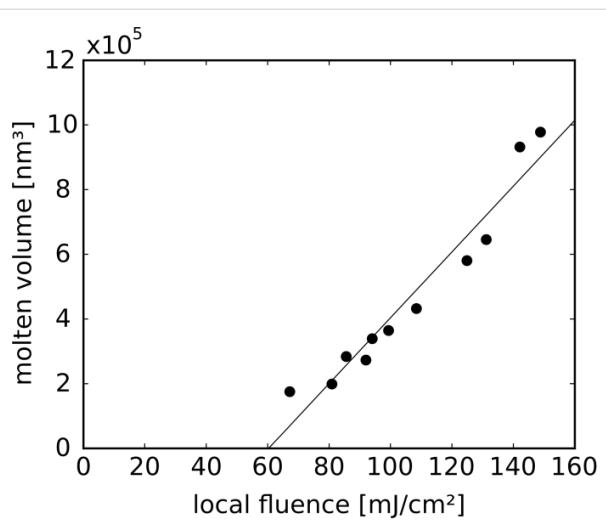
Figure 16: Molten volume at the triangle tips vs local laser fluence.

Figure 15: (a) SEM micrograph of colloid lithography nanotriangles irradiated with a 300 ps laser pulse (wavelength: 800 nm) with high gradient to show all typical states of the melting process in one image. The local fluence increases to the right from 85 to 185 mJ/cm^2.
(b) Detail from (a). The scale bars are 1 μm and 250 nm, respectively, the polarization of the incident light is horizontal.

Figure 15a displays an SEM image of partly molten triangles in an intensity regime between 85 and 185 mJ/cm^2, and Figure 15b shows a blow-up. Note that the intensity gradient used in this irradiation was so steep that the right triangle in Figure 15b, located less than 1 μm from the left one, exhibits considerably larger molten volumes at the tips. Plotting the molten volume, as determined from the SEM images, versus the incident intensity leads to the graph in Figure 16, from which a

For the determination of the melting threshold of a homogeneous Au film, which was also irradiated with a single 300 ps laser pulse, we consider Figure 17. The Si substrate and the film thickness were the same as in Figure 15. Figure 17a shows an overview over the whole irradiated spot and Figure 17b shows a magnified section, in which the contrast has been raised. The border between the light and dark grey region in the upper right corner of Figure 17b can be identified as the transition from the molten to the non-molten region. An even larger magnification (Figure 17c) reveals the change in topography: The grainy structure to the right is characteristic of the as-evaporated Au films, which in our samples have a typical roughness of 5 nm. When the films are molten and solidify quickly on a nanosecond scale, they become smoother and exhibit grain boundary structures. (For larger melting times the films would start to dewet and would develop holes [42].) The melting threshold, $I_{\mathrm{th,melt}}$, calculated from Figure 17 and the corresponding Airy intensity profile, amounts to 540 mJ/cm^2. When comparing this to the threshold value for plasmon-assisted melting $I_{\mathrm{th,melt}}^*$, one arrives at an enhancement of 9 ± 2 due to the plasmonic resonance in the triangles.

The enhancement derived from local melting is in good agreement with the value of 10 obtained by the ablation technique from Figure 8 and Figure 10. We would like to point out, however, that this might be a coincidence. In the case of ablation the relevant fields for generating holes in the Si substrates are located *outside* the plasmonic structures, whereas the plasmon-induced melting takes place due to dissipation *inside* the structures.
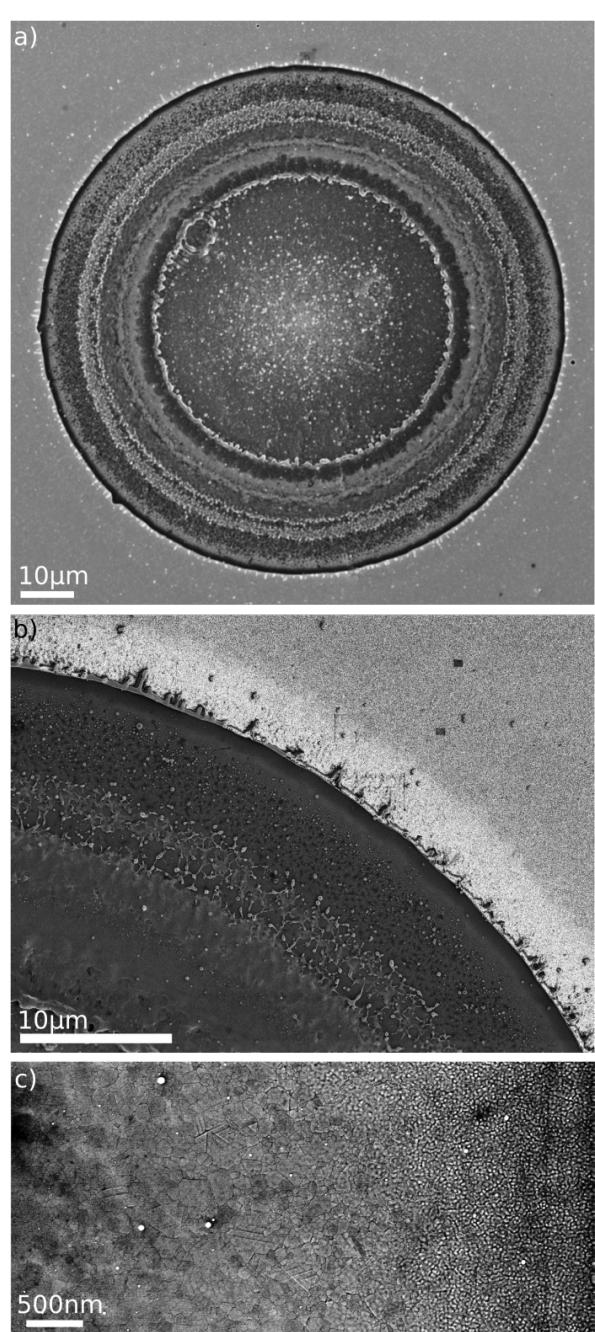
Figure 17: SEM micrographs of a 40 nm Au film on Si, after exposition to a 300 ps laser pulse at 800 nm wavelength. (a) Overview over the ablation spot, (b) and (c) blow-ups of the transition region with two different magnifications.

Mechanism

All the findings described above can be explained by ultrafast heating and subsequent melting of the plasmonic nano-structures. Assuming that the heat is produced in the area of the highest near-field intensity during the laser pulse, the comparatively short thermal diffusion length leads to strong thermal gradients with a length scale that is below the dimen-

sions of the illuminated particle (thermal diffusion length: $l_D = \sqrt{D\tau} \approx 200$ nm with thermal diffusivity of gold $D = \kappa/(c_p \cdot \rho) = 1.27 \cdot 10^{-4}$ m$^2 \cdot$s^{-1} and laser pulse length $\tau = 300$ ps; κ: thermal conductivity; c_p: specific heat capacity; ρ: mass density). For higher intensities, larger parts of the triangles melt. In analogous to fs pulses there is an intensity regime where the nano-structures are removed by the laser irradiation without causing major damage on the Si substrate surface. The removal process of these molten structures is different, however, from the removal of (nearly intact) triangles by fs pulses. It has been described for the case of nanosecond pulses by Habenicht et al. [37]. Basically, the potential energy that is stored in a flat triangle as compared to the round droplet form on a non-wettable surface is transferred into kinetic energy that launches the particle from the surface.

Conclusion

The results reported here provide a test bed for the determination of near fields of plasmonic nanostructures, based on the one hand on an experimental mapping of the regions of pronounced field enhancement, on the other hand on FDTD simulations. When comparing the field-enhancement distributions obtained from experiment with the calculations, one finds excellent agreement concerning the spatial intensity patterns, whereas calculated enhancement factors are typically some-what larger than the experimental ones, yet of the same magnitude. This sheds light on the reliability of FDTD simulations, for which it is apparently crucial that all the details of the plasmonic structures are taken into account, if one aims at a quantitative prediction of the near fields. Although a similar finding has already been reported earlier, this work provides the first quantitative information for the relatively complex higher-order plasmon modes of the triangular structures used here. From this knowledge one can draw conclusions on how trustworthy simulations of even more complicated plasmonic structures, e.g., for the design of sophisticated optical antennas, will be. The method described here should also be applicable for higher order polarizations, like azimuthally or radially polarized laser beams, as they have been used to excite plasmon modes in triangular nanostructures in a confocal microscope [43].

As our study has further shown, the minimum feature size of ablation patterns in Si is limited by a broadening process which is probably related to the diffusion of light-induced charge carriers, restricting structure formation by optical near fields in this material to feature sizes of around 10 nm. Yet nanopat-terning by near-field ablation with femtosecond pulses and the related formation of a nanoscale plasma appears as a novel route for certain applications in biology and medicine, where a chemical patterning of a substrate on scales well below optical wavelengths is of interest. The strong thermal gradients in trian-

gles irradiated with *picosecond l*aser pulses might also be interesting for biological applications. Plasmonic particles heated by laser pulses have been discussed to be used as "nanostoves" for biological tissue in biosensors or for cancer thermotherapy [44,45]. They may also lend themselves as sources of local heat gradients in nano thermoelectronic devices [46]. In addition to the spherical particles described in literature, the selective heating of single tips of the plasmonic triangle would make it possible to compare heating effects under otherwise identical conditions on a very small scale.

Supporting Information

Supporting Information File 1
Line-fit and triangle model.
[http://www.beilstein-journals.org/bjnano/content/supplementary/2190-4286-4-66-S1.pdf]

Acknowledgements

References

1. Nedyalkov, N. N.; Takada, H.; Obara, M. *Appl. Phys. A* **2006,** *2,* 163–168. doi:10.1007/s00339-006-3679-9
2. Farahani, J. N.; Pohl, D. W.; Eisler, H.-J.; Hecht, B. *Phys. Rev. Lett.* **2005,** *95,* 017402. doi:10.1103/PhysRevLett.95.017402
3. McFarland, A. D.; Young, M. A.; Dieringer, J. A.; Van Duyne, R. P. *J. Phys. Chem. B* **2005,** *109,* 11279–11285. doi:10.1021/jp050508u
4. Nie, S.; Emory, S. R. *Science* **1997,** *275,* 1102–1106. doi:10.1126/science.275.5303.1102
5. Hanke, T.; Cesar, J.; Knittel, V.; Trügler, A.; Hohenester, U.; Leitenstorfer, A.; Bratschitsch, R. *Nano Lett.* **2012,** *12,* 992–996. doi:10.1021/nl2041047
6. Schuller, J. A.; Barnard, E. S.; Cai, W.; Jun, Y. C.; White, J. S.; Brongersma, M. L. *Nat. Mater.* **2010,** *3,* 193–204. doi:10.1038/nmat2630
7. Hanke, T.; Krauss, G.; Träutlein, D.; Wild, B.; Bratschitsch, R.; Leitenstorfer, A. *Phys. Rev. Lett.* **2009,** *103,* 257404. doi:10.1103/PhysRevLett.103.257404
8. Heinzelmann, H.; Pohl, D. W. *Appl. Phys. A: Solids Surf.* **1994,** *59,* 89–101. doi:10.1007/BF00332200
9. Durig, U.; Pohl, D. W.; Rohner, F. *J. Appl. Phys.* **1986,** *59,* 3318. doi:10.1063/1.336848
10. Pohl, D. W.; Denk, W.; Lanz, M. *Appl. Phys. Lett.* **1984,** *44,* 651. doi:10.1063/1.94865
11. Bachelot, R.; Gleyzes, P.; Boccara, A. C. *Microsc., Microanal., Microstruct.* **1994,** *5,* 389–397. doi:10.1051/mmm:0199400504-6038900
12. Specht, M.; Pedarnig, J.; Heckl, W.; Hänsch, T. *Phys. Rev. Lett.* **1992,** *68,* 476–479. doi:10.1103/PhysRevLett.68.476
13. Zenhausern, F.; O'Boyle, M. P.; Wickramasinghe, H. K. *Appl. Phys. Lett.* **1994,** *65,* 1623. doi:10.1063/1.112931
14. Cinchetti, M.; Gloskovskii, A.; Nepjiko, S. A.; Schönhense, G.; Rochholz, H.; Kreiter, M. *Phys. Rev. Lett.* **2005,** *95,* 047601. doi:10.1103/PhysRevLett.95.047601
15. Melchior, P.; Bayer, D.; Schneider, C.; Fischer, A.; Rohmer, M.; Pfeiffer, W.; Aeschlimann, M. *Phys. Rev. B* **2011,** *83,* 235407. doi:10.1103/PhysRevB.83.235407
16. Kühler, P.; García de Abajo, F. J.; Solis, J.; Mosbacher, M.; Leiderer, P.; Afonso, C. N.; Siegel, J. *Small* **2009,** *5,* 1825–1829. doi:10.1002/smll.200900393
17. Plech, A.; Leiderer, P.; Boneberg, J. *Laser Photonics Rev.* **2009,** *3,* 435–451. doi:10.1002/lpor.200810044
18. Murazawa, N.; Ueno, K.; Mizeikis, V.; Juodkazis, S.; Misawa, H. *J. Phys. Chem. C* **2009,** *113,* 1147–1149. doi:10.1021/jp809623y
19. Ueno, K.; Juodkazis, S.; Shibuya, T.; Yokota, Y.; Mizeikis, V.; Sasaki, K.; Misawa, H. *J. Am. Chem. Soc.* **2008,** *130,* 6928–6929. doi:10.1021/ja801262r
20. Siegel, J.; Gawelda, W.; Puerto, D.; Dorronsoro, C.; Solis, J.; Afonso, C. N.; de Sande, J. C. G.; Bez, R.; Pirovano, A.; Wiemer, C. *J. Appl. Phys.* **2008,** *103,* 023516. doi:10.1063/1.2836788
21. Boneberg, J.; König-Birk, J.; Münzer, H.-J.; Leiderer, P.; Shuford, K. L.; Schatz, G. C. *Appl. Phys. A* **2007,** *89,* 299–303. doi:10.1007/s00339-007-4138-y
22. Leiderer, P.; Bartels, C.; König-Birk, J.; Mosbacher, M.; Boneberg, J. *Appl. Phys. Lett.* **2004,** *85,* 5370. doi:10.1063/1.1819990
23. Münzer, H.-J.; Mosbacher, M.; Bertsch, M.; Zimmermann, J.; Leiderer, P.; Boneberg, J. *J. Microsc. (Oxford, U. K.)* **2001,** *202,* 129–135. doi:10.1046/j.1365-2818.2001.00876.x
24. Eversole, D.; Luk'yanchuk, B.; Ben-Yakar, A. *Appl. Phys. A* **2007,** *89,* 283–291. doi:10.1007/s00339-007-4166-7
25. Harrison, R. K.; Ben-Yakar, A. *Opt. Express* **2010,** *18,* 22556–22571. doi:10.1364/OE.18.022556
26. Robitaille, A.; Boulais, É.; Meunier, M. *Opt. Express* **2013,** *21,* 9703–9710. doi:10.1364/OE.21.009703
27. Liu, J. M. *Opt. Lett.* **1982,** *7,* 196–198. doi:10.1364/OL.7.000196
28. Born, M.; Wolf, E. *Principles of optics: electromagnetic theory of propagation, interference and diffraction of light;* Cambridge University Press: Cambridge; New York, 1999.
29. Fischer, U. C.; Zingsheim, H. P. *J. Vac. Sci. Technol.* **1981,** *19,* 881. doi:10.1116/1.571227
30. Deckman, H. W.; Dunsmuir, J. H. *Appl. Phys. Lett.* **1982,** *41,* 377. doi:10.1063/1.93501
31. Burmeister, F.; Schäfle, C.; Matthes, T.; Böhmisch, M.; Boneberg, J.; Leiderer, P. *Langmuir* **1997,** *13,* 2983–2987. doi:10.1021/la9621123
32. Burmeister, F.; Schäfle, C.; Keilhofer, B.; Bechinger, C.; Boneberg, J.; Leiderer, P. *Adv. Mater.* **1998,** *10,* 495–497. doi:10.1002/(SICI)1521-4095(199804)10:6<495::AID-ADMA495>3.0.CO;2-A
33. Jensen, T. R.; Malinsky, M. D.; Haynes, C. L.; Van Duyne, R. P. *J. Phys. Chem. B* **2000,** *104,* 10549–10556. doi:10.1021/jp002435e
34. Kosiorek, A.; Kandulski, W.; Chudzinski, P.; Kempa, K.; Giersig, M. *Nano Lett.* **2004,** *4,* 1359–1363. doi:10.1021/nl049361t
35. Kosiorek, A.; Kandulski, W.; Glaczynska, H.; Giersig, M. *Small* **2005,** *1,* 439–444. doi:10.1002/smll.200400099
36. Gwinner, M. C.; Koroknay, E.; Fu, L.; Patoka, P.; Kandulski, W.; Giersig, M.; Giessen, H. *Small* **2009,** *5,* 400–406. doi:10.1002/smll.200800923
37. Habenicht, A.; Olapinski, M.; Burmeister, F.; Leiderer, P.; Boneberg, J. *Science* **2005,** *309,* 2043–2045. doi:10.1126/science.1116505

38. Kolloch, A.; Geldhauser, T.; Ueno, K.; Misawa, H.; Boneberg, J.; Plech, A.; Leiderer, P. *Appl. Phys. A* **2011,** *104,* 793–799. doi:10.1007/s00339-011-6443-8

39. Bärsch, N.; Körber, K.; Ostendorf, A.; Tönshoff, K. H. *Appl. Phys. A* **2003,** *77,* 237–242. doi:10.1007/s00339-003-2118-4

40. Kolloch, A. Plasmon Resonances for Sub-100nm Silicon Ablation: Quantitative Measurement and Nanometer-Scale Ablation Mechanism. Ph.D. Thesis, University of Konstanz, Germany, 2012.

41. Bäuerle, D. *Laser processing and chemistry;* Springer: Berlin, New York, 2000.

42. Bischof, J. Metallische Dünfilmschmelzen nach Pulslaser-Bestrahlung: Phasenumwandlungen und Instabilitäten. Ph.D. Thesis, University of Konstanz, Germany, 1996.

43. Hennemann, L. E.; Kolloch, A.; Kern, A.; Mihaljecic, J.; Boneberg, J.; Leiderer, P.; Meixner, A. J.; Zhang, D. *Beilstein J. Nanotechnol.* **2012,** *3,* 674–683. doi:10.3762/bjnano.3.77

44. Hrelescu, C.; Stehr, J.; Ringler, M.; Sperling, R. A.; Parak, J. W.; Klar, T. A.; Feldmann, J. *J. Phys. Chem. C* **2010,** *114,* 7401–7411. doi:10.1021/jp9097167

45. Stehr, J.; Hrelescu, C.; Sperling, R. A.; Raschke, G.; Wunderlich, M.; Nichtl, A.; Heindl, D.; Kürzinger, K.; Parak, W. J.; Klar, T. A.; Feldmann, J. *Nano Lett.* **2008,** *8,* 619–623. doi:10.1021/nl073028i

46. Kopp, B.; Yi, Z.; Benner, D.; Xie, F.-Q.; Obermair, C.; Schimmel, T.; Boneberg, J.; Leiderer, P.; Scheer, E. *Beilstein J. Nanotechnol.* **2012,** *3,* 703–711. doi:10.3762/bjnano.3.80

k-space imaging of the eigenmodes of sharp gold tapers for scanning near-field optical microscopy

Martin Esmann[1,2], Simon F. Becker[1,2], Bernard B. da Cunha[1,2], Jens H. Brauer[1,2], Ralf Vogelgesang[1,2], Petra Groß[1,2] and Christoph Lienau[*1,2]

Abstract

We investigate the radiation patterns of sharp conical gold tapers, which were designed as adiabatic nanofocusing probes for scanning near-field optical microscopy (SNOM). Field calculations show that only the lowest order eigenmode of such a taper can reach the very apex and thus induce the generation of strongly enhanced near-field signals. Higher-order modes are coupled into the far field at finite distances from the apex. Here, we demonstrate experimentally how to distinguish and separate between the lowest and higher-order eigenmodes of such a metallic taper by filtering in the spatial frequency domain. Our approach has the potential to considerably improve the signal-to-background ratio in spectroscopic experiments at the nanoscale.

Introduction

Metallic nanostructures support collective oscillations of the electron gas, which couple strongly to light. At extended metal–dielectric interfaces, the resulting surface-bound modes, termed surface plasmon polaritons (SPPs), may propagate along the interface. At geometric singularities, i.e., in regions of deep-subwavelength radius of curvature, these modes tend to be spatially confined and are called localized surface plasmons (LSPs). During recent years, experimental realizations of SPP guiding in sub-wavelength dimensions [1] and the transforma-

tion of propagating SPPs into LSPs have drawn tremendous attention within the field of plasmonics. The concept of SPP to LSP transformation has been investigated theoretically and experimentally for different metal nanostructures [2-5] in both the adiabatic [5-7] and the non-adiabatic [8] limit. Theoretically, it has been shown to be particularly promising in its adiabatic limit, i.e., for waveguides with gradually (adiabatically) varying cross-section, for which reflection-free SPP propagation and efficient transformation are predicted [6]. This gives

rise to a new class of probes in apertureless scanning near-field optical microscopy (SNOM) that focus light down to volumes well below the classical diffraction limit [5,6]. In particular, it has been predicted that SPP wavepackets may be localized both in space and time when they are launched onto a tapered metallic waveguide, e.g., a conical tip with a nanometer-sized apex and sufficiently small opening angle [6]. This formation of a strongly confined lightspot is now termed "adiabatic nano-focusing" [6]. The expected nanometer-scale confinement offers the possibility to efficiently couple light into a single nanoobject, making such probes highly attractive for inherently background-free, new spectroscopic applications on the nanometer scale.

Adiabatic nanofocusing has been demonstrated experimentally by grating-coupling of light to SPPs on electrochemically etched gold tapers [9]. Such tapers have been incorporated in SNOM setups and nanostructures such as a single gold nano-particle [10,11] or silicon step edge [12] have been imaged, demonstrating an optical resolution of down to 10 nm. More-over, time-resolved studies showed that the time structure of ultra-fast laser pulses in the few-femtosecond regime hardly changes upon grating coupling to SPPs and during propagation over distances of several tens of microns on the surface of a gold taper [11]. These results have been confirmed by three-dimensional finite difference time domain (FDTD) simulations [11]. These theoretical investigations and experimental demon-strations suggest that pump–probe studies employing adiabatic nanofocusing are well within experimental reach.

Despite its large potential, adiabatic nanofocusing has not yet been established as a standard approach to optical investi-gations on the nanoscale. Arguably, the most critical challenge is reproducibility. Taper probes produced by electrochemical etching as described in [11] differ drastically in their conver-sion efficiency from far-field radiation to nano-localized LSP intensity at the apex. The differences in conversion efficiency exist even for tips having nominally identical, smooth surfaces, appropriate opening angles and small apex radii. Therefore, experiments are time consuming and high quality data are scarce. Scanning electron micrographs of two conical taper probes that were used in our own experiments are shown in Figure 1. Whereas their geometry and morphology appear very similar, they showed very different conversion efficiencies.

Conceptually, the difference in conversion efficiency may be explained as a mode matching problem. When employing a grating coupler to excite SPPs, as done, e.g., in [9-12], different eigenmodes of the taper are excited. Their relative amplitudes are given by their spatial overlap with the incoming field and depend critically upon the exact shape of the tip and the
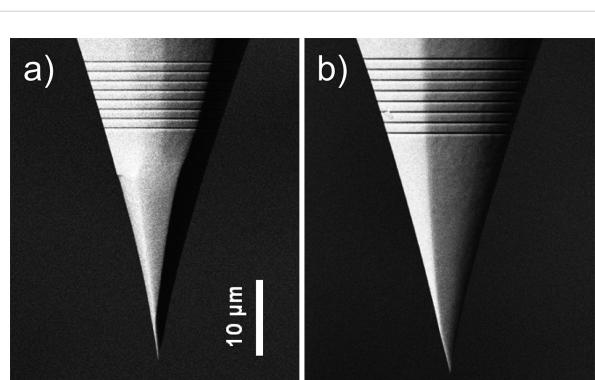
Figure 1: Scanning electron micrographs of two gold tapers that were obtained by electrochemical AC-etching of annealed gold wires fol-lowed by focused ion beam milling of the grating couplers. Field enhancement at the taper apex was much more pronounced for the tip shown in panel a).

incoming phase front. Theoretical studies have shown that only the lowest, rotationally symmetric eigenmode is nanofocused down to the very apex of the tip [13] where it gets highly confined. In contrast, higher order modes radiate into the far-field while propagating along the taper. This far-field coupling can occur within the last micron from the tip apex, making it difficult to distinguish these modes from the nano-localized LSP fields. This hampers efficient background-free nano-focusing with the setup described in [10] and higher order mode suppression remains an unsolved challenge.

In this work we present the first steps toward overcoming this challenge. Our approach seeks to provide direct access to the field distribution in the vicinity of the taper apex. To this end, we apply k-space imaging of the fields emitted from the taper apex. By analyzing the rotational symmetry of the resulting radiation patterns we are able to distinguish between contribu-tions from eigenmodes of different orders. In effect, this opens up new possibilities for optimizing the relative contribution from the lowest mode as well as extracting the near-field contri-butions at the taper apex. We think that this is an important step toward ultrafast pump–probe spectroscopy on the nanoscale. Specifically, we show that we can differentiate between the zeroth and first order mode, which is generally difficult when using conventional far field imaging techniques.

Eigenmodes of a tapered wire

In order to describe the process of linear SPP propagation on the SNOM probe in the framework of classical electrody-namics, it is useful to expand the SPP wavepacket in terms of orthonormal eigenmodes at any point along the waveguide. The concept of adiabatic nanofocusing assumes that the diameter of a tapered waveguide varies only slowly over the distance of one wavelength of the guided SPP. Therefore, a proper local set of

eigenmodes is well approximated by the eigenmodes of an infinitely long waveguide having the local diameter of the taper. For a cylindrical metal wire surrounded by a homogeneous dielectric, these solutions are the well-known wire modes [14-16]. These modes possess a discrete rotational symmetry with respect to the angle φ of a cylindrical coordinate system whose *z*-axis coincides with the wire axis. The symmetry is governed by a quantization number *n*, corresponding to an angular momentum, which manifests itself in a field distribution of the form $\vec{E}(r,z,\varphi) = \vec{E}(r,z) \cdot \exp(in\varphi)$. The propagation of the wire modes is described by a transcendental equation, which can be derived from Maxwell's equations and the appropriate boundary conditions at the metal–dielectric interface [13-16]. It yields the propagation constant k_z along the tapered wire as a function of the dielectric material properties, the wire radius, and the frequency of the SPP mode.

Based on this approach we have numerically calculated the propagation constant for a gradually decreasing wire radius, *R*. The results for the SPP frequency corresponding to a vacuum wavelength of 800 nm on a gold wire (dielectric constant $\varepsilon_1 = -24.7470 + 1.8834i$, which was obtained by fitting experimental data from [17]) surrounded by air ($\varepsilon_2 = 1$) are displayed in Figure 2.

For decreasing radii, the three lowest modes *n* = 0,1,2 (cf. Figure 2, panels a)–c)) behave distinctly different. For the lowest, rotationally symmetric mode with *n* = 0, both the real and imaginary part of the propagation constant are divergent for a vanishing wire radius. Thus, this mode remains strongly bound to the interface while its wavelength shortens, leading to a decrease in SPP group velocity. In effect, the SPP is transformed into a strongly confined LSP. In the region below the

tip, the field emitted by this LSP mode closely resembles that of an oscillating point dipole [18,19]. In the case of a tapered waveguide, the corresponding dipole moment is oriented along the taper axis. Hence, the field as well as the radiation pattern emerging from the apex maintain the rotational symmetry of the eigenmode.

In contrast, for the *n* = 1 mode, the propagation constant approaches the light line, $k_0 = \omega/c_0$, for radii of about 70 nm, indicating that the mode looses its bound character. It is not transformed into a highly confined LSP at the taper end and we therefore refer to it as a loosely bound photonic mode. The third mode, with *n* = 2, already displays a cut-off behavior for a radius only slightly above 600 nm. This mode is not sustained on the wire for smaller radii. The same is true for all higher order modes.

As a consequence, only the *n* = 0 and *n* = 1 eigenmodes of the wire are expected to contribute to near-fields in the vicinity of the taper apex. When scattered into the far-field, the contributions of those two modes cannot be distinguished by using only far-field optics, as their spatial separation is well below the classical diffraction limit. When using tapered nanofocusing probes in a SNOM setup, only the *n* = 0 eigenmode generates the desired, spatially highly resolved signal, containing information about the sample properties on the nanoscale. The *n* = 1 mode, however, is expected to contribute to a non-negligible background signal due to its weak confinement.

Experimental setup

Our experimental setup used for k-space imaging is sketched in Figure 3. The field distribution at the apex of the taper is probed by placing it in front of a gold-coated dielectric surface that
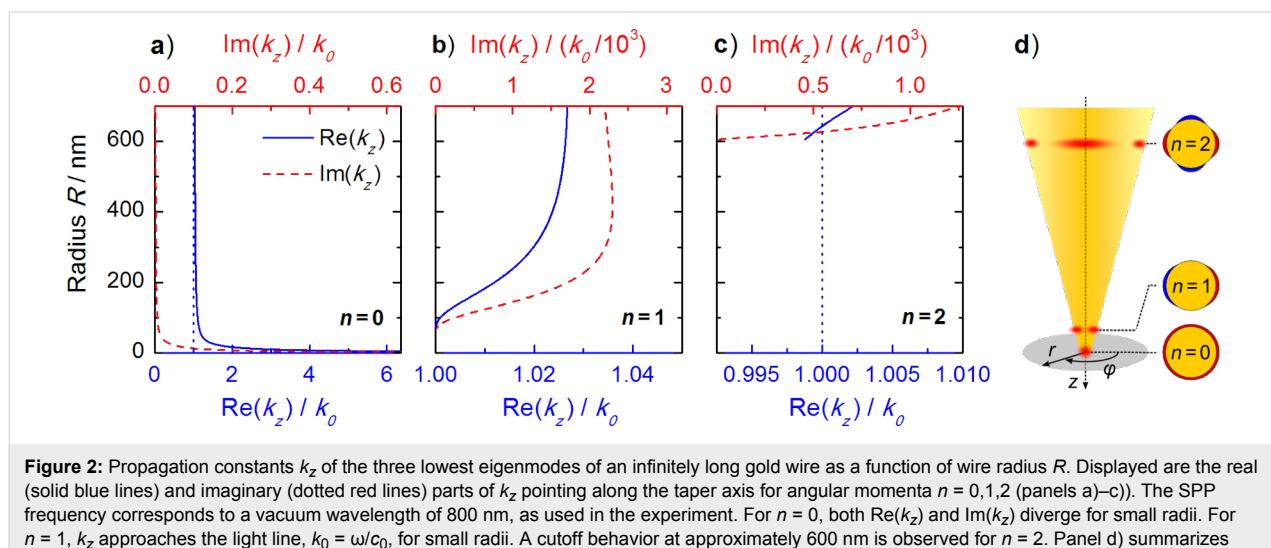
Figure 2: Propagation constants k_z of the three lowest eigenmodes of an infinitely long gold wire as a function of wire radius *R*. Displayed are the real (solid blue lines) and imaginary (dotted red lines) parts of k_z pointing along the taper axis for angular momenta *n* = 0,1,2 (panels a)–c)). The SPP frequency corresponds to a vacuum wavelength of 800 nm, as used in the experiment. For *n* = 0, both Re(k_z) and Im(k_z) diverge for small radii. For *n* = 1, k_z approaches the light line, $k_0 = \omega/c_0$, for small radii. A cutoff behavior at approximately 600 nm is observed for *n* = 2. Panel d) summarizes these findings and schematically illustrates the mode profiles.
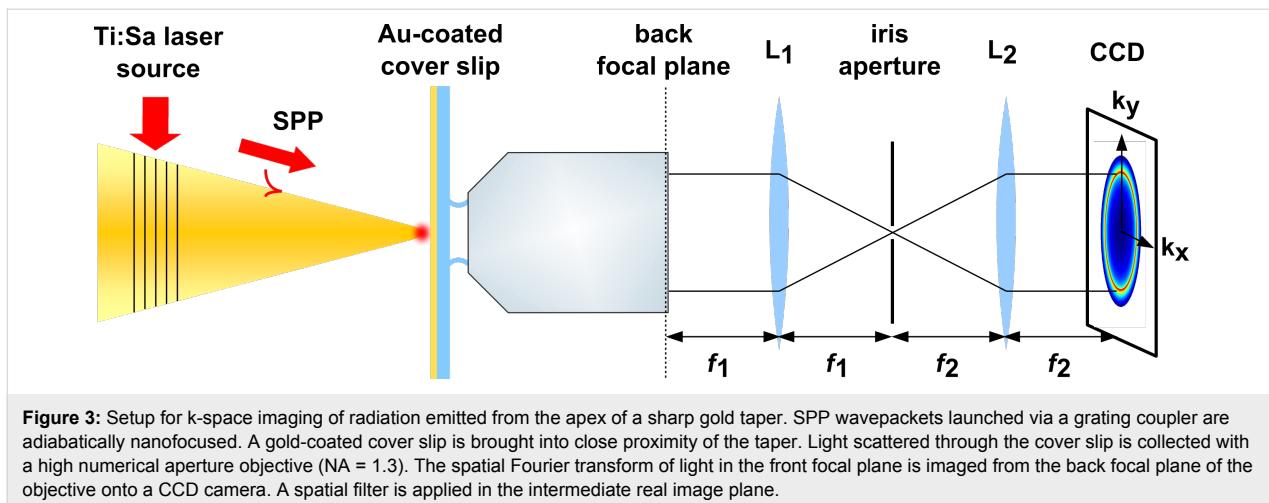
Figure 3: Setup for k-space imaging of radiation emitted from the apex of a sharp gold taper. SPP wavepackets launched via a grating coupler are adiabatically nanofocused. A gold-coated cover slip is brought into close proximity of the taper. Light scattered through the cover slip is collected with a high numerical aperture objective (NA = 1.3). The spatial Fourier transform of light in the front focal plane is imaged from the back focal plane of the objective onto a CCD camera. A spatial filter is applied in the intermediate real image plane.

couples some fraction of the evanescent near-fields at the apex to propagating far-field modes. The angular distribution of these propagating waves is measured with an immersion objective. In the following, we describe the individual parts of the experimental setup.

Tapers as shown in Figure 1 are produced from single-crystalline gold wire by an electrochemical AC-etching technique followed by focused ion beam milling of a grating coupler [11]. Typical cone opening angles are between 20 and 30° and apex radii are well below 30 nm. These tips have a very smooth surface and accordingly high SPP propagation lengths as reported earlier [11]. To excite SPPs on the probe, we use a pulsed titanium sapphire (Ti:Sa) laser source operating at a central wavelength of 800 nm and featuring a 10 nm wide Gaussian spectral distribution. This light is focused onto the grating coupler with a microscope objective (NA = 0.1), applying an average power of 200 µW at a repetition rate of 80 MHz. The SPP wavepacket launched on the coupler propagates toward the taper apex.

The light emitted from the taper apex is then transmitted through a 20 nm thick gold film on a cover slip. The main reason for using a Au-coated sample was to enhance the evanescent light contributions to the k-space images. The gold film has three major effects on those images. (i) It substantially suppresses the transmission of propagating waves ($k_\parallel < k_0$, allowed light), which have to tunnel through the film. For our film, we measure that the transmission is reduced to about 20%. (ii) It enhances the total power radiated into forbidden light modes by about a factor of 2, as can be seen from a simple estimate based on a point dipole model (see., e.g., [20], Ch. 10). (iii) Most importantly, it allows us to probe the near-field coupling between the tip dipole, i.e., the near fields at the tip apex, and its image dipole induced in the metal (see [21,22]).

The light transmitted through the gold-coated cover slip is collected using an oil immersion objective with high numerical aperture (NA = 1.3, Olympus UPlanFLN 100×). The tip-apex position lies within the focal plane of the microscope objective. In this configuration, the objective performs a Fourier transform of the field distribution from the front into the back focal plane. Two additional lenses with focal lengths of f_1 = 150 mm and f_2 = 100 mm, respectively, image the back focal plane onto a CCD camera (Thorlabs DCC1545M-GL) in a 4f-configuration. In the intermediate real image plane, the filtering of scattered light from the grating coupler is realized with an iris aperture.

The distance between probe and cover slip is controlled using a tuning fork-based force sensor in a noncontact-mode atomic force microscope (AFM). This microscope is a modified version of the setup described in [10]. The taper probe is attached to one prong of a quartz tuning fork that oscillates with a peak-to-peak amplitude of 1 nm. The cover slip is mounted onto a three-axis piezoelectric stage (PI P-363.3CD). This allows us to slowly approach the sample to the taper over a distance of several hundreds of nanometers in steps of 30 pm until the tuning fork starts to be damped by tip–sample interactions. The damping occurs on a length scale of less than 5 nm. The sample is subsequently retracted to its original position with the same step size. While recording force-approach curves, the CCD camera is triggered to capture the respective k-space images for selected positions on the approach curve.

Results

We have recorded distance-dependent k-space images of the light transmitted through the gold-coated cover slip for several grating-coupler type nanofocusing tapers. The results of a representative experiment for the taper shown in Figure 1a are described in detail in the following. A sequence of camera

images was recorded at selected positions on the AFM approach curve. The first frame of this sequence taken at a tip–sample spacing of about 150 nm is displayed in Figure 4a. In this image, the bright pattern (labeled position i) corresponds to radiation from the far-field with in-plane k-vectors $k_{||}$ smaller than $k_0 = \omega/c_0$. The ring-like pattern (labeled ii) is associated with in-plane k-vectors $k_{||}$ slightly larger than k_0. It can be attributed to leakage radiation from SPPs excited on the gold film [23-25]. The dark area outside the larger dashed circle (labeled iii) reflects in-plane k-vectors $k_{||}$ larger than $1.3 \cdot k_0$, which are not captured by our oil immersion objective. The area between the two dashed circles (labeled iv) is thus the region of interest (ROI) to us. Here, only forbidden light [24] originating from evanescent fields at the taper apex is detected.

Panels b)–g) of Figure 4 show a sequence of six camera images with equidistant spacing along the corresponding AFM approach curve. For clarity, they exclusively depict the ROI and the intensities have been rescaled. The red arrow in panel g) marks a short-ranged increase in intensity, which is only visible in this panel. A video file of the image sequence is available as Supporting Information File 1.

A quantitative analysis of the full sequence of images is displayed in Figure 5. It has been obtained by radially integrating across the ROI for each position on the approach curve. The resulting integrated intensities are plotted as a function of in-plane angle φ and tip–sample spacing d. To improve the comparability and to simplify the identification of the individual features, each horizontal line, corresponding to a fixed angle φ, was normalized to its maximum after subtraction of its first value during approach (at $d = 150$ nm). The color bar has been restricted to the range from zero to one. Similar plots have been generated from measurements at different spatial positions on our gold film. Within our signal-to-noise ratio, the data show no variation with sample position. This suggests that the possible excitation of localized surface plasmon fields on the gold film has only a very limited effect on our experimental data and supports that our experiments indeed map the emission properties of the nanotaper.

Two qualitatively different decay lengths emerge from these plots. One of them is well below 30 nm and appears most prominently at polar angles around 225°. This area is marked by the red arrow in Figure 4g. The other, much longer decay length occurs in two opposing lobes above and below the region marked by the two dashed white lines. These two different decay lengths have also been observed qualitatively in experiments performed with other tapers. To quantify the short decay length for the given tip, the data inside the marked zone in Figure 5a have been integrated azimuthally. For comparison this has also been done with the data between 100 and 120°. The integrated values are plotted in panel b) and the inset therein, respectively. In this panel, the offset at $d = 150$ nm was not subtracted and was used for normalization to it such that the y-axis gives the relative increase with respect to this offset. An exponential fit to the data points taken during approach (open red squares), offset by 1.0, has been added. The corresponding decay length is 14 nm and the overall increase in intensity amounts to a factor of five.
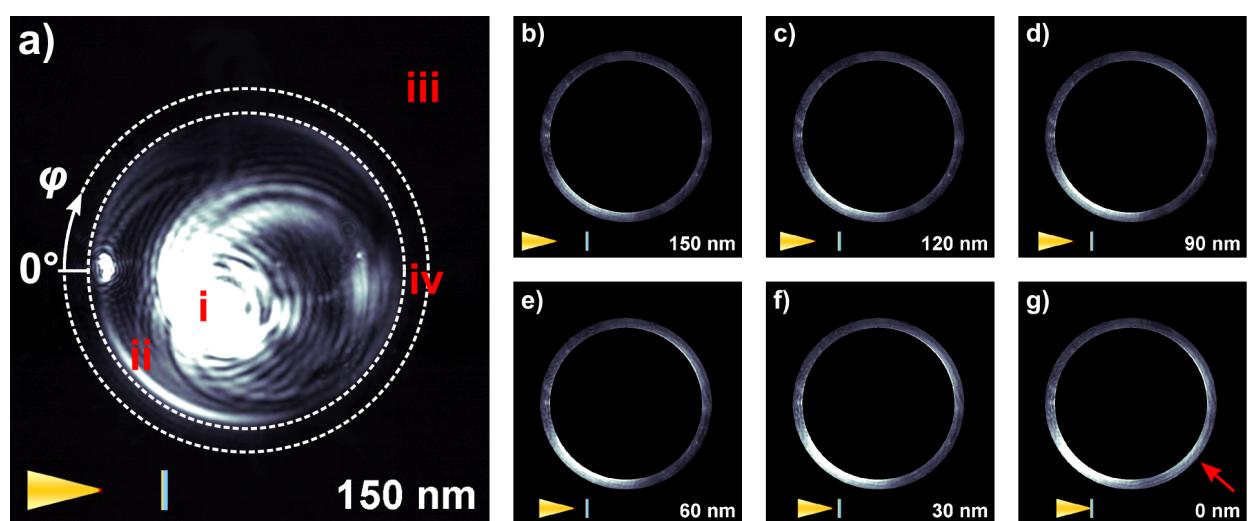
Figure 4: k-space patterns recorded while approaching a gold-coated cover slip to the SNOM probe. Tip-sample spacings are indicated in the lower right corner of the respective images and the corresponding pictographs in the lower left corner. Panel a) shows raw data, the dashed circles mark the region of interest (ROI, labeled iv). Panels b)-g) represent the evolution of the k-space pattern during approach. For clarity, the data are limited to the ROI and are rescaled to the 90th percentile of all pixel intensities within the ROI in panel g).
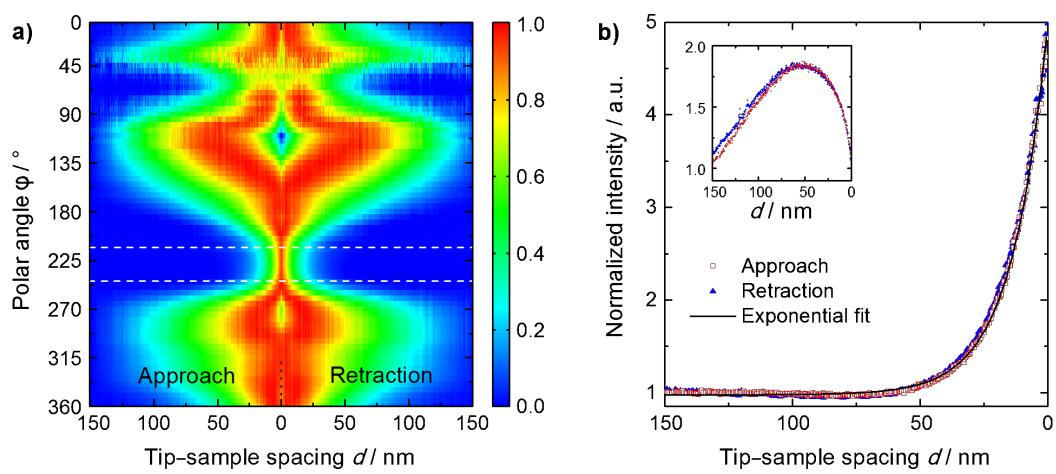
Figure 5: Quantitative analysis of the evolution of k-space patterns during tip approach and retraction. Panel a) shows the angular intensity distribution, radially integrated across the ROI (cf. Figure 4a), as a function of tip–sample spacing. At each angle, the data have been normalized. The region between the two dashed white lines has been averaged with respect to the angle and the data have been plotted in panel b) together with an exponential fit to the part of the data recorded during approach. The decay length is 14 nm. Here, the data have been normalized to the background signal. The inset shows an equal set of data for a different angular region around 110°.

Discussion

The angular decay spectrum displayed in Figure 5a strongly suggests that only those SPP fields that are coupled to the lowest order and first higher order eigenmodes of the taper, propagate as bound modes into close proximity of the taper apex. This is qualitatively understood in the following way: The symmetry of the $n = 1$ mode is that of an in-plane dipole with its dipole moment oriented parallel to the sample surface. Thus, its angular radiation distribution should exhibit two opposing lobes. These lobes are clearly seen in Figure 5a in the quadrants ranging from 90 to 180° and 270 to 360°, respectively. The decay length observed in these two lobes agrees with the expectation for the evanescent decay in air related to the in-plane k-vector components $k_{||}$ within the ROI.

For the eigenmode with $n = 0$ a rotationally symmetric radiation pattern is expected for an ideally symmetric tip. Theoretically, it has been shown that the fields at the tip apex decay with a length slightly shorter than the apex radius [26-28]. Taking image charge effects into account [21,22], the decay in k-space closely resembles the behavior in real space. This short-ranged decay is most prominently encountered in the region marked with the dashed white lines in Figure 5a and the red arrow in Figure 4g. In this region, the line shape nicely follows an exponential decay as can be seen in Figure 5b. The decay length of 14 nm is in convincing agreement with the theoretical expectation. As determined by scanning electron microscopy, our tapers usually have apex radii between 10 and 20 nm. For the region between 0 and 50°, the measured total intensities are small. Therefore, the values obtained in this region should be considered with care.

Interference between the two modes with $n = 0$ and $n = 1$ is expected to give rise to constructive interference in one lobe and destructive interference in the other, resulting in an asymmetric distribution of the intensity in the two lobes as well. In Figure 4, an asymmetry in the intensity of the two opposing lobes is indeed observed. By comparison with the overall intensity detected from the $n = 0$ mode, however, it can be deduced that this effect still cannot fully account for the observed asymmetry.

As can be seen in Figure 4a, an asymmetric signature of surface plasmon polariton resonance leakage is also detected in the raw data (labeled ii). The tails of this resonance extend into that part of k-space that we define as the region of interest (ROI). A substantial amount of the asymmetry in the processed signal (visible in Figure 4b–Figure 4g) can be attributed to this effect. The excitation of this resonance is most likely due to scattering of radiation from the grating coupler as well as emission from higher order modes of the taper. It is therefore possible that this spurious signal overlaps in our k-space images with the desired signatures from the $n = 0$ and $n = 1$ modes and thus contributes to the recorded asymmetry.

To give an estimate of the relative contributions of the $n = 0$ and $n = 1$ modes, we compare the intensities in our k-space images. The relative amplitude of the $n = 0$ and $n = 1$ mode-emission appears similar when approaching the surface. These k-space images probe evanescent fields within a finite wave vector range, extending to about $1.3 \cdot k_0$. The k-space distribution of the (spatially highly confined) $n = 0$ mode extends to much larger k-vectors than that of the $n = 1$ mode. This k-spectrum is

much broader than what is probed in our experiments. Hence only a fraction of the $n = 0$ mode emission can be detected. In high-resolution near-field experiments, however, the entire k-spectrum contributes.

Inside the two lobes with the long-ranged decay, a decrease of the intensity sets in for small values of the tip–sample spacing (see inset in Figure 5b). To account for this behavior, we believe that we need a near-field source that produces a field with a k-space symmetry similar to that of the $n = 1$ mode. Its field amplitude should vary substantially over the last 20 nm. Such fields would be generated by a laterally oriented dipolar emitter located near the tip apex. This dipole emission may reflect contributions of the $n = 1$ mode that are weakly guided towards the taper apex. Earlier FDTD simulations [29] indeed indicate that, for asymmetric grating-excitation on one side of the taper, as done in our experiments, the field near the apex is not just that of a point-like dipole oriented purely along the z-axis. Instead, a slightly asymmetric near-field near the tip apex is predicted. The formation of a laterally oriented dipole field is clearly observed in these simulations. We believe taking these effects into account can readily explain the interference effects observed in the two lobes in Figure 5a.

In view of the discussion above, the results presented in Figure 5a are well understood considering the emission from only the lowest two eigenmodes of the conical taper. Apparently, all higher order modes decouple from the taper already at distances of the order of one wavelength or above. Hence, they contribute only weakly to the recorded forbidden light images presented here. This suggests that k-space filtering is an efficient means for suppressing undesired background fields in adiabatic nanofocusing SNOM.

Conclusion

In summary, we have presented a method to investigate the radiation patterns of adiabatic nanofocusing SNOM probes. Our experiments demonstrate that SPP fields coupled to the lowest two eigenmodes are efficiently funneled toward the taper apex. Most importantly, we show that the $n = 0$ eigenmode produces a spatially highly localized near-field at the apex, as predicted by theory, whereas the loosely bound $n = 1$ mode is much less confined. Their contributions are readily identified by analyzing the evolution of angular radiation patterns over the course of an approach curve. This opens up the possibility to separate the rapidly decaying $n = 0$ mode from the undesired higher modes by k-space filtering.

These findings form the basis for further improvements and novel applications. The rapidly decaying contribution to the k-space images provides a direct measure of the desired $n = 0$

mode. Hence, we can use this signal to optimize adiabatic nanofocusing into the lowest order mode. This minimizes background from higher order modes and thus provides a major advancement towards background-free scanning near-field optical spectroscopy. Since we are able to further separate the near-field contributions by k-space filtering, we can now apply this method to spectroscopic studies of the coupling between nano-localized fields and single quantum objects. Such experiments are currently underway in our laboratory.

Supporting Information

Video compiled from k-space images taken during an approach curve. This is a full length sequence of the images shown in Figure 4.

Supporting Information File 1
Video of an approach curve
[http://www.beilstein-journals.org/bjnano/content/supplementary/2190-4286-4-67-S1.avi]

Acknowledgements

References

1. Gramotnev, D. K.; Bozhevolnyi, S. I. *Nat. Photonics* **2010,** *4,* 83–91. doi:10.1038/nphoton.2009.282
2. Aubry, A.; Lei, D. Y.; Fernández-Dominguez, A. I.; Sonnefraud, Y.; Maier, S. A.; Pendry, J. B. *Nano Lett.* **2010,** *10,* 2574–2579. doi:10.1021/nl101235d
3. Gramotnev, D. K. *J. Appl. Phys.* **2005,** *98,* 104302. doi:10.1063/1.2130520
4. Luo, Y.; Pendry, J. B.; Aubry, A. *Nano Lett.* **2010,** *10,* 4186–4191. doi:10.1021/nl102498s
5. Babadjanyan, A. J.; Margaryan, N. L.; Nerkararyan, K. V. *J. Appl. Phys.* **2000,** *87,* 3785–3788. doi:10.1063/1.372414
6. Stockman, M. I. *Phys. Rev. Lett.* **2004,** *93,* 137404. doi:10.1103/PhysRevLett.93.137404
7. Durach, M.; Rusina, A.; Stockman, M. I.; Nelson, K. *Nano Lett.* **2007,** *7,* 3145–3149. doi:10.1021/nl071718g

8. Issa, N.; Guckenberger, R. *Plasmonics* **2007,** *2,* 31–37.
    doi:10.1007/s11468-006-9022-7
9. Ropers, C.; Neacsu, C. C.; Elsaesser, T.; Albrecht, M.; Raschke, M. B.;
    Lienau, C. *Nano Lett.* **2007,** *7,* 2784–2788. doi:10.1021/nl071340m
10. Sadiq, D.; Shirdel, J.; Lee, J. S.; Selishcheva, E.; Park, N.; Lienau, C.
    Nano Lett. **2011,** *11,* 1609–1613. doi:10.1021/nl1045457
11. Schmidt, S.; Piglosiewicz, B.; Sadiq, D.; Shirdel, J.; Lee, J. S.;
    Vasa, P.; Park, N.; Kim, D.-S.; Lienau, C. *ACS Nano* **2012,** *6,*
    6040–6048. doi:10.1021/nn301121h
12. Neacsu, C. C.; Berweger, S.; Olmon, R. L.; Saraf, L. V.; Ropers, C.;
    Raschke, M. B. *Nano Lett.* **2010,** *10,* 592–596. doi:10.1021/nl903574a
13. Verhagen, E.; Spasenović, M.; Polman, A.; Kuipers, L. *Phys. Rev. Lett.*
    2009, *102,* 203904. doi:10.1103/PhysRevLett.102.203904
14. Stratton, J. A. *Electromagnetic Theory;* McGraw-Hill: New York and
    London, 1941.
15. Ashley, J.; Emerson, L. *Surf. Sci.* **1974,** *41,* 615–618.
    doi:10.1016/0039-6028(74)90080-6
16. Pfeiffer, C. A.; Economou, E. N.; Ngai, K. L. *Phys. Rev. B* **1974,** *10,*
    3038–3051. doi:10.1103/PhysRevB.10.3038
17. Johnson, P. B.; Christy, R. W. *Phys. Rev. B* **1972,** *6,* 4370–4379.
    doi:10.1103/PhysRevB.6.4370
18. Koglin, J.; Fischer, U. C.; Fuchs, H. *Phys. Rev. B* **1997,** *55,*
    7977–7984. doi:10.1103/PhysRevB.55.7977
19. Esteban, R.; Vogelgesang, R.; Kern, K. *Nanotechnology* **2006,** *17,*
    475–482. doi:10.1088/0957-4484/17/2/022
20. Novotny, L.; Hecht, B. *Principles of Nano-Optics;* Cambridge University
    Press: Cambridge, 2006. doi:10.1017/CBO9780511813535
21. Knoll, B.; Keilmann, F. *Opt. Commun.* **2000,** *182,* 321–328.
    doi:10.1016/S0030-4018(00)00826-9
22. Raschke, M. B.; Lienau, C. *Appl. Phys. Lett.* **2003,** *83,* 5089–5091.
    doi:10.1063/1.1632023
23. Simon, H. J.; Guha, J. K. *Opt. Commun.* **1976,** *18,* 391–394.
    doi:10.1016/0030-4018(76)90158-9
24. Hecht, B.; Bielefeldt, H.; Novotny, L.; Inouye, Y.; Pohl, D. W.
    Phys. Rev. Lett. **1996,** *77,* 1889–1892.
    doi:10.1103/PhysRevLett.77.1889
25. Drezet, A.; Hohenau, A.; Stepanov, A. L.; Ditlbacher, H.;
    Steinberger, B.; Galler, N.; Aussenegg, F. R.; Leitner, A.; Krenn, J. R.
    Appl. Phys. Lett. **2006,** *89,* 091117. doi:10.1063/1.2339043
26. Esteban, R.; Vogelgesang, R.; Kern, K. *Phys. Rev. B* **2007,** *75,*
    195410. doi:10.1103/PhysRevB.75.195410
27. Behr, N.; Raschke, M. B. *J. Phys. Chem. C* **2008,** *112,* 3766–3773.
    doi:10.1021/jp7098009
28. Park, D. J.; Piglosiewicz, B.; Schmidt, S.; Kollmann, H.; Mascheck, M.;
    Groß, P.; Lienau, C. *Ann. Phys. (Berlin, Ger.)* **2013,** *525,* 135–142.
    doi:10.1002/andp.201200216
29. Lee, J. S.; Han, S.; Shirdel, J.; Koo, S.; Sadiq, D.; Lienau, C.; Park, N.
    Opt. Express **2011,** *19,* 12342–12347. doi:10.1364/OE.19.012342

Controlling the near-field excitation of nano-antennas with phase-change materials

Tsung Sheng Kao, Yi Guo Chen and Ming Hui Hong[*]

Full Research Paper

Open Access

Address:
Department of Electrical and Computer Engineering, National University of Singapore, 4 Engineering Drive 3, 117576 Singapore

Email:
Ming Hui Hong[*] - elehmh@nus.edu.sg

* Corresponding author

Abstract

By utilizing the strongly induced plasmon coupling between discrete nano-antennas and quantitatively controlling the crystalline proportions of an underlying $Ge_2Sb_2Te_5$ (GST) phase-change thin layer, we show that nanoscale light localizations in the immediate proximity of plasmonic nano-antennas can be spatially positioned. Isolated energy hot-spots at a subwavelength scale can be created and adjusted across the landscape of the plasmonic system at a step resolution of $\lambda/20$. These findings introduce a new approach for nano-circuitry, bio-assay addressing and imaging applications.

Introduction

With the rapid development of nanophotonics, increasing attention has been focused on the precise control of the highly confined optical fields on a nanoscale. To achieve the goal of controlling nanoscale light localizations, conventional focusing methods have been proved insufficient as the optical wavelength is on a much larger microscale, whereas promising approaches that use various types of nanostructures and manipulate different characteristics of an incident light beam have emerged [1-15]. For instance, a method was suggested, which is based on the use of plasmon interference where an isolated energy hot-spot can be created and positioned at an appointed location in a confined area through the active control of light illumination on nanohole arrays with optimized amplitudes and phases [1]. With other methods, it is also possible to control the near-field excitation of nano-antennas by controlling polarization singularities and subwavelength spatial phase variations at the focus of high-order beams [2]. The above approaches all provide new opportunities to control light behaviour on a nanoscale. However, they can only be performed through complex nanosystems or sophisticated manipulation of the incident light beams. Moreover, it is usually impossible to excite a single desired mode of the nanostructure and subsequently create a nanoscale energy hot-spot which may only exist in a small field of view.

Here we demonstrate a novel approach in which the constituent plasmonic resonators placed on a thin film of phase-change material can be selectively excited, generating isolated near-field energy hot-spots with selective excitation under a monochromatic plane wave illumination. Unlike other proposed techniques, our method for energy hot-spot positioning is based on a quantitative control of the crystalline proportions of the phase-change thin film rather than the complicated manipulations of an incident light beam. This makes such a near-field energy controllable template much easier to be implemented. To analyse this hybrid plasmonic system, numerical simulations were conducted by the finite-difference-time-domain (FDTD) method (FDTD Solutions 8.5, Lumerical Inc.) with realistic material parameters and Joule loss factors [16,17]. The simulation model was established and is shown in the schematic diagram Figure 1. This near-field energy controllable system consists of five gold nano-antennas with deep subwavelength spacing and an underlying thin layer of $Ge_2Sb_2Te_5$ (GST) phase-change material supported by a transparent quartz substrate. In simulation, the gradually varying lengths of the antennas l are 120, 135, 150, 180, and 218 nm from the shortest to the longest one at a corresponding gap g of 12, 14, 14, 16, and 20 nm, respectively. These different choices in the lengths and gaps of antennas are made in order to have a comparable field enhancement on one excited nano-antenna, whereas the others remain completely unexcited. The width w and thickness h of all the antennas are 40 nm, while the centre-to-centre distance d between the nearest neighbouring antenna is 100 nm.

Results and Discussion

The underlying GST thin film is a phase-change material that has been widely applied in commercial optical disks, optical switchers and phase-change memory [18-20]. GST has many attractive intrinsic properties including the large contrast of the complex refractive index between its amorphous and crystalline phases, an ultra-short tuning time (less than 30 ns), a high stability at room temperature, and a large cycle number [19,21,22]. The modulation of switching the phase states of a GST thin film can be easily accomplished by various well-developed methods, such as electric current, optical pumping and thermal stimulus [23,24]. In the near-infrared (NIR) range, a drastic change in the real part of the refractive index from the phase transition and low absorption loss allow GST to significantly alter the dielectric environment of a plasmonic system while keeping the loss manageable. Regarding the use of a GST phase-change thin film as a controllable medium, a recent research has experimentally demonstrated that the lattice resonance of a gold nanodisk array can be actively tuned in a wide range of 500 nm by controlling the GST transition phases [25].
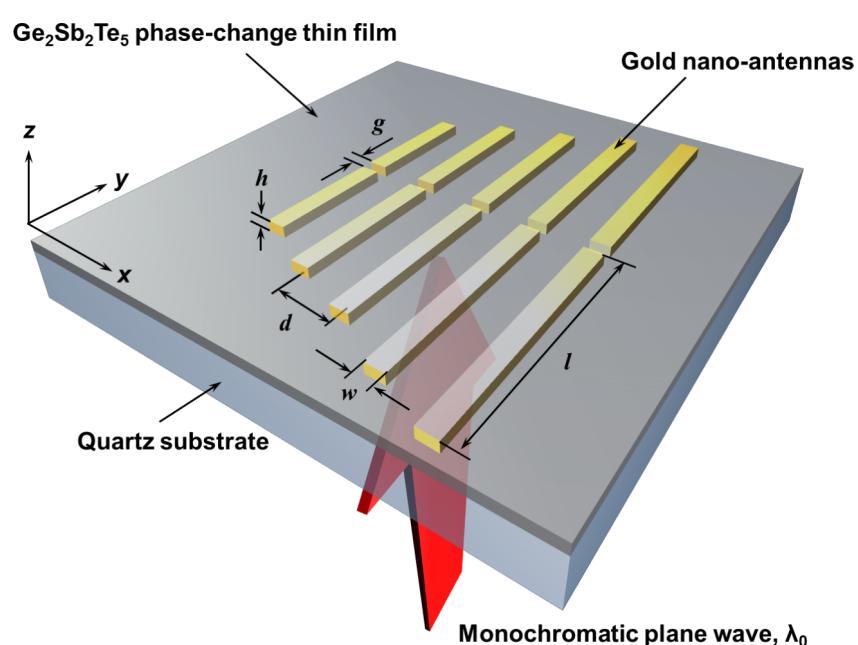
Figure 1: Schematic diagram of a near-field energy controllable template. With a monochromatic plane wave illumination on a nano-antenna system, the near-field intensity distributions can be selectively excited on constituent dipole nano-antennas by controlling different intermediate phases of an underneath phase-change thin film ($Ge_2Sb_2Te_5$, GST). The hybrid plasmonic system of gold nano-antennas and phase-change materials can be fabricated on a transparent quartz substrate. The length of the antenna l ranges from 120 to 218 nm, while the centre-to-centre distance d between the nearest neighbouring antennas is 100 nm. The gap between the nano-antennas is optimized to achieve the selective excitation of the antennas and changed from 12 to 20 nm. The thickness h and the width w of antennas are both 40 nm, while the thickness of a GST thin layer is 15 nm.

In order to demonstrate the quantitative control of the crystalline proportions of a GST thin film, corresponding far-field spectral simulations to the experimental transmission measurements were conducted to estimate the amount of crystallized phase-change molecules. Since GST is known as a nucleation-dominated material, many small crystalline nuclei were formed first when the local temperature reaches the crystallization point of constituent phase-change molecules. Then numerous randomly-distributed small crystals joined together to form a crystalline structure [26,27]. Thus, we assume that the GST thin film at intermediate phases is composed of different proportions of amorphous and crystalline molecules, and that the refractive index of such a GST thin film can be expressed as a weighted average value of the complex indices of GST in the completely amorphous ($n_a(\lambda)$, $k_a(\lambda)$) and crystalline ($n_c(\lambda)$, $k_c(\lambda)$) states,

$$n_{\mathrm{mix}}\left(\lambda\right) = m \times n_c\left(\lambda\right) + \left(1-m\right) \times n_a\left(\lambda\right), \qquad (1)$$

$$k_{\mathrm{mix}}\left(\lambda\right) = m \times k_c\left(\lambda\right) + \left(1-m\right) \times k_a\left(\lambda\right), \qquad (2)$$

where m denotes the proportion of crystallized phase-change molecules ranging from 0% (amorphous) to 100% (crystalline), and the values of ($n_a(\lambda)$, $k_a(\lambda)$) and ($n_c(\lambda)$, $k_c(\lambda)$) are obtained from [17]. With these supposed material parameters carried out in the FDTD simulation, the corresponding refractive index values and the transmission spectra of a GST thin film at different intermediate states can be obtained by carefully selecting the proportion value m.

The phase transition of a sputtered GST phase-change thin film was performed by a homogeneous heating on a hot-plate with a crystallization temperature of 135 °C. This constant temperature was set to provide a slow phase transition rate, which facilitated a finer control of the crystalline proportions of samples. As the heating time increased, the GST thin film gradually changed from the amorphous state to the crystalline state. A UV–vis–NIR spectrophotometer (SHIMADZU, Co.) was employed to measure the transmission spectra of the GST thin film at different intermediate phases. Figure 2 shows the comparison between the experimental spectra measurements (solid lines) and the simulated far-field transmission spectra (dashed lines) of a GST thin film switched at different intermediate phases. A good agreement in both spectral results suggests that a phase-change GST thin film can be well controlled at different crystallization levels and the change of corresponding refractive index values of an underneath GST thin film may significantly alter the dielectric environment of a plasmonic system. Here a 15 nm GST thin film was used as an example.
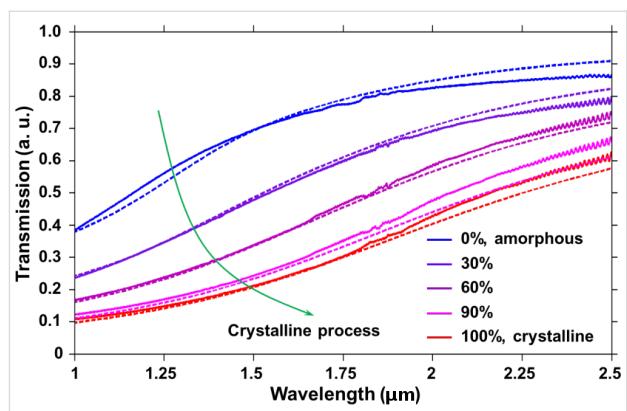
Figure 2: Comparison between the experimental spectra measurements (solid lines) and the simulated far-field transmission spectra (dashed lines) of a GST thin film switched at different intermediate phases. A good agreement of the spectral results shows the quantifiable phase-change modulation of a GST nano thin film at different crystalline proportions.

With the quantifiable phase-change modulation, the main characteristic features of controlling nanoscale field excitations at different transition phases are illustrated in Figure 3a–e. As shown, the nanoscale energy hot-spot is positioned on the dipole nano-antennas landscape as a function of the crystalline proportion of a GST thin film. In this plasmonic system, a plane wave is normally incident onto the array with a polarization direction parallel to the antennas in the *y* direction, and the illumination wavelength is 2.16 μm. When the underneath GST thin film is in the amorphous state, only the longest nano-antenna is excited, generating a subwavelength energy hot-spot at the gap centre of the antenna. By adjusting the proportion value *m* of crystallized phase-change molecules, the GST crystalline level with different dielectric properties is gradually changed and the excitation wavelength at the field enhancement peak of each nano-antenna can be tuned as the spectral shift shown in Figure 3g–j. Once one of the peaks corresponds to the illumination wavelength, only one corresponding nano-antenna is excited, indicating an energy hot-spot to be created at the gap centre. Through this process, the relation between the hot-spot localization and the corresponding crystalline proportion of the GST thin film can also be obtained. Thus, the nanoscale energy hot-spot can be simply repositioned from one nano-antenna to another by switching the crystalline proportion and a step resolution of λ/20 (100 nm) can be obtained much beyond the diffraction limit.

Although a clear movement and positioning of the isolated energy hot-spot can be achieved, the challenge of lower field intensity with an increase of GST crystalline proportions still needs to be addressed. These weak energy localizations may result from more metal-like portion generated when the phase-change material is changed to the crystalline state, leading to
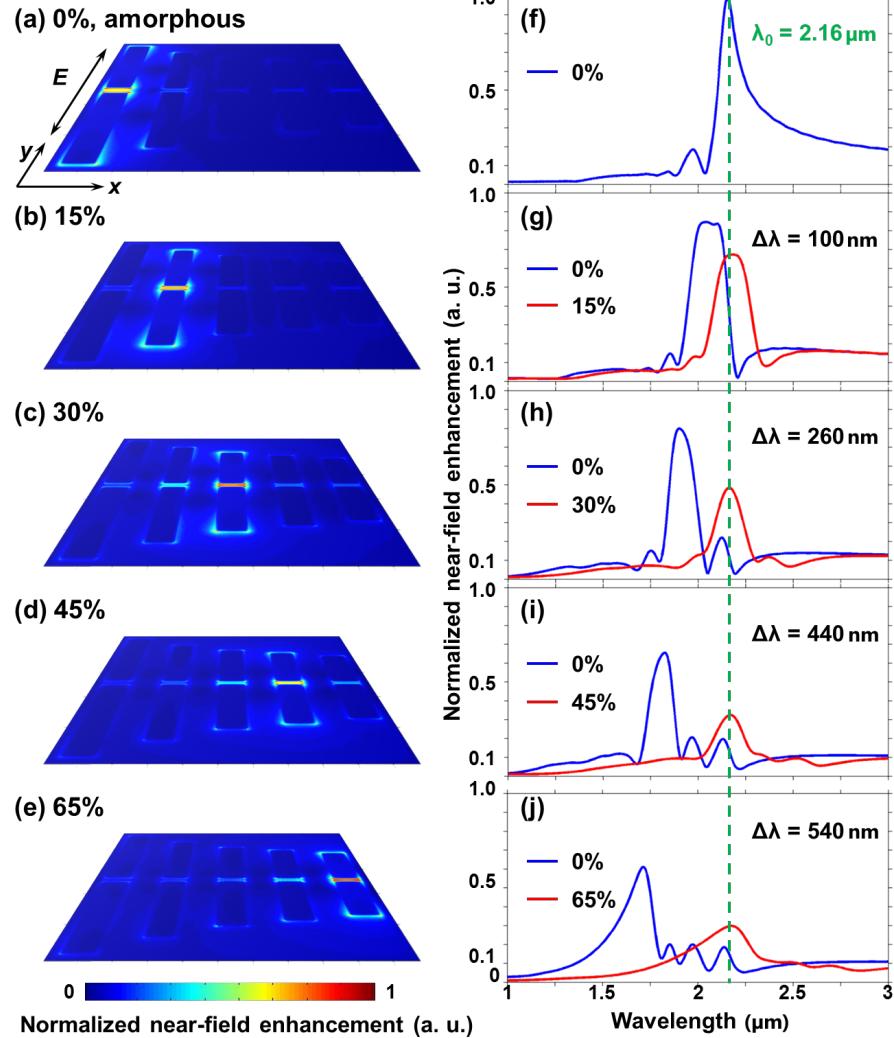
Figure 3: Controlling the near-field excitation of nano-antennas with a quantitative modulation on the phase transition of an underneath GST thin layer. When the crystalline proportion of the phase-change thin film is changed from the amorphous state (0%) to a portion of 65% crystallization, the nano-antennas can be selectively excited at different intermediate phases, generating nanoscale light localizations positioned on the landscape of constituent dipole nano-antennas. A plane wave is normally incident onto the array at an excitation wavelength of 2.16 µm and the polarization direction is parallel to the antennas in the *y* direction. The centre-to-centre distance between neighbouring antennas is 100 nm, giving a step resolution of *λ*/20 in this plasmonic nanosystem.

enhanced absorption and thus decreasing the transmitted light intensity. By exploiting different plasmonic resonators or changing the thickness and composites of the underlying phase-change materials, the energy loss may be reduced, increasing the feasibility to implement this near-field energy controllable template for positioning nanoscale energy hot-spots on the nanostructure landscape.

As illustrated in [15], strong plasmon coupling between the constituent dipole antennas plays an important role in a closely packed nano-antenna array. The mutual interactions among the plasmonic resonators are hybridized and may interfere constructively at one single resonator and destructively at all the others. Thus, each antenna can be individually excited at its resonance frequency. The selective field excitation features for the coupled antenna array can also be represented in our hybridized plasmonic nanosystem. Figure 4a and b show that the arrays of nano-antennas with the same geometric parameters are placed on a GST phase-change thin film, but spatially separated with different centre-to-centre spacing *d*, while Figure 4c and d show that the calculated near-field field enhancement is modulated at the gap centres of each nano-antennas in the two arrays, respectively. In Figure 4c, at a separation distance of 100 nm, each antenna exhibits a shaper resonance peak, where all the other antennas are strongly suppressed. Compared with an uncoupled system, an array of dipole antennas with a sep-
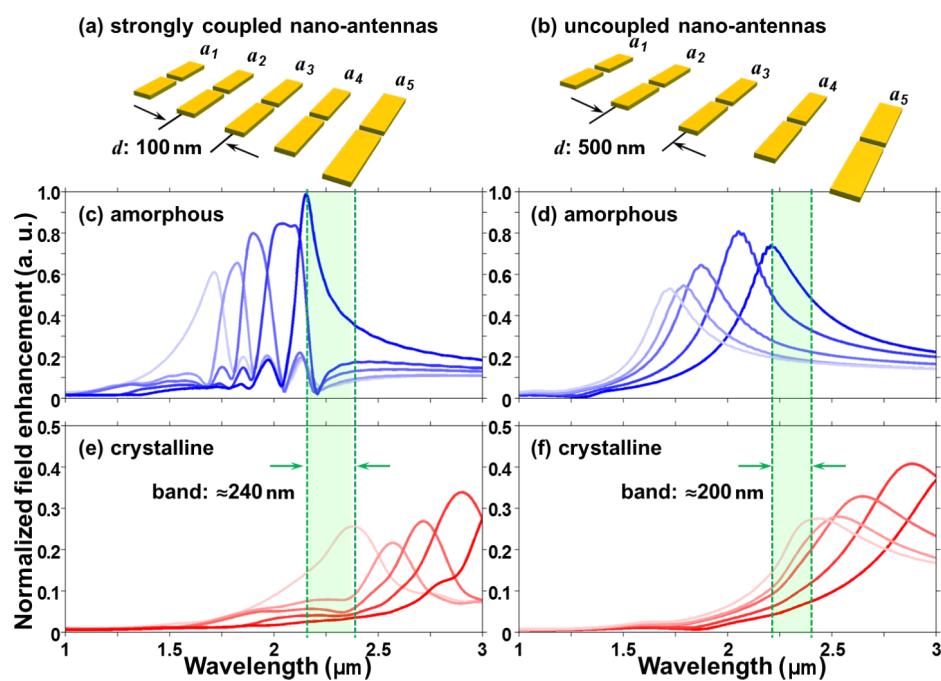
Figure 4: Comparisons between the strong plasmon coupling and uncoupled nano-antennas system. The antennas in the two arrays have the same geometric parameters but different centre-to-centre spacing *d*. Simulation results, (c) and (d), show a good excitation selectivity in the strong plasmon coupled nano-antenna array due to the sharp spectral features. By controlling the crystalline proportions of an underlying GST thin film, the resonance peaks of each antenna may cross a selected illumination wavelength, indicating that the antennas are individually excited. Also, a broader range of choosing feasible illumination wavelengths as the green band shows in (e) and (f) can be obtained in the strong plasmon coupling system by switching the GST completely from the amorphous state to the crystalline state.

aration distance of 500 nm shows poor excitation selectivity due to the relatively broad resonance profile as shown in Figure 4d. More importantly, in our proposed hybrid plasmonic nanosystem, a strict selection of illumination wavelengths is not necessarily required. The dipole nano-antennas can be individually excited by controlling the intermediate phases of an underneath GST thin film from the amorphous state to the crystalline state at a selected illumination wavelength. This facilitates the implementation of the new approach for us. Moreover, with a good control of the GST phase transition states, more diversities of plasmonic resonators such as nano-antennas can be included to extend the plasmonic system, allowing the nanoscale energy hot-spot to be positioned over a large area. In this hybrid plasmonic nanosystem, the strong plasmon interactions also provide a wider range of choices of feasible illumination wavelengths. The range is determined by the excitation wavelengths at the resonance peak of the shortest antenna in the crystalline state and the longest antenna in the amorphous state as the green band indicates in Figure 4e and f.

Conclusion

In conclusion, we have demonstrated that in a hybrid plasmonic nanosystem, the constituent nano-antennas can be selectively excited with a selected illumination wavelength and near-

field enhancement can be positioned at the gap centres of each antenna by controlling the intermediate phases of an underlying GST phase-change thin film. In the strong plasmon coupling nano-antenna array, a step resolution of λ/20 much beyond the diffraction limit can be obtained. Such a hybrid plasmonic system is easy to be implemented and the nanoscale energy hot-spot can be positioned in a large field of view by extending the system with different plasmon resonators, suggesting a further step toward applications such as nano-imaging, bio-assay addressing and nano-circuitry.

Acknowledgements

References

1. Gjonaj, B.; Aulbach, J.; Johnson, P. M.; Mosk, A. P.; Kuipers, L.; Lagendijk, A. *Nat. Photonics* **2011,** *5,* 360–363. doi:10.1038/nphoton.2011.57

2. Volpe, G.; Cherukulappurath, S.; Parramon, R. J.; Molina-Terriza, G.; Quidant, R. *Nano Lett.* **2009,** *9,* 3608–3611. doi:10.1021/nl901821s

3. Sentenac, A.; Chaumet, P. C. *Phys. Rev. Lett.* **2008,** *101,* 013901. doi:10.1103/PhysRevLett.101.013901

4. Volpe, G.; Molina-Terriza, G.; Quidant, R. *Phys. Rev. Lett.* **2010,** *105,* 216802. doi:10.1103/PhysRevLett.105.216802

5. Stockman, M. I. *Phys. Rev. Lett.* **2004,** *93,* 137404. doi:10.1103/PhysRevLett.93.137404

6. Schroer, C. G.; Lengeler, B. *Phys. Rev. Lett.* **2005,** *94,* 054802. doi:10.1103/PhysRevLett.94.054802

7. Gramotnev, D. K.; Bozhevolnyi, S. I. *Nat. Photonics* **2010,** *4,* 83–91. doi:10.1038/nphoton.2009.282

8. Stockman, M. I.; Faleev, S. V.; Bergman, D. J. *Phys. Rev. Lett.* **2002,** *88,* 067402. doi:10.1103/PhysRevLett.88.067402

9. Schnell, M.; García-Etxarri, A.; Huber, A. J.; Crozier, K.; Aizpurua, J.; Hillenbrand, R. *Nat. Photonics* **2009,** *3,* 287–291. doi:10.1038/nphoton.2009.46

10. Aeschlimann, M.; Bauer, M.; Bayer, D.; Brixner, T.; Cunovic, S.; Dimler, F.; Fischer, A.; Pfeiffer, W.; Rohmer, M.; Schneider, C.; Steeb, F.; Strüber, C.; Voronine, D. V. *Proc. Natl. Acad. Sci. U. S. A.* **2010,** *107,* 5329–5333. doi:10.1073/pnas.0913556107

11. Kao, T. S.; Huang, F. M.; Chen, Y.; Rogers, E. T. F.; Zheludev, N. I. *Appl. Phys. Lett.* **2010,** *96,* 041103. doi:10.1063/1.3291675

12. Kao, T. S.; Jenkins, S. D.; Ruostekoski, J.; Zheludev, N. I. *Phys. Rev. Lett.* **2011,** *106,* 085501. doi:10.1103/PhysRevLett.106.085501

13. Kao, T. S.; Rogers, E. T. F.; Ou, J. Y.; Zheludev, N. I. *Nano Lett.* **2012,** *12,* 2728–2731. doi:10.1021/nl2043437

14. Noh, H.; Chong, Y.; Stone, A. D.; Cao, H. *Phys. Rev. Lett.* **2012,** *108,* 186805. doi:10.1103/PhysRevLett.108.186805

15. Zhang, S.; Ye, Z.; Wang, Y.; Park, Y.; Bartal, G.; Mrejen, M.; Yin, X.; Zhang, X. *Phys. Rev. Lett.* **2012,** *109,* 193902. doi:10.1103/PhysRevLett.109.193902

16. Johnson, P. B.; Christy, R. W. *Phys. Rev. B* **1972,** *6,* 4370–4379. doi:10.1103/PhysRevB.6.4370

17. Yamada, N. Development of Materials for Third Generation Optical Storage Media. In *Phase Change Materials: Science and Applications;* Raoux, S.; Wuttig, M., Eds.; Springer-Verlag: Berlin-Heidelberg, Germany, 2009; pp 199–226. doi:10.1007/978-0-387-84874-7_10

18. Wuttig, M.; Lüsebrink, D.; Wamwangi, D.; Wełnic, W.; Gilleßen, M.; Dronskowski, R. *Nat. Mater.* **2007,** *6,* 122–128. doi:10.1038/nmat1807

19. Yamada, N. *Phys. Status Solidi B* **2012,** *249,* 1837–1842. doi:10.1002/pssb.201200618

20. Xiong, F.; Liao, A. D.; Estrada, D.; Pop, E. *Science* **2011,** *332,* 568–570. doi:10.1126/science.1201938

21. Yamada, N.; Otoba, M.; Kawahara, K.; Miuagawa, N.; Ohta, H.; Akahira, N.; Matsunaga, T. *Jpn. J. Appl. Phys.* **1998,** *37,* 2104–2110. doi:10.1143/JJAP.37.2104

22. Loke, D.; Lee, T. H.; Wang, W. J.; Shi, L. P.; Zhao, R.; Yeo, Y. C.; Chong, T. C.; Elliott, S. R. *Science* **2012,** *336,* 1566–1569. doi:10.1126/science.1221561

23. Chu, C. H.; Shiue, C. D.; Cheng, H. W.; Tseng, M. L.; Chiang, H.-P.; Mansuripur, M.; Tsai, D. P. *Opt. Express* **2010,** *18,* 18383–18393. doi:10.1364/OE.18.018383

24. Chang, C. M.; Chu, C. H.; Tseng, M. L.; Chiang, H.-P.; Mansuripur, M.; Tsai, D. P. *Opt. Express* **2011,** *19,* 9492–9504. doi:10.1364/OE.19.009492

25. Chen, Y. G.; Kao, T. S.; Ng, B.; Li, X.; Luo, X. G.; Luk'yanchuk, B.; Maier, S. A.; Hong, M. H. *Opt. Express* **2013,** *21,* 13691–13698. doi:10.1364/OE.21.013691

26. Raoux, S.; Rettner, C. T.; Jordan-Sweet, J. L.; Kellock, A. J.; Topuria, T.; Rice, P. M.; Miller, D. C. *J. Appl. Phys.* **2007,** *102,* 094305. doi:10.1063/1.2801000

27. Russo, U.; Ielmini, D.; Lacaita, A. L. *IEEE Trans. Electron Devices* **2007,** *54,* 2769–2777. doi:10.1109/TED.2007.904976

License and Terms

Probing the plasmonic near-field by one- and two-photon excited surface enhanced Raman scattering

Katrin Kneipp[*] and Harald Kneipp

Full Research Paper

Address:
Physics Department, Technical University of Denmark, 2800 Kgs
Lyngby, Denmark

Email:
Katrin Kneipp[*] - katrin.kneipp@fysik.dtu.dk; Harald Kneipp -
harald.kneipp@fysik.dtu.dk

* Corresponding author

Abstract

Strongly enhanced and spatially confined near-fields in the vicinity of plasmonic nanostructures open up exciting new capabilities for photon-driven processes and particularly also for optical spectroscopy. Surface enhanced Raman signatures of single molecules can provide us with important information about the optical near-field. We discuss one- and two-photon excited surface enhanced Raman scattering at the level of single molecules as a tool for probing the plasmonic near-field of silver nanoaggregates. The experiments reveal enhancement factors of local fields in the hottest hot spots of the near-field and their dependence on the photon energy. Also, the number of the hottest spots and their approximate geometrical size are found. Near-field amplitudes in the hottest spots can be enhanced by three orders of magnitudes. Nanoaggregates of 100 nm dimensions provide one hot spot on this highest enhancement level where the enhancement is confined within less than 1nm dimension. The near-field enhancement in the hottest spots increases with decreasing photon energy.

Introduction

The resonance frequencies of collective oscillations of the electrons in the conduction band in metal nanostructures, which are called surface plasmons, fall in the optical range of the electromagnetic spectrum. This results in a strong coupling between incident light and surface plasmons. The interaction gives rise not only to beautifully colored glass windows in old cathedrals but also to strongly enhanced and spatially highly confined local fields in the vicinity of such plasmonic structures [1,2]. Exploiting these optical near-fields opens up exciting new capabilities for photon-driven processes and particularly for optical spectroscopy. Surface-enhanced Raman scattering (SERS) might be one of the most prominent effects to demonstrate the potential of spectroscopy performed in the near-field. SERS enables Raman measurements on a single molecule [3]. Vice

versa, here we show that single molecules and their Raman signatures can be useful tools for probing plasmonic near-fields.

The measurement of Raman signals from single molecules requires high optical field intensities in order to compensate for the extremely small Raman cross sections. Enhancement of the near-field intensity is the key effect in surface enhanced Raman scattering. High local fields are generated by a redistribution of field intensities in the vicinity of a plasmonic nanostructure. This results in a wide intensity distribution within the near-field. Sites that provide extremely high local fields, so-called "hot spots" exist along with areas showing much lower level of field intensity. Theory predicts the highest local fields in gaps between silver and gold nanostructures, e.g., in aggregates of nanoparticle of various sizes and shapes reaching from dimers [4-7], and trimers [8] to selfsimilar structures formed by silver- or gold nanospheres [9]. High local fields can also exist in fractal films or cavities of these noble metals [10]. The recently reported super-resolution imaging of SERS on silver nanoaggregates has directly confirmed nanoparticle junctions to be responsible for single molecule SERS [11].

Computations show dramatic variations in near-field intensities within a few nanometers. Even sophisticated optical experiments cannot reveal these dramatic spatial variations. However, surface plasmons can be also excited by low energy [12] and high energy electrons [13,14]. Therefore, as an alternative to optical methods, electron energy loss spectroscopy (EELS) is emerging as a novel tool to probe plasmonic near-fields of metal nanostructures at nanometer-resolutions and even below [15-19]. We have applied EELS for probing the local distribution of plasmonic fields at nanometer scale for nanoaggregates formed by silver particles [18].

Here we discuss experiments for probing the optical near-field of silver nanoaggregates by using one- and two-photon excited Raman scattering. The applied excitation wavelengths do not match the electronic transitions of the target molecules, i.e., SERS spectra are measured without additional contributions of an intrinsic molecular resonance Raman enhancement. The experiments are performed in a way that single molecules reside exclusively in the hottest hot spots provided in the near-field. We employ surface-enhanced pumped anti-Stokes Raman scattering (SEPARS) and one- and two-photon excited surface enhanced Raman (SERS) and hyper Raman (SEHRS) signals, respectively for estimating the maximum field enhancement in these hot spots. Measuring SERS signals over wide concentration ranges of a target molecule displays the step-by-step occupation of the near-field volume by Raman active molecules and enables to infer a geometrical size of the hottest hot spots as well as their number.

Results and Discussion
Plasmonic silver nanoaggregates

The highest SERS enhancement levels obtained so far are related to silver or gold nanoparticles that form aggregates as "SERS-active substrates" and by using excitation in the near infrared [20-22]. The first SERS spectra of single molecules had been measured by using small aggregates of silver nanoparticles and still, such aggregates seem to be the favorite "plasmonic substrate" for single-molecule SERS [23]. Most single-molecule SERS studies are using excitation wavelengths that are resonant with electronic transitions in the target molecule and, by this way, exploit a superposition of enhanced local fields and resonance Raman scattering (SERRS) [7,23-28]. These resonant conditions, and even pre-resonant conditions, greatly reduce the requirements for local field intensities since these experiments take advantage of the large cross section for the molecular Raman resonance [29,30]. However, exploiting extremely high local fields also enables Raman measurements from single molecules without the support of an intrinsic molecular resonance Raman enhancement [29,31-36]. Figure 1 shows typical silver nanoaggregates that provide extremely high near-field enhancement levels, which are suitable for single-molecule SERS under non-resonant conditions. The silver structures were prepared by a standard citrate reduction procedure [37].
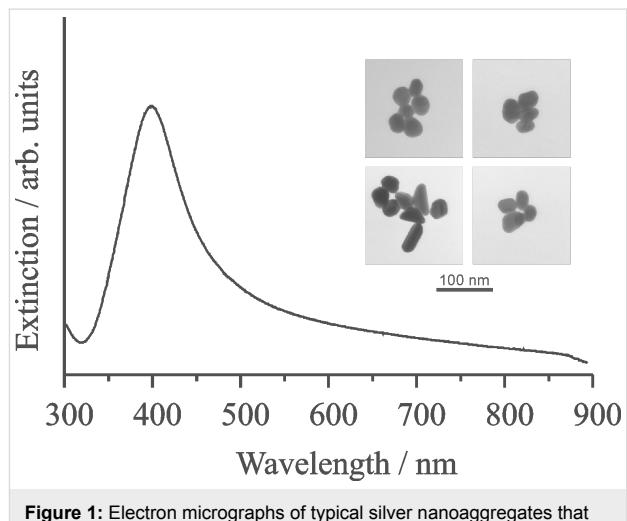
Figure 1: Electron micrographs of typical silver nanoaggregates that were used in this study and the extinction spectrum of their aqueous solution.

In this study, SERS experiments are carried out in solutions of silver nanoaggregates under the condition that the concentration of the target molecules is by a factor of 10–100 smaller than the concentrations of the plasmonic nanoaggregates. This means that, statistically, single nanoaggregates carry a single target molecule, while most of the aggregates are "empty". Single-molecule SERS experiments have shown that it is likely that these single molecules reside in the hottest hot spots of the

nanoaggregates [29]. This is also supported by computations that show that high field gradients related to hot spots in plasmonic near-fields might direct single molecules to the hottest spots [38]. Experiments performed under these conditions exclusively probe the hottest spots of the near-fields in an ensemble of plasmonic nanoaggregates.

Probing the field enhancement in the hottest hot spots of the near-field

As we discussed above, single molecules can be subnanometer-size sensors for probing the near-field of nanoaggregates. Here we infer the enhancement factor for the near-field in the hottest hot spots by considering the anti-Stokes to Stokes signal ratios during surface-enhanced pumped anti-Stokes Raman scattering (SEPARS) experiments as well as the ratios between two- and one-photon excited surface enhanced hyper Raman and Raman scattering SEHRS and SERS, respectively.

Surface-enhanced pumped anti-Stokes Raman scattering(SEPARS)

While Stokes Raman scattering starts from the vibrational ground states of a molecule, anti-Stokes Raman scattering is related to scattering with molecules in the first excited vibrational states. Therefore, the ratio between anti-Stokes and Stokes Raman signals is determined by the ratio of the number of molecules N_1 and N_0 in these two states, i.e., by the Boltzmann population. This results in much weaker anti-Stokes Raman signals than Stokes signals, particularly for higher frequency vibrational modes. However, the situation can be dramatically changed in a very strong surface-enhanced Raman process. This is illustrated in Figure 2: Isolated silver or gold nanoparticles support a surface-enhanced Raman signal of crystal violet shown in the Stokes spectrum (Figure 2a). As expected, the anti-Stokes SERS spectrum (Figure 2b) displays the lower frequency modes only. This situation changes when aggregates are employed as enhancing structures for spectra (Figure 2c) and Figure 2d). Now a strong anti-Stokes spectrum appears.

In particular, this spectrum shows strong anti-Stokes lines also for the higher-energy Raman modes. The strong anti-Stokes SERS signal is related to the effect of surface enhanced pumped anti-Stokes Raman scattering (SEPARS). During SEPARS, Stokes scattering with an extremely high effective cross section populates the first excited vibrational levels in addition to the thermal population [20,33,39]. This results in an increase of anti-Stokes signals. In Figure 2c and Figure 2d, SEPARS can be observed due to highly localized and enhanced fields of silver nanoaggregates, which result in extremely high effective SERS cross sections. This is in contrast to the relatively weakly enhanced local fields for isolated silver particles that were used
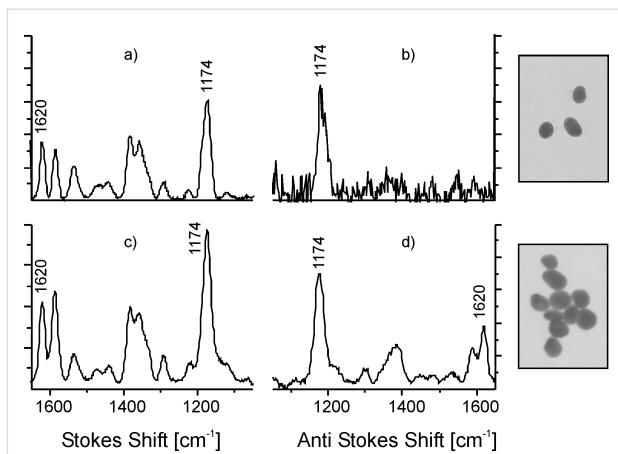
Figure 2: Stokes and anti-Stokes SERS spectra of crystal violet under conditions of "normal" SERS (a,b) and extremely strong SERS (c,d) [31]. Spectra were measured by using 830 nm non-resonant excitation. Reprinted with permission from [22], Copyright 2006 American Chemical Society.

in Figure 2a and Figure 2b. Figure 3 displays the energy level diagram for non-resonant and resonant Stokes and anti-Stokes Raman scattering along with rate equations that describe the population of the first excited vibrational level.

While for non-resonant Raman scattering, a strong Stokes process appears to be the only way to "pump" vibrational levels, in case of resonant and pre-resonant Raman scattering, other mechanism(s) such as ultrafast internal conversion after electronic excitation and/or fluorescence exist as main source for the population of excited vibrational states. This has been confirmed by time resolved pump–probe anti-Stokes SERS studies on rhodamine 6G on silver nanostructures with an excitation wavelength of 633 nm [40]. These experiments identified a rise time of the pumped anti-Stokes signal of about 0.8 ps related to the population of the excited vibrational level by ultrafast internal conversion. Population pumping due to a Raman process follows the excitation pulse instantaneously. Therefore, for the extraction of information on effective SERS cross sections, SERS enhancement factors and enhanced near-fields, population pumping should be employed under non-resonant Raman conditions. Here we discuss SEPARS by using non-resonant excitation in the NIR wavelengths range. Since the ratio between anti-Stokes and Stokes Raman signals is determined by the ratio between N_1 and N_0, a simple equation for the anti-Stokes to Stokes signal ratio P_{aS}/P_S can be derived from the left rate equation in Figure 3 by assuming steady state and weak saturation [20]

$$\frac{P_{aS}}{P_S} = \sigma^{SERS} \times \tau_1 \times n_L + e^{-\frac{h\nu_M}{kT}}, \quad (1)$$
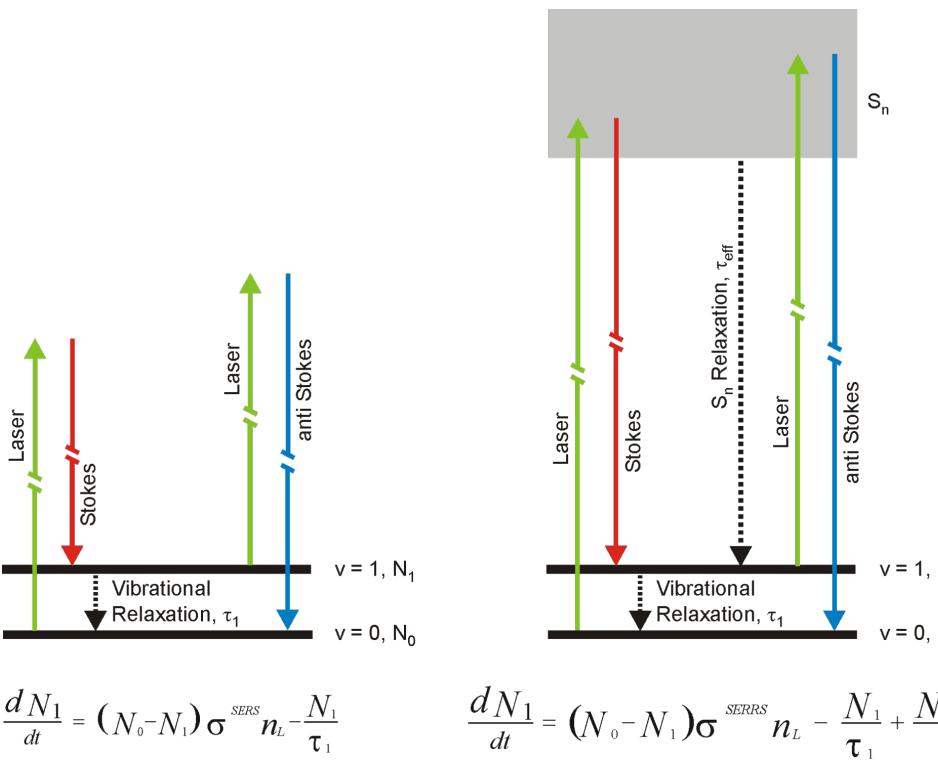
Figure 3: Non-resonant (left) and resonant (right) Stokes and anti-Stokes Raman scattering in an energy level diagram. The rate equations describe the population of the first excited vibrational level. N_1 and N_0 are the numbers of molecules in the excited and ground vibrational state, respectively. σ^{SERS} and σ^{SERRS} are effective SERS and SERRS cross sections, respectively, σ^{abs} describes electronic absorption. τ_1 is the lifetime of the first excited vibrational state, τ_{eff} the inverse rate constant for the population of the first excited vibrational level by internal conversion followed by vibrational relaxation and/or by fluorescence. n_L is the number of laser photons per cm^2 and second applied for the excitation.

where ν_M is the molecular vibrational frequency, T is the temperature of the sample, and h and k are the Planck and Boltzmann constant, respectively. The first term in Equation 1 describes the anti-Stokes to Stokes signal ratio related to SERS vibrational pumping due to a strong Raman Stokes process. In "normal" non-resonant and also in resonant Raman scattering with cross sections on the order of 10^{-30} to 10^{-24} cm^2, this term can be neglected since it is small compared to the thermal population described by the second term. In order to account for experimentally observed anti-Stokes to Stokes signal ratios in SERS experiments on silver nanoaggregates, as it is demonstrated for example in Figure 2c and Figure 2d, the product of cross section and vibrational lifetime in Equations 1 must be on the order of 10^{-27} cm$^2 \cdot$s. With vibrational lifetimes on the order of 10 ps [40], effective cross sections that can account for Raman pumping of a molecular vibration have to be at least on the order of 10^{-16} cm^2.

In general, an effective SERS cross section can be written as [39]

$$\sigma^{SERS} = \sigma^{RS}_{ads} \left| A\left(\nu_L\right) \right|^2 \left| A\left(\nu_S\right) \right|^2 ,$$

$$\text{with } \left| A(\nu) \right|^2 = \frac{\left| E(\nu) \right|^2}{\left| E^{(0)}(\nu) \right|^2} , \tag{2}$$

where $A(\nu)$ describes the enhancement of the near-field at the location of the molecule, $E(\nu)$ is the local optical field (laser and the scattered field, respectively) and $E^{(0)}(\nu)$ is the field in the absence of the metal nanostructure. σ^{RS}_{ads} is the Raman cross section of a molecule in contact with the metal compared to σ^{RS}_{free} of a molecule without coupling to the metal. The ratio $\sigma^{RS}_{ads}/\sigma^{RS}_{free}$ describes the enhancement effects related to "chemical" or "first layer" mechanisms in SERS [41,42].

SERS vibrational pumping based on effective Raman cross sections on the order of 10^{-16} cm^2 has been also observed for adenine attached to silver nanoaggregates [33]. The molecule absorbs in the UV, i.e., the applied excitation photons at 830 nm

are at a much lower energy than the electronic transitions and SERS on adenine cannot benefit from a molecular-resonance Raman effect. Therefore, effective SERS cross sections on order of 10^{-16} cm^2 compared to typical non-resonant Raman cross sections on the order of 10^{-30} cm^2 imply SERS enhancement factors of around 10^{14}. Anti-Stokes to Stokes signal ratios measured on different structures from 100 nm aggregates to larger fractal silver structures that were several micrometers in size show that enhancement factors on the order of 10^{14} in non-resonant SERS are independent of the size and shape of the aggregates. However, they critically depend on the gap size between the nanoparticles forming the aggregate [22,33,43]. In general, enhanced local fields *and* "chemical" enhancement can contribute to such enormous non-resonant total enhancement factors. SEPARS experiments provide us with information about the total effective SERS cross section (see Equation 2). In the following section, we discuss hyper Raman scattering as a method to separate information about the near-field enhancement and for probing local fields in hot spots in more detail.

Surface enhanced two-photon excited hyper Raman scattering

During hyper Raman scattering (HRS), two photons interact simultaneously with the molecules. This process results in an incoherent scattering signal shifted relative to the second harmonic of the excitation laser. Figure 4 explains hyper Raman scattering in an energy level diagram. HRS follows symmetry selection rules that are different from those in Raman scattering, and therefore it can probe vibrations that are forbidden in Raman scattering.

As it is generated by two-photon excitation, the HRS signal is a quadratic function of the excitation intensity. Extremely small cross sections on the order of 10^{-65} cm^{4}s/photon make the utilization of HRS as a practical spectroscopic tool nearly impossible. However, HRS particularly benefits from optical near-fields. The effective cross section for surface enhanced hyper Raman scattering (SEHRS) can be written as

$$\sigma^{\text{SEHRS}} = \sigma_{\text{ads}}^{\text{HRS}} \left| A\left(\nu_{\text{L}}\right) \right|^4 \left| A\left(\nu_{\text{hS}}\right) \right|^2 , \qquad (3)$$

where $\sigma_{\text{ads}}^{\text{HRS}}$ describes a "chemically" enhanced hyper Raman cross section compared to that of a "free" molecule, $A(\nu)$ describes the enhancement of the near-fields at the excitation and hyper Raman scattered wavelengths, respectively.

While one-photon excited SERS depends on the field amplitude enhancement in the near-field to the power of four (see Equation 2), surface enhanced hyper Raman scattering (SEHRS) increases with the field enhancement factor $A(\nu)$ to
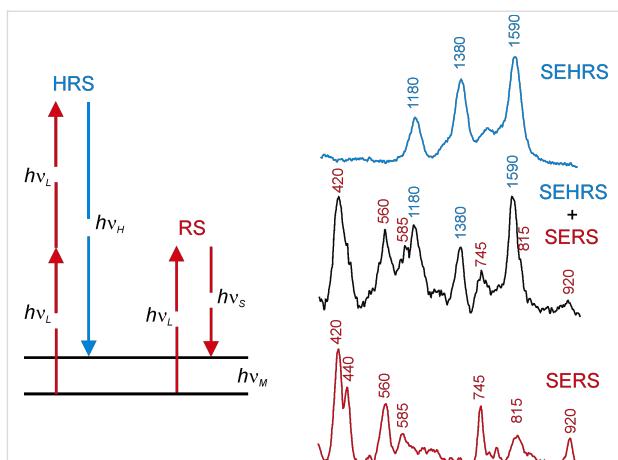
Figure 4: Schematic of hyper Raman- and Raman scattering (left) and surface enhanced Raman- and hyper Raman spectra of crystal violet on silver nanoaggregates (right, excitation 850 nm, 10^7 W/cm^2). SEHRS and SERS signals of crystal violet measured in the same spectrum by simultaneously using the first and second diffraction order of the spectrograph (middle trace). In the upper and the lower trace, SEHRS and SERS spectra are differentiated by placing a NIR absorbing filter in front of the spectrograph or by switching off the mode locked regime of the Ti:sapphire laser, respectively [44]. Reprinted with permission from [22], Copyright 2006 American Chemical Society.

the power of six, because of its quadratic dependence on the excitation intensity [44,45]. This different dependence allows to infer the field enhancement E_{loc}^2/E_0^2 in the hot spots of the nanoaggregates from the ratio between their one- and their two-photon excited surface enhanced Raman and hyper Raman response, respectively. Despite very different signal levels of "normal" Raman and hyper Raman scattering, SERS and SEHRS spectra appear at comparable signal levels and can be measured in the same spectrum as it is demonstrated in Figure 4 [44]. This shows that hyper Raman scattering must experience a much stronger enhancement effect than Raman scattering. Since it is reasonable that the chemical enhancement effect for Raman and hyper Raman scattering is on the same order of magnitude, we can ascribe extremely high SEHRS signals to the near-field. Comparing SEHRS-and SERS-signal levels in more detail [44,45], we find SEHRS enhancement levels that are up to 10^6 times higher than the SERS enhancement levels. This results in an enhancement on the order of 10^3 for the field amplitudes in the hottest spots of the near-field (see Equations 2 and Equations 3). Field enhancement factors of 10^3 give rise to "electromagnetic" SERS enhancement factors on the order of 10^{12}. With a "chemical" contribution to SERS enhancement on the order of 10^2 [42], the total SERS enhancement factors reach 10^{14} as we inferred from anti-Stokes to Stokes signal ratios in SEPARS experiments. An interesting question is the dependence of the near-field enhancement on the photon energy. The ratio between SEHRS and SERS signals measured vs the excitation wavelengths delivers direct information about this depen-

dence. Figure 5 shows the result of experiments, in which a tunable ps Ti:sapphire was used for excitation. The experiments show an increase of the local optical field with increasing wave lengths. Increasing intensities for local fields in the hot spots with decreasing photon energy have also been theoretically predicted [46].

Probing the number of hottest hot spots and their geometrical size

Near-field intensities in the vicinity of plasmonic nanostructures such as silver nanoaggregates show strong spatial variations. Very early SERS experiments already did show that an extremely high enhancement level, as it was obtained in SERS vibrational pumping, is available for very few molecules only [20]. Our experiments that were reported in the previous section exploit an extremely high enhancement level as it is available in these hottest spots. This was achieved by working at a very low concentration of the target molecules so that molecules exclusively reside in the hottest hot spots [29]. In the following, we want to determine how many molecules can find a place at the hottest hot spots. Based on this information, we can infer the number of hot spots and their geometrical size.

SERS signal vs concentration of the target molecule

The experiments were performed in aqueous solutions of silver nanoaggregates described above (Figure 1). The concentration of the nanoaggregates was on the order of 10^{-10} M. A NaCl solution of 10^{-3} M concentration was added to the solution of the aggregates in order to achieve an optimum chemical SERS-enhancement. Each of the silver aggregates provides a total enhancement factor on the order of 10^{14} when 830 nm excita-
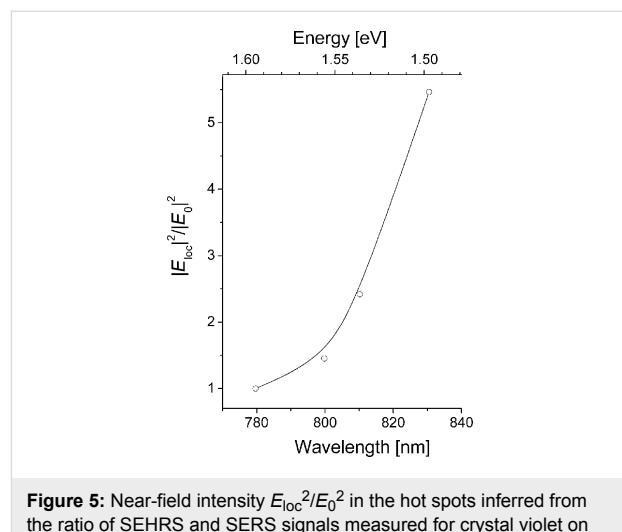
Figure 5: Near-field intensity E_{loc}^2/E_0^2 in the hot spots inferred from the ratio of SEHRS and SERS signals measured for crystal violet on silver nanoaggregates while using excitation wavelengths between 780 and 830 nm. Reprinted with permission from [18]. Copyright 2013 Springer.

tion is used. This level of enhancement was confirmed by checking anti-Stokes to Stokes signal ratios in SEPARS experiments. SERS samples of rhodamine 6G concentrations between 10^{-15} and 10^{-6} M were prepared by adding aqueous solutions of the dye at appropriate concentrations in 1:15 ratios to the solutions of silver nanoaggregates. After non-resonant 830 nm excitation, the Raman scattered light was collected in an 180°-scattering geometry from probed volume of a 10–20 nL inside 1 mL of sample solution by using the same microscope objective for excitation and collection of the scattered light. Figure 6 shows the dependence of SERS signal on the concentrations of the target molecule.
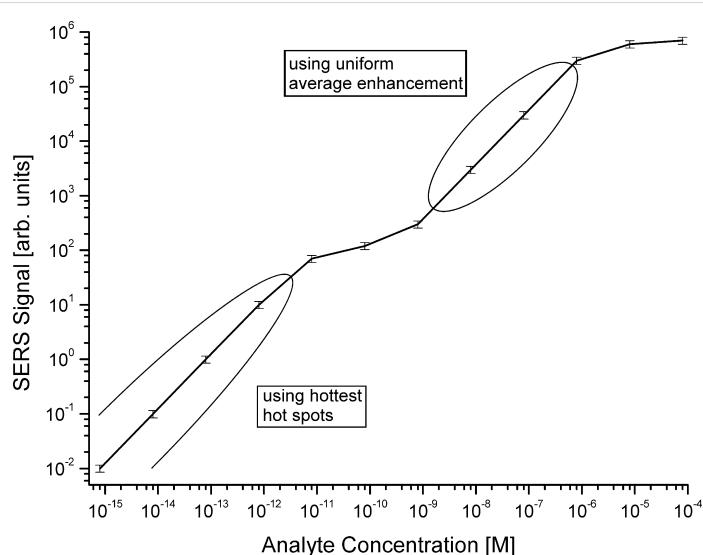
Figure 6: SERS signal of the 1510 cm^{-1} Raman line of rhodamine 6G (see Figure 7) vs concentrations of the molecule between 10^{-15} and 10^{-6} M, excitation at 830 nm.

For illustration, Figure 7 displays two SERS spectra, which were measured at low concentrations of rhodamine 6G molecules. Due to a relatively large scattering volume of approx. 10 nL, these low-concentration SERS spectra are "many molecule spectra" and were collected from ca. 6 000 (spectrum a) and 6 molecules (spectrum b). The silver nanoaggregates move in and out of the probed volume because of Brownian motion. However, for the applied probed volumes (≥10 nL) the number of analyte-loaded nanoaggregates in the probed volume remains statistically constant also at low analyte concentrations.
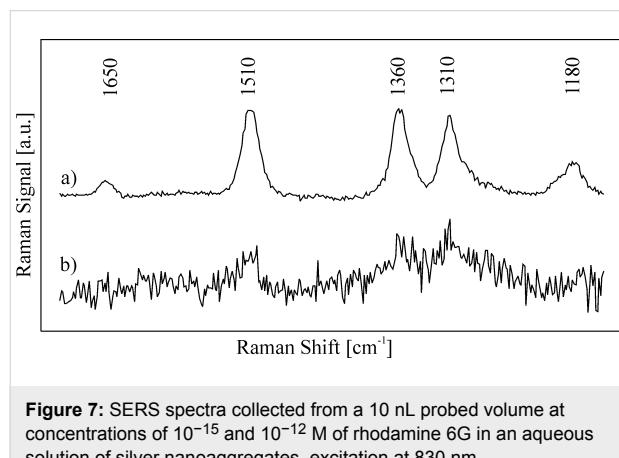
Figure 7: SERS spectra collected from a 10 nL probed volume at concentrations of 10^{-15} and 10^{-12} M of rhodamine 6G in an aqueous solution of silver nanoaggregates, excitation at 830 nm.

Coming back to the plot shown in Figure 6, we can see a linear dependence (slope 1 in the double-logarithmic plot) for analyte concentrations between concentrations of 10^{-15} and 5×10^{-12} M, i.e., which are at least two orders of magnitude below the concentration of the nanoaggregates. In this concentration range with $c_{analyte} \ll c_{nanoagggregate}$, it is statistically unlikely that two molecules are attached to the same aggregate. Each molecule finds its own enhancing nanostructure where it can occupy the hottest hot spots. As we discussed above, high field gradients might direct single molecules to the hottest spots [22,29,38].

Conducting experiments in this low concentration range and reducing the probed volume to a size that only one target molecule or less on average are present in the volume results in a Poisson distribution of the scattering signals measured in time sequence. This statistics reflects the probability of the presence of 0, 1, 2, or 3 molecules in the probed volume during the actual measurement [31-33,47]. Both, the linear increase of the SERS signal vs the concentration of the target molecules in a "many-molecule experiment" displayed in Figure 6 as well as the Poisson distribution of scattering signals in single molecule SERS indicate that each molecule experiences the same extremely high SERS enhancement level, i.e., that molecules reside exclusively in the hottest hot spots.

When the concentration of the target molecule approaches the concentration of the nanoaggregates, the linear relation between the concentration and the SERS signal no longer exists. In this "transition range" statistically more than one molecule can occupy the same nanoaggregate. Experiments show that in the concentration range of the analyte between ca. 10^{-11} and 10^{-9} M, i.e., around a 1:1 concentration of target molecules and nanoaggregates, the SERS signal increases much slower than expected. This indicates that molecules now also start to occupy spots that provide lower enhancement levels at relatively wide intensity distributions. In agreement with losing the linear dependence of SERS power vs analyte concentration at $c_{analyte} \approx c_{nanoagggregate}$, single molecule SERS experiments performed in this concentration range also show no Poisson statistics in the distribution of the measured signals.

For higher concentrations of the analyte with $c_{analyte} \gg c_{nanoagggregate}$, concentrations between ca. 10^{-9} and 10^{-6} M in Figure 6, the SERS signals depend again linearly on the analyte concentrations. Under these conditions, 100–10000 molecules are attached to the same nanoaggregate and experience an average uniform enhancement. This regime is used in numerous applications of SERS for quantitative studies, such as in chemical analysis (see examples in [48]).

The loss of the linear relation between the concentration of the target molecule and the SERS signal at approximately 1:1 concentration between aggregates and molecules indicates that only one molecule per nanoaggregate can experience an extremely high enhancement, i.e., there exists only one hottest hot spot per nanoaggregate of about 100 nm dimension (see Figure 1). Moreover, the hottest spot must have very small dimensions since it provides space for only one molecule. Considering a nanoaggregate at a dimension of ca. 100 nm (Figure 1), its surface area is on the order of 3×10^{-14} m^2 and assuming a hot spot at the dimension of a small molecule, i.e., on the order of 10^{-20} m^2, implies that only 0.00003 % of the surface of the nanoaggregates provide electromagnetic SERS enhancement factors on the order of 10^{12}. For more regular Ag films over nanospheres (AgFON) substrates, it has been found that 0.0003% of the surface provides an enhancement factor larger than 10^{10} [49] and 0.003% exhibit enhancement factors larger than 10^9 [50].

Conclusion

SERS experiments at the single molecule level open up interesting ways for probing the optical near-field in the hottest hot spots of plasmonic nanostructures. Our studies identify field enhancement factors on the order of 10^3 with corresponding electromagnetic SERS enhancement factors on the order of 10^{12} for one-photon excited surface enhanced Raman signals and

10^{18} for two-photon excited surface enhanced hyper Raman signals. In agreement with theory [46], the intensities obtained in the hottest spots of the plasmonic near-field increase with increasing wavelengths. Monitoring the SERS signal while increasing the number of target molecules shows that in the near-field of nanoaggregates composed by 4–8 individual silver particles with dimensions of ca. 100 nm (Figure 1) only one hottest hot spot per nanoaggregate exists and that the dimension of these hottest spots must be in the subnanometer range.

Near-fields are always related to high field gradients. Beyond the capabilities for probing the near-field by SERS discussed previously, SERS studies can also provide interesting ways for probing field gradients. Due to the failure of the assumption that the field is constant over molecular dimensions, new selection rules and polarization behavior in Raman signals can be obtained, which could be used to infer information about field gradients [51].

References

1. Stockman, M. I. *Phys. Today* **2011,** *64,* 39–44. doi:10.1063/1.3554315
2. Novotny, L. *Phys. Today* **2011,** *64,* 47–52. doi:10.1063/PT.3.1167
3. Kneipp, K. *Phys. Today* **2007,** *60,* 40–46. doi:10.1063/1.2812122
4. McMahon, J. M.; Gray, S. K.; Schatz, G. C. *Phys. Rev. B* **2011,** *83,* No. 115428. doi:10.1103/PhysRevB.83.115428
5. Halas, N. J.; Lal, S.; Chang, W.-S.; Link, S.; Nordlander, P. *Chem. Rev.* **2011,** *111,* 3913–3961. doi:10.1021/cr200061k
6. Lee, J.-H.; Nam, J.-M.; Jeon, K.-S.; Lim, D.-K.; Kim, H.; Kwon, S.; Lee, H.; Suh, Y. D. *ACS Nano* **2012,** *6,* 9574–9584. doi:10.1021/nn3028216
7. Yoshida, K.-i.; Itoh, T.; Tamaru, H.; Biju, V.; Ishikawa, M.; Ozaki, Y. *Phys. Rev. B* **2010,** *81,* No. 115406. doi:10.1103/PhysRevB.81.115406
8. Haran, G. *Acc. Chem. Res.* **2010,** *43,* 1135–1143. doi:10.1021/ar100031v
9. Li, K.; Stockman, M. I.; Bergman, D. J. *Phys. Rev. Lett.* **2003,** *91,* 227402. doi:10.1103/PhysRevLett.91.227402
10. Podolskiy, V. A.; Shalaev, V. M. *Laser Phys.* **2001,** *11,* 26–30.
11. Weber, M. L.; Litz, J. P.; Masiello, D. J.; Willets, K. A. *ACS Nano* **2012,** *6,* 1839–1848. doi:10.1021/nn205080q
12. Bharadwaj, P.; Bouhelier, A.; Novotny, L. *Phys. Rev. Lett.* **2011,** *106,* 4. doi:10.1103/PhysRevLett.106.226802
13. Nelayah, J.; Kociak, M.; Stephan, O.; de Abajo, F. J. G.; Tencé, M.; Henrard, L.; Taverna, D.; Pastoriza-Santos, I.; Liz-Marzán, L. M.; Colliex, C. *Nat. Phys.* **2007,** *3,* 348–353. doi:10.1038/nphys575
14. Barwick, B.; Flannigan, D. J.; Zewail, A. H. *Nature* **2009,** *462,* 902–906. doi:10.1038/nature08662
15. Koh, A. L.; Bao, K.; Khan, I.; Smith, W. E.; Kothleitner, G.; Nordlander, P.; Maier, S. A.; McComb, D. W. *ACS Nano* **2009,** *3,* 3015–3022. doi:10.1021/nn900922z
16. Chu, M.-W.; Sharma, P.; Chang, C.-P.; Liou, S. C.; Tsai, K.-T.; Wang, J.-K.; Wang, Y.-L.; Chen, C. H. *Nanotechnology* **2009,** *20,* No. 235705. doi:10.1088/0957-4484/20/23/235705
17. Guiton, B. S.; Iberi, V.; Li, S.; Leonard, D. N.; Parish, C. M.; Kotula, P. G.; Varela, M.; Schatz, G. C.; Pennycook, S. J.; Camden, J. P. *Nano Lett.* **2011,** *11,* 3482–3488. doi:10.1021/nl202027h
18. Kadkhodazadeh, S.; Wagner, J. B.; Joseph, V.; Kneipp, J.; Kneipp, H.; Kneipp, K. *Plasmonics* **2012,** *8,* 763–767. doi:10.1007/s11468-012-9470-1
19. Iberi, V.; Mirsaleh-Kohan, N.; Camden, J. P. *J. Phys. Chem. Lett.* **2013,** *4,* 1070–1078. doi:10.1021/jz302140h
20. Kneipp, K.; Yang, W.; Kneipp, H.; Itzkan, I.; Dasari, R. R.; Feld, M. S. *Phys. Rev. Lett.* **1996,** *76,* 2444–2447. doi:10.1103/PhysRevLett.76.2444
21. Kneipp, K.; Wang, Y.; Kneipp, H.; Perelman, L. T.; Itzkan, I.; Dasari, R. R.; Feld, M. S. *Phys. Rev. Lett.* **1997,** *78,* 1667. doi:10.1103/PhysRevLett.78.1667
22. Kneipp, K.; Kneipp, H.; Kneipp, J. *Acc. Chem. Res.* **2006,** *39,* 443–450. doi:10.1021/ar050107x
23. Dieringer, J. A.; Lettan, R. B.; Scheidt, K. A.; Van Duyne, R. P. *J. Am. Chem. Soc.* **2007,** *129,* 16249–16256. doi:10.1021/ja077243c
24. Nie, S.; Emroy, S. R. *Science* **1997,** *275,* 1102–1106. doi:10.1126/science.275.5303.1102
25. Xu, H. X.; Bjerneld, E. J.; Kall, M.; Borjesson, L. *Phys. Rev. Lett.* **1999,** *83,* 4357–4360. doi:10.1103/PhysRevLett.83.4357
26. Michaels, A. M.; Jiang, J.; Brus, L. *J. Phys. Chem. B* **2000,** *104,* 11965–11971. doi:10.1021/jp0025476
27. Meixner, A. J.; Vosgrone, T.; Sackrow, M. *J. Lumin.* **2001,** *94,* 147–152. doi:10.1016/S0022-2313(01)00248-4
28. Moula, G.; Rodriguez-Oliveros, R.; Albella, P.; Sanchez-Gil, J. A.; Aroca, R. F. *Ann. Phys. (Berlin, Ger.)* **2012,** *524,* 697–704. doi:10.1002/andp.201200149
29. Kneipp, K.; Kneipp, H. *Appl. Spectrosc.* **2006,** *60,* 322A–334A. doi:10.1366/000370206779321418
30. Pettinger, B.; Schambach, P.; Villagómez, C. J.; Scott, N. *Annu. Rev. Phys. Chem.* **2012,** *63,* 379–399. doi:10.1146/annurev-physchem-032511-143807
31. Kneipp, K.; Kneipp, H.; Manoharan, R.; Hanlon, E. B.; Itzkan, I.; Dasari, R. R.; Feld, M. S. *Appl. Spectrosc.* **1998,** *52,* 1493–14987. doi:10.1366/0003702981943059
32. Kneipp, K.; Kneipp, H.; Deinum, G.; Itzkan, I.; Dasari, R. R.; Feld, M. S. *Appl. Spectrosc.* **1998,** *52,* 175–178. doi:10.1366/0003702981943275
33. Kneipp, K.; Kneipp, H.; Kartha, V. B.; Manoharan, R.; Deinum, G.; Itzkan, I.; Dasari, R. R.; Feld, M. S. *Phys. Rev. E* **1998,** *57,* R6281–R6284. doi:10.1103/PhysRevE.57.R6281
34. Maruyama, Y.; Ishikawa, M.; Futamata, M. *Chem. Lett.* **2001,** 834–835. doi:10.1246/cl.2001.834
35. Blackie, E. J.; Le Ru, E. C.; Etchegoin, P. G. *J. Am. Chem. Soc.* **2009,** *131,* 14466–14472. doi:10.1021/ja905319w
36. Treffer, R.; Lin, X. M.; Bailo, E.; Deckert-Gaudig, T.; Deckert, V. *Beilstein J. Nanotechnol.* **2011,** *2,* 628–637. doi:10.3762/bjnano.2.66
37. Lee, P. C.; Meisel, D. *J. Phys. Chem.* **1982,** *86,* 3391–3395. doi:10.1021/j100214a025
38. Xu, H.; Käll, M. *Phys. Rev. Lett.* **2002,** *89,* No. 246802. doi:10.1103/PhysRevLett.89.246802
39. Kneipp, K.; Kneipp, H.; Itzkan, I.; Dasari, R. R.; Feld, M. S. *Chem. Rev.* **1999,** *99,* 2957–2975. doi:10.1021/cr980133r
40. Kozich, V.; Werncke, W. *J. Phys. Chem. C* **2010,** *114,* 10484–10488. doi:10.1021/jp101219e
41. Otto, A. In *Light scattering in solids IV. Electronic scattering, spin effects, SERS and morphic effects;* Cardona, M.; Guntherodt, G., Eds.; Springer-Verlag: Berlin, Germany; pp 289–418. doi:10.1007/3-540-11942-6_24
42. Campion, A.; Kambhampati, P. *Chem. Soc. Rev.* **1998,** *27,* 241–250. doi:10.1039/a827241z

43. Kleinman, S. L.; Sharma, B.; Blaber, M. G.; Henry, A.-I.; Valley, N.; Freeman, R. G.; Natan, M. J.; Schatz, G. C.; Van Duyne, R. P. *J. Am. Chem. Soc.* **2013,** *135,* 301–308. doi:10.1021/ja309300d

44. Kneipp, K.; Kneipp, H.; Itzkan, I.; Dasari, R. R.; Feld, M. S.; Dresselhaus, M. S. In *Optical Properties of Nanostructured Random Media;* Shalaev, V. M., Ed.; Topics in Applied Physics, Vol. 82; Springer-Verlag: Berlin, Germany, 2002; pp 227–247.

45. Kneipp, J.; Kneipp, H.; Kneipp, K. *Proc. Natl. Acad. Sci. U. S. A.* **2006,** *103,* 17149–17153. doi:10.1073/pnas.0608262103

46. Stockman, M. I. In *Surface-Enhanced Raman Scattering: Physics and Applications;* Kneipp, K.; Moskovits, M.; Kneipp, H., Eds.; Topics in Applied Physics, Vol. 103; Springer-Verlag: Berlin, Germany, 2006; pp 47–65.

47. Zhou, Z.; Wang, G.; Xu, Z. *Appl. Phys. Lett.* **2006,** *88,* 034104. doi:10.1063/1.2166474

48. McNay, G.; Eustace, D.; Smith, W. E.; Faulds, K.; Graham, D. *Appl. Spectrosc.* **2011,** *65,* 825–837. doi:10.1366/11-06365

49. Fang, Y.; Seong, N.-H.; Dlott, D. D. *Science* **2008,** *321,* 388–392. doi:10.1126/science.1159499

50. Chien, F. C.; Huang, W. Y.; Shiu, J.-Y.; Kuo, C. W.; Chen, P. L. *Opt. Express* **2009,** *17,* 13974–13981. doi:10.1364/OE.17.013974

51. Ayars, E. J.; Hallen, H. D.; Jahncke, C. L. *Phys. Rev. Lett.* **2000,** *85,* 4180–4183. doi:10.1103/PhysRevLett.85.4180

Dye-doped spheres with plasmonic semi-shells: Lasing modes and scattering at realistic gain levels

Nikita Arnold[*], Boyang Ding[§], Calin Hrelescu and Thomas A. Klar

Abstract

We numerically simulate the compensation of absorption, the near-field enhancement as well as the differential far-field scattering cross section for dye-doped polystyrene spheres (radius 195 nm), which are half-covered by a silver layer of 10–40 nm thickness. Such silver capped spheres are interesting candidates for nanoplasmonic lasers, so-called spasers. We find that spasing requires gain levels less than 3.7 times higher than those in commercially available dye-doped spheres. However, commercially available concentrations are already apt to achieve negative absorption, and to narrow and enhance scattering by higher order modes. Narrowing of the plasmonic modes by gain also makes visible higher order modes, which are normally obscured by the broad spectral features of the lower order modes. We further show that the angular distribution of the far-field scattering of the spasing modes is by no means dipole-like and is very sensitive to the geometry of the structure.

Introduction

Noble metal nanoparticles are of current interest both in fundamental and applied science because of their localized plasmonic resonances (LPR) in the visible and near infrared range of the optical spectrum. The simplest nanoparticle geometry is spherical, but the spectral position of the nanoparticle plasmon of a solid sphere can only be tuned by increasing its radius (given a specific refractive index of the embedding medium), which leads to a redshift with increasing radius [1]. The price one has to pay for this size-based wavelength-tuning is,

however, a substantial spectral broadening due to radiative damping. An alternative way to tune the LPR spectrally is to change the shape of the nanoparticle. First, one can relax the radial homogeneity of the nanoparticle and turn from solid nanoparticles to noble metal nanoshells [2,3]. Second, one can also relax the angular symmetry and turn from nanoshells with spherical symmetry to semi-shells, sometimes also called nano-caps or nano-cups. Such semi-shells can be produced either via the evaporation of noble metals on top of dielectric spheres

[4-6], via the electrochemical deposition through a self-assembled template of dielectric spheres [7], via the attachment of seed particles to dielectric spheres that are partially embedded in a polymer matrix and a subsequent electroless plating [8], or via opening holes in originally closed shells via e-beam sputtering [9] or ion beam milling [10].

The semi-shells show a rich spectrum of localized plasmon resonance modes that was investigated analytically and numerically [11-13]. It became common to label the different modes according to the symmetries of the modes of the spherically symmetric closed metallic shells. The semi-shell modes can be derived from the closed-shell modes by slowly opening the closed shell. Labeling is hence carried out by using the multipolar and azimuthal numbers (l,m) [7,11]. While in a spherically symmetric shell, each multipolar mode is $(2l+1)$ times degenerate, the symmetry breaking that is introduced by opening a hole in the shell not only lifts this degeneracy, but also introduces a further mode splitting via the coupling of the shell plasmons with the rim plasmon modes of the circular opening [11]. The excitability of the localized plasmon modes depends on the polar and azimuthal angles of the direction of illumination and on the orientation of the electric field vector. In a recent experimental work, some of the most prominent eigenmodes of metallic voids have been imaged using a near-field microscope [14]. A further prominent feature of semi-shells with broken symmetry (compared to angularly symmetric shells) is their capability to scatter light preferentially into certain directions [15,16]. Recently, we have shown that localized plasmonic modes of the semi-shells are apt to direct the fluorescence from the dyes contained in their dielectric cores into the forward direction [17]. Plasmonic semi-shells or nanovoids have also been used for important applications such as biosensing [18], plasmon-enhanced solar cells [19,20], or as substrates for surface-enhanced Raman scattering [21,22] and coherent anti-Stokes Raman scattering [23].

A severe problem for all plasmonic applications is the damping of plasmons due to Ohmic losses in the metal and due to radiative losses. However, a solution for this dilemma is possible because plasmons are Bosons and can hence be emitted via stimulated emission [24]. This might be used to minimize losses in metamaterials [25,26] and it has also been proposed for the compensation of losses in plasmonic shells [27,28]. Loss-compensation in the case of solid gold nanospheres embedded in a gain medium has been experimentally verified by Noginov et al. [29] and more recently confirmed by Strangi et al. [30]. The cancellation of the losses in hybrid materials that comprise resonant nanoparticle plasmons and gain materials finally leads to a self-sustaining laser-like generator called the spaser [31-36]. In this contribution, we find that there is a finite range of gain values in which the absorption is overcompensated within a certain wavelength region, but the spaser does not self-start yet. The existence of such a finite range has been debated before [37-41].

A true nano-spaser based on localized plasmons should be sub-wavelength confined in all three dimensions (3D). Experimentalists approached such 3D nano-spasers within the last few years [42-48]. The smallest nano-spaser so far has been claimed by a team around Noginov, Shalaev and Wiesner [49] who reported that gold nanoparticles with a diameter of 14 nm, covered by a silica shell of 15 nm thickness, doped with the dye OG-488 show laser emission. The nanostructures reported in this experimental study were, however, fully spherically symmetric. Very recently, it has been proposed that symmetry breaking might have advantages because a low gain threshold is required [50] and the coherent emission becomes directional [51]. In both theoretical papers, a geometry was assumed, in which a dye-doped dielectric sphere was covered by a semi-shell of noble metals.

The authors of [50,51] assumed metal-capped and dye-doped spheres comprising a spectrally flat, dispersion-less gain. This does not reflect realistic dye molecules, which provide gain only within a limited spectral range. However, it is a useful approach to search for the spectral mode that will lase most easily. In this work, we would like to take the complementary approach by starting with two given Lorentzian lines for the molecular absorption and the Stokes-shifted emission of a given realistic dye molecule that fluoresces in the visible region. We tune specific plasmonic resonances into the emission maximum of the dye molecules by adjusting the thickness of the silver caps on the dye-doped spheres. In particular, we assume a doping concentration, a size of the spheres and the type of dye molecules as given by the commercially available polystyrene spheres "Firefli* Fluorescent Green" from Thermo-Scientific, Waltham, MA, USA, which we have used in an experimental study on the spectral and directional Purcell effect [17]. With this self-restriction to the parameters of commercially available dye-doped spheres, we make a realistic estimate of how far away one is from nanoparticle spasing (we find: a factor of 3.7 in necessary gain, only) and which other effects, such as a spectral narrowing of the scattering cross section or a change in absorption should already be observable in the case of the available gain. We find that narrowing of the Mie scattering spectrum and small signal gain could become detectable.

Numerical modeling

Figure 1 depicts the geometry of the silver capped spheres and the orientation of the incoming electromagnetic wave. A dye-doped polystyrene (PS) sphere of 390 nm diameter is capped

with a semi-shell of silver. The coordinate system is fixed such that the z-axis defines the axis of rotational symmetry of the semi-shell and points inwards into the metallic cap. The direction of the *k*-vector of the linearly polarized plane wave is given by two spherical angles (θ,φ) in which θ denotes the polar angle between the *k*-vector and the z axis, and φ denotes the azimuthal angle in the x–y plane. The electric field always remains in the x–z plane. In particular, the (0,0) direction denotes an illumination from the open, uncovered side of the PS sphere (as shown in Figure 1), while (180,0) denotes an illumination from the silver-capped side and (90,0) denotes an illumination from the side, in which the electric field is parallel to the z-axis such that axial plasmonic modes can be excited. The thickness of the silver shell and the concentration of the dye molecules are varied throughout the paper.

Figure 1: Geometry of the sphere and the illuminating plane wave. The *k*-vector of the plane wave is defined by (θ,φ), in which θ denotes the angle between the *k*-vector and z axis and φ is the polar angle counted from the x-axis. The shown geometry hence depicts the (0,0) illumination.
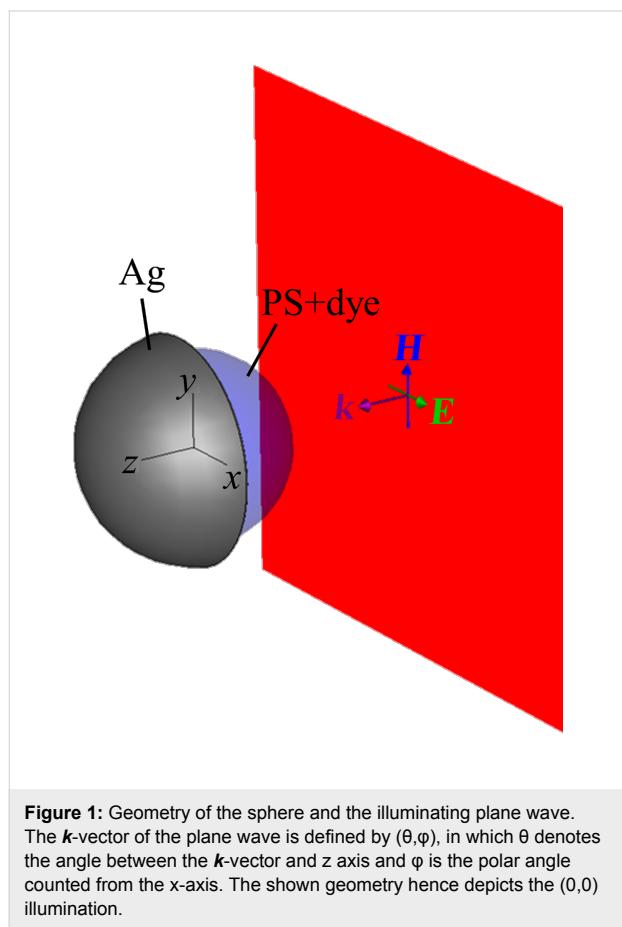
Realistic modeling of 3D plasmonic structures with gain in the visible-light range is non-trivial and requires certain care. As mentioned before, semi-shell structures possess many multipolar eigenmodes that are located closely together in frequency space [11], and many of the modes are easily overlooked when modeling is carried out without gain, because they are strongly damped because of the dispersion of the metal. If, however,

damping is compensated by gain, the modes might become ultra-sharp and can still be overlooked if they are narrower than the frequency step used in simulations. The situation is somewhat similar to the scattering by weakly dissipating plasmonic spheres, in which very narrow higher order resonances can dominate [52]. These effects are even more pronounced for the anisotropic dielectric permittivity with transverse or longitudinal gain [53]. Computational details are discussed in the section "Numerical" at the end of the paper.

The dielectric constant of silver was taken from Johnson and Christy [54]. The dielectric constant of the gain material was described by a double Lorentzian function:

$$\varepsilon_{\text{Sphere}} = \varepsilon_{\text{PS}} + A \cdot \Delta\varepsilon_{\text{Dye}} \frac{\omega_{\text{abs}}^2}{\omega_{\text{abs}}^2 - \omega^2 - i\omega\gamma}$$
$$-E \cdot \Delta\varepsilon_{\text{Dye}} \frac{\omega_{\text{em}}^2}{\omega_{\text{em}}^2 - \omega^2 - i\omega\gamma} \tag{1}$$

The coefficient $\Delta\varepsilon_{\text{Dye}}$ describes the strength of the transition (for the time being the same strength of absorption and emission is assumed [55]), $\omega_{\text{abs}} = 4.02 \cdot 10^{15}$ s^{-1} (468 nm) and $\omega_{\text{em}} = 3.67 \cdot 10^{15}$ s^{-1} (513 nm), $\gamma = 5.0 \cdot 10^{14}$ s^{-1} ($\Delta\lambda_{\text{FWHM}} \approx$ 60 nm), and we assume a purely real $\varepsilon_{\text{PS}} = 2.6$ for polystyrene. The coefficient A is set to "1" and the coefficient E is set to "0" if we assume a purely absorbing medium (all dye molecules in the ground state) and A = 0, E = 1 in case of a fully inverted medium. Coefficients between 0 and 1 are used to simulate partial inversions, in which A + E = 1 holds.

Unsaturated Lorentzian gain does not allow for simulations very close to the lasing threshold (leading to unphysical infinite scattering cross sections and a diverging gain [36,56]), nor does it have much of a physical meaning beyond the threshold in CW operation. However, a classical electromagnetic calculation with a Lorentzian gain is fully legitimate as long as the lasing threshold is approached from below [36]. Here, we define the extinction cross section as $\sigma_{\text{ex}} = \sigma_{\text{sc}} + \sigma_{\text{ab}}$, irrespectively of the sign of σ_{ab}.

To get realistic simulation parameters, we determined the chromophore density in dye-doped polystyrene (PS) spheres, which are commercially available from Thermo-Scientific (Waltham, MA, USA). Those spheres are doped with "Firefli* Fluorescent Green" dye with an absorption peak near 468 nm and an emission peak at 513 nm. The concentration of the dye molecules inside the PS spheres was derived by taking the optical density (OD) of a solution of dye-doped spheres and subtracting the scattering component of the OD. The concentration of the

spheres was quantified by measuring the scattering strength at a wavelength far from the absorption of the dyes. From this, we estimated an absorption constant in the range of 2300 cm^{-1}, which translates into a transition strength of $\Delta\varepsilon_{Dye} = 0.004$. In the simulations, we often considered cases of pure absorption or pure emission, which correspond to the cases in which all the dye molecules are in the absorbing ground state or all dye molecules are in the emitting state respectively (full inversion, which is achievable in a four level system). We also considered a 50/50 combination of two Lorentzian lines, which corresponds to half of the chromophores being excited (A = E = 1/2 in Equation 1). For the dye concentration of these commercially available PS spheres, we do not observe any spasing, yet. Hence, we also considered substantially higher dye concentrations, i.e., we applied $\Delta\varepsilon_{Dye} > 0.004$. Primarily for didactical reasons we also went to dye concentrations beyond the lasing threshold. As a reference, the peak of the imaginary part of the dielectric constant ε''_{max} is related to $\Delta\varepsilon_{Dye}$ at the central emission wavelength via the equation $\varepsilon''_{max} = \Delta\varepsilon_{Dye} \cdot \omega_{em}/\gamma = 7.34\ \Delta\varepsilon_{Dye}$.

Results and Discussion
Matching the plasmonic resonance to the gain spectrum

Before we include the gain material in the calculations, we tune the plasmonic resonance of the semi-shells to overlap with the emission band of the fluorophores by adjusting the thickness h of the silver caps on the undoped PS spheres of 390 nm diameter. Figure 2 shows the extinction, scattering, and absorption spectra in panels a,b,c, respectively, for thicknesses varying from $h = 10$ to 40 nm as indicated by the color coding. The linearly polarized, electromagnetic plane wave impinges the structure from the "open sphere side", i.e., in the (0,0) direction as depicted in Figure 1. In Figure 2d all three cross sections are compared for the specific sample with $h = 20$ nm, showing that the total extinction spectrum is dominated by the scattering. However, the most prominent resonances are seen in the absorption spectra. On the black curve ($h = 10$ nm) in Figure 2c, one clearly sees several plasmonic maxima, for which the maxima become sharper with decreasing wavelength. When the thickness of the semi-shells is decreased, the series of absorp-
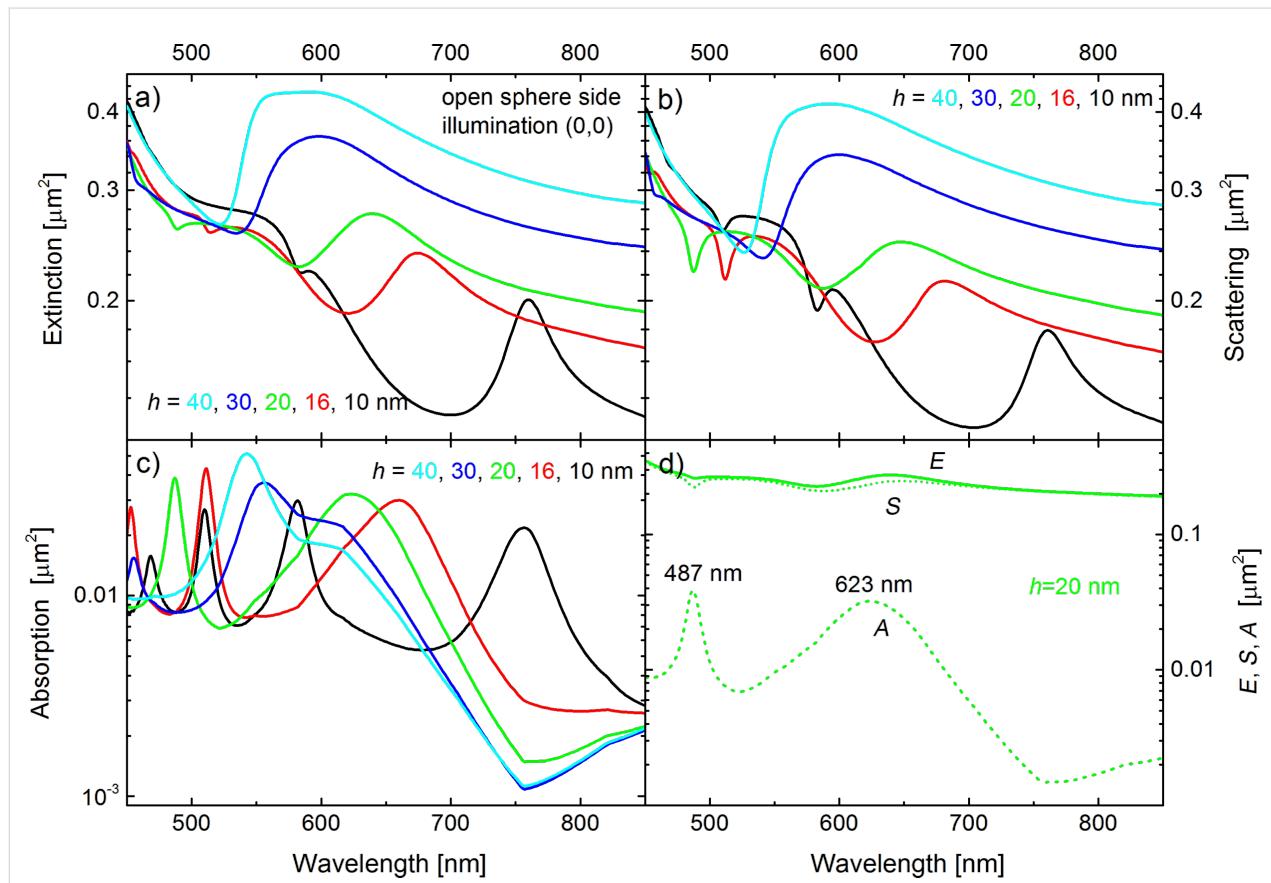
Figure 2: Cross sections of the (a) extinction, (b) scattering and (c) absorption of a PS sphere of diameter $d = 390$ nm, without fluorophores, and capped with a Ag semi-shell of variable thickness h, as given by the color coding. The incident plane wave was oriented in (0,0) direction, i.e., impinging from the open sphere side. The plasmonic resonances are most prominent in the absorption spectra. (d) compares the extinction (E), scattering (S) and absorption (A) spectra for the specific shell thickness $h = 20$ nm.

tion peaks shifts to the red. For instance, the peak near 510 nm corresponds to the third resonance (counted from the long wavelength side) in the case of the 10 nm thick semi-shell (black curve), but to the second resonance in the case of 16 nm thickness (red curve). At a closer look, one can observe some minor peaks, sometimes masked as a shoulder of a main peak. The spectrum of resonances is quite rich and it is not straightforward to assign a specific (l,m) mode to the peaks, which will become clearer later, when we use gain to sharpen the resonances. Only the longest-wavelength mode can safely be assigned to an $l = 1$ mode.

Figure 3 shows the mode profiles in case of the semi-shell with $h = 20$ nm. Specifically, it shows an $l = 1$ and an $l = 2$ mode with resonances in the absorption spectra at 623 and 487 nm, respectively (c.f. Figure 2d). The upper panels in Figure 3 show the field enhancement $|\boldsymbol{E}|/E_0$, in which E_0 is the amplitude of the electric field in the incident plane wave. The images are cut in the x–z plane, i.e., the plane spanned by the $\boldsymbol{k}$-vector (z-axis)

and the polarization of the electric field (x-axis). A three dimensional representation of the near field enhancement just outside the semi-shell structure is given on the lower left of both panels. At 623 nm, the plasmonic mode of the semi-shell can be derived from a pure dipolar resonance if the shell was not a semi-shell but a fully closed shell. Hence it is termed an $l = 1$ resonance [11]. Because of the opening of the semi-shell (with respect to the closed shell), the $l = 1$ resonances loose degeneracy and the mode depicted in Figure 3a is the transverse $l = 1$ mode (the axial mode is not excitable by a plane wave in the (0,0) direction) [16]. The mode at 487 nm is essentially an $l = 2$ mode. Both modes are constructively coupled to the rim mode [11] and originate from the long-wavelength l modes of the full shell [57]. The lower right graphs are polar graphs of the differential scattering cross section.

Figure 4 shows the extinction, scattering, and absorption cross sections of the $h = 20$ nm semi-shell structure for different illumination directions. The cross sections for the (0,0) direction


Figure 3: Mode characteristics of the two absorption maxima in Figure 2d ((0,0), i.e., sphere side illumination, $h = 20$ nm), at $\lambda = 623$ (a) and 487 nm (b). The upper images show the field enhancement $|\boldsymbol{E}|/E_0$ in the propagation–polarization x–z plane. The 3D graphs on the lower left of (a) and (b) show $|\boldsymbol{E}|/E_0$ in air near the surface of the semi-shell, i.e., the near-field just outside the structure. The mode at 623 nm is a "void like" dipolar mode ($l = 1$), while the mode at 487 nm is a $l = 2$ mode. The 3D spherical plots show the differential scattering cross sections on a linear scale. The maximum of the differential and the total σ_{sc} are given in the legends.

Figure 4: Dependence of the cross sections of the semi-shell structure with a core diameter *d* = 390 nm and a Ag thickness *h* = 20 nm on the direction of irradiation. Illumination from the open sphere side (0,0) (black curve), or from the Ag-capped side (180,0) (red curve), or from the sphere side with the plane wave impinging under the oblique angles θ = 41.4°, φ = 54.2° with the electric field in the x–z plane (green curve). Other parameters and notations are the same as in Figure 1. Illumination under oblique angles leads to many more resonances because of the loss of degeneracy by cylindrical symmetry.

(illumination from the open sphere side) are redrawn from Figure 2d for comparison (black curves). Red curves correspond to illumination from the silver capped side, along the negative z-axis (180,0). Further, we compare both results with the cross sections obtained by an illumination under the oblique angles (41.4, 54.2). These angles sound a bit arbitrary, but they are equivalent to two consecutive rotations of the structure by −30° about the x- and y- axes, while leaving the incident wave intact. We see that the extinction cross sections of the sphere side (0,0) and the cap side (180,0) coincide, while the absorption and scattering cross sections differ in magnitude but not in the spectral shape. In contrast, there is a significant difference in the spectral shape for the (41.4, 54.2) orientation. Two new resonances appear (between 700 and 800 nm), the main resonance at 640 nm disappears in the scattering spectrum (while still being visible at 623 nm in the absorption). A clear absorption peak appears at 545 nm where there was only a weak shoulder under (0,0) or (180, 0) illumination, however, the *l* = 2 absorption peak at 487 nm is similar to what we observed for the (0,0) direction. This is an important finding, because we will

spectrally overlap this *l* = 2 absorption peak with the emission line of the dye molecules in the subsequent sections of the paper. Figure 4d compares the extinction, scattering, and absorption cross sections for the case of the oblique incidence.

Plasmons supported by gain

In order to fine-tune the *l* = 2 absorption peak to the emission line of the dye molecules, we plot the corresponding negative $Im(\varepsilon_{Sphere})$ into Figure 5c together with the absorption peaks of the semi-shells with thicknesses between 14 and 20 nm. As the shell thickness varies, the *l* = 2 absorption peak scans across the dye emission line. Figure 5a and Figure 5b show the corresponding extinction and the scattering cross sections and Figure 5d shows all three cross sections for the case of *h* = 16 nm. For all calculations shown in Figure 5 we used a dielectric constant ε_{sphere} defined in Equation 1, which includes the contribution of the dye molecules to the dielectric constant. The dotted line in Figure 5c represents $Im(\varepsilon_{Sphere})$. We used $\Delta\varepsilon_{Dye} = 0.004$ and ω_{em} matching the center of the emission line at λ = 513 nm. We further used A = 0 and E = 1 in Equation 1,
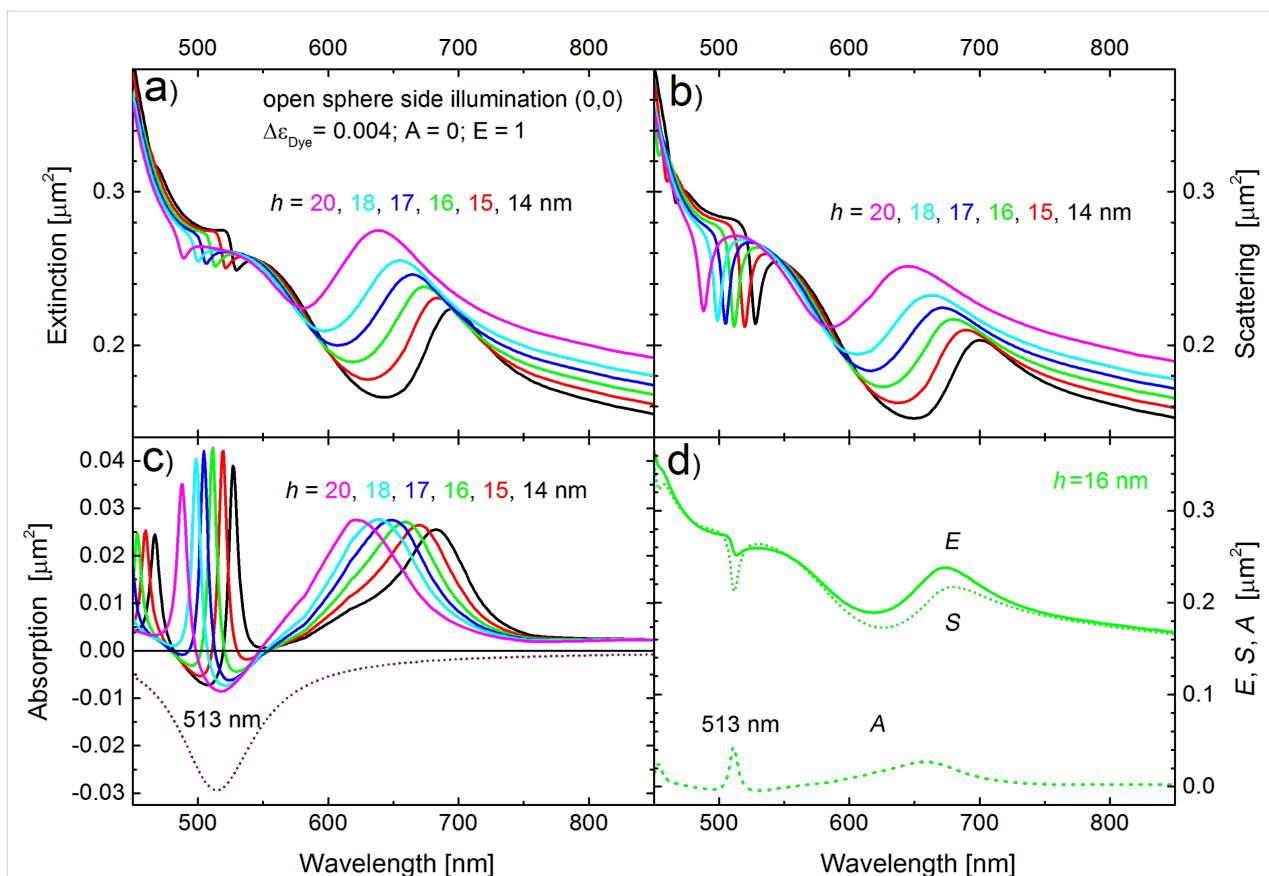
Figure 5: Fine-tuning of the Ag semi-shell resonances to the emission band of the dye. Parameters and the organization of panels a–d are the same as in Figure 2 apart from the thickness *h*, color coded in the plots, and ε_{Sphere} from Equation 1, which now includes dye molecules. Dimensionless values of $Im(\varepsilon_{Sphere})$ are shown in panel (c) by a dotted curve.

which correspond to a full inversion of all dye molecules inside the PS spheres. This results in a negative absorption of our composite structure over a considerable spectral range. When *h* = 16 nm (green curves in Figure 5a–c) the *l* = 2 absorption resonance perfectly coincides with the center of the emission line at 513 nm. Besides, the absorption peak is the largest and the scattering is the lowest for this specific shell thickness as compared to the other thicknesses. We note in passing that the absorption cross sections in Figure 5c become negative for some wavelengths around the *l* = 2 peak at 513 nm and for $\Delta\varepsilon_{Dye}$ = 0.004. We will discuss this in more detail at the end of this paper. Figure 5d shows the extinction (*E*, solid curve), scattering (*S*, dotted) and absorption (*A*, dashed) cross sections for the semi-shell thickness *h* = 16 nm.

We now vary the amount of the active dye material inside the PS spheres in the simulations. Figure 6a–c shows the extinction, scattering, and absorption cross sections, respectively, for the case of a semi-shell thickness *h* = 16 nm, for which the emission line of the dye molecules and the absorption resonance of the semis-shell structures coincide. The strengths $\Delta\varepsilon_{Dye}$ of the

absorption (a Lorentzian curve peaked at 468 nm) and the gain (a Lorentzian curve peaked at 513 nm) are color-coded as shown in the inset of Figure 6b. Hence, the cross sections of the undoped semi-shell structures are given by the black curve ($\Delta\varepsilon_{Dye}$ = 0), the case of a purely absorbing commercially available PS sphere ($\Delta\varepsilon_{Dye}$ = 0.004, A =1, E = 0 in Equation 1) is given by the red line, the fully inverted case is given by the dark blue curve and the 50% inverted case by the green curve. The cyan, magenta, purple, and olive curves correspond to PS spheres that are hypothetically doped with fully inverted dye molecules to yield E $\Delta\varepsilon_{Dye}$ = 0.010, 0.015, 0.020, and 0.030, respectively. $Im(\varepsilon_{Sphere})$ is plotted into Figure 6c as a dotted curve for $\Delta\varepsilon_{Dye}$ = 0.004, A = 0 and E = 1.

The onset of lasing is given by singularities in the absorption and scattering cross sections and occurs near $\Delta\varepsilon_{Dye}$ = 0.0146, which means at concentrations less than 3.7 times larger than available in commercial PS spheres. Hence, we conclude that lasing should be possible in custom made PS spheres with a moderately enhanced dye concentration. No lasing is observed yet at the commercially available gain strength of
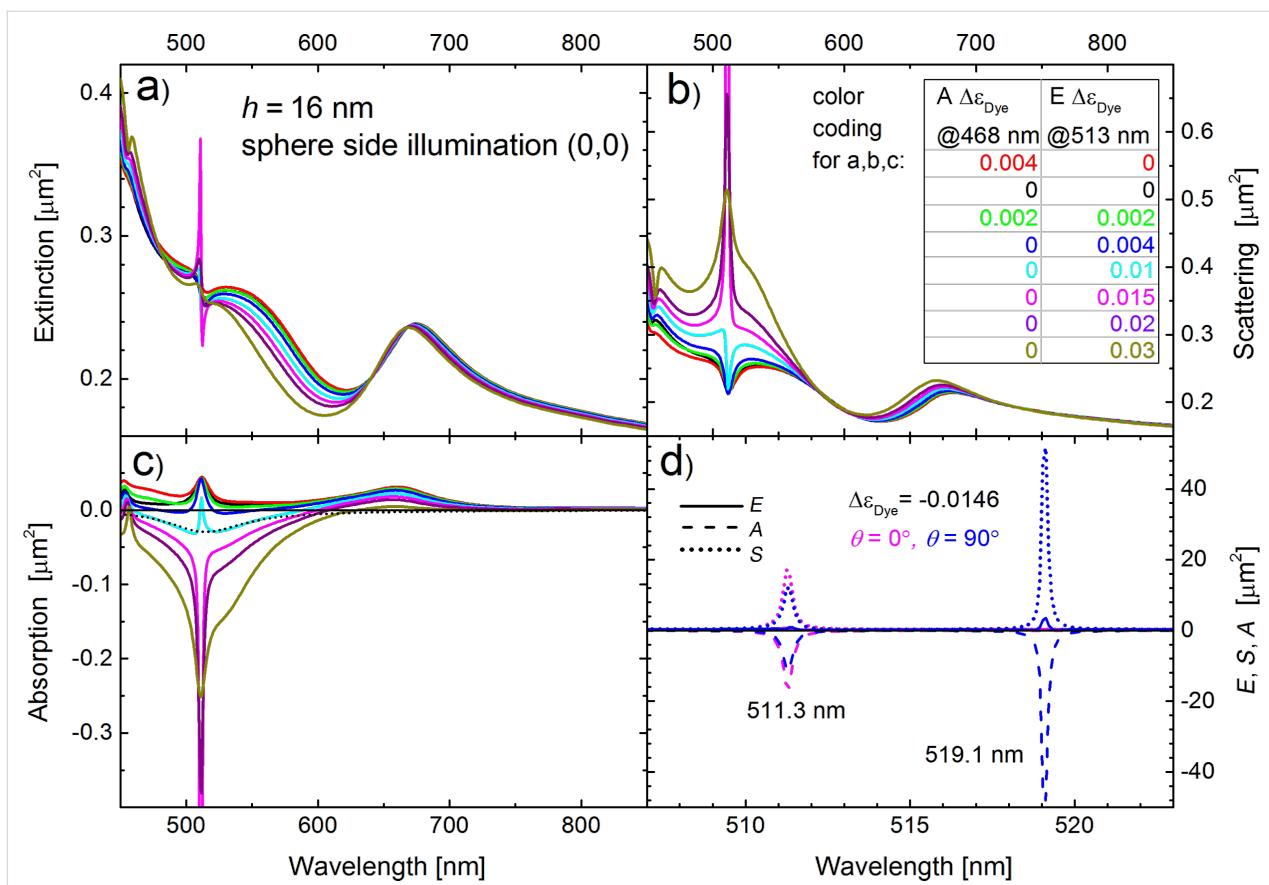
Figure 6: Approach to lasing for a semi-shell thickness of h = 16 nm. Parameters and order of panels a,b,c are the same as in Figure 2. The strengths of the absorption and the gain (cf. Equation 1) are color-coded as shown in the inset of (b). The dimensionless $\mathrm{Im}(\varepsilon_{\mathrm{Sphere}})$ is shown in (c) by the dotted curve. Panel (d) shows a zoom of the extinction (solid curves), scattering (dotted) and absorption (dashed) spectra near the lasing threshold ($\Delta\varepsilon_{\mathrm{Dye}}$ = 0.0146, A = 0, E = 1) close to the l = 2 resonance. The magenta lines refer to the sphere side irradiation (0,0), while the blue lines are calculated for an illumination from the x-direction (θ = 90°, φ = 0°) so that the incident light is polarized in axial z-direction. In this case a second resonance appears near 519 nm, in addition to the resonance near 511 nm, which exists for both orientations.

$\Delta\varepsilon_{\mathrm{Dye}}$ = 0.004, but the absorption cross section becomes slightly negative in the vicinity of the absorption peak (discussed in more detail below). When approaching laser threshold, the full width at half maximum (FWHM) of the scattering and absorption peaks goes to zero [51], which is an artifact of the purely classical calculation. Nevertheless, this singularity in cross sections indicates the transition from an amplifier to self-sustained lasing. A CW operation of a nano-spaser above the threshold ($\Delta\varepsilon_{\mathrm{Dye}}$ > 0.0146) is possible only with continuous pumping, in which the field strength and linewidth are dictated by the gain saturation and spontaneous emission noise [36,56,58]. We do not discuss the thermal stability of such a system, which is strongly material-dependent.

In panels a–c of Figure 6, only the (0,0) illumination direction (open sphere side) is considered. Figure 6d compares the (0,0) direction (magenta curves) with the (90,0) direction (blue curves), in which the electric field is now polarized along the z-axis and hence allows for the excitation of axial cap plas-

mons. Note that the abscissa is zoomed in to span 507 to 523 nm, and the ordinate is enlarged to span −50 to 55 μm² in order to show the almost diverging peaks for $\Delta\varepsilon_{\mathrm{Dye}}$ = 0.0146. The solid lines in Figure 6d are the extinction cross sections, the dashed lines the absorption and the dotted lines the scattering cross sections. One clearly sees that the resonance at 511.3 nm is strongly excited in both cases, for (0,0) and for (90,0) illumination. However, a second resonance at 519.1 nm appears for the (90,0) illumination, which is not excitable with (0,0) illumination for symmetry reasons. We note that only because of the substantially narrowed spectral lines (due to gain), both resonances are discernible. Without gain, both peaks merge because of the relatively broad width of the damped plasmonic resonances (cf. Figure 5b and Figure 5c). The marginal spectral shift from 513 nm for $\Delta\varepsilon_{\mathrm{Dye}}$ = 0.004 (Figure 5d) to 511.3 nm in case of the lasing gain of $\Delta\varepsilon_{\mathrm{Dye}}$ = 0.015 can be attributed to slight differences in the dielectric constant (Equation 1) of the PS sphere near the resonance for different gain levels, as well as to numerical discretization issues.

In order to investigate the spasing modes in more detail, we plot the differential scattering cross sections in Figure 7 for the case of (0,0) illumination and for the cases of no dye molecules (Figure 7a), a currently commercially available concentration (Figure 7b) and for a dye doping close to the lasing threshold (Figure 7c). We plot the cross sections close to the resonances at 513 nm (Figure 7a and Figure 7b) and 511.3 nm (Figure 7c). While the differential scattering cross sections in case of undoped spheres (Figure 7a) and spheres doped with available concentrations (Figure 7b) look very similar and show Mie-type forward scattering, the pattern completely changes near the lasing threshold (Figure 7c). Here, the light is scattered predominantly in two lobes in the x–z plane, which point backward in z-direction (remember that the incident wave is along the positive z-direction). Further, the total scattering cross section is approx. 0.2 μm^2 in case of no dye doping and commercially available doping, but increases significantly to approx. 17.1 μm^2 close to the lasing threshold [29].

Figure 8 shows the (near-)field enhancement $|\boldsymbol{E}|/E_0$ close to the semi-shell structure and the differential scattering cross sections in the case of (90,0) illumination, for a near-threshold gain (A = 0, E = 1) and for the two resonances (cf. Figure 6d, blue curves). Figure 8a and Figure 8b are calculated at 511.3 nm, close to the first spasing peak, and Figure 8c, and Figure 8d are calculated at 519.1 nm, close to the second peak that cannot be excited with (0,0) illumination. While the near-field distribution for the peak at 511.3 nm (Figure 8a) looks very similar (but with much stronger fields) to the case of the undoped semi-shell structure (Figure 3b), the near field distribution at 519.1 nm (Figure 8c) looks very different and resembles an (l = 3, m = 3) orbital. Clearly, this eigen-resonance is easily overlooked in experiments, in which semi-shells with insufficient or no gain are investigated because it would be hidden within the natural width of the l = 2 resonance at 513 nm, and it can also be overlooked in numerical calculations because the wavelength stepping needs to be small enough not to miss it.

The mode at 511.3 nm can be excited with both the (0,0) and the (90,0) illumination directions. Hence we can compare the scattering diagrams for both cases at a gain close to threshold (Figure 7c and Figure 8b, respectively). The total scattering cross section is larger in the case of the (0,0) illumination than for the (90,0) direction (17.1 μm^2 versus 12.3 μm^2, respectively), but the angular distributions look very similar. In stark contrast, the 519.1 nm mode, which is excitable only through (90,0) illumination, shows a decisively different far-field scattering distribution (Figure 8d). It is also worth mentioning that the near-field distributions (Figure 3b, Figure 8a, Figure 8c) look very different to the far-field differential cross sections (Figure 7c, Figure 8b, Figure 8d).
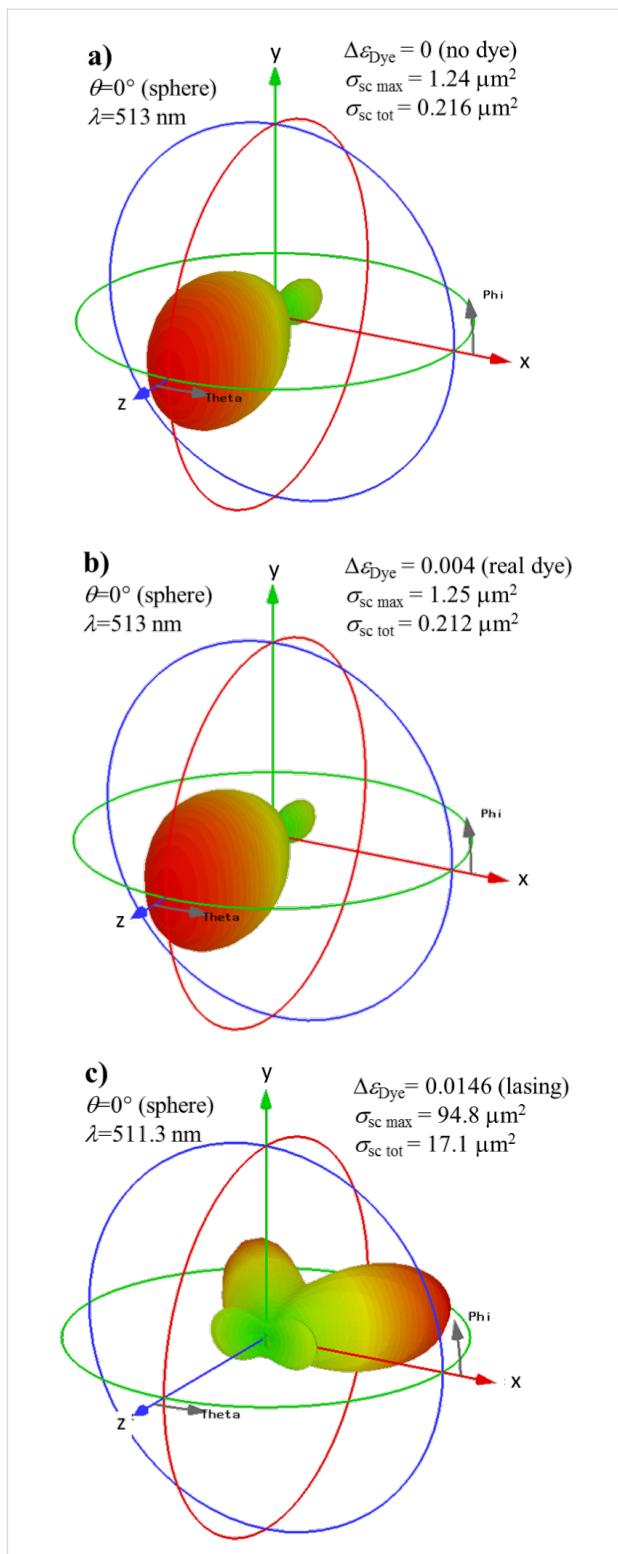
Figure 7: Differential scattering cross section σ_{sc}, linear scale, for resonant semi-shells with thickness h = 16 nm at $\lambda \approx 513$ nm. The irradiation is from the (0,0) direction; the strength of the emission (gain, A = 0, E = 1) is (a) $\Delta\varepsilon_{Dye}$ = 0 (no dye molecules at all), (b) 0.004 (commercially available dye concentration and total inversion) and (c) 0.0146 (lasing condition). The maximum of the differential and the total σ_{sc} are given in the legends.
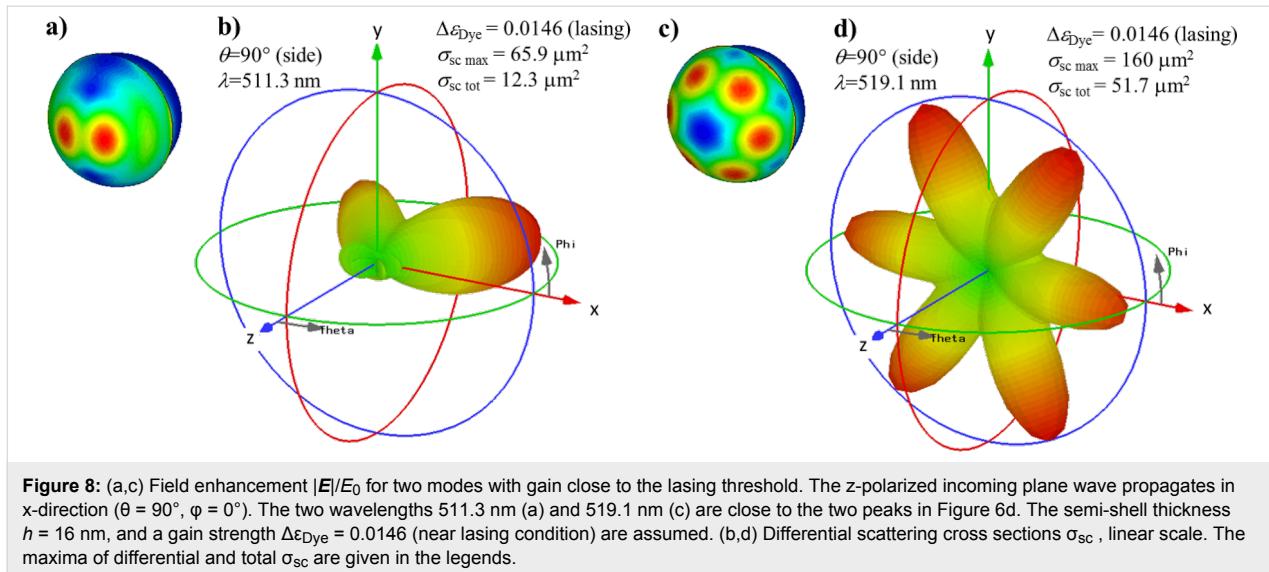
Figure 8: (a,c) Field enhancement $|E|/E_0$ for two modes with gain close to the lasing threshold. The z-polarized incoming plane wave propagates in x-direction ($\theta = 90°$, $\varphi = 0°$). The two wavelengths 511.3 nm (a) and 519.1 nm (c) are close to the two peaks in Figure 6d. The semi-shell thickness h = 16 nm, and a gain strength $\Delta\varepsilon_{Dye}$ = 0.0146 (near lasing condition) are assumed. (b,d) Differential scattering cross sections σ_{sc}, linear scale. The maxima of differential and total σ_{sc} are given in the legends.

This observation becomes even more prominent when we look at a semi-shell of a slightly increased thickness of h = 20 nm instead of 16 nm. Figure 9a shows the extinction (solid lines), scattering (dotted lines) and absorption cross sections (dashed lines) for illumination from the (0,0) direction (magenta lines) and the (90,0) direction (blue lines) and hence Figure 9a directly corresponds to Figure 6d. Again, a shorter wavelength resonance, this time near 491 nm, is excitable for both illumination directions (0,0) and (90,0), while the longer wavelength "axial" resonance, this time at 497.5 nm, is only excitable in case of (90,0) illumination. Note, that appreciably larger gain of approximately $\Delta\varepsilon_{Dye}$ = 0.0217 is needed in case of the h = 20 nm Ag semi-shell to reach the lasing threshold as compared to only $\Delta\varepsilon_{Dye}$ = 0.0146 in case of the thinner shell of h = 16 nm. This is explained by two facts: a) larger losses in a thicker metal, and b) the absorption peak of the h = 16 nm shell coincides with the Lorentzian gain profile (cf. Figure 5c), while the peak of the h = 20 nm shell does not. Panels (b,c), (d,e), and (g,f) of Figure 9 show the near-field distributions and the far-field scattering for the semi-shell structure with h = 20 nm for the following conditions: (0,0) illumination at 490.7 nm (b,c), (90,0) illumination at 490.7 nm (d,e) and (90,0) illumination at 497.5 nm (f,g). Note that in case of (b–e) $\Delta\varepsilon_{Dye}$ = 0.0217 was used instead of 0.020 as in (a) and (f,g) because the lasing thresholds for the 497.5 nm resonance and the 490.7 nm resonance turned out to be slightly different. These graphs should be compared to the respective graphs for the h = 16 nm Ag semi-shells, namely Figure 7c for the (0,0) illumination and Figure 8 for the (90,0) illumination. We start with the discussion of the long-wavelength resonances 519.1 nm (Figure 8c,d) and 497.5 nm (Figure 9f,g), which can only be excited with the axially polarized (90,0) illumination. The near-field distributions (Figure 8c and Figure 9f) as well as the differential scat-

tering cross sections (Figure 8d and Figure 9g) look very similar. Only the relative strengths of the six lobes show some differences. The same tendency is observed for the "transverse" shorter-wavelength resonances at 511.3 and 491 nm (compare Figures 7c, 8a,b and 9b–e). We would like to note that the patterns of the differential cross sections change dramatically within a narrow range of parameters, which can be easily overlooked in the experiments as well as in the simulations. The present scattering diagrams differ strongly from the more symmetric ones reported in [51], in which smaller and thinner semi-shell structures were simulated. (The results from this report are fully reproducible by our numerical framework). All this corroborates the observation that one cannot easily foretell the pattern of the differential scattering cross sections from the appearance of the plasmonic eigenmode.

Lastly, let us discuss, which spectroscopic footprints can be expected from a commercially available dye-doping level that yields $\Delta\varepsilon_{Dye}$ = 0.004. Obviously, one cannot expect spasing, because a 3.7 times larger dye concentration is mandatory for that in the current geometry. However, already at moderate doping levels, some unusual spectroscopic signals should be observable. Figure 10 compares the differential cross sections for semi-shell thicknesses h = 20 nm (solid curves) and h = 16 nm (dashed curves), at dye concentrations that can be found in commercially available PS spheres. All other parameters are the same as in Figure 2. The most striking result is that for h = 20 nm the absorption becomes negative near 513 nm, and for h = 16 nm it becomes negative near 500 and 530 nm. This means that the structures show an overcompensation of absorption at these wavelengths but no lasing yet. Changes in absorption for such concentrations are actually more pronounced for the off-resonance thickness h = 20 nm. Further, the
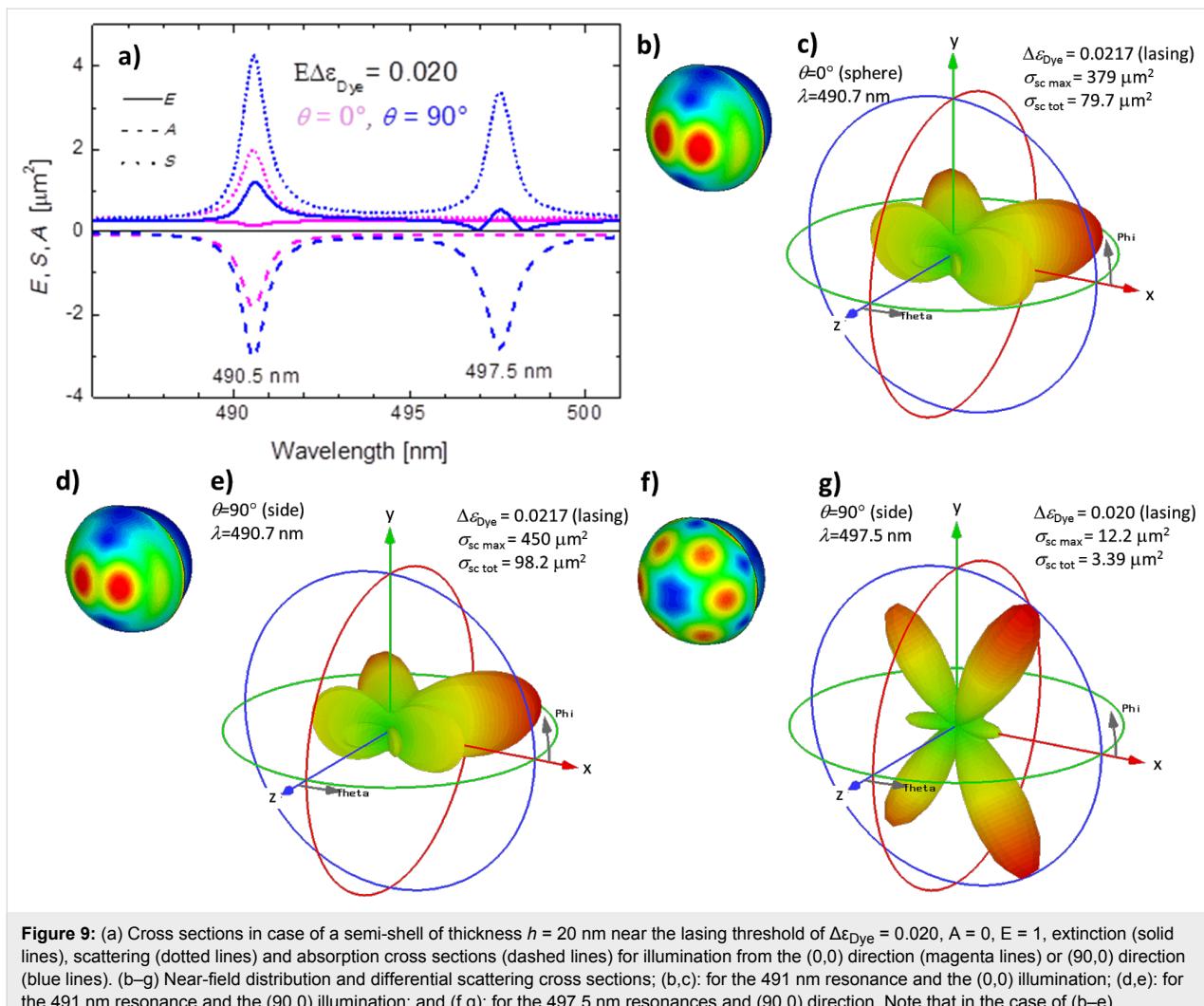
Figure 9: (a) Cross sections in case of a semi-shell of thickness *h* = 20 nm near the lasing threshold of $\Delta\varepsilon_{Dye}$ = 0.020, A = 0, E = 1, extinction (solid lines), scattering (dotted lines) and absorption cross sections (dashed lines) for illumination from the (0,0) direction (magenta lines) or (90,0) direction (blue lines). (b–g) Near-field distribution and differential scattering cross sections; (b,c): for the 491 nm resonance and the (0,0) illumination; (d,e): for the 491 nm resonance and the (90,0) illumination; and (f,g): for the 497.5 nm resonances and (90,0) direction. Note that in the case of (b–e) $\Delta\varepsilon_{Dye}$ = 0.0217 was used instead of 0.020 as in (a) and (f,g), see main text.

features in the scattering spectrum are sharpened by gain and so do the (positive) peaks in the absorption spectrum at wavelength ranges, at which the absorption is not yet overcompensated, for instance the peaks at 487 nm in the case of the *h* = 20 nm semi-shells (Figure 10 c, solid lines). Finally, Figure 10d compares all cross sections on one plot for the full inversion of the dye molecules with realistic concentration for both thicknesses *h* = 20 nm (dark blue), and *h* = 16 nm (cyan). In Figure 10d the solid curves refer to extinction (*E*), dotted to scattering (*S*) and dashed to absorption (*A*).

Conclusion

Dye-doped polystyrene spheres capped with a thin semi-shell of silver show rich spectra of absorption, scattering and extinction, which contain many peaks and shoulders. Without gain, i.e., as long as the dye molecules are not pumped, the spectra are broad and hiding some of the eigenmodes. However, these become clearly observable when the gain is switched on, which leads to

a compensation of absorption and hence sharpens the plasmon resonances. Specifically, we showed that a mode of *l* = 3, *m* = 3 symmetry is only 8 nm away from a *l* = 2 mode. This tiny difference can certainly not be resolved without gain-narrowing of plasmonic resonances. We deliberately focused on the discussion of the gain that is required for spectral sharpening and compared the required gain to the gain available in commercially available polystyrene spheres. We find that for the investigated geometries spasing requires gain levels less than 3.7 times higher than those in commercially available dye-doped spheres. Furthermore, the directionality of the differential scattering cross section changes with the amount of gain, depends on the fine details of the structure geometry and is sensitive to the direction of illumination. All this demands a high manufacturing accuracy of semi-shell based spasers.

With gain, some "conventional intuition" might become wrong. For example that lower multipolar modes are usually the

Figure 10: Differential cross sections for semi-shell thicknesses *h* = 20 nm (solid curves) and *h* = 16 nm (dashed curves), at dye concentrations as in commercially available PS spheres. All other parameters are the same as in Figure 2. For *h* = 20 nm the absorption becomes negative near 513 nm, while for *h* = 16 nm it becomes negative near 500 and 530 nm. The structures show overcompensation of absorption at these wavelengths but no lasing yet. (d) Comparison of all cross sections on one plot for $\Delta\varepsilon_{Dye}$ = 0.004, A = 0.004, E = 1 for both thicknesses *h* = 20 nm (dark blue), and *h* = 16 nm (cyan).

stronger ones. This intuition is based on the expansion into powers of the Mie-parameter (*a*/λ) where *a* is the typical structure size. This expansion still holds. However, when the denominator in one of the scattering/absorption terms goes to zero, this term dominates, irrespectively of the power of (*a*/λ) associated with it. Some of the higher modes may dominate simply because they best match the spectral bandwidth of the gain media.

Numerical

Here we summarize several subtleties, crucial for reliable simulations. Conventional finite difference time domain (FDTD) approaches require an analytical approximation of the dispersion of the metal dielectric constant [59], which is not always satisfactory. Active media with optical gain may introduce instabilities into FDTD codes, unless auxiliary differential equations with gain saturation are used [60]. We tackle these difficulties using the (mainly iterative) frequency domain solver of the CST MWS® software with open boundaries, realized by perfectly matched layers (PML, 10 mesh layers). The computa-

tional domain (without PML) is a cube with a side of about 1 μm. For excitation, a linearly polarized plane wave is applied. No symmetries were used in order to make the numerical framework fully suitable for oblique incidence under angles (θ ≠ 0, φ ≠ 0) and for asymmetric structures.

Special care has to be taken of sharp edges and vertices leading to numerical hot spots, which are, however, unrealistic because in experiments all vertices will show some natural rounding and even if very large curvatures could be realized, ultra-high field enhancement is unphysical on a scale below 1 nm because of nonlocality and quantum effects [61,62]. We used blended edges with radii of curvature R_{blend} = 5 nm.

The numerically prepared Lorentzian gain can be read into the CST software package as a list of ε values only if ε″ is artificially made positive. Afterwards, the properties of the material can be manually reverted to ε″ < 0 in the "history list". The CST software calculates scattering and absorption cross sections σ_{sc}, σ_{ab} by using internal algorithms. However, the absorption

calculation fails for the active structures, when σ_{ab} becomes negative. For this reason, a Power Flow Monitor through a spherical face surrounding the structure was created, and the integral power flow through it was recalculated into σ_{ab}. The extinction cross section is always defined as $\sigma_{ex} = \sigma_{sc} + \sigma_{ab}$, irrespectively of the sign of σ_{ab}. Far-field patterns are calculated by the internal CST routines, which project the fields on the sides of the bounding box into the far-fields via fast Fourier transform.

Adaptive meshing is a must for the accurate representation of the fields in the regions where their gradients are high [63], though it affects less such global characteristics as σ_{ex}, σ_{sc} and σ_{ab}. For time-efficient calculations distributed computing (DC) and parallelization capabilities of the CST package were used, usually with six solver servers, each calculating its own frequency point independently in parallel, and threaded over 2 CPUs. In a typical run, 12 employed CPUs needed a wall-time of about 2 h for the full spectra with about 300 frequency points. Usually 10 adaptive mesh runs were sufficient, resulting in 80–90 kcells, with the cell edge length varying between ≈ 1 nm near (smoothened) sharp metallic features and ≈ 50 nm in the free air regions.

Acknowledgements

References

1. Kreibig, U.; Vollmer, M. In *Optical Properties of Metal Clusters;* Toennies, J. P., Ed.; Springer Series in Materials Science, Vol. 25; Springer: Berlin, 1995.
2. Zhou, H. S.; Honma, I.; Komiyama, H.; Haus, J. W. *Phys. Rev. B* **1994,** *50,* 12052–12056. doi:10.1103/PhysRevB.50.12052
3. Averitt, R. D.; Sarkar, D.; Halas, N. J. *Phys. Rev. Lett.* **1997,** *78,* 4217–4220. doi:10.1103/PhysRevLett.78.4217
4. Takei, H. *J. Vac. Sci. Technol., B* **1999,** *17,* 1906–1911. doi:10.1116/1.591066
5. Love, J. C.; Gates, B. D.; Wolfe, D. B.; Paul, K. E.; Whitesides, G. M. *Nano Lett.* **2002,** *2,* 891–894. doi:10.1021/nl025633l
6. Liu, J.; Maaroof, A. I.; Wieczorek, L.; Cortie, M. B. *Adv. Mater.* **2005,** *17,* 1276–1281. doi:10.1002/adma.200500035
7. Coyle, S.; Netti, M. C.; Baumberg, J. J.; Ghanem, M. A.; Birkin, P. R.; Bartlett, P. N.; Whittaker, M. *Phys. Rev. Lett.* **2001,** *87,* 176801. doi:10.1103/PhysRevLett.87.176801
8. Charnay, C.; Lee, A.; Man, S.-Q.; Moran, C. E.; Radloff, C.; Bradley, R. K.; Halas, N. J. *J. Phys. Chem. B* **2003,** *107,* 7327–7333. doi:10.1021/jp034309r
9. Lassiter, J. B.; Knight, M. W.; Mirin, N. A.; Halas, N. J. *Nano Lett.* **2009,** *9,* 4326–4332. doi:10.1021/nl9025665
10. Ye, J.; Van Dorpe, P.; Van Roy, W.; Lodewijks, K.; De Vlaminck, I.; Maes, G.; Borghs, G. *J. Phys. Chem. C* **2009,** *113,* 3110–3115. doi:10.1021/jp8072409
11. Cole, R. M.; Baumberg, J. J.; Garcia de Abajo, F. J.; Mahajan, S.; Abdelsalam, M.; Bartlett, P. N. *Nano Lett.* **2007,** *7,* 2094–2100. doi:10.1021/nl0710506
12. Cortie, M.; Ford, M. *Nanotechnology* **2007,** *18,* 235704. doi:10.1088/0957-4484/18/23/235704
13. Wang, Q.; Tang, C.; Chen, J.; Zhan, P.; Wang, Z. *Opt. Express* **2011,** *19,* 23889–23900. doi:10.1364/OE.19.023889
14. Lacharmoise, P. D.; Tognalli, N. G.; Goñi, A. R.; Alonso, M. I.; Fainstein, A.; Cole, R. M.; Baumberg, J. J.; Garcia de Abajo, J.; Bartlett, P. N. *Phys. Rev. B* **2008,** *78,* 125410. doi:10.1103/PhysRevB.78.125410
15. Zhang, Y.; Barhoumi, A.; Lassiter, J. B.; Halas, N. J. *Nano Lett.* **2011,** *11,* 1838–1844. doi:10.1021/nl2008357
16. King, N. S.; Li, Y.; Ayala-Orozco, C.; Brannan, T.; Nordlander, P.; Halas, N. J. *ACS Nano* **2011,** *5,* 7254–7262. doi:10.1021/nn202086u
17. Ding, B.; Hrelescu, C.; Arnold, N.; Isic, G.; Klar, T. A. *Nano Lett.* **2013,** *13,* 378–386. doi:10.1021/nl3035114
18. Himmelhaus, M.; Takei, H. *Sens. Actuators, B* **2000,** *63,* 24–30. doi:10.1016/S0925-4005(99)00393-7
19. Lal, N. N.; Soares, B. F.; Sinha, J. K.; Huang, F.; Mahajan, S.; Bartlett, P. N.; Greenham, N. C.; Baumberg, J. J. *Opt. Express* **2011,** *19,* 11256–11263. doi:10.1364/OE.19.011256
20. Dunbar, R. B.; Pfadler, T.; Lal, N. N.; Baumberg, J. J.; Schmidt-Mende, L. *Nanotechnology* **2012,** *23,* 385202. doi:10.1088/0957-4484/23/38/385202
21. Mahajan, S.; Richardson, J.; Brown, T.; Bartlett, P. N. *J. Am. Chem. Soc.* **2008,** *130,* 15589–15601. doi:10.1021/ja805517q
22. Mahajan, S.; Cole, R. M.; Soares, B. F.; Pelfrey, S. H.; Russell, A. E.; Baumberg, J. J.; Bartlett, P. N. *J. Phys. Chem. C* **2009,** *113,* 9284–9289. doi:10.1021/jp900661u
23. Steuwe, C.; Kaminski, C. F.; Baumberg, J. J.; Mahajan, S. *Nano Lett.* **2011,** *11,* 5339–5343. doi:10.1021/nl202875w
24. Sudarkin, A. N.; Demkovich, P. A. *Sov. Phys. - Tech. Phys.* **1989,** *34,* 764–766.
25. Klar, T. A.; Kildishev, A. V.; Drachev, V. P.; Shalaev, V. M. *IEEE J. Sel. Top. Quantum Electron.* **2006,** *12,* 1106–1115. doi:10.1109/JSTQE.2006.880597
26. Xiao, S.; Drachev, V. P.; Kildishev, A. V.; Ni, X.; Chettiar, U. K.; Yuan, H.-K.; Shalaev, V. M. *Nature* **2010,** *466,* 735–738. doi:10.1038/nature09278
27. Campione, S.; Capolino, F. *Nanotechnology* **2012,** *23,* 235703. doi:10.1088/0957-4484/23/23/235703
28. Campione, S.; Albani, M.; Capolino, F. *Opt. Mater. Express* **2011,** *1,* 1077–1089. doi:10.1364/OME.1.001077
29. Noginov, M. A.; Zhu, G.; Bahoura, M.; Adegoke, J.; Small, C. E.; Ritzo, B. A.; Drachev, V. P.; Shalaev, V. M. *Opt. Lett.* **2006,** *31,* 3022–3024. doi:10.1364/OL.31.003022
30. Strangi, G.; De Luca, A.; Ravaine, S.; Ferrie, M.; Bartolino, R. *Appl. Phys. Lett.* **2011,** *98,* 251912. doi:10.1063/1.3599566
31. Bergman, D. J.; Stockman, M. I. *Phys. Rev. Lett.* **2003,** *90,* 027402. doi:10.1103/PhysRevLett.90.027402
32. Lawandy, N. M. *Appl. Phys. Lett.* **2004,** *85,* 5040–5042. doi:10.1063/1.1825058
33. Protsenko, I. E.; Uskov, A. V.; Zaimidoroga, O. A.; Samoilov, V. N.; O'Reilly, E. P. *Phys. Rev. A* **2005,** *71,* 063812. doi:10.1103/PhysRevA.71.063812

34. Gordon, J. A.; Ziolkowski, R. W. *Opt. Express* **2007,** *15,* 2622–2653. doi:10.1364/OE.15.002622

35. Zheludev, N. I.; Prosvirnin, S. L.; Papasimakis, N.; Fedotov, V. A. *Nat. Photonics* **2008,** *2,* 351–354. doi:10.1038/nphoton.2008.82

36. Stockman, M. I. *J. Opt. (Bristol, U. K.)* **2010,** *12,* 024004. doi:10.1088/2040-8978/12/2/024004

37. Stockman, M. I. *Phys. Rev. Lett.* **2007,** *98,* 177404. doi:10.1103/PhysRevLett.98.177404

38. Mackay, T. G.; Lakhtakia, A. *Phys. Rev. Lett.* **2007,** *99,* 189701. doi:10.1103/PhysRevLett.99.189701

39. Kinsler, P.; McCall, M. W. *Phys. Rev. Lett.* **2008,** *101,* 167401. doi:10.1103/PhysRevLett.101.167401

40. Wuestner, S.; Pusch, A.; Tsakmakidis, K. L.; Hamm, J. M.; Hess, O. *Phys. Rev. Lett.* **2010,** *105,* 127401. doi:10.1103/PhysRevLett.105.127401

41. Stockman, M. I. *Phys. Rev. Lett.* **2011,** *106,* 156802. doi:10.1103/PhysRevLett.106.156802

42. Hill, M. T.; Oei, Y.-S.; Smalbrugge, B.; Zhu, Y.; de Vries, T.; van Veldhoven, P. J.; van Otten, F. W. M.; Eijkemans, T. J.; Turkiewicz, J. P.; de Waardt, H.; Geluk, E. J.; Kwon, S.-H.; Lee, Y.-H.; Nötzel, R.; Smit, M. K. *Nat. Photonics* **2007,** *1,* 589–594. doi:10.1038/nphoton.2007.171

43. Nezhad, M. P.; Simic, A.; Bondarenko, O.; Slutsky, B.; Mizrahi, A.; Feng, L.; Lomakin, V.; Fainman, Y. *Nat. Photonics* **2010,** *4,* 395–399. doi:10.1038/nphoton.2010.88

44. Lee, J. H.; Khajavikhan, M.; Simic, A.; Gu, Q.; Bondarenko, O.; Slutsky, B.; Nezhad, M. P.; Fainman, Y. *Opt. Express* **2011,** *19,* 21524–21531. doi:10.1364/OE.19.021524

45. Ding, K.; Liu, Z. C.; Yin, L. J.; Hill, M. T.; Marell, M. J. H.; van Veldhoven, P. J.; Nöetzel, R.; Ning, C. Z. *Phys. Rev. B* **2012,** *85,* 041301. doi:10.1103/PhysRevB.85.041301

46. Kwon, S.-H.; Kang, J.-H.; Seassal, C.; Kim, S.-K.; Regreny, P.; Lee, Y.-H.; Lieber, C. M.; Park, H.-G. *Nano Lett.* **2010,** *10,* 3679–3683. doi:10.1021/nl1021706

47. Oulton, R. F.; Sorger, V. J.; Zentgraf, T.; Ma, R.-M.; Gladden, C.; Dai, L.; Bartal, G.; Zhang, X. *Nature* **2009,** *461,* 629–632. doi:10.1038/nature08364

48. Lu, Y.-J.; Kim, J.; Chen, H.-Y.; Wu, C.; Dabidian, N.; Sanders, C. E.; Wang, C.-Y.; Lu, M.-Y.; Li, B.-H.; Qiu, X.; Chang, W.-H.; Chen, L.-J.; Shvets, G.; Shih, C.-K.; Gwo, S. *Science* **2012,** *337,* 450–453. doi:10.1126/science.1223504

49. Noginov, M. A.; Zhu, G.; Belgrave, A. M.; Bakker, R.; Shalaev, V. M.; Narimanov, E. E.; Stout, S.; Herz, E.; Suteewong, T.; Wiesner, U. *Nature* **2009,** *460,* 1110–1112. doi:10.1038/nature08318

50. Pan, J.; Chen, Z.; Chen, J.; Zhan, P.; Tang, C. J.; Wang, Z. L. *Opt. Lett.* **2012,** *37,* 1181–1183. doi:10.1364/OL.37.001181

51. Meng, X.; Guler, U.; Kildishev, A. V.; Fujita, K.; Tanaka, K.; Shalaev, V. M. *Sci. Rep.* **2013,** *3,* No. 1241. doi:10.1038/srep01241

52. Tribelsky, M. I.; Luk'yanchuk, B. S. *Phys. Rev. Lett.* **2006,** *97,* 263902. doi:10.1103/PhysRevLett.97.263902

53. Fan, X.; Shen, Z.; Luk'yanchuk, B. *Opt. Express* **2010,** *18,* 24868–24880. doi:10.1364/OE.18.024868

54. Johnson, P. B.; Christy, R. W. *Phys. Rev. B* **1972,** *6,* 4370–4379. doi:10.1103/PhysRevB.6.4370

55. Strickler, S. J.; Berg, R. A. *J. Chem. Phys.* **1962,** *37,* 814–822. doi:10.1063/1.1733166

56. Khurgin, J. B.; Sun, G. *Opt. Express* **2012,** *20,* 15309–15325. doi:10.1364/OE.20.015309

57. Prodan, E.; Radloff, C.; Halas, N. J.; Nordlander, P. *Science* **2003,** *302,* 419–422. doi:10.1126/science.1089171

58. Baranov, D. G.; Andrianov, E. S.; Vinogradov, A. P.; Lisyansky, A. A. *Opt. Express* **2013,** *21,* 10779–10791. doi:10.1364/OE.21.010779

59. Vial, A.; Laroche, T. *Appl. Phys. B* **2008,** *93,* 139–143. doi:10.1007/s00340-008-3202-4

60. Prokopeva, L. J.; Trieschmann, J.; Klar, T. A.; Kildishev, A. V. *Proc. SPIE* **2011,** *8172,* 81720B. doi:10.1117/12.898619

61. Garcia de Abajo, F. J. *J. Phys. Chem. C* **2008,** *112,* 17983–17987. doi:10.1021/jp807345h

62. Zuloaga, J.; Prodan, E.; Nordlander, P. *Nano Lett.* **2009,** *9,* 887–891. doi:10.1021/nl803811g

63. Hoffmann, J.; Hafner, C.; Leidenberger, P.; Hesselbarth, J.; Burger, S. *Proc. SPIE* **2009,** *7390,* 73900J. doi:10.1117/12.828036

License and Terms

Observation and analysis of structural changes in fused silica by continuous irradiation with femtosecond laser light having an energy density below the laser-induced damage threshold

Wataru Nomura[*1], Tadashi Kawazoe[1], Takashi Yatsui[1], Makoto Naruse[2] and Motoichi Ohtsu[1]

Full Research Paper

Address:
[1]School of Engineering, The University of Tokyo, and The Nanophotonics Research Center, The University of Tokyo, 2-11-16 Yayoi, Bunkyo-ku, Tokyo, 113-8656 Japan, and [2]National Institute of Information and Communications Technology, 4-2-1 Nukui-kita, Koganei, Tokyo 184-8795, Japan

Email:
Wataru Nomura[*] - nomura@nanophotonics.t.u-tokyo.ac.jp

* Corresponding author

Abstract

The laser-induced damage threshold (LIDT) is widely used as an index for evaluating an optical component's resistance to laser light. However, a degradation in the performance of an optical component is also caused by continuous irradiation with laser light having an energy density below the LIDT. Therefore, here we focused on the degradation in performance of an optical component caused by continuous irradiation with femtosecond laser light having a low energy density, i.e., laser-induced degradation. We performed an in situ observation and analysis of an increase in scattering light intensity in fused silica substrates. In experiments conducted using a pulsed laser with a wavelength of 800 nm, a pulse width of 160 fs and pulse repetition rate of 1 kHz, we found that the scattered light intensity increased starting from a specific accumulated fluence, namely, that the laser-induced degradation had a threshold. We evaluated the threshold fluence F_t as 6.27 J/cm^2 and 9.21 J/cm^2 for the fused silica substrates with surface roughnesses of 0.20 nm and 0.13 nm in R_a value, respectively, showing that the threshold decreased as the surface roughness increased. In addition, we found that the reflected light spectrum changed as degradation proceeded. We analyzed the details of the degradation by measuring instantaneous reflectance changes with a pump–probe method; we observed an increase in the generation probability of photogenerated carriers in a degraded silica substrate and a damaged silica substrate and observed a Raman signal originating from a specific molecular structure of silica. From these findings, we concluded that compositional changes in the molecular structure occurred during degradation due to femtosecond laser irradiation having an energy density below the LIDT.

Introduction

Since the invention of the laser, it has been widely known that damages occur at the surface or interior of optical components when irradiated with laser light having a high energy density. A lot of research has been conducted in the area of laser-induced damage. For example: mechanism for picosecond [1,2] and femtosecond (fs) laser [3,4], effect of surface geometry [5,6], damage threshold [7,8], and so on. The laser-induced damage originates in photoionization of molecules caused by local electric fields generated at ultrafine structures in the substrates, such as indentations/protrusions in the surface or impurities in the interior. Recently, with advances made in the development of light sources, such as the trend towards lasers with higher power, shorter pulses, and shorter wavelengths, there has been a demand for the development of optical components having even higher damage resistance. Laser resistance is evaluated by an index called the laser-induced damage threshold (LIDT), which is measured by the 200-on-1 method according to ISO 11254-2 [9,10], for example. With this method, 200 locations on a sample surface are irradiated with single shots of pulsed laser light having different energy densities. The presence/absence of damage sites due to the irradiation is visually checked, and the minimum energy density at which damages are found is defined as the LIDT. However, the practical problem is that the performance of an optical component, such as transmittance, reflectance, etc., is degraded by continuous irradiation with laser light having an energy density below the LIDT. The cause of such degradation in performance, namely, laser-induced degradation of the optical component, is not fully understood. In addition, the resistance cannot be evaluated by tests based on ISO 11254-2, and therefore, a technique for the quantitative evaluation of such degradation would be useful. Furthermore, if the relation between laser-induced degradation and surface roughness is revealed, it may contribute to the development of a surface polishing technology for optical components with higher resistance against not only laser-induced damage but also degradation. Moreover, the clarification of the mechanism and knowledge about the details of the laser-induced degradation may provide an opportunity to develop novel laser processing techniques. Thus, our study about laser-induced degradation is a contribution to the progress in nanotechnology.

Therefore, we performed in situ a quantitative detection of laser-induced degradation in flat fused silica substrates, serving as the target material. The continuous irradiation with fs pulsed laser light has an energy density below the LIDT. We also analyzed the origin of the laser-induced degradation. Section 1 in Results and Discussion describes experiments in which we continuously irradiated substrates with fs pulsed laser light having a low energy density below the LIDT and detected the laser-induced degradation by measuring the scattered light. In addition, by simultaneously measuring the reflected-light spectrum during this process, we observed spectral changes as the laser-induced degradation proceeded. Section 2 in Results and Discussion describes the measurement of instantaneous reflectance changes using a pump–probe method carried out to analyze the details of these spectral changes. From an increase in photo-generated carriers and the power spectrum of their relaxation lifetime, we found that compositional changes in the molecular structure occurred as laser-induced degradation proceeded.

Results and Discussion

1 Evaluation of laser-induced degradation of fused silica

1.1 Surface roughness dependence of threshold fluence in laser-induced degradation

First, to quantitatively observe laser-induced degradation due to continuous irradiation with a laser light having an energy density below the LIDT, we conducted an experiment in which we continuously irradiated a silica substrate with fs laser light and measured the relative increase in scattered light from the substrate surface. As measurement samples, we used high-purity fused silica flat substrates in which the OH impurity content was 0.8 ppm or less. We used two samples: sample A, which was prepared by planarizing a substrate using standard chemical-mechanical polishing (CMP) [11], and sample B, which was prepared by performing optical near-field etching on a substrate prepared under the same conditions as sample A. The samples A and B had a minimum average surfaces roughnesses R_a of 0.20 nm and 0.13 nm, respectively [12]. Since we employed a continuous-wave laser with the wavelength of 532 nm and power of 2 W for optical near-field etching, the sample B did not have any laser-induced damage or degradation caused by this preparation. Optical near-field etching is a surface planarization technique for selectively removing only minute protrusions in the surface of a substrate, and can flatten the planer substrate polished by CMP. Thus, it is effective in reducing the drop in LIDT caused by electric field enhancement induced by the surface structure [5,6]. It has been reported that a dielectric multilayer mirror fabricated by using a silica substrate planarized by this technique exhibited an LIDT that was increased from 8.2 J/cm^2 to 14 J/cm^2 compared with the mirror before planarization processing, according to a 200-on-1 laser resistance test based on ISO 11254-2 [13].

Figure 1a shows the experimental set-up. For the light source, we used a regeneratively amplified fs Ti:sapphire laser (Coherent, Inc., Legend Elite F-1K) with a wavelength of 800 nm, a power of 1.0 W, a repetition frequency of 1 kHz, and a pulse width of 160 fs. The laser light was incident on the

surface of the substrates at an incident angle of 45° and with an energy density of 6.0 mJ/cm^2. This energy density is sufficiently lower than the LIDT of fused silica for the same wavelength and pulse width, namely, about 0.5 J/cm^2 [14,15]. Scattered light from the samples was collected by a Si photodiode (Hamamatsu Photonics K.K., S3883) placed perpendicularly to the substrate, and lock-in detection was performed at the repetition frequency of the laser using a lock-in amplifier (Stanford Research Systems, Inc., SR830).

We evaluated the two silica substrates using the relative increase in the scattered light intensity S, $\Delta S(F) = (S(F) - S(0))/S(0)$, versus the accumulated fluence F (J/cm^2) of the irradiated light. In the experiment, we continuously irradiated samples A and B with laser light having fluences up to $F = 3.5 \times 10^4$ J/cm^2 and 8.8×10^4 J/cm^2, respectively, and after the experiment, we confirmed that there were no sites showing laser-induced damage in the surfaces of the samples by using an optical microscope. The results of measuring $\Delta S(F)$ for samples A and B, ΔS_A and ΔS_B, are shown by the black and red solid lines in Figure 1b, respectively. We observed a tendency for the scattered light to increase with continuing irradiation, showing that this method succeeded in quantitatively measuring the laser-induced degradation. In addition, for both ΔS_A and ΔS_B, the scattered light intensity increased logarithmically from specific fluences, showing that there was a threshold fluence at which laser-induced degradation started. To determine this threshold fluence, F_t, the regions where ΔS_A and ΔS_B rose were fitted with an approximation $g(F) = P\log(F) - Q$. The approximation curves are shown by the green and blue dotted lines in Figure 1b, where $g_A(F)$ was defined over the range

6.3×10^3 J/cm$^2 < F < 1.2 \times 10^4$ J/cm^2 for ΔS_A, and g_B (F) was defined over the range $F > 9.2 \times 10^3$ J/cm^2 for ΔS_B. The constants P and Q are as shown in Table 1. When F_t at which $g_A(F) = 0$ and $g_B(F) = 0$ is determined from these equations, for the samples A and B, we calculated $F_{tA} = 6.3 \times 10^3$ J/cm^2 (1.1×10^6 shots) and $F_{tB} = 9.2 \times 10^3$ J/cm^2 (1.5×10^6 shots), under the laser energy density of 6.0 mJ/cm^2. This result shows that the degradation starting threshold for sample B is 1.4-times higher than that for sample A. As described above, sample B was a substrate prepared by selectively removing only the ultra-fine surface structure from the substrate of sample A, and the LIDT of a mirror using a substrate identical to this was improved by a factor of 1.7 [13]. Since the degradation starting threshold F_t and the LIDT improvement factor are in good agreement, this result indicates the laser-induced degradation occurs with a partly similar mechanism of laser-induced damage, namely multiphoton ionization caused by local electric fields generated at indentations or protrusions. Also, the constants P which define the rate of increase of $g_A(F)$ and $g_B(F)$ are $P_A = 0.062$ and $P_B = 0.016$, differing by a factor of 3.9, which shows that laser-induced degradation originating from the surface structure proceeds more rapidly.

Table 1: Constants P and Q for approximation curves $g_A(F)$ and $g_B(F)$.

	P	Q
$g_A(F)$	0.062	0.24
$g_B(F)$	0.016	0.062
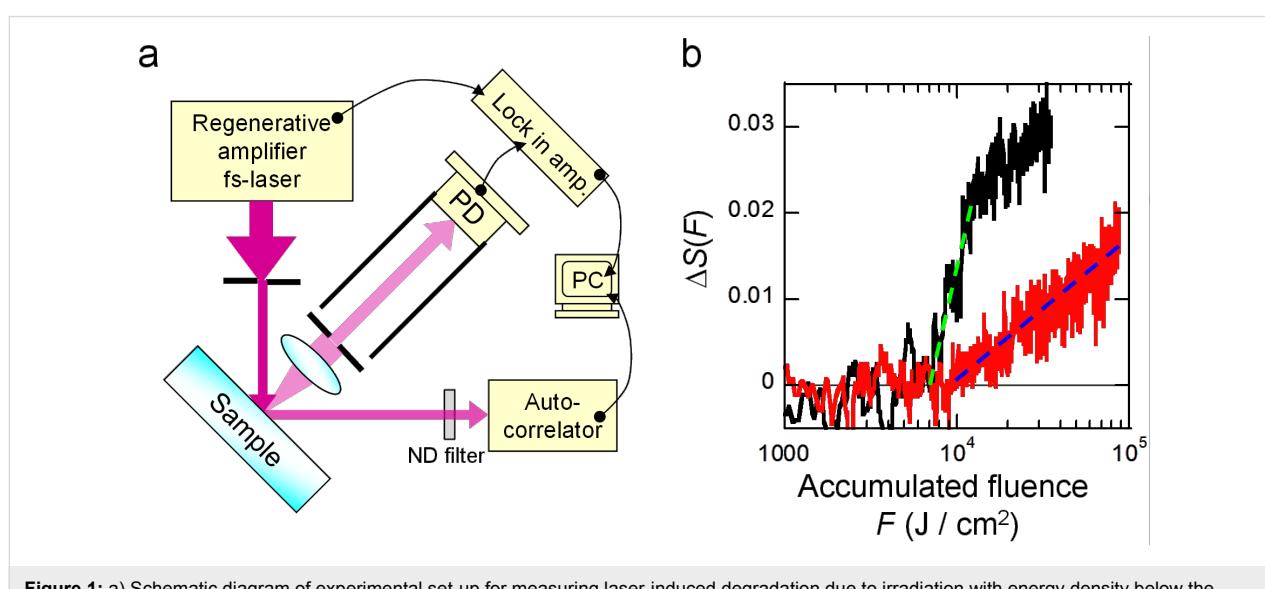
Figure 1: a) Schematic diagram of experimental set-up for measuring laser-induced degradation due to irradiation with energy density below the LIDT. b) Relative increase in scattered light intensity, ΔS, versus accumulated fluence, F, for samples A and B. Black and red solid lines show ΔS_A and ΔS_B, respectively. The green and blue dotted lines show approximation curves $g_A(F)$ and $g_B(F)$ for regions where ΔS_A and ΔS_B rise.

1.2 In situ evaluation of spectral change in reflected light

To analyze the laser-induced degradation, we evaluated the reflected light spectrum at the same time as the scattered light intensity measurement. As shown in Figure 1a, reflected light was introduced from the sample into an autocorrelator with a spectrometer function (APE GmbH, pulseCheck). We used a fused silica substrate identical to sample A and set the energy density of incident light on the substrate to 17 mJ/cm^2, which is below the LIDT. Spectral data was obtained at four fluences, namely, $F_1 = 5.1 \times 10^3$ J/cm^2, $F_2 = 1.9 \times 10^5$ J/cm^2, $F_3 = 5.9 \times 10^5$ J/cm^2, and $F_4 = 1.3 \times 10^6$ J/cm^2.

The solid black line in Figure 2a shows the wavenumber spectra of the reflected light, centered on the central wavelength of the laser (800 nm). Under all conditions, in addition to the central frequency of the laser, we observed the 2nd peak on the long-wavelength side. When these wavenumber spectra were fitted with the sum of two Gaussian functions, as shown by the solid red lines in Figure 2a, the center wavenumbers on the 2nd peaks K were determined to be $K_1 = 84$ cm^{-1}, $K_2 = 86$ cm^{-1}, $K_3 = 92$ cm^{-1}, and $K_4 = 94$ cm^{-1} for the fluences F_1 to F_4, respectively. The relative increase in the scattered light intensity, ΔS, and K versus the irradiated fluence, F, are plotted in the black solid line and the red squares in Figure 2b, respectively. The monotonically increasing trends with respect to F agreed well in both ΔS and K, showing that the 2nd peak of the spec-

trum shifted to lower energy side as the degradation proceeded. We estimated the origin of the 2nd peaks were Raman signals of degraded silica and this result represented the compositional changes in the molecular proceeds with the laser-induced degradation proceeded.

2 Analysis of degradation via pump–probe method

2.1 Time-resolved measurement of reflectance

To analyze in detail the spectral changes occurring with laser-induced degradation due to continuous irradiation with laser light having an energy density below the LIDT, as confirmed in the previous section, we conducted an experiment to evaluate the time-resolved changes in reflectance via a pump–probe method. The experimental setup is shown in Figure 3. The laser used was a mode-locked Ti:sapphire laser (Coherent, Inc., Mira Optima 900-D) with a wavelength of 750 nm, a pulse width of 90 fs, and a repetition frequency of 80 MHz. Using a beamsplitter, the laser light was split with an intensity ratio of reflected light to transmitted light of 1:19. As pump light, the transmitted light was made perpendicularly incident on the sample surface via an optical delay and a chopper with a frequency of 2 kHz. P-polarized probe light, with a polarization orthogonal to that of the pump light, was incident on the substrate at an angle of incidence of about 70°, and the reflected probe light was received by a Si photodiode (Hamamatsu Photonics K.K., S3883). The received signal was detected with
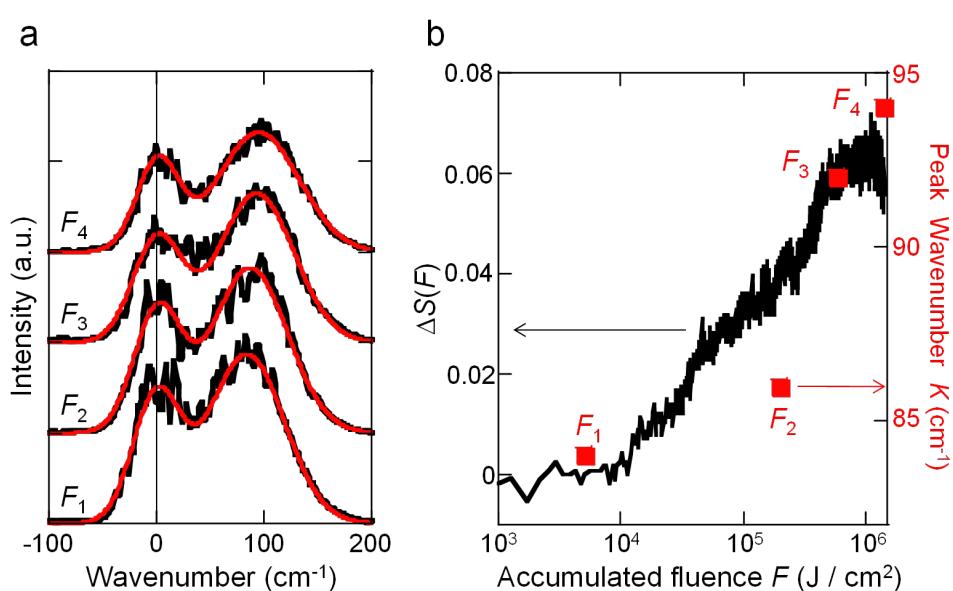

Figure 2: a) Wavenumber spectra of reflected light from silica substrate for accumulated fluences F_1 to F_4, where $F_1 = 5.1 \times 10^3$ J/cm^2, $F_2 = 1.9 \times 10^5$ J/cm^2, $F_3 = 5.9 \times 10^5$ J/cm^2, and $F_4 = 1.3 \times 10^6$ J/cm^2. The black and red solid lines indicate the measured values and approximation curves given by the sum of two Gaussian functions, respectively. The vertical axis shows arbitrary units and the baselines of F_1 to F_4 are essentially equivalent. b) Dependence of relative increase in scattered light intensity, ΔS (black line), and peak wavenumber in reflected light spectra K (red squares) on accumulated fluence, F.
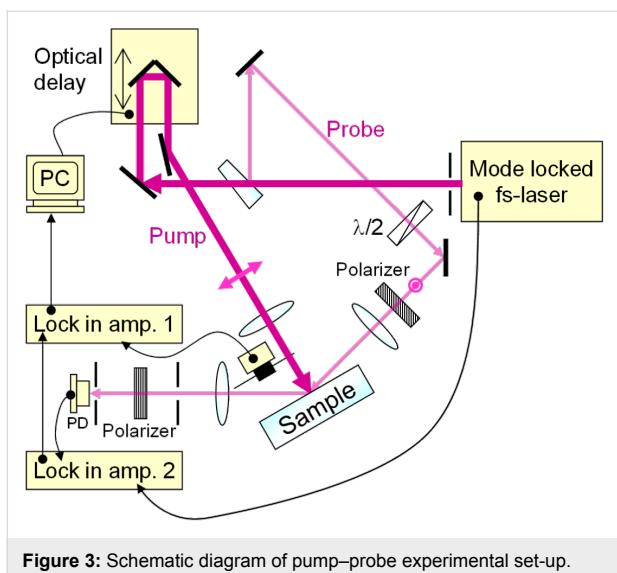
Figure 3: Schematic diagram of pump–probe experimental set-up.

double lock-in detection using two lock-in amplifiers (Stanford Research Systems, Inc., SR844 and SR830) based on the repetition frequency of the laser pulses and the frequency of the chopper. The laser light used as the pump light in this experiment had an energy density of 1.6 μJ/cm^2, and no increase in light scattering was observed even when the silica substrate was continuously irradiated with this laser light with a accumulated fluence exceeding 1.0×10^7 J/cm^2, thus confirming that the progression of laser-induced degradation could be ignored in this pump–probe experiment. We performed measurements on three samples, which were all high-purity fused silica substrates polished by CMP, identical to sample A: Sample C, on which no laser was irradiated; Sample D, which showed laser-induced degradation by being irradiated with the regeneratively amplified fs laser with a wavelength of 800 nm, an energy density of

17 mJ/cm^2, a repetition frequency of 1kHz and a pulse width of 160 fs to an accumulated fluence of 3.5×10^4 J/cm^2, namely 2.1×10^7 shots; and Sample E, in which laser-induced damage visually recognizable as damage sites was caused by 1000 shots of irradiation with an energy density of 100 mJ/cm^2 using the same fs laser.

In the evaluation, we used a relative change $\Delta R = (R - R_0)/R_0$, where R_0 is the reflected light intensity in the case where only the probe light was radiated, and R is the reflected light intensity obtained in the pump–probe experiment. The measurement results ΔR_C, ΔR_D, and ΔR_E for samples C, D, and E are plotted in Figure 4a as black squares, blue circles, and red triangles, respectively. The horizontal axis of the graph is the time delay, t, of the probe light relative to the pump light, where the peak of ΔR_C is taken as $t = 0$. ΔR_C is well-approximated by $\Delta R_{fit} = 5.5 \operatorname{sech}^2(t/(9 \times 10^{-14}))$, which is shown by the green solid line in Figure 4a, and nonlinear polarization reflecting the pulse width of the laser was observed. In contrast, ΔR_D, and ΔR_E showed temporal broadenings of about several 100 fs. Because these decay times are close to the photogenerated carrier lifetime of silica 150 fs [16,17], it is assumed the temporal changes in the reflectance were originated from the photogenerated carrier in samples D and E. In other words, in Samples D and E, we concluded that the generation probability of photogenerated carriers was higher than in Sample C because electric field enhancement occurred due to laser-induced degradation and laser-induced damage.

2.2 Spectrum analysis
To analyze this in more detail, we obtained the power spectrum by subtracting the nonlinear polarization component represented by ΔR_{fit} from ΔR_D, and ΔR_E. The results are shown by
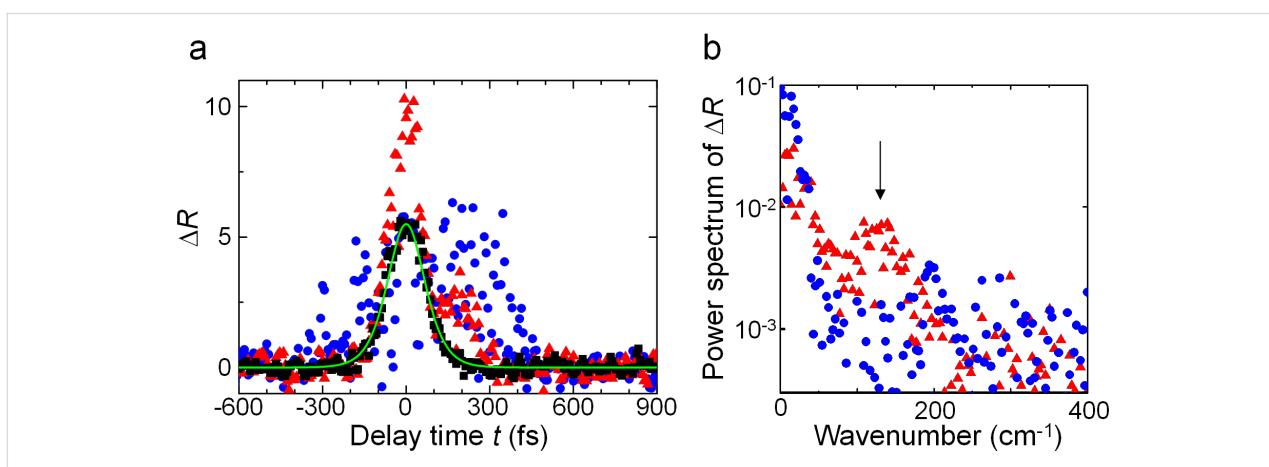

Figure 4: a) Instantaneous relative increase in reflected light intensity, ΔR, measured by pump–probe method. Black squares, blue circles, and red triangles indicate measurement results for samples C, D, and E, respectively. The solid green line indicates the approximation curve $\Delta R_{fit} = 5.5 \operatorname{sech}^2(t/(9 \times 10^{-14}))$ for ΔR_C. b) Power spectrum obtained by subtracting the ΔR_{fit} component from ΔR_D, and ΔR_E. The blue circles and red triangles indicate the analysis results for ΔR_D, and ΔR_E, respectively. The arrow indicates 128 cm^{-1}.

the blue circles and red triangles in Figure 4b, respectively. For sample D, a signal having a weak peak close to 195 cm^{-1} was obtained, whereas for sample E, a broad peak around 128 cm^{-1} was found, thus giving different signals. The peak at 128 cm^{-1} was consistent with the Raman signal of α-quartz, which is formed of six-membered rings of Si and O [18]. It has been reported that the Raman signal from silica with a specific molecular structure is increased by irradiation with fs laser light having an energy density above the LIDT [19], and sample E is also thought to be mainly formed of six-membered rings in a similar fashion. Although there is no molecular structure of silica that corresponds to the peak for sample D, the result indicates that compositional changes occur due to laser-induced degradation. As we found in section 1.1, the laser-induced degradation originates in multiphoton ionization. The laser-induced damage by fs laser occurs by multiphoton ionization and consequent avalanche ionization [3,4]. Since there are no breakdowns, it is estimated that avalanche ionization does not occur in the laser-induced degradation due to its low energy density. While the carriers generated by just multiphoton ionization are not enough to cause breakdown, they change amorphous silica to a more stable molecular structure. As also indicated in the results in section 1.2, the spectrum shifted, namely the compositional change carried on as laser-induced degradation proceeds. It provides nanoscale nonuniformity of the refractive index which increases scattering of light, decreases transmittance, and accelerates the progress of the laser-induced degradation.

Conclusion

In this paper, we focused on the degradation in performance of optical components due to continuous irradiation with laser light having an energy density below the LIDT, i.e., laser-induced degradation. We examined the degradation of fused silica substrates in response to fs laser irradiation and performed an in situ observation of the laser-induced degradation, as well as an analysis of the underlying mechanism. By monitoring the scattered light intensity versus the accumulated irradiation fluence, we succeeded in quantitatively detecting the laser-induced degradation. We confirmed that the total irradiation threshold at which laser-induced degradation starts changed depending on the size of the ultrafine structure in the surface. In addition, we also found that the spectrum of reflected light shifted as the laser-induced degradation proceeded. By analyzing the details of this behavior with a pump–probe method, we observed an increase in photogenerated carriers, and from the power spectrum, we obtained results indicating that the molecular structure of the silica undergoes compositional changes due to the laser-induced degradation.

From the findings we obtained in this study, it can be concluded that, to increase the resistance of a substrate to laser-induced de-

gradation, it is effective to improve the substrate's flatness, similarly to the case of the LIDT. In addition, because it is possible to estimate the molecular structure formed by the laser-induced degradation from the spectral information, there is a possibility of achieving more effective measures against laser-induced degradation. The measurement method employed here for the fs laser light and the flat fused silica substrates can also be applied to other types of laser and optical components and is expected to contribute to the development of optical components having high resistance to laser-induced degradation in the future.

Acknowledgements

References

1. Bliss, E. S. *Opto-electronics (London)* **1971,** *3,* 99–108. doi:10.1007/BF01424087
2. Wood, R. M. *Laser Damage in Optical Materials;* Hilger: Boston, 2002.
3. Schaffer, C. B.; Brodeur, A.; Mazur, E. *Meas. Sci. Technol.* **2001,** *12,* 1784–1794. doi:10.1088/0957-0233/12/11/305
4. Mao, S. S.; Quéré, F.; Guizard, S.; Mao, X.; Russo, R. E.; Petite, G.; Martin, P. *Appl. Phys. A* **2004,** *79,* 1695–1709. doi:10.1007/s00339-004-2684-0
5. Génin, F. Y.; Salleo, A.; Pistor, T. V.; Chase, L. L. *J. Opt. Soc. Am. A* **2001,** *18,* 2607–2616. doi:10.1364/JOSAA.18.002607
6. Bloembergen, N. *Appl. Opt.* **1973,** *12,* 661–664. doi:10.1364/AO.12.000661
7. Stuart, B. C.; Feit, M. D.; Herman, S.; Rubenchik, A. M.; Shore, B. W.; Perry, M. D. *Phys. Rev. B* **1996,** *53,* 1749–1761. doi:10.1103/PhysRevB.53.1749
8. Jia, T. Q.; Li, R. X.; Liu, Z.; Xu, Z. Z. *Appl. Phys. A* **2002,** *74,* 503–507. doi:10.1007/s003390100903
9. Becker, J.; Bernhardt, A. *Proc. SPIE* **1994,** *2114,* 703–713. doi:10.1117/12.180881
10. ISO 11254–2, *Test methods for laser induced damage threshold of optical surfaces. Part 2: S on 1 test*, International Organization for Standardization. 2001.
11. Cook, L. M. *J. Non-Cryst. Solids* **1990,** *120,* 152–171. doi:10.1016/0022-3093(90)90200-6
12. Yatsui, T.; Hirata, K.; Nomura, W.; Tabata, Y.; Ohtsu, M. *Appl. Phys. B* **2008,** *93,* 55–57. doi:10.1007/s00340-008-3142-z
13. Hirata, K. *Proc. SPIE* **2011,** *7921,* 79210M. doi:10.1117/12.875808
14. Miura, K.; Qiu, J.; Inouye, H.; Mitsuyu, T.; Hirao, K. *Appl. Phys. Lett.* **1997,** *71,* 3329–3331. doi:10.1063/1.120327

15. Sudrie, L.; Couairon, A.; Franco, M.; Lamouroux, B.; Prade, B.;
    Tzortzakis, S.; Mysyrowicz, A. *Phys. Rev. Lett.* **2002,** *89,* 186601.
    doi:10.1103/PhysRevLett.89.186601
16. Audebert, P.; Daguzan, P.; Dos Santos, A.; Gauthier, J. C.;
    Geindre, J. P.; Guizard, S.; Hamoniaux, G.; Krastev, K.; Martin, P.;
    Petite, G.; Antonetti, A. *Phys. Rev. Lett.* **1994,** *73,* 1990–1993.
    doi:10.1103/PhysRevLett.73.1990
17. Saeta, P. N.; Greene, B. I. *Phys. Rev. Lett.* **1993,** *70,* 3588–3591.
    doi:10.1103/PhysRevLett.70.3588
18. Bates, J. B. *J. Chem. Phys.* **1972,** *56,* 1910–1917.
    doi:10.1063/1.1677474
19. Chan, J. W.; Huser, T.; Risbud, S.; Krol, D. M. *Opt. Lett.* **2001,** *26,*
    1726–1728. doi:10.1364/OL.26.001726

Exploring plasmonic coupling in hole-cap arrays

Thomas M. Schmidt[1], Maj Frederiksen[1], Vladimir Bochenkov[1,2]
and Duncan S. Sutherland[*1,§]

Abstract

The plasmonic coupling between gold caps and holes in thin films was investigated experimentally and through finite-difference
time-domain (FDTD) calculations. Sparse colloidal lithography combined with a novel thermal treatment was used to control the
vertical spacing between caps and hole arrays and compared to separated arrays of holes or caps. Optical spectroscopy and FDTD
simulations reveal strong coupling between the gold caps and both Bloch Wave-surface plasmon polariton (BW-SPP) modes and
localized surface plasmon resonance (LSPR)-type resonances in hole arrays when they are in close proximity. The interesting and
complex coupling between caps and hole arrays reveals the details of the field distribution for these simple to fabricate structures.

Introduction

The interaction of metal nanostructures, both highly symmetric
and asymmetric, with light has been investigated extensively in
the last years. Localized surface plasmon resonances (LSPR's)
at these structures provide a wealth of interesting phenomena
with a broad range of proposed applications [1]. Structures have
been fabricated by both chemical synthesis, e.g., nanoshells [2],
nanoeggs [3], nanorice [4] and lithography, e.g., nanodiscs [5],
nanorings [6] to nanocaps [7] giving different degrees of ease of
fabrication and control of shape, relative position and orienta-
tion of structures. Nanocaps have attracted interest by
combining simple production [8] and both unique properties
such as bending of light [9] resulting from reduced symmetry
compared to nanoshells and other more common plasmonic
effects such as enhanced local electromagnetic fields [8].
Another related plasmonic structure of interest relates to
nanocavities either as isolated structures such as nanoholes in
metallic thin films [10] or as interconnected nanocavities in a
metallic matrix [11]. LSPR's at cavities and nanoholes can

couple to the propagating surface plasmon polariton (SPP) modes as well as generate the high local electromagnetic fields. These enhanced local electromagnetic fields of the different plasmonic structures have been applied to enhance optical transitions such as in Raman spectroscopy [12] (as surface enhanced Raman scattering – SERS) and fluorescence [13] (as surface enhanced fluorescence – SEF) where the strong electromagnetic fields can greatly enhance excitation and emission. Other uses of the enhanced local electromagnetic fields are as nanoscale lenses to carry out high resolution near field optical lithography [14], as antennas [15] for directing light emission at the nanoscale or increasing interaction cross-sections for example for light harvesting applications [16].

Interactions between resonances at plasmonic nanostructures in close proximity can significantly alter their optical properties and give spectral tuneability and higher localized fields. These highly interesting interactions can be explained by the hybridization model which describes the complex plasmonic interactions as a combination of elementary plasmon modes [17]. Good examples of this are seen in the cases of nanorice [4], nanostars [18], semishells [8] and nanoparticle dimers [19,20]. Such hybridized systems have shown promise for enhancement of plasmonic sensing systems [2,4,21]. Nanocap-hole arrays are extremely simple coupled structures to produce based on colloidal lithography with the potential for use in sensing applications. They have recently been applied for SERS enhancement [22].

Here we focus on investigating the optical properties of short range ordered arrays of nanocap-holes coupled structures and interpret them in terms of hybridization of their more elementary components. We fabricate these structures utilizing colloidal monolayer masks as a template and compare experimental extinction data to finite-difference time-domain (FDTD) simulations. We show strong coupling of the dipolar and quadrupolar nanocap resonances with the Bloch wave-SPP (BW-SPP) and LSPR type hole array resonances.

Experimental
Nanostructure design
Figure 1a shows a schematic of the design of the plasmonic gold structures fabricated by colloidal lithography: Cap structure, hole structure and cap/hole structure. The fabrication route can be seen on the schematic in Figure 1d. The common mask system for fabricating all the structures means that they have the same distribution and orientation as well as similar geometric features. Due to the needs of the fabrication process the gold structures are in contact with the polystyrene (PS) particle, glass substrate and/or the clean room tape which modify the local dielectric environment of the nanopar-

ticle and have to be taken into account when understanding the spectral features.

Materials
White sulfate latex polystyrene particles with diameter of 0.11 μm were obtained from Invitrogen Denmark. Deionized water with 18.2 MΩ resistivity from a Millipore Milli-Q water system. Poly(methyl methacrylate) (PMMA) (M_w 120,000), Polystyrene (M_w 280,000), PDDA (poly(diallydimethylammonium chloride)) (M_w 200,000–350,000), PSS (poly(sodium 4-styrenesulfonate)) (M_w 70,000) and toluene were obtained from Aldrich Denmark. Poly aluminum chlorohydrate (PAX XL 60) was obtained from Kemwater Denmark. Round glass cover slides of soda-lime glass # 3 from Menzel–Gläser (d = 24 mm) Germany. Silicon wafers (thickness of 356–406 μm with a diameter of 76.2 ± 0.63 mm), pre-cut about half way through for controlled breaking from SI-MAT Germany.

Sample preparation
Sample preparations were done as previously described by Schmidt et al. [23]. The round glass cover slide or silicon wafer substrates were cleaned by sequential ultrasonic agitation for 10 min in acetone, ethanol and deionized water followed by drying under N_2 flow. Just before fabrication the surface was cleaned from any residual organic contaminated by a 20 min UV/ozone treatment in a purpose built machine with the sample placed ≈10 mm from a 100 W mercury grid lamp from BHK Inc. Colloidal assembly of the nanoparticles to generate dispersed colloidal monolayers masks was carried out by an approach described elsewhere [24]. In brief the surfaces were modified with a polyelectrolyte triple layer by sequential deposition from a 2% w/v PDDA, a 2% w/v PSS and a 5% w/v PAX XL 60 all in deionized water solution. Each layer was deposited by sequential exposure of the surface to the solution for 30 s, rinsing in deionized water for 30 s and dried under N_2 flow.

The assembly of the colloidal particles onto the triple layer modified substrates was then carried out by exposure of the dry substrates to a 0.2% solution of polystyrene particles in deionized water for 120 s followed by rinsing in deionized water for 60 s and careful drying under N_2 flow. Care was taken to dry quickly and to prevent rewetting of the surface. The assembled colloidal monolayer masks were modified by evaporation of a thin film of gold (between 10–40 nm in thickness) utilizing a homebuilt system for Electron Beam stimulated Physical Vapor Deposition, EB-PVD, (2 kV e-gun, base pressure 1×10^{-7} Torr, deposition rate of 0.1–0.4 nm/s) to generate cap/hole arrays. The cap and hole arrays were generated in the same process and were separated physically by tape striping with a transparent
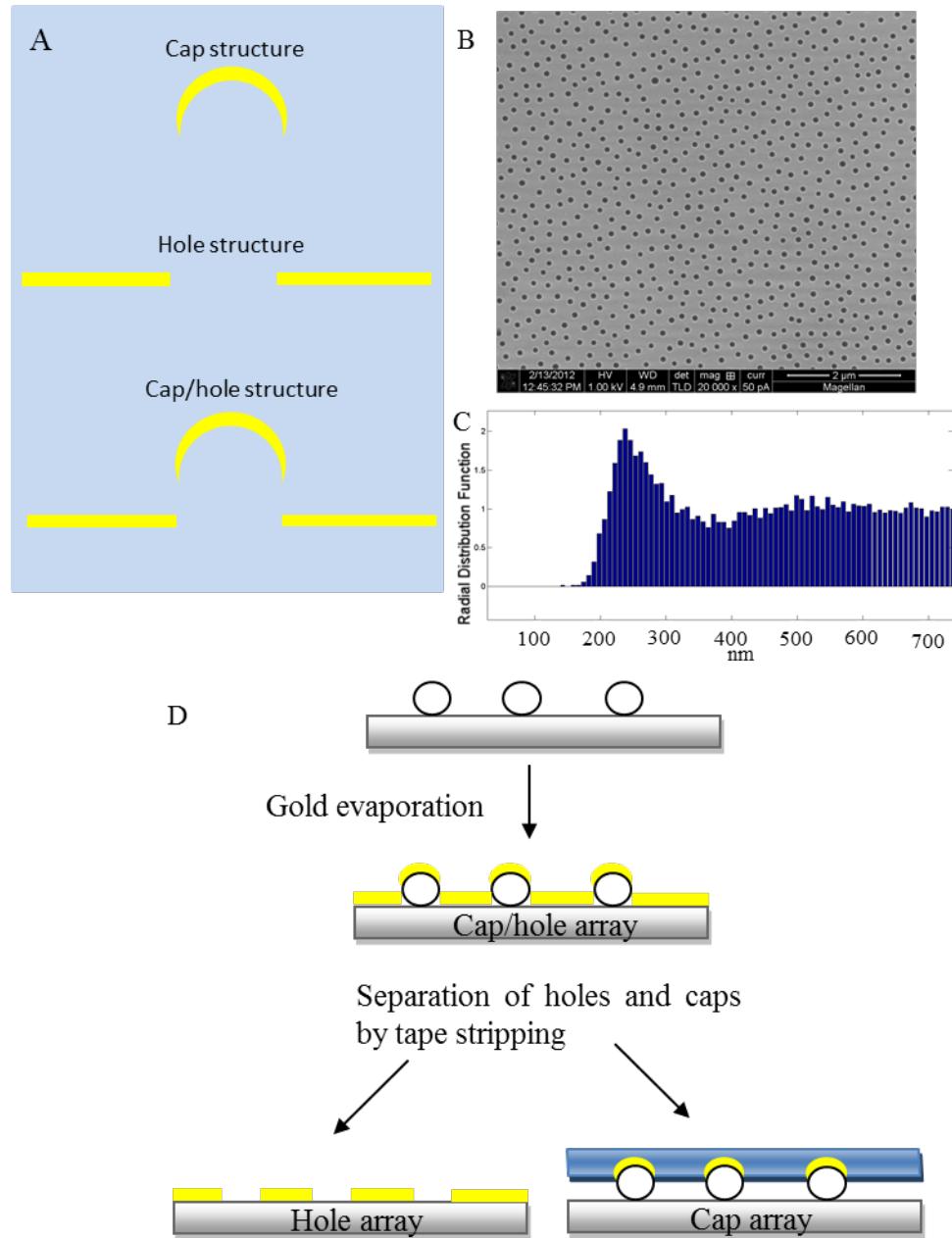
Figure 1: A) Schematic of the design of the plasmonic gold structures fabricated by colloidal lithography. B) SEM image showing the distribution of a 110 nm hole array in 20 nm thin Au film after removal of the gold-caps by tape stripping. C) Radial distribution function showing the characteristic average spacing between holes of the same hole array. D) Fabrication route for the plasmonic structures.

adhesive tape (90 μm thick blue PVC Tape from Semiconductor Production Systems). The tape was subsequently placed onto a glass substrate for characterization. The tape stripped cap/hole arrays left behind hole arrays.

Characterization

The optical spectra were measured using a UV-3600 UV–vis–NIR spectrophotometer from Shimadzu with a wave-length range of 185–3300 nm in dual beam mode. A spectral resolution of 5.0 nm and a sampling interval of 1.0 nm were used. An area of around 10 mm high and 3 mm wide was probed. AFM images were taken with an atomic force microscopy (AFM) from Multimode with Veeco nanoscope 5 used in tapping mode. Olympus OMCL-TR400PSA-2 cantilevers with a resonant frequency between 11 and 34 kHz and a tip radius of less than 20 nm were used. The SEM images

were taken with a Nova 600 NanoLab XHR Magellan scanning electron microscope (SEM) from FEI generally with energies of 1–5 kV and nominal spot size ≈1 nm.

Computer simulations of extinction spectra and charge/field plots analysis were carried out using the finite-difference time-domain method (FDTD Solutions, Lumerical). The gold material was modeled using the fit to experimentally measured dielectric data [25]. Constant refractive index values $n = 1.58$ and $n = 1.52$ were used for polystyrene and glass, respectively. Hole arrays were simulated on glass in air, the combined arrays were simulated on glass with the caps on top of polystyrene spheres 110 nm in diameter. For closer spacing of cap and hole arrays the polystyrene spheres were truncated at the glass interface. The caps were simulated in air. The non-uniform mesh was applied to the whole simulation box and a uniformly fine-meshed region with the grid size of 1.5 nm was used to reproduce the curved structures and avoid the sharp edges. For all the simulations the direction of the light propagation is normal to the surface and the polarization horizontal in the figure plane as in the experiment. The charge and field plots were analyzed for the resonance frequencies, obtained from simulated spectra.

Results and Discussion

The colloidal lithography approach enables the simple and robust fabrication of short range ordered (SRO) arrays of nanostructures [5,26-28]. Figure 1b shows the distribution of a hole array after removal of the capped particles by tape stripping. The well separated short range ordered array is resulting from the electrostatic repulsion between already adsorbed particles and later arriving ones during the particle deposition step of the colloidal lithography fabrication. The radial distribution function of the holes can be seen in Figure 1c. SRO hole arrays fabricated by this approach have been studied in terms of their optical response and been used in sensing applications extensively in recent years [29-34]. The arrays of structures of the different sample types studied here are made from the same specific colloidal mask pattern giving them identical distributions, see Figure 1d. The structures have a characteristic center to center spacing around 220–250 nm and average diameter of 110 nm with a standard deviation of 5 nm.

We explore the plasmonic resonances of SRO hole arrays, cap arrays and coupling between cap and hole arrays by UV–vis extinction spectroscopy. Figure 2 shows experimental extinction spectra of arrays of holes, arrays of caps or of coupled Cap/hole arrays schematically shown in Figure 1a formed from dispersed monolayers of 107 nm colloids with Au film thickness of 20 nm. The cap array and hole array are generated by physically separating the coupled cap/hole arrays by tape striping and thus show the extinction spectra of the specific cap

and hole arrays used in the cap/hole arrays. The coupled cap/hole arrays cannot be explained by a simple addition of the two component spectra (even taking into account that the cap array is red shifted by the higher refractive environment resulting from the tape used for striping) suggesting that coupling is occurring. We first explore and understand the origin of the component spectra. The hole array shows a resonant peak that can be seen at 620 nm and a dip at around 700 nm. The exact origin of these two spectral features has been debated in recent years [29,33-35] and what has emerged is that coupling of SPP-modes with LSPR modes appears to be occurring. Sannomiya et al. [33] have assigned the peak as a collective BW-SPP type mode that can be excited by the incoming EM-field and the dip as a more localized resonance with the holes comparable to LSPR's in metal disks or other cavities [11]. Recent work has focused on refractive index sensitivity increases observed when restructuring the substrate around the holes and have suggested that the both the BW-SPP and LSPR type assigned resonances have considerable localized character [34]. Here we have carried out FDTD simulations of holes on glass substrates as hexagonally close packed periodic arrays in a similar way to previous work [33] and plot the field and charge distributions in 3D in an effort to understand the origin of these two resonances (the peak and dip seen experimental in Figure 2 and via simulations in Figure 3a). So we have experimental SRO arrays but the optics are described by simulations of periodic arrays. The field plots for the dip position (Figure 3c) shows a clear dipole resonance localized at the contact point between the edge of the hole and the substrate. The charge plots for this resonance (Figure 3c) show that the charge within the edge of the hole reflects the charge of the surrounding upper and lower gold surfaces which resembles a first order SPP mode. The localized field characteristics and the extended charges on the surface imply a coupling between an SPP mode and a more localized
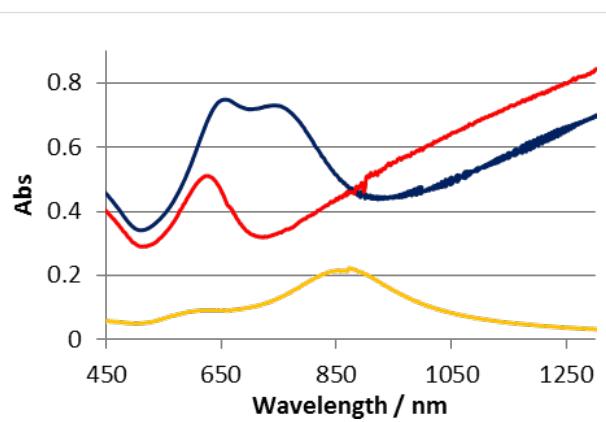

Figure 2: Extinction spectra of arrays of cap (yellow), hole (red) and cap/hole (blue) structures with 110 nm diameter in 20 nm gold on glass substrates.

mode. It can be regarded as an in phase coupling of a dipolar cavity mode with the first order SPP Bloch wave mode. The redistribution of the field to the substrate side of the metal film is expected from the high refractive index substrate and has important ramifications for the refractive index sensitivity of the structures [36]. The picture for the higher energy (peak) position is more complex. The field shows again a high magnitude at the edge of the hole with a redistribution to the substrate side (down in Figure 3b) but clearly less localized to the hole itself than the field plots for the dip. The charge plots surprisingly show a different phase at the hole wall compared to the surrounding metal surfaces. We note that although FDTD calcu-

lations similar to these have been carried out before, apparently the charge distributions have not been plotted previously. The charge distributions can be understood to arise from a BW-SPP wave of higher order as shown in Figure 4. The frequency of a second order BW-SPP wave would not coincide with that of any dipolar hole LSPR resonance. The local field distribution arises then from the shape of the metal surface rather than a localized resonance. The excitation of different order SPP modes directly via holes in metal films (as opposed to indirectly via coupling to LSPR resonances at holes) was suggested from theoretical approaches [35]. Here we clarify the assignment of the BW-SPP modes in our system (which is typical of
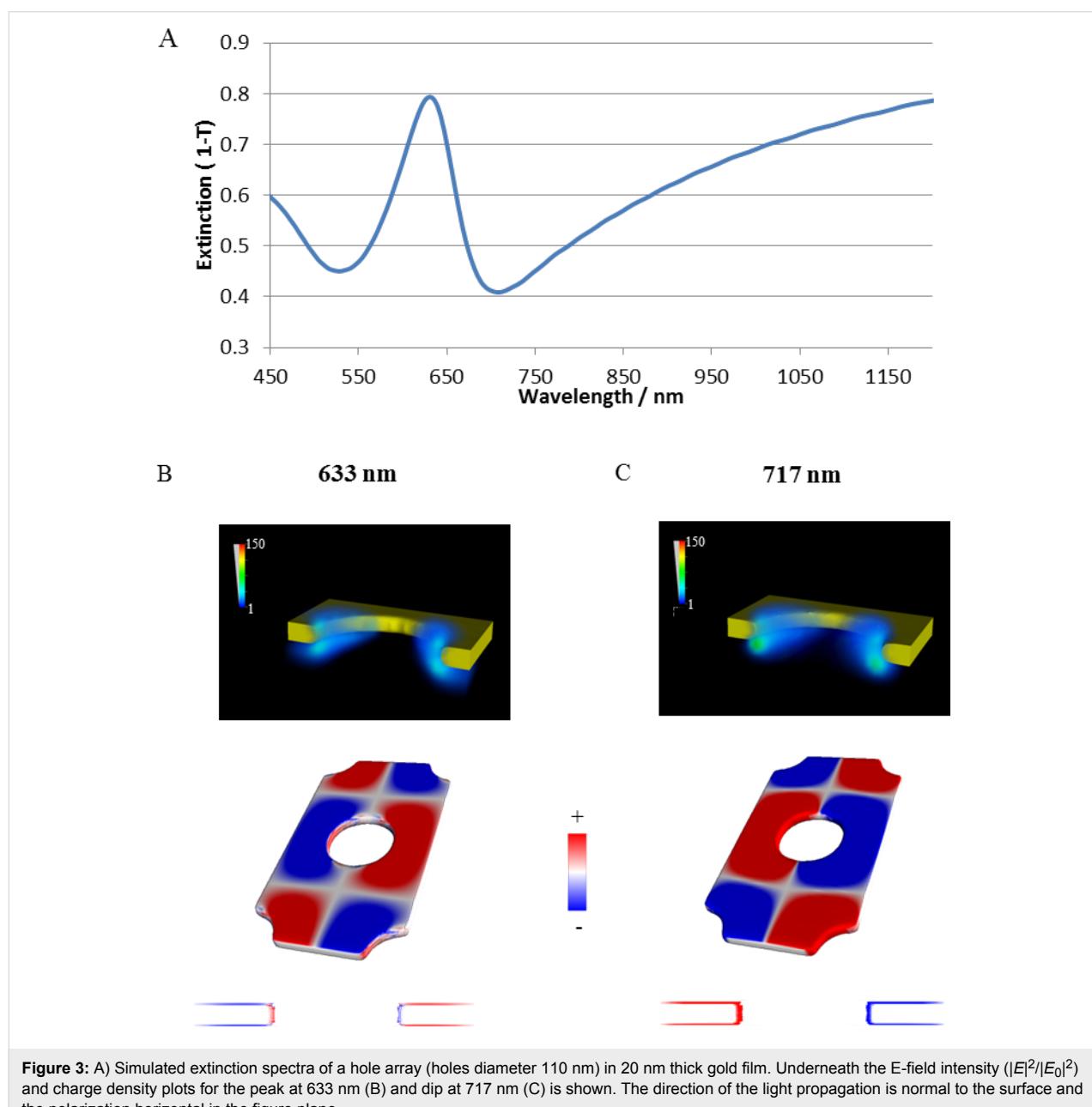
Figure 3: A) Simulated extinction spectra of a hole array (holes diameter 110 nm) in 20 nm thick gold film. Underneath the E-field intensity ($|E|^2/|E_0|^2$) and charge density plots for the peak at 633 nm (B) and dip at 717 nm (C) is shown. The direction of the light propagation is normal to the surface and the polarization horizontal in the figure plane.

the systems used currently [33,34] in literature) as a second order SPP mode, with the localized distribution of the field arising from the abrupt presence of a hole in the metal film rather than an LSPR type character. We assign the dip to be a bonding hybridization of dipolar LSPR modes at the holes and a first order SPP mode. These assignments are consistent with the recent experimental and theoretical reports [30,33].
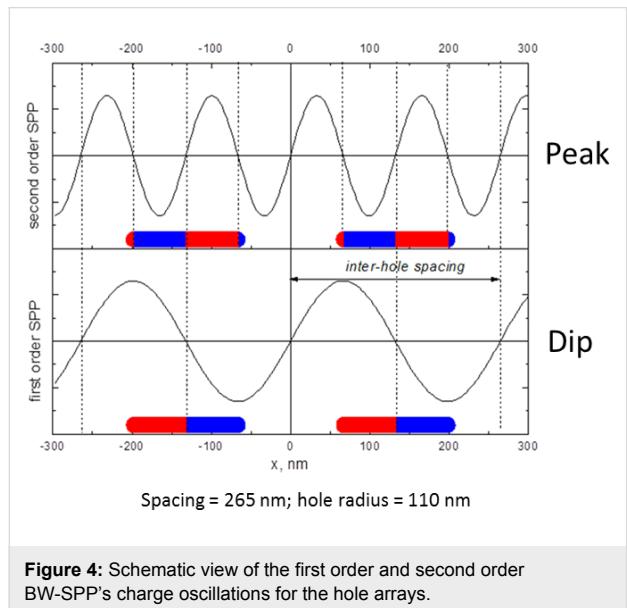
Figure 4: Schematic view of the first order and second order BW-SPP's charge oscillations for the hole arrays.

The cap array shows a main LSPR peak at 860 nm and a minor LSPR peak at approximately 610 nm. This spectral profile has previously been identified as corresponding to dipolar and quadrupolar modes respectively [37]. FDTD simulations of caps were carried out with caps immersed in air and simulated extinction spectra are shown in Figure 5a. The forms of the experimental spectra are reproduced identifying the two resonances: a low energy resonance with a relatively high intensity and a high energy but low intensity resonance. E-field intensity ($|E|^2/|E_0|^2$) and charge density plots (shown in Figure 5b) confirm the low energy resonance as a dipolar mode and the high energy resonance as a quadrupolar mode. This is in accordance with previous studies of semi-shells [37,38]. The spectral position of the experimental cap resonances are red shifted by the higher refractive index of the polymeric tape.

The extinction spectrum of as-prepared cap/hole array in Figure 6a (blue) contains two LSPR peaks one at 650 nm and one at 740 nm. We have experimentally explored the existence of coupling between the cap and hole arrays by a novel approach to vary the vertical spacing between the arrays. We make use of the glassy properties of the templating polystyrene colloids by heating the particles to temperatures close to and above the glass transition of polystyrene to allow reshaping of

the colloid giving increased wetting of the silica surface and thereby reducing the vertical distance between the caps and holes. Any coupling between caps and hole arrays should be strongly distance dependent. Figure 6a shows experimental spectra of cap/hole arrays after no thermal treatment (blue) or heating to 116 °C (red) or 125 °C (green) respectively (the temperatures should be compared to the glass transition of bulk PS (ca. 106–110 °C). AFM measurements confirmed that the height of the caps relative to the gold surface is reduced from ≈120 nm to 85 nm hole arrays (see Supporting Information File 1, Figure S1) as a result of reshaping of the colloids with the highest temperature implying that the gap between the lower rim of the caps and the upper edge of the hole array is <10 nm. The extinction spectra reveal a systematic red shift in the low energy peak for the higher temperature thermal treatments. While the reshaping of the PS particle can have resulted in a change of the dielectric environment around the cap and resulted in some shift in the position of the resonance peaks purely from a refractive index sensitivity origin, the magnitude of the change in the spectral profile with decreasing gap between the caps and hole arrays strongly supports the idea of coupling between them.

To visualize the plasmonic modes of cap/hole array structures FDTD calculations of the combination of the SRO hole arrays (seen in Figure 3) and caps in appropriate refractive index were made. Calculated extinction spectra are shown in Figure 6b for a distance of 55 nm (blue) and 45 nm (red) between the edge of a cap and the top surface of the gold film, respectively. The form of the spectra with the red shift of the dominant peak and associated peak splitting when reducing the distance between the cap and hole arrays is reproduced. A higher energy peak (554 nm) observed in the calculated spectra is clearly defined which is present in the experimental spectral only as a weak shoulder. The field and charge plots for the closest separation configuration are shown in Figure 7b–e for the three peaks seen in the calculated spectra (554 nm, 657 nm, 803 nm) as well as the dip at long wavelength (1045 nm). The charge plots reveal that the highest energy resonance results from the coupling between a quadrupolar cap resonance and the BW-SPP (higher energy) hole resonance. The charges at the lower edge of the cap are in phase with the charges on the inside of the hole which apparently leads to a shift to higher energy by electro-static destabilization. The three lower energy resonances (the two peaks and the low energy dip) result from coupling between the dipolar cap resonance and hole resonances. The peak at 657 nm and the dip at 1045 nm can be understood in terms of in phase (anti-bonding) and out of phase (bonding) coupling respectively between the dipolar cap peak and localized hole resonance (seen as the lower energy dip in the hole spectra (Figure 3a and identified as a coupling between a dipolar LSPR
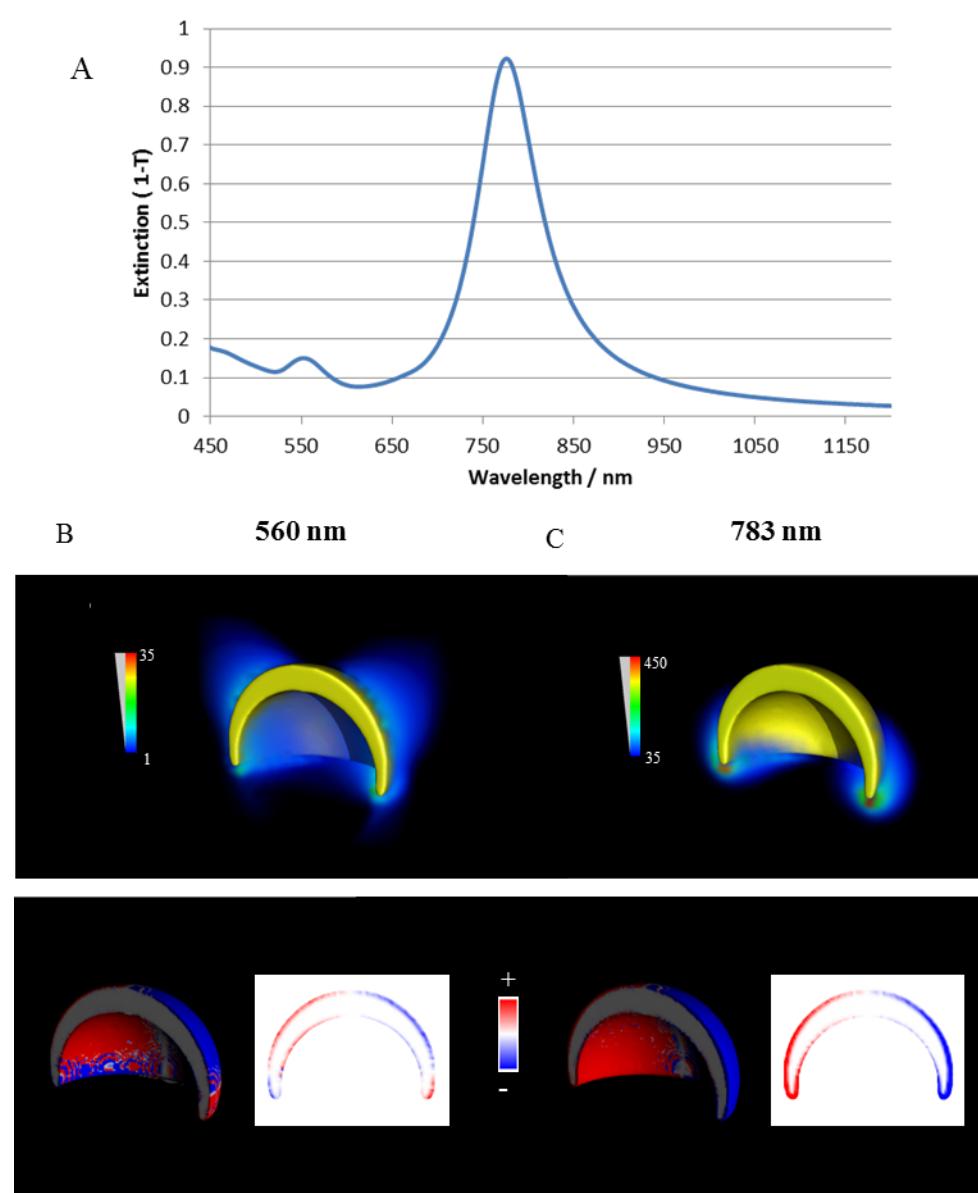
Figure 5: A) Simulated extinction spectra of a 20 nm thick gold cap (110 nm in diameter). Underneath the E-field intensity ($|E|^2/|E_0|^2$) and charge density plots for the peaks at 560 nm (B) and 783 nm (C) are shown. The direction of the light propagation is normal to the surface and the polarization horizontal in the figure plane.

cavity mode and the first order BW-SPP). The bonding lower energy resonance (dip at 1045 nm) results from a shift to lower energy driven by a simple electrostatic stabilization. The anti-bonding higher energy resonance (peak at 657 nm) results from a shift to higher energy resulting from electrostatic destabilization around between the hole edge and the lower rim of the cap. The elemental hole plasmon is largely shifted to the lower surface of the metal as a result of the high dielectric substrate. The anti-bonding higher energy peak shows the same field distribution as the elemental hole resonance, while the electrostatic stabilization in the bonding mode leads to a redistribution

of the field to the gap between the upper edge of the hole and the lower rim of the cap. The broad and strong resonance at 803 nm interestingly shows a different phase at the upper and lower metal surfaces which indicates a role for the dark anti-symmetric SPP mode (here revealed as an anti-symmetric BW-SPP mode by coupling to the bright dipolar cap mode). The significant coupling to the far field for this mode results from the large structural asymmetry between the cap and the BW-SPP. The field distributions, particularly for the two anti-symmetric modes (peak at 803 nm and dip at 1045 nm) show a strong field confinement between the cap and the hole with field

Figure 6: A) Extinction spectra of 110 nm PS particle gold cap/hole array with a gold film thickness of 30 nm where samples were not heated (blue) or post-heated to 116 °C (red) or 125 °C (green). B) Simulations of the non-heated structure in 6a (Blue) and with the cap lowered 10 nm (red).
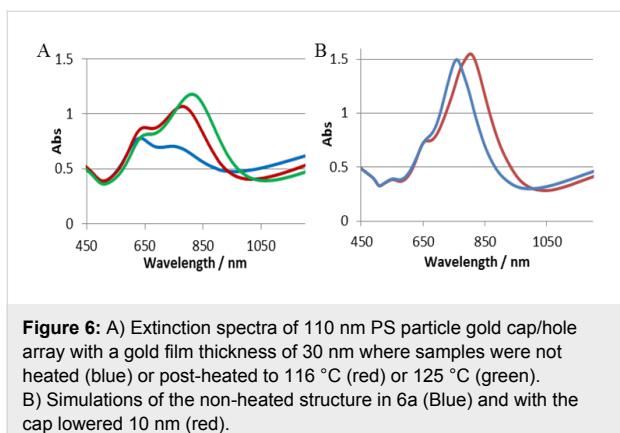
enhancement up to 25 and 29. Figure 8 shows the coupling schemes schematically superimposed on the calculated extinction spectra for the elementary cap and hole spectra (right and left respectively) and the coupled system (central).

Conclusion

We have studied the coupling between elementary cap and hole resonances. The cap/hole system is easy to produce and here we present a novel method to increase the coupling between cap arrays and hole arrays utilizing the glass transition of polystyrene colloidal particles used as a templating mask. The strong coupling results in localization of high field sites between the cap and the upper edges of the holes which has


Figure 7: A) Simulated extinction spectra of a 20 nm thick cap/hole structure (diameter 110 nm). Underneath the E-field intensity ($|E|^2/|E_0|^2$) and charge density plots for the peaks at 554 nm (B), 657 nm (C), 803 nm (D) and dip at 1045 nm (E) are shown. In the 3D charge density plots insets of the hole parts without the cap are shown from the bottom and the top for easier presentation of the charges at the gold film surface. The cap was still taken into account for these plots. The direction of the light propagation is normal to the surface and the polarization horizontal in the figure plane.

Figure 8: Hybridization diagram of the gold cap/hole structures showing the coupling between the hole and cap modes.

been used in recent work to enhance optical processes [22] . We provide a detailed description of the modes, interestingly identifying bonding between the caps and both bright symmetric and dark antisymmetric SPP modes. The coupling of LSPR modes to dark anti-symmetric SPP modes has not to our knowledge been previously reported. The coupling present in this simple to fabricate system can be used both to study dark SPP modes and/or for rational design of sensors through plasmon enhancement of optical processes (e.g., SERS or SEF) and/or engineering of the near field (lifting the SPP modes out of the substrate) for refractive index sensing.

Supporting Information

Supporting Information File 1

AFM measurements of the height from the gold film surface to the gold cap on the top the PS particle. [http://www.beilstein-journals.org/bjnano/content/supplementary/2190-4286-6-1-S1.pdf]

Acknowledgements

References

1. Willets, K. A.; Van Duyne, R. P. *Annu. Rev. Phys. Chem.* **2007,** *58,* 267–297. doi:10.1146/annurev.physchem.58.032806.104607
2. Tam, F.; Moran, C.; Halas, N. J. *J. Phys. Chem. B* **2004,** *108,* 17290–17294. doi:10.1021/Jp048499x
3. Wang, H.; Wu, Y. P.; Lassiter, B.; Nehl, C. L.; Hafner, J. H.; Nordlander, P.; Halas, N. J. *Proc. Natl. Acad. Sci. U. S. A.* **2006,** *103,* 10856–10860. doi:10.1073/pnas.0604003103
4. Wang, H.; Brandl, D. W.; Le, F.; Nordlander, P.; Halas, N. J. *Nano Lett.* **2006,** *6,* 827–832. doi:10.1021/Nl060209w
5. Hanarp, P.; Käll, M.; Sutherland, D. S. *J. Phys. Chem. B* **2003,** *107,* 5768–5772. doi:10.1021/Jp027562k
6. Aizpurua, J.; Hanarp, P.; Sutherland, D. S.; Käll, M.; Bryant, G. W.; García de Abajo, F. J. *Phys. Rev. Lett.* **2003,** *90.* doi:10.1103/Physrevlett.90.057401
7. Takei, H.; Himmelhaus, M.; Okamoto, T. *Opt. Lett.* **2002,** *27,* 342–344. doi:10.1364/ol.27.000342
8. Ye, J.; Van Dorpe, P.; Van Roy, W.; Lodewijks, K.; De Vlaminck, I.; Maes, G.; Borghs, G. *J. Phys. Chem. C* **2009,** *113,* 3110–3115. doi:10.1021/Jp8072409
9. Mirin, N. A.; Halas, N. J. *Nano Lett.* **2009,** *9,* 1255–1259. doi:10.1021/Nl900208z
10. Rindzevicius, T.; Alaverdyan, Y.; Sepulveda, B.; Pakizeh, T.; Käll, M.; Hillenbrand, R.; Aizpurua, J.; García de Abajo, F. J. *J. Phys. Chem. C* **2007,** *111,* 1207–1212. doi:10.1021/Jp065942q
11. Dreier, J.; Eriksen, R. L.; Albrektsen, O.; Pors, A.; Simonsen, A. C. *J. Phys. Chem. Lett.* **2010,** *1,* 260–264. doi:10.1021/Jz9000664
12. Jackson, J. B.; Halas, N. J. *Proc. Natl. Acad. Sci. U. S. A.* **2004,** *101,* 17930–17935. doi:10.1073/pnas.0408319102
13. Kinkhabwala, A.; Yu, Z. F.; Fan, S. H.; Avlasevich, Y.; Müllen, K.; Moerner, W. E. *Nat. Photonics* **2009,** *3,* 654–657. doi:10.1038/Nphoton.2009.187
14. Srituravanich, W.; Pan, L.; Wang, Y.; Sun, C.; Bogy, D. B.; Zhang, X. *Nat. Nanotechnol.* **2008,** *3,* 733–737. doi:10.1038/nnano.2008.303
15. Taminiau, T. H.; Stefani, F. D.; Segerink, F. B.; van Hulst, N. F. *Nat. Photonics* **2008,** *2,* 234–237. doi:10.1038/nphoton.2008.32
16. Aubry, A.; Lei, D. Y.; Fernández-Domínguez, A. I.; Sonnefraud, Y.; Maier, S. A.; Pendry, J. B. *Nano Lett.* **2010,** *10,* 2574–2579. doi:10.1021/Nl101235d
17. Prodan, E.; Radloff, C.; Halas, N. J.; Nordlander, P. *Science* **2003,** *302,* 419–422. doi:10.1126/science.1089171
18. Hao, F.; Nehl, C. L.; Hafner, J. H.; Nordlander, P. *Nano Lett.* **2007,** *7,* 729–732. doi:10.1021/Nl062969c
19. Nordlander, P.; Oubre, C.; Prodan, E.; Li, K.; Stockman, M. I. *Nano Lett.* **2004,** *4,* 899–903. doi:10.1021/Nl049681c
20. Hao, F.; Nordlander, P.; Burnett, M. T.; Maier, S. A. *Phys. Rev. B* **2007,** *76,* 245417. doi:10.1103/Physrevb.76.245417
21. Larsson, E. M.; Alegret, J.; Käll, M.; Sutherland, D. S. *Nano Lett.* **2007,** *7,* 1256–1263. doi:10.1021/nl0701612
22. Wen, X. L.; Xi, Z.; Jiao, X. J.; Yu, W. H.; Xue, G. S.; Zhang, D. G.; Lu, Y. H.; Wang, P.; Blair, S.; Ming, H. *Plasmonics* **2013,** *8,* 225–231. doi:10.1007/s11468-012-9379-8
23. Schmidt, T. M.; Bochenkov, V. E.; Espinoza, J. D. A.; Smits, E. C. P.; Muzafarov, A. M.; Kononevich, Y. N.; Sutherland, D. S. *J. Phys. Chem. C* **2014,** *118,* 2138–2145. doi:10.1021/Jp4110823

24. Hanarp, P.; Sutherland, D. S.; Gold, J.; Kasemo, B. *Colloids Surf., A*
    2003, *214,* 23–36. doi:10.1016/S0927-7757(02)00367-9
25. Johnson, P. B.; Christy, R. W. *Phys. Rev. B* **1972,** *6,* 4370.
    doi:10.1103/PhysRevB.6.4370
26. Bochenkov, V. E.; Sutherland, D. S. *Nano Lett.* **2013,** *13,* 1216–1220.
    doi:10.1021/nl304675w
27. Dmitriev, A.; Hägglund, C.; Chen, S.; Fredriksson, H.; Pakizeh, T.;
    Käll, M.; Sutherland, D. S. *Nano Lett.* **2008,** *8,* 3893–3898.
    doi:10.1021/nl8023142
28. Fredriksson, H.; Alaverdyan, Y.; Dmitriev, A.; Langhammer, C.;
    Sutherland, D. S.; Zäch, M.; Kasemo, B. *Adv. Mater.* **2007,** *19,* 4297.
    doi:10.1002/adma.200700680
29. Prikulis, J.; Hanarp, P.; Olofsson, L.; Sutherland, D.; Käll, M. *Nano Lett.*
    2004, *4,* 1003–1007. doi:10.1021/Nl0497171
30. Schwind, M.; Kasemo, B.; Zorić, I. *Nano Lett.* **2013,** *13,* 1743–1750.
    doi:10.1021/nl400328x
31. Dahlin, A.; Zäch, M.; Rindzevicius, T.; Käll, M.; Sutherland, D. S.;
    Höök, F. *J. Am. Chem. Soc.* **2005,** *127,* 5043–5048.
    doi:10.1021/ja043672o
32. Dahlin, A. B.; Jönsson, P.; Jonsson, M. P.; Schmid, E.; Zhou, Y.;
    Höök, F. *ACS Nano* **2008,** *2,* 2174–2182. doi:10.1021/nn800254h
33. Sannomiya, T.; Scholder, O.; Jefimovs, K.; Hafner, C.; Dahlin, A. B.
    Small **2011,** *7,* 1653–1663. doi:10.1002/smll.201002228
34. Bochenkov, V. E.; Frederiksen, M.; Sutherland, D. S. *Opt. Express*
    2013, *21,* 14763–14770. doi:10.1364/oe.21.014763
35. Park, T.-H.; Mirin, N.; Lassiter, J. B.; Nehl, C. L.; Halas, N. J.;
    Nordlander, P. *ACS Nano* **2008,** *2,* 25–32. doi:10.1021/Nn700292y
36. Brian, B.; Sepúlveda, B.; Alaverdyan, Y.; Lechuga, L. M.; Käll, M.
    Opt. Express **2009,** *17,* 2015–2023. doi:10.1364/OE.17.002015
37. Cortie, M.; Ford, M. *Nanotechnology* **2007,** *18,* 235704.
    doi:10.1088/0957-4484/18/23/235704
38. Ye, J.; Verellen, N.; Van Roy, W.; Lagae, L.; Maes, G.; Borghs, G.;
    Van Dorpe, P. *ACS Nano* **2010,** *4,* 1457–1464.
    doi:10.1021/Nn901519p